PHD. DISSERTATION

UNIVERSIDAD DE GRANADA

Programa de Doctorado en Física y Ciencias del Espacio

UNIVERSIDAD NACIONAL DE COLOMBIA

Doctorado en Ciencias Física

Crecimiento higroscópico del aerosol atmosférico: aproximación mediante teledetección

Atmospheric aerosol hygroscopic growth: approaching through remote sensing

Andrés Esteban Bedoya Velásquez

GFAT Grupo Física de la Atmósfera

IISTA Instituto Interuniversitario de Investigación del Sistema Tierra en Andalucía

Unidad de Excelencia UGR

SIATA

Editor: Universidad de Granada. Tesis Doctorales
Autor: Andrés Esteban Bedoya Velásquez
ISBN: 978-84-1306-284-6
URI: http://hdl.handle.net/10481/56793

♪♫ *… Con lágrimas no se curan heridas,*

opino que no se debe de llorar, la mente

que no se dé por destruida, nació para

LEGISLAR PARA PENSAR*…*♪♫

Roberto Roena

Agradecimientos

Éste no es solo el trabajo escrito más extenso que he realizado en mi vida, sino que ha sido el más enriquecedor desde el ámbito mental, social y profesional. El orden no es en vano, pues considero que he ganado una fortaleza mental comparable con la del profesor 'X'. Creo que pasar por un doctorado es algo que te deja con algunos TOCs, o te convierte en un ser de luz (que no se gradúa), o te deja calvo por completo, o simplemente te pone una camisa de fuerza y 'pal mental'… De situarme en alguna, creo que los TOCs son lo mío en estos cuatro años. En el ámbito social, es indescriptible lo que este proceso me dejó, una cantidad amigos en latitudes inimaginables que de solo pensarlo se me olvida que mi beca de doctorado es condonable. El ámbito profesional, el cual fue mi objetivo primordial, no es que esté de último porque no crecí en este aspecto; por el contrario, siento que venía dando pasos pequeños y temerosos, y ahora son largos y estructurados: el avance ha sido sorprendente. Un aspecto que quería dejar para el final es el personal/sentimental/amoroso o en pocas palabras mi esposa, que durante este proceso la convertí en mi saco de boxeo, mi psicóloga, mi auditora, por usar una palabra … en mi TODO. Considero que de las decisiones 100 % acertadas que se pueden tomar en la vida, yo invertí una o la única con el SÍ que nos dimos hace casi cuatro años ya.

Comenzando con la esperada alfombra roja, los primeros en desfilar serán las personas que que me acompañaron más de cerca para conseguir este logro, mi esposa, mis padres, mi abuela y una mención muy especial para mis suegros y mi cuñado, todos conforman mi entorno de fortaleza, los que me llevaron de la mano día tras día y no me permitieron dejar de soñar con mi pasión, investigar y enseñar. Desde niño siempre te consideré como un ejemplo a seguir como persona dedicada y perseverante, una luchadora incansable, entonces a ti madre te sigo dedicando estos logros, porque son nuestros. A mi padre por las jornadas interminables en las cuales me enseñabas lo que era la vida, transmitiéndome el deseo por seguir estudiando siempre. A mi abuela por su inagotable amor, sus comidas deliciosas y su 'chispa' de felicidad siempre que me veía llegar a casa. A mi Carolina, mi compañera de viaje (Pa' donde sea va), mi mujer alegre, soñadora, mi apoyo, mi fuerza, mi deseo de seguir, mi alimento espiritual… te viviré eternamente agredecido por todos los instantes que me has regalado en la vida y por tanto amor incondicional.

Desde el aspecto académico, un sincero agradecimiento a mis directores, el Dr. Juan Luis Guerrero Rascado y el Dr. Carlos David Hoyos Ortiz, no me resta sino agradecerles por su paciencia, orientación, palabras de aliento y efectividad en cada uno de los pasos que fuimos dando en este proceso. A la profesora Elena Montilla por ser un pilar tanto en el aspecto personal como en científico, al igual que el profesor Lucas Alados Arboledas. Ambos no solo me acogieron en sus lugares de investigación, sino que se esforzaron porque cada día fuese muy productivo y lleno de retos. A la profesora Claudia García quiero agradecerle por estar siempre pendiente de mí, por su incondicional apoyo a nivel personal y académico/administrativo. Finalmente, al Dr. Martial Haeffelin por recibirme en su grupo durante mi estancia en SIRTA.

Este paso académico duró cuatro años, y me dejó millones de vivencias y de personas que sería imposible no mencionar, las cuales están vinculadas al gran grupo que me reavivo mi pasión por investigar. A los GFATies mi más humilde agradecimiento tanto desde el aspecto académico, pues fueron pilares invaluables este proceso, y desde lo personal, porque se conviertieron en grandes amigos. Comenzando por Pablinho, Jose, Juanito, Chabe, al amigão Greg, Roberto, Maria José, Gloria, Alberto, Juan Antonio, Fran, Anderson, Dani, Paco Pepe y Hassan. También a todas personas que vinculadas o no con alguien del GFAT, hicieron mi experiencia en Graná imposible de olvidar: a Fati, Alo, Ruth, Pili, Diana, Angie, Ronald, Antonio y ofrezco disculpas por los que se me pasen, pero seguro que les estoy muy agradecido.

Un espacio fundamental para los de siempre, los de la vida, los que así no tengan que ver con este 'atípico' mundo en el que me metí, siempre están ahí, como la bandada de hermanos (as) que nunca tuve, a Mao el 'nomo', Tulín, Carlitos el 'mente', Santi, Anita la 'prima', Lau 'tati', Raul el 'niño', Esteban el 'niche', Jota, Dani Jimenez y Caliche. Quería agradecer especialmente a Dave y Maria Nelly, grandes amigos, ustedes han sido un gran apoyo en mi vida, en mi carrera y particularmente durante este proceso en mi estabilidad mental, muchas gracias por simpre tocar la puerta así en ocasiones la casa estuviese aparentemente abandonada. Finalmente, a unas amigas relativamente nuevas en este camino de la vida, pero que no dudo seguiremos remando juntos, muchas gracias a Dani Bolaños, Manu Hoyos y Mili, con el poco tiempo de conocernos me han mostrado lo valiosa que es su amstad.

Finalmente, doy las gracias a las entidades/instituciones que me permitieron realizar este doctorado, a mi alma mater la Universidad Nacional de Colombia-sede Medellín, Universidad de Granada, IISTA-CEAMA, ACTRIS, SIRTA, AUIP, SIATA, Colciencias e ICETEX.

Muchas gracias a todos los que de manera directa o indirecta hicieron parte de este proceso

Outline

Abstract

This PhD dissertation focuses on the study of aerosol hygroscopic phenomena under real atmospheric conditions combining active and passive remote sensing measurements together with in situ and ancillary instrumentation. This work provides different methodologies for studying water uptake by atmospheric aerosol particles by using their optical and microphysical properties under changes in relative humidity.

Data acquisition was a hard task because up to three different locations were used. Firstly, data at the Andalusian Institute for Earth System Research (IISTA-CEAMA) in Granada (Spain) were considered from 2012 to 2016, including the data acquired by the SLOPE I (Sierra Nevada Lidar AerOsol Profiling Experiment) field campaign in 2016. Secondly, data at the SIATA-tower station (Sistema de Alerta Temprana de Medellín y el Valle de Aburrá), located in Medellín (Colombia) from a 3.5-year database of continuous measurements of automatic remote sensing, meteorological and in situ instruments were analyzed. Finally, database acquired at the SIRTA observatory (Site Instrumental de Recherche par Télédétection Atmosphérique) located approximately 20 km Southwest of Paris (France), allowed for analyzing 4.5 years of data from different instrumentation (remote sensing, meteorological and in situ instruments).

Active remote sensors involved in this thesis were a multiwavelength Raman lidar, Doppler lidar, and Jenoptik CHM15K, Vaisala CL31 and CL51 ceilometers. On other hand, passive remote sensors such as a Sun photometer, and RPG-HATPRO and MP3000 microwave radiometers were also used. To determine particle concentration, in situ data are taken from PM_1, $PM_{2.5}$, and the Aerosol Chemical Speciation Monitor. Finally, some meteorological sensors were used for retrieving temperature, relative humidity, and wind speed and direction.

In this work, the backscatter coefficient (β) is used to study the hygroscopic growth properties. This optical property can be retrieved by different instruements, either from Raman lidars or ceilometers. In addition, relative humidity was measured together with β obtained from the microwave radiometer and radiosondes launched during specific campaings. Other instrumentation mentioned above was used as ancillary information to this study.

The main goal of this thesis is to investigate the aerosol hygroscopicity growth process in the real atmospheric conditions. The methodology proposed is divided into temporal and vertical evolution frames. The simultaneous increase/decrease of the relative humidity and β in temporal and vertical windows, among other criteria are analyzed. This procedure leads to deeply analyze about 18 cases for vertical evolution methodology and up to 15 cases for temporal evolution. This fact allowed for establishing the database of this phenomenon at three different sites and creating innovative easy-to-apply instrumentation setups. In addition, this work helped to determine the role that organic and inorganic aerosols play in the hygroscopicity growth.

Following the same structure of a research manuscript, chapter 1 is devoted to an overview of this topic. The fundamentals basis are given in chapter 2. Chapter 3 presents the sites and instrumentation involved, focusing the attention on remote sensing instrumentation at all the stations, namely IISTA-CEAMA, SIATA-tower, and SIRTA observatory. The methodologies used in this work are presented in chapter 4, explaining the procedures to perform a temporal and vertical evaluation of the aerosol hygroscopicity under unmodified atmospheric conditions. Chapter 5 presents the results associated to the error characterization of the microwave radiometers at the IISTA-CEAMA and SIATA-tower stations, in order to define trustworthy regions of the temperature and relative humidity profiles. This characterization was performed for all-weather, free-cloud, daytime and night-time conditions to have a better understating of the instrument in terms of its accuracy and precision. Chapter 6 is devoted to an aerosol hygroscopicity growth case evaluated during the SLOPE I field campaign (16/06/2016) at the IISTA-CEAMA station. This case develops one of the methodologies stated as vertical evolution analysis of the hygroscopicity where Raman lidar, Doppler lidar, radiosondes and microwave radiometer are involved. Chapter 7 presents the results obtained under temporal evolution methodology by using relative humidity and wind speed and direction from a 30m-tower combined with attenuated backscatter from a Vaisala ceilometer, together with on-line in situ measurements of aerosol concentration. This 4.5-year study allows for deeply analyzing 8 hygroscopic growth cases at the SIRTA observatory. Chapter 8 makes an evaluation of the vertical and temporal evolution methodologies just by using automatic remote sensors (ceilometers) and microwave radiometers at both the IISTA-CEAMA and SIATA-tower stations. Finally, in chapter 9 are presented the general conclusions and perspectives of the future work. This study leads to analyze up to 18 potential aerosol

hygroscopic growth cases between vertical and temporal evaluations at the SIATA-tower station, and six at the IISTA-CEAMA station in the vertical frame.

During this thesis, some data quality assurance tests have been carried out to the multiwavelength Raman lidar system. The measurements with lidar have been performed following the measurement protocols proposed by EARLINET. In order to retrieve optical products, the data- pre-processing have been done with lidar and ceilometer systems and also calibrations to the microwave radiometer were performed to assure the optimal operation. The error propagation involved in optical and hygroscopic properties retrieved has been calculated using the Monte Carlo technique.

The results obtained in this thesis establish a remote sensing database of the hygroscopicity properties, which will have an impact in the future studies about the role of certain aerosol emissions and their interaction with water vapor linked to their effect in the radiative forcing calculations.

Resumen

Esta tesis doctoral se centra en el estudio del fenómeno de crecimiento higroscópico del aerosol en condiciones atmosféricas reales, combinando medidas de detección remota activa y pasiva, junto con in situ e instrumentación auxiliar. Este estudio proporciona diferentes metodologías para el estudio de la captación de agua por las partículas de aerosol atmosférico usando sus propiedades ópticas y microfísicas bajo cambios de humedad relativa.

La adquisición de los datos fue una tarea difícil puesto que en este trabajo se usaron tres estaciones en lugares diferentes. La primera, en el Instituto Interuniversitario de Investigación del Sistema Tierra en Andalucía (IISTA-CEAMA) en Granada (España). Allí se usó un total de 5 años de información (desde 2012 hasta 2016), incluyendo los datos de la campaña SLOPE I (Sierra Nevada Lidar AerOsol Profiling Experiment) en 2016. El segundo es la estación de la torre SIATA (Sistema de Alerta temprana de Medellín y el Valle de Aburrá), ubicada en Medellín (Colombia). En esta ciudad fue posible analizar 3.5 años de medidas continuas de detección remota, datos meteorológicos e in situ. Finalmente, en el observatorio del SIRTA (Site Instrumental de Recherche par Télédétection Atmosphérique) ubicado aproximadamente 20 km al suroeste del centro de la ciudad de París (Francia) fue posible usar la infraestructura y la base de datos de 4.5 años de diferente instrumentación (detección remota, meteorológica e in situ).

Los sensores remotos involucrados en esta tesis fueron un lidar multiespectral Raman, un lidar Doppler y los ceilómetros CHM15K, Vaisala CL31 y CL51. Por otro lado, tambien se usaron un fotómetro solar y los radiómetros de microondas RPG-HATPRO y MP3000. Para determinar la concentración de partículas, se usaron datos in situ de PM_1, $PM_{2.5}$ y el ACSM (por sus siglas en inglés: Aerosol Chemical Speciation Monitor). Finalmente, se usaron algunos sensores para obtener temperatura, humedad relativa y velocidad y dirección de viento.

En este trabajo el coeficiente de retrodispersión (β) se usa para estudiar las propiedades de crecimiento higroscópico. Esta propiedad óptica puede ser obtenida con diferentes instrumentos, tanto por los sistemas lidar Raman como por ceilómetros. Además, la humedad realtiva fue medida junto con β, obtenida con el radiómetro de microondas y radiosondas lanzadas durante campañas específicas. La restante

instrumentación mencionada anteriormente se emplea como información auxiliar para este estudio.

El objetivo principal de esta tesis es investigar el proceso de crecimiento higroscópico del aerosol en condiciones atmosféricas reales. La metodología propuesta está dividida en marcos de evolución temporal y vertical. Los crecimiento/decrecimiento simultáneos de la humedad relativa y β son analizados en ventanas temporales y verticales, junto con otros criterios. Este estudio permite analizar en detalle alrededor de 18 casos para la metodología de evolución vertical y 15 para la evolución temporal. Este hecho permite establecer una base de datos de este fenómeno para tres lugares diferentes y crear unas configuraciones de instrumentos novedosas y fáciles de aplicar. Adicionalmente, este trabajo ayudó a determinar el papel que desempeñan los aerosoles orgánicos e inorgánicos en el crecimiento higroscópico.

Siguiendo la misma estructura de un artículo de investigación, el capítulo 1 está dedicado a una descripción general de este tema. En el capítulo 2 se da la base teórica. El capítulo 3 presenta los sitios experiementales e instrumentos involucrados, centrándose en la instrumentación de sensores remotos en todas las estaciones, es decir, en IISTA-CEAMA, torre SIATA y observatorio SIRTA. Las metodologías utilizadas en este trabajo se presentan en el capítulo 4, explicando cómo se estudió la evaluación temporal y vertical de la higroscopicidad de los aerosoles en condiciones atmosféricas sin modificar. El capítulo 5 presenta los resultados asociados a la caracterización del error de los radiómetros de microondas en las estaciones del IISTA-CEAMA y torre SIATA, con el fin de definir las regiones confiables de los perfiles de temperatura y humedad relativa. Esta caracterización se realizó para condiciones de todo tipo, sin nubes, diurnas y nocturnas para tener una mejor comprensión del instrumento en términos de precisión y exactitud. El capítulo 6 está dedicado al estudio de un caso de crecimiento higroscópico de aerosol evaluado durante la campaña SLOPE I (16/06/2016) en la estación IISTA-CEAMA. Este caso desarrolla la metodología de evolución vertical de la higroscopicidad en el que se usaron el lidar Raman, lidar Doppler, radiosondas y radiómetro de microondas. En el capítulo 7 se presentan los resultados obtenidos para la evolución temporal utilizando la humedad relativa, y la velocidad y dirección del viento tomados en una torre a la altura de 30 m, combinados con el coeficiente de retrodispersión atenuado del ceilómetro Vaisala junto con mediciones in situ de concentración de partículas de aerosol. Este estudio de 4.5 años permite analizar en detalle 8 casos de crecimiento

higroscópico en el observatorio SIRTA. El capítulo 8 hace una evaluación de las metodologías de evolución vertical y temporal mediante el uso de sensores remotos automáticos (ceilómetros y radiómetros de microondas) en las estaciones de IISTA-CEAMA y torre SIATA. Este estudio permitió analizar hasta 18 casos potenciales de crecimiento higroscópico para evolución vertical y temporal en la estación de torre SIATA, y seis en la estación IISTA-CEAMA en el marco de evolución vertical. En el capítulo 9 se presentan las conclusiones generales de esta tesis y el trabajo futuro.

Durante esta tesis se han realizado algunas pruebas de calidad de los datos para el sistema lidar Raman multiespectral. Las medidas lidar han sido realizadas siguiendo los protocolos de la red EARLINET. Con el fin de obtener los productos ópticos se realizó el preprocesamiento de datos de sistemas lidar y ceilómetro, y también se realizaron calibraciones del radiómetro de microondas para garantizar un funcionamiento óptimo. La propagación de errores de las propiedades ópticas e higroscópicas se ha calculado utilizando la técnica de Monte Carlo.

Los resultados obtenidos en esta tesis establecen una base de datos de detección remota de las propiedades de higroscopicidad que tendrá un impacto en los futuros estudios sobre el papel de ciertas emisiones de aerosoles y su interacción con el vapor de agua, relacionando su efecto con el forzamiento radiativo.

1. Introduction

Atmospheric aerosol particles play a crucial role in the Earth´s climate, principally by means of the radiative effect due to the two principal aerosol-related interactions: (i) aerosol-radiation interaction (ARI), which has a direct effect on the Earth's radiative fluxes, mainly by scattering and absorbing of solar and thermal radiation, and (ii) aerosol-cloud interaction (ACI), which is associated to changes on cloud properties and precipitation, since the aerosol particles might act as cloud condensation nuclei (CCN) and ice nuclei (IC) (Boucher et al., 2013).

Water vapor plays a major role in the aerosol-radiation interaction due to the capacity of some atmospheric aerosol particles to take up water from the environment. This process is the so-called hygroscopic growth, in which aerosol particles uptake water and increase their size under high relative humidity (RH) conditions (Hänel, 1976). During this process, the aerosol particles change their optical and microphysical properties mostly affecting the light scattering cross section, light absorption and deposition efficiency, which is linked to the lifetimes of aerosol particles and their capacity to act as CCN. Aerosol hygroscopic growth have been widely studied by means of the enhancement factor $f_{\xi}^{\lambda}(\lambda, RH)$, where ξ is an aerosol optical/microphysical property. $f_{\xi}^{\lambda}(\lambda, RH)$ is defined as the ratio between some of the aerosol optical/microphysical properties at wet atmospheric conditions and the corresponding reference value at dry conditions (Hänel 1976; Ferrare et al. 1998; Feingold et al., 2003; Veselovskii et al., 2009; Granados-Muñoz et al., 2015; Titos et al., 2014, 2016, and references therein). The magnitude of the $f_{\xi}^{\lambda}(RH)$ depends on the aerosol chemical composition and size.

Several studies have been carried out over the past years in order to study the aerosol water uptake and its effects on their properties. In situ techniques are the most used tones to quantify this impact through the aerosol hygroscopic growth factor (g(RH)), associated to aerosol diameter increase by water uptake by using the Humidified Tandem Differential Mobility Analyzer (HTDMA) (e.g. Swietlicki et al., 2008). In addition, instrumentation like humidrograph tandem nephelometers is used to measure the RH increase step-wise from dry (20-40 %) to wet RH (up to 90%) environments (e.g. Covert et al., 1972; Titos et al, 2016). These studies have also been implemented on airborne

missions, where the most used equipment is the Differential Aerosol Sizing and Hygroscopicity Spectrometer Probe (DASH-SP) (Sorooshian et al., 2008) or the white-light humidified optical particle spectrometer (WHOPS) (Rosatti et al., 2015). One approach to evaluate the effect of RH on the aerosol optical properties can be applying Mie model calculations (e.g. Adam et al., 2012; Fierz-Schmidhauser et al., 2010; Zieger et al., 2013) using the measured size distribution and chemical composition as inputs. For this calculation, information on g(RH) is needed a priori. This factor can be determined experimentally (using HTDMA measurements for example) or it can be inferred from the individual growth factors of the different chemical compounds. The assumption of some aerosol properties such as the refractive index or the growth factor based on the chemical composition is the main drawback of this method, but in literature can be found some results at comparing Mie approximation to remote sensing approach. Generally, the main limitation of the in situ techniques is the modification of the air sample, causing changes in the atmospheric aerosol properties.

To overcome this limitation, it is possible to use remote sensing, inasmuch as it can measure under ambient conditions without air sample modification. In the last decades, lidar technique has been used for hygroscopic growth studies with co-located radiosoundes (RS) (e.g., Ferrare et al., 1998; Granados-Muñoz et al., 2015; Fernández et al., 2015). Additionally, by using Raman lidar (RL) calibrated water vapor mixing ratio profiles r (z) and temperature profiles from ancillary instrumentation is possible to obtain RH and aerosol backscatter/extinction profiles, using them simultaneously for hygroscopic growth studies (e.g. Whiteman, 2003; Navas-Guzmán et al., 2014; Barrera-Verdejo et al., 2016). Taking advantage of Navas-Guzmán et al. (2014) multi-instrumental approach to estimate RH is presented to enhance the possibility to chasing aerosol hygroscopic growth under unmodified atmospheric conditions supported by high resolved vertical turbulent fluxes and wind information from Doppler lidar (DL), obtaining a very satisfactory results. This methodology allows measuring the water vapor and aerosol profiles by the same system and, thus, the same air volume is probed, avoiding the possible radiosonde drift and temporal sampling mismatch.

Recent studies presented by Zieger et al. (2011) and Rosati et al. (2016) showed also a good agreement between in-situ and RL extinction coefficients after taking into account the RH effect on the in-situ measured extinction coefficient. Therefore, it is

possible to use aerosol extinction coefficient to compare with in-situ airborne measures and elastic lidar to study hygroscopic growth in unmodified ambient conditions.

In spite of their promising capabilities, most of the lidar systems do not operated continuously at present due to the costs and maintenance requirements and, thus, the number of hygroscopic growth cases found by this setup is typically small (Vesolovskii et al., 2009; Granados-Muñoz et al., 2015; Fernández et al., 2018). Unlike sophisticated lidars, automatic lidars and ceilometers (ALCs) are robust systems over long-term periods, and can be self-operated 24/7. In particular, Vaisala ceilometers presents a reduced overlap height (up to 30 m agl) respect to lidars (more than 600 m agl), overcoming some of the limitations. Haeffelin et al. (2016) demonstrated that an experimental setup combining a ceilometer and meteorological measurements from an instrumented tower can be successfully used to forecast fog events, but it also can be extended to study hygroscopic growth events that precedes fog formation. Based on this experimental setup, new possibilities could be open to identify automatically atmospheric hygroscopic growth potential cases, isolating a relative higher number of cases than other remote sensing cases.

Thus, the general objective of this thesis is to study the hygroscopic growth enhancement of the aerosol particles in urban atmospheres by using active and passive remote sensing techniques, namely elastic lidar, Raman lidar, Doppler lidar, ceilometers, radiosondes, microwave radiometer, and Sun photometer. To achieve this general goal, several specific objectives have been established, listed as follows:

Specific objective #1: To exhaustively characterize the uncertainties associated to relative humidity profiles retrieved from the MWR, with the aim of defining trustworthy atmospheric regions to work with the instrument and to propose calibration methods for relative humidity profiles by combining different remote sensing instrumentation.

Specific objective #2: To statistically classify the potential hygroscopic growth cases and to infer the best seasons of the year to perform such kind of studies, helping to the definition of future measurement campaigns.

Specific objective #3: To implement methodologies for the systematic study of the hygroscopic enhancement with the synergy of automatic remote sensing instrumentation: ceilometer and MWR.

Specific objective #4: To evaluate the hygroscopic growth enhancement factor throughout the aerosol optical and microphysical properties and their relation with relative humidity, by using the combination of active and passive remote sensing techniques and applying the respective algorithms. For this, special attention is paid on the automatic monitoring equipment.

To accomplish the proposed objectives, the thesis dissertation is organized in the following chapters:

Chapter 2 points out the fundamental concepts related to the aerosol hygroscopic behavior and the basis of the active and passive remote sensing techniques used throughout this dissertation.

Chapter 3 describes the experimental facilities involved in this work, together with a description of the main instrumentation used.

Chapter 4 is devoted to the methodology description. Firstly, the microwave radiometer (MWR) performance is examined in order to assess the error for the retrieving temperature and RH profiles. The second part describes the methodology implemented to identify hygroscopic growth cases in the vertical column combining lidar, DL, MWR, RS and in situ instrumentation. The third part of this chapter explains the methodology proposed to study hygroscopic growth in the horizontal frame (time-evolution) by means of the synergy between a ceilometer and instrumented tower. Finally, a methodology based on automatic remote sensors is presented to explore potential hygroscopic growth cases combining ceilometer and MWR, both vertically and horizontally.

Chapter 5 presents the results related to the MWR performance installed at the IISTA-CEAMA station in Granada (Bedoya-Velásquez et al., 2018b) and also at SIATA-tower station in Medellín. Chapter 6 presents a hygroscopic growth case analyzed by combining RL, DL, RS, MWR located at the IISTA-CEAMA station (at 680 m asl) station and in situ instrumentation located at SNS at 2600 m agl (Bedoya-Velásquez et al., 2018a) during the SLOPE I field campaign (explica el signfcado de slope). Chapter 7 presents the researchrelated to hygroscopic studies at the SIRTA station in Palaisseau (France), performed by the combination of a Vaisala CL 31 ceilometer and co-located instrumented tower (Bedoya-Velásquez et al., 2019). Chapter 8 presents the results of the hygroscopic growth studies using only automatic remote sensors, namely ceilometer and MWR, in

both sites, the IISTA-CEAMA and the SIATA-tower stations. Finally, Chapter 9 is devoted to the conclusions of the thesis and the perspectives of this work.

References

Adam, M., Putaud, J. P., Martins dos Santos, S., Dell'Acqua, A., and Gruening, C.: Aerosol hygroscopicity at a regional background site (Ispra) in Northern Italy, Atmos. Chem. Phys., 12, 5703– 5717, https://doi.org/10.5194/acp-12-5703-2012, 2012.

Alados-Arboledas, L., and Guerrero-Rascado, J. L.: Hygroscopic growth study in the framework of EARLINET during the SLOPE I campaign: synergy of remote sensing and in situ instrumentation, Atmos. Chem. Phys., 18, 7001-7017, https://doi.org/10.5194/acp-18-7001-2018, 2018a.

Barrera-Verdejo, M., Crewell, S., Löhnert, U., Orlandi, E., and Di Girolamo, P.: Ground-based lidar and microwave radiometry synergy for high vertical resolution absolute humidity profiling, Atmos. Meas. Tech., 9, 4013–4028, https://doi.org/10.5194/amt- 9-4013-2016, 2016.

Bedoya-Velásquez, A. E., Navas-Guzmán, F., Granados-Muñoz, M. J., Titos, G., Román, R., Casquero-Vera, J. A., Ortiz-Amezcua, P., Benavent-Oltra, J. A., de Arruda Moreira, G., Montilla-Rosero, E., Hoyos, C. D., Artiñano, B., Coz, E., Olmo-Reyes, F. J., Alados-Arboledas, L., and Guerrero-Rascado, J. L.: Hygroscopic growth study in the framework of EARLINET during the SLOPE I campaign: synergy of remote sensing and in situ instrumentation, Atmos. Chem. Phys., 18, 7001-7017, https://doi.org/10.5194/acp-18-7001-2018, 2018a.

Bedoya-Velásquez, A. E., Navas-Guzmán, F., Moreira, G., Román, R., Cazorla, A., Ortiz-Amezcua, P., Benavent-Oltra, J.A., Alados-Arboledas, L., Olmo-Reyes, F.J., Foyo-Moreno, I., Montilla-Rosero, E., Hoyos, C.D., Guerrero-Rascado, J.L.: Seasonal analysis of the atmosphere during five years by using microwave radiometry over a mid-latitude site, Atmos. Res., Volume 218, 78-89, ISSN 0169-8095, https://doi.org/10.1016/j.atmosres.2018.11.014, 2018b.

Bedoya-Velásquez, A.E., Titos, G., Bravo-Aranda, B.A., Haeffelin, M., Favez, O, Petit, J.E., Casquero-Vera, J.A, Olmo-Reyes, F.J., Montilla-Rosero, E., Hoyos, C.D., Alados-

Arboledas, L., and Guerrero- Rascado. J.L.: Long-term aerosol optical hygroscopicity study at the ACTRIS SIRTA observatory: synergy between ceilometer and in-situ measurements. Atmos. Chem and Phys. Discussion, https://doi.org/10.5194/acp-2019-12, 2019.

Boucher, O., Randall, D., Artaxo, P., Bretherton, C., Feingold, G., Forster, P., Kerminen, V.-M., Kondo, Y., Liao, H., Lohmann, U., Rasch, P., Satheesh, S. K., Sherwood, S., Stevens, B., and Zhang,

Covert, D. S., Charlson, R. J., and Ahlquist, N. C.: A study of the relationship of chemical composition and humidity to light scattering by aerosols, J. Appl. Meteorol., 11, 968–976, 1972.

Feingold, G. and Morley, B.: Aerosol hygroscopic properties as measured by lidar and comparison with in situ measurements, J. Geophys.Res., 108, D11, doi:10.1029/2002JD002842, 2003.

Fernández, A. J., Apituley, A., Veselovskii, I., Suvorina, A., Henzing, J., Pujadas, M., and Artiñano., B.: Study of aerosol hygroscopic events over Cabauw experimental site for atmospheric research (CESAR) using the multi-wavelength Raman lidar Caeli, Atmos. Environ., 120, 484–498, 2015.

Fernández, J., Molero, F., Becerril-Valle, M., Coz, E., Salvador, P., Artíñano, B., Pujadas, M.: Application of remote sensing techniques to study aerosol water vapour uptake in a real atmosphere, Atmospheric Research, Volume 202, Pages 112-127, ISSN 0169-8095, https://doi.org/10.1016/j.atmosres.2017.11.020, 2018.

Ferrare, R.A., Melfi, S.H., Whiteman, D.N., Evans, K, D and Leifer, R.: Raman lidar measurements of aerosol extinction and backscattering. 1. Methods and comparisons, J. Geophys. Res., 103, 19,663–19,672, 1998.

Fierz-Schmidhauser, R., Zieger, P., Vaishya, A., Monahan, C., Bialek, J., O'Dowd, C. D., Jennings, S. G., Baltensperger, U., and Weingartner, E.: Light scattering enhancement factors in the marine boundary layer (Mace Head, Ireland), J. Geophys. Res., 115, D20204, https://doi.org/10.1029/2009jd013755, 2010.

Granados-Muñoz M.J, Navas-Guzmán, F., Bravo-Aranda, J. A., Guerrero-Rascado, J. L., Lyamani, H., Valenzuela, A., Titos, G., Fernández-Gálvez, J., and Alados-Arboledas, L.:

hygroscopic growth of atmospheric aerosol particles based on active remote sensing and radiosounding measurements: selected cases in southeastern Spain. Atmos. Meas. Tech., 8, 705–718, 2015.

Hänel, G.: The Properties of Atmospheric Aerosol Particles as Functions of the Relative Humidity at Thermodynamic Equilibrium with the Surrounding Moist Air, in: Advances in Geophysics, edited by: Landsberg, H. E. and Mieghem, J. V., 73–188, Elsevier, 1976.

Navas-Guzmán, F., Fernández-Gálvez, J., Granados-Muñoz, M.J, Guerrero-Rascado, J.L., Bravo-Aranda, J.A., and Alados-Arboledas, L.: Tropospheric wáter vapour and relative humidiyty profiles from lidar and microwave radiometry. Atmos. Meas. Tech., 7, 1201-1211, 2014.

Rosati, B., Herrmann, E., Bucci, S., Fierli, F., Cairo, F., Gysel, M., Tillman, R., Größ, J., Gobbi, G.P., Di Liberto, L., Di Donfrancesco, G., Wiedensolher, A., Weingartner, E., Virtanen, A., Mentel, T.F., and Baltensperger, U.: Studying the vertical aerosol extinction coefficient by comparing in situ airborne data and elastic backscatter lidar, Atmos. Chem. Phys., 16, 4539–4554, doi:10.5194/acp-16-4539-2016, 2016.

Rosati, B., Wehrle, G., Gysel, M., Zieger, P., Baltensperger, U., and Weingartner, E.: The white-light humidified optical particle spectrometer (WHOPS) – a novel airborne system to characterize aerosol hygroscopicity, Atmos. Meas. Tech., 8, 921–939, https://doi.org/10.5194/amt-8-921-2015, 2015.

Sorooshian, A., Hersey, S., Brechtel, F. J., Corless, A., Flagan, R. C., and Seinfeld, J. H.: Size-Resolved Aerosol Hygroscopic Growth Measurements: Differential Aerosol Sizing and Hygroscopicity Spectrometer Probe (DASH-SP), Aerosol. Sci. Tech., 42:6, 445-464, DOI: 10.1080/02786820802178506, 2008.

Swietlicki, E., Hansson, H.C., Hämeri, K., Svenningsson, B., Massling, A., Mcfiggans, G., mcmurry, P.H., Petäjä, T., Tunved, P., Gysel, M., Topping, D., Weingartner, E., Baltensperger, U., Rissler, J., Wiedensohler, A., Kulmala, M.: Hygroscopic properties of submicrometer atmospheric aerosol particles measured with H-TDMA instruments in various environments—a review. TellusB, vol. 6, issue 3, 432-469, 2008.

Titos, G., Cazorla, A., Zieger, P., Andrews, E., Lyamani, H., Granados- Muñoz, M.J., Olmo, F.j and Alados-Arboledas, L.: Effect of hygroscopic growth on the aerosol light-scattering

coefficient: A review of measurements, techniques and error sources. Atmospheric Environment, 141, 494-507, 2016.

Titos, G., Jefferson, A., Sheridan, P. J., Andrews, E., Lyamani, H., Alados-Arboledas, L., and Ogren, J. A.: Aerosol light-scattering enhancement due to water uptake during the TCAP campaign, Atmos. Chem. Phys., 14, 7031–7043, doi:10.5194/acp-14-7031-7043,2014.

Veselovskii, I., Whiteman, D. N., Kolgotin, A., Andrews, E., and Korenskii, M.: Demonstration of aerosol property profiling by multi-wavelength lidar under varying relative humidity conditions, J. Atmos. Ocean. Tech., 26, 1543–1557, 2009.

Whiteman, D. N.: Examination of the traditional Raman lidar technique. II. Evaluating the ratios for water vapor and aerosols, Appl. Optics, 42, 2593–2608, 2003.

Zieger, P., Fierz-Schmidhauser, R., Weingartner, E., and Baltensperger, U.: Effects of relative humidity on aerosol light scattering: results from different European sites, Atmos. Chem. Phys., 13, 10609–10631, https://doi.org/10.5194/acp-13-10609- 2013, 2013.

Zieger, P., Weingartner, E., Henzing, J., Moerman, M., de Leeuw, G., Mikkilä, J., Ehn, M., Petäjä, T., Clémer, K., van Roozendael, M., Yilmaz, S., Frieß, U., Irie, H., Wagner, T., Shaiganfar, R., Beirle, S., Apituley, A.,Wilson, K., and Baltensperger, U.: Comparison of ambient aerosol extinction coefficients obtained from in-situ, MAX-DOAS and LIDAR measurements at Cabauw, Atmos. Chem. Phys., 11, 2603–2624, https://doi.org/10.5194/acp- 11-2603-2011, 2011.

2. Fundamentals

This chapter introduces the basis of the research making easier the understanding of the topic and the results presented in this thesis. First, the atmospheric aerosol and their principal sources are described. Second, the atmospheric aerosol optical and microphysical properties used in this thesis are presented. Third, the aerosol water uptake theory is explained. Finally, the principles of active and passive remote sensing are presented, paying special attention to the lidar and microwave radiometry techniques.

As this dissertation is centered on the first kilometers of the troposphere where atmospheric aerosols and water vapor plays a crucial role, it is worthy to define the principal sources of these aerosol particles. The atmospheric aerosol is defined as a complex system composed by a gas (air) and solid and/or liquid particles suspended in it, excluding clouds, which are considered as a separate phenomenon (Horvath, 1998). The presence of these aerosol particles alter the radiative forcing, defined as the net change in the energy balance of the Earth system due to some agents (Boucher et al., 2013). There are many processes involved in the atmospheric aerosols formation (Fig. 2.1), as a result of these processes it is possible to better understand the origin, chemical composition or size, among others aspects related to these particles. Associated to their origin, aerosols are classified in anthropogenic and natural (marine, biomass burning and mineral dust, among others). These aerosols can cause an impact in the climate system and might be part of feedbacks mechanisms (Kaufman et al., 2005). Following this classification, only anthropogenic aerosols can be considered as an external cause of climate change (Boucher et al., 2013). Anthropogenic aerosols like road and industry emissions, agriculture activities, among others, represents between 26 to 42 % of the total aerosol load in the globe (IPCC, 2013).

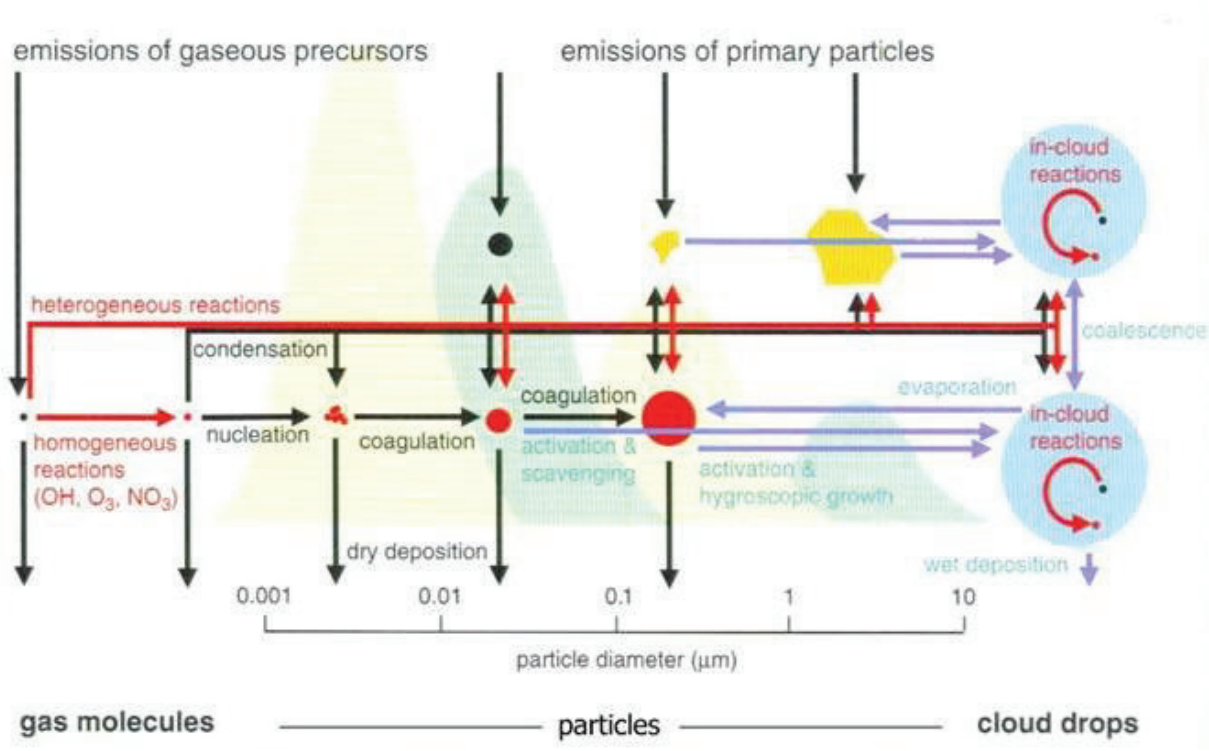

Figure 2.1. *Major microphysical and chemical processes that influence the size distribution and chemical composition of the atmospheric aerosols (adapted from Brasseur, Prinn, and Pzsenny, Atmospheric Chemistry in a Changing World, IGBP Series, Springer, 2003).*

The role of anthropogenic and natural aerosol particles and greenhouse gases in the climate system has been studied in depth to evaluate the radiative forcing effect on Earth's surface temperature as it is shown in Fig. 2.2. The two principal ways of the aerosol-related interactions are: (i) the aerosol-radiation interaction (ARI) that produces a direct effect on the Earth's radiative fluxes, mainly by scattering and absorbing solar and thermal radiation, and (ii) the aerosol-cloud interaction (ACI) associated to changes in cloud properties and precipitation, since the aerosol particles act as cloud condensation nuclei (CCN) and ice nuclei (IN) (Boucher et al., 2013). Both aerosol interactions result in a net radiative effect on the global energy budget.

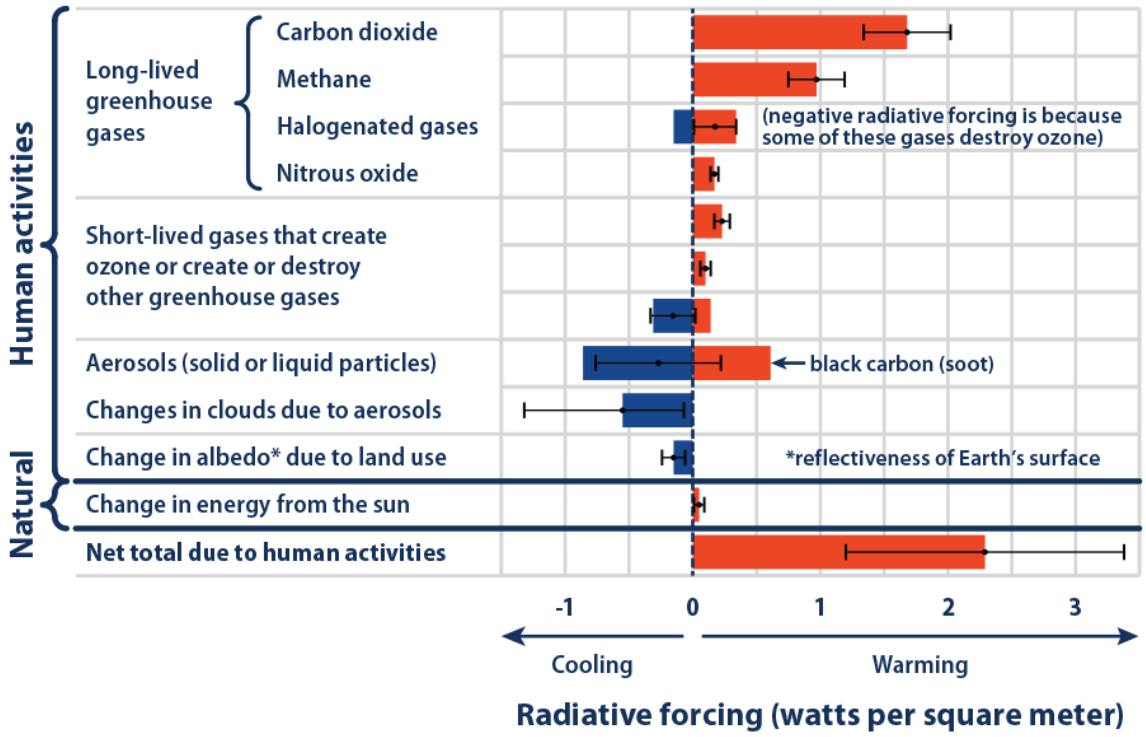

Figure 2.2. *The total amount of radiative forcing caused by human activities, including indirect effects, between 1750 and 2011. Radiative forcing is calculated in watts per square meter, which represents the size of the energy imbalance in the atmosphere. Each colored bar represents the measure and the black bars refers to uncertainties. The natural change in the energy received from the Sun over this time period is provided for reference (Boucher et al., 2013).*

2.1 Aerosoloptical and microphysical properties

2.1.1 Aerosol Optical properties

As it was mentioned in the previous section, atmospheric aerosol plays a crucial role in the net solar radiation that reaches Earth's surface, firstly by blocking the incoming radiation (absorption) and secondly, by re-distributing the energy once it interacts with the particles suspended in the atmosphere (scattering). In general, this aerosol-radiation interaction in the atmosphere is described by the well-known Beer-Lambert-Bouger law, which establishes a logarithmic dependence between the transmitted radiation through a medium (atmosphere in our case) and the distance the radiation travels through that medium (Liou, 2002), as it follows:

$$T(z,\lambda) = e^{-\int_0^z \alpha(\xi,\lambda)d\xi} \tag{2.1}$$

where $T(z,\lambda)$ is the transmittance as function of the height z respect to the Earth's surface and it is considered λ as the wavelength of interest and $\alpha(\xi,\lambda)$ is the total extinction coefficient which takes into account the absorption and scattering processes by particles and molecules. The absorption of electromagnetic radiation at the level of particles and molecules, involves transitions between energy levels including decay processes not necessarily radiative depending on the intensity and wavelength of the incident radiation.

According to the Eq. 2.1 it is possible to define the aerosol optical depth (AOD) as the integral of the particle extinction coefficient along the distance between surface and the top of the atmosphere (TOA)

$$AOD(\lambda) = \int_0^{TOA} \alpha(\lambda,z)dz \tag{2.2}$$

The scattering of radiation from particles and molecules consists of the change of direction respect to the incident radiation. This process depends on size, shape and complex refractive index of the particle and the wavelength of the incident radiation, and they can be divided in elastic and inelastic. Elastic scattering is a mechanism in which the frequency scattered by a particle is equal to the incident frequency, thus, the particle or molecule preserves the level of rotational-vibrational energy during the scattering process. This process depends on the physical properties of the scatters, and on the wavelength λ of the incident radiation. For the mathematical treatment of such processes, the so-called size parameter is used, as follows

$$x = \frac{2\pi a}{\lambda} \tag{2.3}$$

where a is the radius of the scatterer (molecule or particle) and λ is the wavelength of the radiation. In such a way, there are basically three types of interactions:

- For $\frac{x<0.6}{n}$, with n the real part of the refractive index, the process is known as Rayleigh scattering and the scattering cross section is inversely proportional to the forth power of the wavelength. For cloud free atmospheres, it is applied to air molecules with sizes normally 0.001 μm.
- For $x > 5\mu m$, the process is mainly a diffuse reflection, which in the Earth's atmosphere does not occur frequently.

- For $\frac{0.6}{n} < x < 5\mu m$, the process is known as Mie scattering and is applied to scatterers larger than 0.01 μm, as is the case with aerosol particles.

The mathematical procedure to obtain the scattering coefficients, Rayleigh and Mie, is not developed here, but they are summarized in Kovalev 2004. Thus, Rayleigh scattering is the result of the electromagnetic radiation interaction with scatterers of sizes smaller than the incident wavelength, producing predominantly vibrational transitions on the scatterers, which macroscopically can be seen as the induction of the electric polarizability effect forming dipoles that radiates on the same frequency of excitation. The molecular scattering coefficient integrated over 4π stereo radians is

$$\sigma_R(\omega) = \frac{8\pi}{3}\left[\frac{\pi^2(n^2-1)^2}{N^2\lambda^4}\right] \tag{2.4}$$

where N is the numeric density of the scatters. In the remote sensing field, the volumetric backscatter coefficient is also used, which is defined as follows

$$\beta_\pi^R(\lambda) = N\sigma_\pi^R(\lambda) = 1.39\left[\frac{550}{\lambda(nm)}\right]^4 x10^{-8} cm^{-1} sr^{-1} \tag{2.5}$$

Mie scattering is also an elastic process, in which the scatter has a size compared to the wavelength of the incident radiation. For this treatment it is assumed a size parameter A size parameter X ($Ka = \frac{2\pi a}{\lambda}$). For isotropic dielectric scatters $X < 0.5$, and the same behavior can be observed as for Rayleigh scattering. Also, it assumes a spherical dielectric disperser with radius a.

In this case it is needed to introduce the Mie efficiency for scattering $Q_s(X,n)$, which depends on the irradiance

$$Q_s(X,n) = \frac{\sigma_s^M}{\pi a^2} = \frac{1}{\pi(Ka)^2}\iint_0^\pi [i_2(\theta)cos^2\varphi + i_1(\theta)sen^2\varphi]sen\theta d\theta d\varphi \tag{2.6}$$

where k is the wavenumber, σ_s^M is the Mie scattering cross section i_1 and i_2 are the Mie intensity functions for linear or non-polarized radiation, and θ, φ are the angular distribution of the scattered radiation terms. Thus, as it was defined above and considering some assumptions, for remote sensing it is possible to define a volumetric backscatter coefficient as follows

$$\beta_\pi^M(\lambda) = \frac{1}{2k^3}\int_{a_1}^{a_2}\{i_1(\pi,X,\lambda,n) + i_2(\pi,X,\lambda,n)\}N(\alpha)d\alpha \tag{2.7}$$

where the size-parameter limits of integration a_1 and a_2 define the effective radius for the distributions of the scatterers. For the calculation of this coefficient, it is necessary to know the distribution of particles in the atmosphere, which is a job for the experimentalist to evaluate the distribution model that fits the characteristics of the atmosphere under study.

Inelastic scattering, so-called Raman scattering, is a process of emission of inelastic radiation in which there is a change in the quantum state of the molecules where its frequency is shifted by an amount $|\Delta\upsilon|$ respect its initial value, which is characteristic for each molecule. If the molecule absorbs energy, it is excited to a higher level decreasing the energy of the scattered photon, so that the frequency of the scattered radiation will be smaller ($\upsilon_s = \upsilon_i - |\Delta\upsilon|$), moving towards infrared regions in the electromagnetic spectrum (Stokes). If the molecule transfers energy to the scattered photon decreasing its energy level, the frequency of the scattered photon increases, therefore the frequency of the scattered radiation will be greater ($\upsilon_s = \upsilon_i + |\Delta\upsilon|$), causing shifts towards blue regions of the electromagnetic spectrum (Anti- Stokes).

Other optical properties can be retrieved by using extinction coefficient terms. One derivation by using these properties is the Angström law (Ångström, 1964), which defines the spectral dependence of the AOD as follows

$$AOD_\lambda = AOD_o \lambda^{-AE} \tag{2.9}$$

where AOD_o and AE are the Angström turbidity coefficients. AE characterizes the spectral and size dependency of the aerosol (Shifrin, 1995), meanwhile AOD_o is related to the aerosol load in the atmospheric column. Another properties less used in this work are single scattering albedo, phase function, among others, where definitions can be found in Goody et al. (1989).

2.1.2 Microphysical properties

One of the main aerosol microphysical properties is the number size distribution, which is very useful to describe the physical state of the system, but there are other properties derived like size, total concentration and shape. In this work, it is only described the number particle size distribution as the number of particles present in the atmosphere according to size as follows

$$M(r) = \frac{dN}{dr} \tag{2.10}$$

where r is the particle radius, N is the total number of particles and M is the number of particles in the range $[r, r + dr]$. This definition is expressed in its logarithmic form due to the large range of aerosol particles sizes (between 0.001 to 100 µm). Similarly, volume particle size distribution is defined as the volume of particles present in the atmosphere according to size:

$$v(r) = \frac{dV}{d\,lnr} \tag{2.11}$$

Thus, assuming spherical particles, to the volume size distribution can be related to the number size distribution as:

$$v(r) = \frac{4\pi}{3} r^3 \frac{dN}{d\,lnr} \tag{2.12}$$

Following the same procedure, the mass size distribution is deriving considering a constant density for the particles, ρ:

$$m(r) = \frac{dM}{d\,lnr} = \frac{4\pi}{3} \rho r^3 \frac{dN}{d\,lnr} \tag{2.13}$$

It is possible to find many expressions in the literature to represent the particle size distribution, including the Junge power law and the gamma distribution, among others (D'Almeida et al., 1991; Liou, 2002).

2.2 Aerosol water uptake theory

One of the key factors associated to the aerosol radiative forcing is the so-called aerosol hygroscopicity, which is the capacity of aerosol particles to uptake water from the environment and increase their size, subsequently modifying their optical and microphysical properties under high relative humidity (RH) conditions. Thus, the particle size increase affects the scattering cross sections, particle deposition, and in the end the aerosol-cloud interactions. This size increase by water uptake is described by the so-called hygroscopic growth factor, which is usually defined as

$$g(RH) = \frac{D(RH)}{D_{dry}} \tag{2.14}$$

where D_{dry} is the particle diameter at dry conditions and $D(RH)$ at the actual RH, respectively.

In the last decades, other aerosol properties such as mass, extinction or scattering coefficients have been used to study this phenomenon (e.g. Hänel 1976; Ferrare et al. 1998; Feingold et al., 2003; Veselovskii et al., 2009; Granados-Muñoz et al., 2015; Titos et al., 2014, 2016, and references therein). In order to link any of these variations in the aerosol properties (apart from the size) due to water uptake, the so-called enhancement factor is defined as follows

$$f_{\xi}^{\lambda}(\lambda, RH) = \frac{\xi(\lambda,RH)}{\xi(\lambda,RH_{ref})} \tag{2.15}$$

where $\xi(\lambda, \mathrm{RH})$ represents an aerosol optical/microphysical property evaluated at certain RH. The value of $\xi(\lambda, RH_{ref})$ is obtained by estimating the property ξ at the lowest RH within the evaluated atmospheric layer ($\mathrm{RH_{ref}}$). The aerosol hygroscopicity depends on the particle dry diameter, temperature, water properties (density and water activity, the latest defined as the ratio between the partial vapor pressure of water in the solution and the partial vapor pressure of pure water at the same temperature) and the solubility of the chemical substances involved, i.e. organic aerosols (OA) and inorganic aerosols (IA). The aerosol hygroscopicity is deeply described the by Köhler theory, which is rigorously explained in Pruppacher et al. (1998) and Seinfeld and Pandis (2012). In this thesis, a brief overview of the basics of this theory is given in the following sections, including the solute effect (Raoult's law) and curvature effect (Kelvin effect).

2.2.1 Raoult's law

To describe the changes due to the interaction between the aerosol particles and water vapor in the atmosphere, the Raoult's law is used. For this, a binary flat system, composed by an aerosol particle dissolved in liquid water, is considered. Normally, aerosols have a mass fraction that is soluble in water (i.e. for salts, the mass fraction with water solubility is equals to one). Raoult's law establishes that if the particles contain soluble matter, the water vapor pressure of equilibrium will be decrease with the increase in the number of soluble ions of the particles. Thus,

$$e = a_w e_s \tag{2.16}$$

where a_w is the water activity, e is the water vapor pressure and e_s is the saturation water vapor pressure. For ideal solutions, a_w is given as the molar fraction of the water in the solution

$$a_w = \frac{n_w}{n_{sol}+n_w} = \left[1 + \frac{6vm_{sol}M_w}{M_{sol}\rho_w\pi(d^3-d_{sol}^3)}\right]^{-1} \quad (2.17)$$

where n_{sol} and n_w are moles number of the solute and water, respectively, v is number of soluble ions per molecule, M_{sol} is the molar weight of solute, m_{sol} mass of solute, ρ_w water density, d diameter of the droplet and d_{sol} diameter of the solute.

2.2.2 Kelvin effect

The water vapor pressure on a curved surface is not equal to the water vapor pressure on a flat surface. Thus, it is necessary to modify slightly the Raoult's law where it was supposed a flat surface, because aerosols and water droplets have a curved surface. The Kelvin effect is much more relevant as the size of the particles decreases, because the curvature of the particle surface increases. The reason for this effect is the influence of the droplet size in the surface tension of the drop (Shneider et al., 1998). The mathematical description is briefly presented here. First, it is necessary take into account the internal energy of the chemical reaction when the drop is forming, i. e. the Gibbs free energy (G) which is linked with the chemical potential as:

$$\mu = \frac{G}{n_m} \quad (2.18)$$

where n_m is the number of moles. After some steps in the calculation and considering the gaseous and liquid phases, it is possible to determine the difference between chemical potentials between those phases by means of the Gibbs-Duhem formula, obtained from the first law of the thermodynamics. Under some considerations like a system with just one specie, and evaluating for constant temperature ($dT = 0$) and an ideal gaseous phase (because molar volume at gaseous phase is greater than liquid phase), we found:

$$\mu_l - \mu_g = -RT\int_{e_o}^{e}\frac{1}{p}de = -RT\ln S \quad (2.19)$$

where μ_l and μ_g are the chemical potential at liquid and gaseous phase, respectively and S is the saturation ratio defined as the ratio between the water vapor pressure e and the

saturation vapor pressure over a flat pure water surface $e_s(r_\infty)$,. Thus the Gibbs free energy takes the following form:

$$\Delta G = -\frac{\pi d^3 \rho_l}{6M_w} RT \ln(S) + \pi d^2 \sigma \tag{2.20}$$

σ is the surface tension and $\pi d^2 \sigma$ is the contribution of the surface energy to the Gibbs free energy term. If the solution has not reached saturation ($S < 1$), the difference in the Gibbs free energy grows in a monotone way with the diameter of the particle. When solution becomes saturated ($S = 1$) the logarithm is neglected, thus the difference in the Gibbs free energy also grows monotonously. Under conditions of supersaturation ($S > 1$), the term d^2 dominates until a certain diameter, after that d^3 becomes relevant. This implies that the drop is only stable if it is can reach a critical diameter (D_{crit}). To find the stable condition of the droplet, and then obtain D_{crit}, is needed to derivate the Gibbs free energy $\left(\frac{\partial \Delta G}{\partial d}\right) = 0$. Once this process is done, D_{crit} is expressed as follows:

$$D_{crit} = \frac{4M_w \sigma}{\rho_l RT \ln(S)} \tag{2.21}$$

Then, for obtaining the Kelvin effect expression, the Eq. (2.21) is included in the expression for the saturation pressure over a curved surface:

$$e = e_s exp\left(\frac{4M_w \sigma}{\rho_l RTd}\right) \tag{2.22}$$

2.2.3 Köhler theory

The combination of Raoult's law and Kelvin law is the base of the Köhler theory, which explains the relationship between S and droplet diameter for an aqueous solution by the following equation:

$$\frac{e}{e_s} = RH = \left[1 + \frac{6\nu m_{sol} M_w}{M_{sol} \rho_w \pi (d^3 - d_{sol}^3)}\right]^{-1} exp\left(\frac{4M_w \sigma}{\rho_l RTd}\right) \tag{2.23}$$

An example of Köhler curve is shown in Fig. 2.5 for a NaCl particle with a dry size of D = 50 nm, taking σ = 0.072 Jm^{-2} at T = 298K from Seinfeld and Pandis (2012). The contributions of the Kelvin's law (S >1) and the Raoult's effect (S < 1) are shown separately.

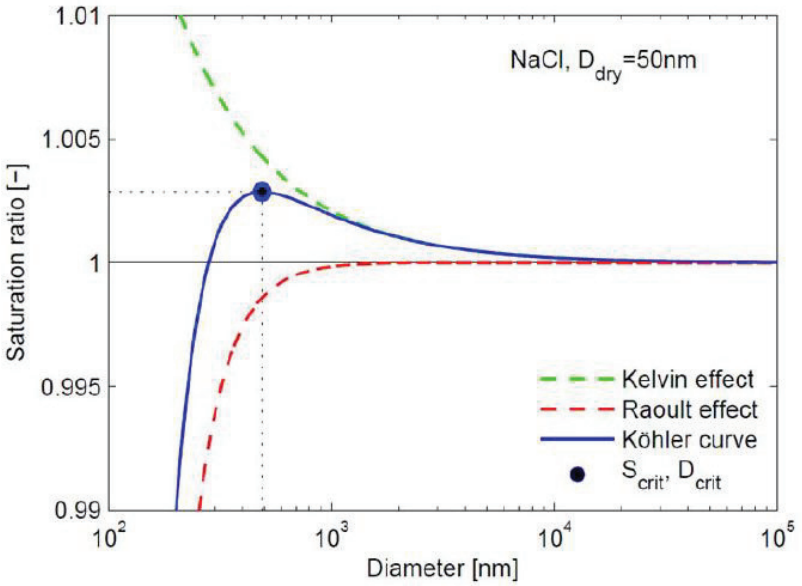

Figure 2.1 *Köhler curve of NaCl particles with a dry size of D=50 nm, and taking σ =0.072 Jm^{-2} at T =298K from Seinfeld and Pandis, 2006).*

Regarding to the particle behaviour under humidified ambient conditions, many inorganic salts and some organic species presents solid crystals forms at sufficiently low RH. According to thermodynamics, solid particles dissolve at certain RH, known as deliquescence RH (RH_{deliq}). The phase transition from liquid to solid (crystallization) not occur at RH_{deliq}, the droplet remains supersaturated until it crystallizes at another RH, known as efflorescence relative humidity (RH_{efflor}), depending on the nucleation kinetics. The result is the phenomenon of hysteresis (Fig. 2.6), meaning that exists a RH where both solid crystals and liquids may exist, depending of the particle behaviour against RH.

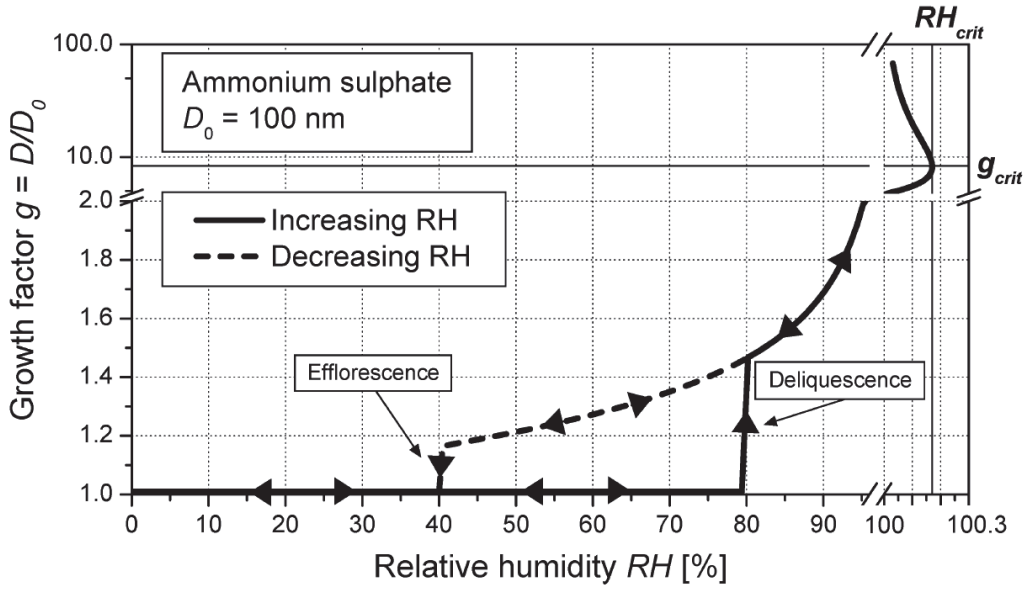

Figure 2.2 *Hysteresis of ammonium sulphate particles. Dissolution and crystallization occur at deliquescent RH (RH_{deliq}) and efflorescence RH (RH_{efflor}), respectively. RH_{crit} and g_{crit} show the critical RH and growth factor for cloud activation, respectively.*

2.2.4 Parameterization: enhancement factor

In spite of the Köhler theory (Eq. 2.23) is described on an easy way, this practical application is prevented mainly because not all the involved variables are always known. Nevertheless, Hänel et al. (1976) proposed the following simple parameterization:

$$f_{\xi}^{\lambda}(RH) = \left(\frac{1-RH/100}{1-RH_{ref}/100}\right)^{-\gamma_{\lambda}} \tag{2.24}$$

where ξ refers to any aerosol optical/microphysical property and γ_{λ} is a parameter related to the aerosol hygroscopicity. This parameter depends on the aerosol type and wavelength. Along this thesis, the optical property used is particle backscatter coefficient (β_{par}) at different wavelengths depending on the involved instrumentation and, thus, the particle backscatter enhancement factor is denoted as $f_{\beta}(\lambda, RH)$. Estimations of $f_{\beta}(\lambda, RH)$ uncertainty are very scarce because of their high complexity. Some studies (e. g. Adam et al., 2012; Zieger et al., 2013) provided estimations based on sensitivity analysis using Mie model calculations, reporting errors around 20% for the scattering enhancement factor ($f_{\sigma}(\lambda, RH)$). Titos et al. (2016) reported uncertainty estimations based on Monte-Carlo techniques, concluding that the more hygroscopic the aerosol, the higher is the

uncertainty in $f_\sigma(\lambda, RH)$, especially at RH > 80 %. For moderate-hygroscopic aerosol particles, a lower limit was established for the uncertainty in $f_\sigma(\lambda, RH)$ of around 30-40% using nephelometry techniques.

2.3 Active and passive remote sensing

Remote sensing is defined as the acquisition of information related to an object or phenomenon without having contact with it. Currently, remote sensing systems are used located on aircrafts and ground and satellite platforms, from which it is possible to detect objects remotely. Remote sensing techniques are classified as passive and active. The first one uses sources of radiation external to the system. In particular, some of the most common passive remote sensing techniques applied for atmospheric studies are based of the detection ofsolar, lunar, stellar and microwave radiation, among others. Conversely, in active remote sensing techniques, the system has their own source of radiation. In particular, some of the widely active remote sensing technique applied in atmospheric sciences are lidar and radar. Lidar technique (LIgth Detection and Ranging) is the basis of the robust lidar systems and their automatic version known as ceilometers, which collect the backscattered radiation by atmospheric constituents to obtain information of physical properties from the atmospheric aerosol particles, as well as clouds and gases.

2.3.1 Lidar and ceilometer fundamentals

Lidar is an active remote sensing technique, in which the laser sends pulsed radiation towards the atmosphere (Fig. 2.7), taking advantage of the particle-radiation interaction to obtain information of the atmospheric aerosol optical and microphysical properties with high spatial and temporal resolution. These instruments are composed by three sub-systems, namely transmitter (laser), receiver (telescope and optical box) and recorder (transductor from analog to digital signal) (Measures, 1992 and Argall, 2002).

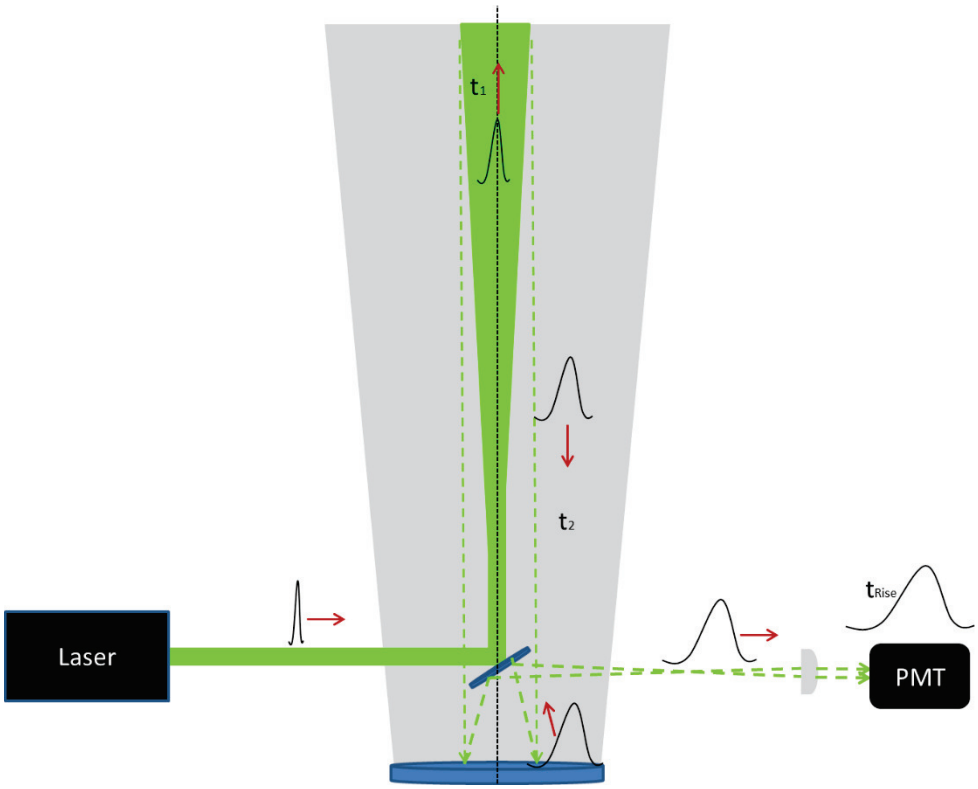

Figure 2.3 *Scheme of lidar system setup*

The power P received from a distance z, where a set of molecules and particles are suspended in the atmosphere, can be expressed as a simple form by means of the following five factors:

$$P(z,t) = \mathrm{C}\,(\mathrm{t})G(z,t)\beta(z,t)\,T^2(z,t)T_{wv}^2(z,t) \tag{2.25}$$

where z is the range, t is the time, $C\,(t)$ is the calibration constant, $G(z,t)$ is the geometrical form factor, $\beta(z,t)$ is the total backscatter coefficient due to particles and molecules, $T(z,t)$ is the attenuation due to particles and molecules (except for water vapor), and, $T_{wv}\,(z,t)$ is the attenuation due to water vapor molecular absorption.The calibration constant can be described as follows

$$C(t) = P_0(t)\frac{ct}{2}A\varepsilon \tag{2.26}$$

where $P_0(t) = \frac{E_0}{\tau}$ is the average power of a single laser pulse, which contains the E_0 as the initial energy of the pulse, τ is the temporal length of the pulse and ct is the length of the volume illuminated by the laser pulse (where c is the speed of light in vacuum, $c = 3 \cdot 10^8 \frac{m}{s}$). The factor ½ appears due to the double path that light travels in the interaction of the laser pulse with the illuminated volume (Fig 2.8.), A is the effective area of the

telescope, responsible for collecting the backscattered radiation and ε is the efficiency of the system (including transmission and reception and detection).

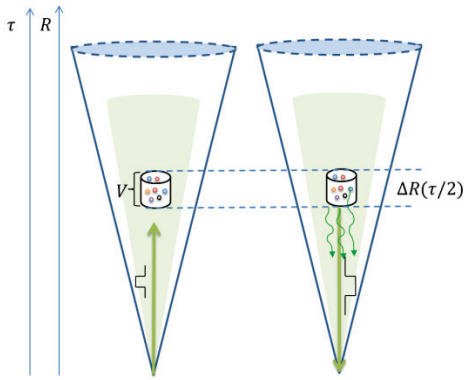

Figure 2. 4. *Schematic interaction of a laser pulse sent to the atmosphere, where V is the volume illuminated by the laser beam, ΔR the thickness of the probed volume and τ is the duration time of the laser pulse.*

The geometrical factor $G(z)$ is defined through

$$G(z) = \frac{O(z)}{z^2} \tag{2.27}$$

where $O(z)$ is the so-called overlap function, accounting for the incomplete overlap between the field-of-view (FOV) of the receiving telescope and the laser beam, as a function of the range. The term of quadratic decay of the range is due to the spherical shape of the waves that reach the telescope with a radius z from the scattering volume.

One of the basic products obtained from lidar and ceilometer systems is the attenuated backscatter, which is defined as follows

$$\beta^{att}(z,t) \equiv \beta(z,t)\, T^2(z,t) \tag{2.28}$$

The backscatter coefficient term can be expressed as

$$\beta(z,\lambda) = \sum_j n_j \frac{d\sigma_{j,sca}}{d\Omega}(\pi,\lambda) \tag{2.29}$$

where $\frac{d\sigma_{j,sca}}{d\Omega}(\pi,\lambda)$ is the scattering differential section for molecules and particles at 180° for a given wavelength and n_j is the number concentration of scatterers in the volume illuminated by the laser pulse.

The transmittance term for both molecules and particles can be written as follows

$$T(z,t) \equiv exp\left(-\int_{z_1}^{z_2} \alpha_T(z,t)dz\right) \quad (2.30)$$

If we consider the water vapor part, we obtain

$$T_{wv}(z,t) \equiv exp\left(-\int_{z_1}^{z_2} \sigma_{a,wv}(z,t)dz\right) \quad (2.31)$$

where α_T is the total extinction coefficient ($\alpha_T(z,\lambda) = \sum_j n_j \sigma_{j,ext}(\lambda)$, $\sigma_{j,ext}$ is the differential cross section for extinction), including the extinction due to particles (α_{par}) and molecules (α_{mol}). $\sigma_{a,wv}$ is the water vapor absorption coefficient in the atmosphere, and $z_1$and z_2 define the region where the sampled volume is located.

Finally, combining the equations (2.26), (2.27) and (2.30) the simplest form of the elastic lidar equation is obtained:

$$P(z,t,\lambda) = P_0(t)\frac{ct}{2}A\varepsilon\frac{O(z)}{z^2}\beta(z,t,\lambda)exp\left[-2\int_{z_1}^{z_2}\alpha_T(\xi,t,\lambda)d\xi\right] \quad (2.32)$$

2.3.2 Microwave radiometry fundamentals

The microwave radiometry is a passive remote sensor that performs automatic measurements of sky brightness temperature at two bands: the oxygen V band (51-58 GHz) and water vapor K band (22-31 GHz) associated to temperature and water vapor and liquid water, respectively. As it was explained in the last sections for lidar technique, the atmospheric extinction makes possible to evaluate the effects of the radiation-matter interactions processes, but in radiometry field these processes can be evaluated through the radiative transfer equation (RTE). Therefore, based on RTE and the brightness temperatures measured by MWR, it is possible to study the state of the atmosphere.

A brief description of the theory associated to the microwave radiation and atmospheric components will be given here, but deeply explanations can be found in Liou (1980) and Petty (2006). The extinction caused by atmospheric thermal emission can be measured through the thermal total extinction coefficient (α_{Th}), which takes into account both absorption (α_{Th}^a) and scattering (α_{Th}^s) frequency-dependent processes(Fig. 2.9).

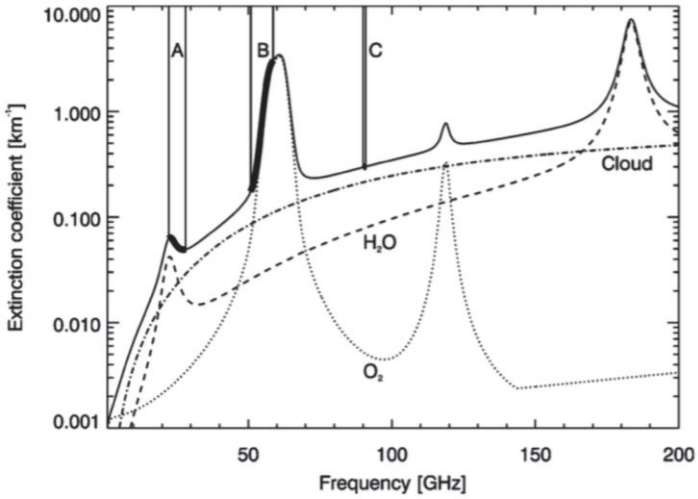

Figure 2. 5 *Extinction coefficient in the microwave spectrum at 850 hPa. The dashed line shows the water vapor contribution, the dotted line the oxygen contribution, and the dotted-dashed line the theoretical cloud liquid contribution of a cloud with 0.2 gm^{-3} LWC (Liquid water content), using the US-standard atmosphere. The solid line is the sum of all contributions (Löhnert et al., 2004).*

As we already mentioned, the scattering efficiency depends on the size parameter. Therefore, the atmosphere can be approximated as a non-scattering medium for frequencies lower than 100 GHz, considering just large particles like hydrometeors (precipitating particles) (Janssen, 1993).

Considering monochromatic radiation with frequency v, travelling towards an infinitesimal layer of air with thickness dR, the intensity I_v can be written as:

$$I_v^a = -\alpha_{Th}^a \, I_v \, dR \tag{2.33}$$

According to the Kirchhoff's law, the absorption of any medium in local thermodynamic equilibrium is equal to its emissivity. Therefore, the net change in the radiation intensity through the layer is:

$$dI_v = dI_v^a + I_v^{emi} = -\alpha_{Th}^a \, I_v \, dR + \alpha_{Th}^a B(T) dR = \alpha_{Th}^a \, [B(T) - I_v] \, dR \tag{2.34}$$

where $B(T)$ is the Plank function and the Eq. (2.34) is the known as Schwarzschild's Equation (Petty, 2006). Regarding to the thermal emission of the blackbody equation at temperature T and considering $B(T)$ in the Rayleigh-Jeans approximation $\left(\frac{hv}{k_b T} \ll 1\right)$, where h is the Planck constant ($h = 6.626\ 10^{-34} \frac{m^2 kg}{K}$), k_b is the Boltzmann constant

($k_b = 1.3810\ 10^{-23}\frac{m^2 kg}{sK}$) and v is the frequency of the radiation, $B(T)$ takes the following form:

$$B(T) = \frac{2hk_b v^2}{c^2} \tag{2.35}$$

As it is seen on Eq. (2.35), the radiation intensity is often scaled to an equivalent blackbody temperature (i.e. brightness temperature) as:

$$T_B \equiv B^{-1} I_v = \frac{\lambda^2}{2k_b} I_v \tag{2.36}$$

Considering T_B for ground-based MWR system, which is receiving down-welling thermal radiation T_B^g, and using the last result (Eq. 2.36) in Eq.(2.34), then integrating from ground to space it is possible to obtain the RTE considering a plane-parallel atmosphere:

$$T_B^g = T_B^{cos} e^{-AOD} + \int_0^\infty \alpha_{Th}^a(R) T(R) e^{-AOD(R)} dR \tag{2.37}$$

where T_B^{cos} is the cosmic background ($\sim 2.73\ K$) (Janssen, 1993), $T(R)$ is the physical temperature and e^{-AOD} is the transmission term.

2.4 References

Adam, M., Putaud, J. P., Martins dos Santos, S., Dell'Acqua, A. and Gruening, C.: Aerosol hygroscopicity at a regional background site (Ispra) in Northern Italy, Atmos. Chem. Phys., 12, 5703-5717, doi:10.5194/acp-12-5703-2012, 2012.

Ångström, A.: The parameters of atmospheric turbidity, *Tellus*, *16*(1), 64-75, 1964.

Argall, P.: LIDAR. Encyclopedia of Imaging Science and Technology, 869-889. Retrieved from Purple crow LIDAR, 2002.

Boucher, O., Randall, D., Artaxo, P., Bretherton, C., Feingold, G., Forster, P., Kerminen, V.-M., Kondo, Y., Liao, H., Lohmann, U., Rasch, P., Satheesh, S. K., Sherwood, S., Stevens, B., and Zhang, X. Y.: Clouds and Aerosols, in: Climate Change 2013: The Physical Science Basis. Contribution of Working Group I to the FifthAssessment Report of the Intergovernmental Panel on Climate Change, edited by: Stocker, T. F., Qin, D., Plattner,

G.-K., Tignor, M., Allen, S. K., Boschung, J., Nauels, A., Xia, Y., Bex, V., and Midgley, P. M., Cambridge University Press, Cambridge, UK and New York, NY, USA, 2013.

D'Almeida, G. A., Koepke, P., and Shettle, E.P.: Atmospheric aerosols: global climatology and radiative characteristics, A. Deepak Pub, 1991.

Feingold, G. and Morley, B.: Aerosol hygroscopic properties as measured by lidar and comparison with in situ measurements, J. Geophys. Res., 108, D11, doi:10.1029/2002JD002842, 2003.

Ferrare, R.A., Melfi, S.H., Whiteman, D.N., Evans, K, D and Leifer, R.: Raman lidar measurements of aerosol extinction and backscattering. 1. Methods and comparisons, J. Geophys. Res., 103, 19,663–19,672, 1998.

Goody, R., R. West, L. Chen, and D. Crisp.: The correlated-k method for radiation, *Rad. Transfer*, *42*(6), 539-550, 1989.

Granados-Muñoz M.J, Navas-Guzmán, F., Bravo-Aranda, J. A., Guerrero-Rascado, J. L., Lyamani, H., Valenzuela, A., Titos, G., Fernández-Gálvez, J., and Alados-Arboledas, L.: hygroscopic growth of atmospheric aerosol particles based on active remote sensing and radiosounding measurements: selected cases in southeastern Spain. Atmos. Meas. Tech., 8, 705–718, 2015.

Hänel, G.: The Properties of Atmospheric Aerosol Particles as Functions of the Relative Humidity at Thermodynamic Equilibrium with the Surrounding Moist Air, in: Advances in Geophysics, edited by: Landsberg, H. E. and Mieghem, J. V., 73–188, Elsevier, 1976.

Horvath, H.: Influence of atmospheric aerosols upon the global radiation balances, in Atmospheric Particle, edited by R. M. H. a. R. v. Grieken, pp. 543-596, John Wiley & Sons, 1998.

Janssen, M.: Atmospheric remote sensing by microwave radiometry, Wiley-interscience publication, Wiley, New York, 1993.

Kaufman, Y. J., O. Boucher, D. TanrÃ©, M. Chin, L. A. Remer, and T. Takemura.: Aerosol anthropogenic component estimated from satellite data, Geophysical Research Letters, 32(17), 1-4, 2005.

Kovalev, V. A.: Elastic Lidar: Theory, Practice, and Analysis Methods. Wiley-Interscience, 2004.

Liou, K. N.: An introduction to atmospheric radiation (Vol. 84). California: Elsevier Science, 2002.

Liou, K.-N.: An Introduction to Atmospheric Radiation, Academic Press, Inc., United States of America, 1980.

Löhnert, U., Crewell, S., and Simmer, C.: An integrated approach toward retrieving physically consistent profiles of temperature, humidity, and cloud liquid water, Journal of Applied Meteorology, 43, 1295–1307, 2004.

Löhnert, U., van Meijgaard, E., Baltink, H. K., Groß, S., and Boers, R.: Accuracy assessment of an integrated profiling technique for operationally deriving profiles of temperature, humidity, and cloud liquid water, Journal of Geophysical Research: Atmospheres, 112, doi:10.1029/2006JD007379, 2007.

Measures, R. M.: Laser remote sensing: fundamentals and applications. Malabar: Krieger Publishing company, 1992.

Petty, G.W.: Afirst course in Atmospheric Radiation. Second Edition, Sundog Publishing, United States of America, 2006.

Pruppacher, H. R., J. D. Klett, and P. K. Wang, Microphysics of clouds and precipitation, Taylor&Francis, pp. 381-382, 1998.

Rissler J. et al., Hygroscopic properties of biomass burning and combustion aerosols, cap 3-4, 2003.

Seinfeld, J. H., and S. N. Pandis, Atmospheric chemistry and physics: from air pollution to climate change, John Wiley & Sons, 2012.

Shifrin, K. S.: Simple relationships for the Ångström parameter of disperse systems, Applied Optics, 34(21), 4480-4485, 1995.

Shneider J., Physical chemistry: Thermodynamics of aerosol particles,cap 4, 1998.

T. Leblanc, I. M.: Evaluation and optimization of lidar temperature analysis algorithms using simulated data. Journal of Geophysical research, 6177-6187, 1998.

Titos, G., Cazorla, A., Zieger, P., Andrews, E., Lyamani, H., Granados- Muñoz, M.J., Olmo, F.j and Alados-Arboledas, L.: Effect of hygroscopic growth on the aerosol light-scattering

coefficient: A review of measurements, techniques and error sources. Atmos. Env., 141, 494-507, 2016.

Titos, G., Jefferson, A., Sheridan, P. J., Andrews, E., Lyamani, H., Alados-Arboledas, L., and Ogren, J. A.: Aerosol light-scattering enhancement due to water uptake during the TCAP campaign, Atmos. Chem. Phys., 14, 7031–7043, doi:10.5194/acp-14-7031-7043, 2014.

Veselovskii, I., Whiteman, D. N., Kolgotin, A., Andrews, E., and Korenskii, M.: Demonstration of aerosol property profiling by multi-wavelength lidar under varying relative humidity conditions, J. Atmos. Ocean. Tech., 26, 1543–1557, 2009.

Weitkamp, C.: Range- Resolved Optical Remote Sensing of the Atmosphere. Germany: Springer, 2005.

Wiegner, M. and Geiß, A.: Aerosol profiling with the Jenoptik ceilometer CHM15kx, Atmos. Meas. Tech., 5, 1953–1964, doi:10.5194/amt-5-1953-2012, 2012.

Zieger, P., Fierz-Schmidhauser, R., Weingartner, E., and Baltensperger, U.: Effects of relative humidity on aerosol light scattering: results from different European sites, Atmos. Chem. and Phys., 13, 10 609–10 631, doi:10.5194/acp-13-10609-2013, http://www.atmos-chem-phys.net/13/10609/2013/, 2013.

3. Facilities and instrumentation

This thesis has been developed at three different locations (Fig 3.1.). The first one is the Andalusian Institute for Earth System Research (Centro Andaluz del Medio Ambiente, IISTA-CEAMA), located in Granada (Spain, 37.16°N, 3.61°W, 680 m asl). The second facility is the SIATA (Sistema de Alerta Temprana de Medellín y el Valle de Aburrá) station, located in Medellín (Colombia, 6.26ºN, 75.59ºW, 1470 asl). The last one is at the SIRTA observatory (Site Instrumental de Recherche par Télédétection Atmosphérique), located approximately 20 km Southwest of Paris city center, on the Saclay plateau (France, 48.713 º N, 2.208 ºE, 160 m asl). A detailed description of these facilities is given in the following sections.

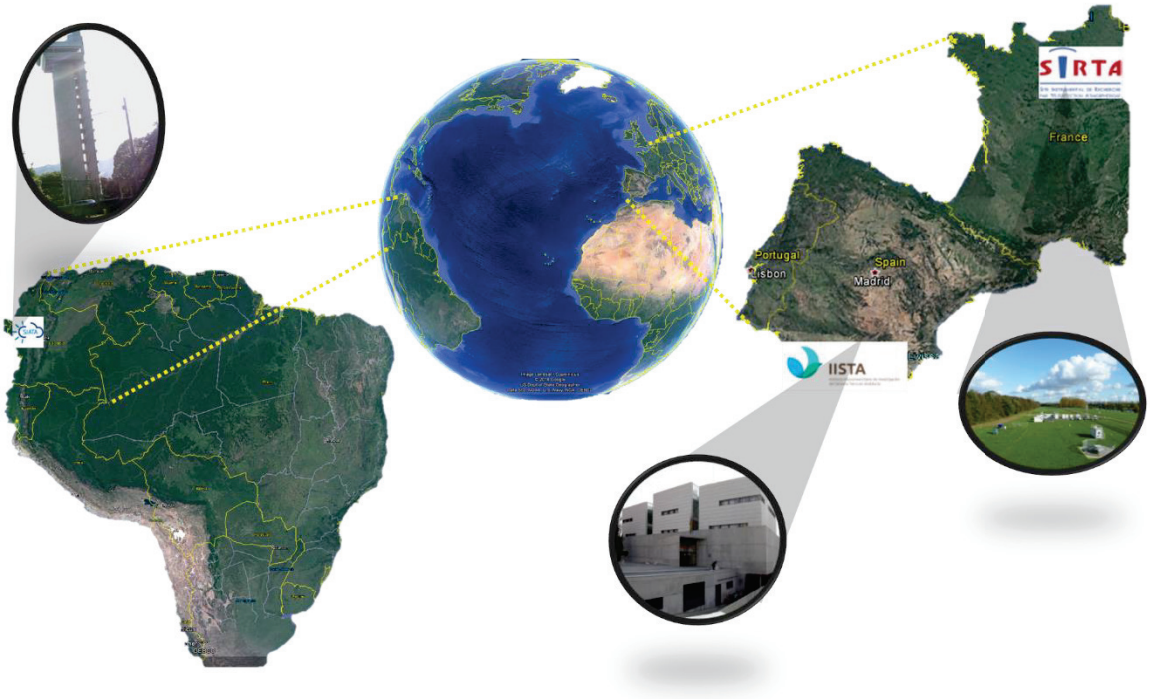

Figure 3.1. *Location of the stations involved in this thesis: SIATA (Colombia), IISTA-CEAMA (Spain) and SIRTA (France).*

3.1 IISTA-CEAMA station

IISTA-CEAMA is an urban station located at the South-East of the Spain at Granada city (37.16°N, 3.61°W, 680 m asl). This station, which is part of the ACTRIS program, is managed by the University of Granada (UGR). Granada is characterized by its complex

terrain surrounded by mountains with elevations between 1000 and 3398 m asl, mainly affected by semicontinental climate conditions responsible for large seasonal temperature differences with hot summers and cool winters. Regarding the long transport aerosol sources, this city is predominantly affected by mixed aerosol particles coming from Europe and mineral dust particles from the African continent (Lyamani et al., 2006a, b; Guerrero-Rascado et al., 2008a, 2009; Córdoba-Jabonero et al., 2011; Titos et al., 2012; Navas-Guzmán et al., 2013; Valenzuela et al., 2014; Benavent-Oltra et al., 2017; Cazorla et al., 2017). Transported smoke, principally comes from North America, North Africa and the Iberian Peninsula, can also affect the study area (Alados-Arboledas et al., 2011; Navas-Guzmán et al., 2013; Preißler et al., 2013; Pereira et al., 2014; Ortiz-Amezcua et al., 2014, 2017). The principal local sources are road traffic, domestic-heating (during wintertime) and biomass burning (Titos et al., 2017). Moreover, the probability of marine particles reaching the city is low despite the short distance to the coast (about 50 km away) due to the orography of the region, with mountains blocking the path from the sea to the city. Titos et al. (2014) showed that the contribution of marine aerosols to PM10 mass concentration at IISTA-CEAMA station is almost negligible (<3%).

3.1.1 Active remote sensors at the IISTA-CEAMA station

One of the instruments used in this study is the multi-wavelength Raman lidar MULHACEN (Raymetrics S.A., Greece), located at IISTA-CEAMA station (Fig. 3.2). MULHACEN is included in EARLINET (European Aerosol Lidar Network) (Pappalardo, et al., 2014) and SPALINET (Spanish and Portuguese Aerosol Lidar Network) (Sicard et al., 2009), now operating in the framework of ACTRIS-2 (Aerosols, Clouds and Trace gases Research Infrastructure). It emits laser pulses at 355, 532 (parallel and perpendicular polarization channels) and 1064 nm, and it receives elastic backscattered photons at 355, 532 and 1064 nm in analog and photon counting modes. It also collects Raman backscattered photons at 607 and 387 nm from molecular nitrogen (N_2) and at 408 nm from water vapor (H_2O) in photon counting mode during routine nighttime measurements. Detailed information about this system is listed on Table 3.1. Such kind of configuration allows for deriving not only vertically-resolved particle optical properties but also water vapor mixing ratio profiles. Nominal vertical resolution for the lidar backscattered signals is 7.5 m. Atmospheric information retrieved from lower

regions is limited by the full overlap height, which is reached at 1220 m agl due to the system configuration (Guerrero-Rascado et al., 2010; Navas-Guzmán et al., 2011). A full description of this instrument can be found in Guerrero-Rascado et al. (2008a, 2009). Aerosol particle backscatter coefficient profiles, β_{par} (z), are retrieved by the well-known Klett-Fernald method (Fernald et al., 1972, Fernald, 1984; Klett, 1981, 1985). The total uncertainty for β_{par} retrieved with this method is usually within 20% (e.g. Preißler et al., 2011).

Figure 3.2. *Raman lidar MULHACEN system working at IISTA-CEAMA facilities in Granada (Spain).*

Table 3.1 *Characteristics of the MULHACEN system*

Emitter
Laser source (class IV): Nd:YAG (Quantel CFR Series)
Wavelength (nm): 355, 532, 1064
Energy/pulse (mJ): 60, 65,110
Repetition rate frequency of the laser (Hz):1, 2, 5, 10
Beam diameter: 6 mm
Beam divergence: < 0.1 mrad
Collector
Telescope: Cassegrain
Primary mirror diameter (mm): 400
Secondary mirror diameter (mm): 90
Focal length (mm): 3998
Detection
Transductor: LICEL
Detectors: APD (1064 nm), PMT (rest of the channels)
Detection mode: Analog and photon counting
Wavelengths (nm): 355, 387, 408, 532p, 532s, 607, 1064
1064 nm-acquisition mode: 12 Bit-20 MHz
532, 355 nm-acquisition's mode: 12 Bit-20 MHz
Photon counting mode (387, 408, 607 nm): 250 MHz
Vertical resolution: 7.5 m
Temporal resolution: 1 min/profile (used here), but it is variable

The CHM15k Nimbus ceilometer (Lufft manufacturer), which belongs to ICENET (Cazorla et al., 2017), operates with a pulsed Nd:YAG laser which emits radiation towards the atmosphere at 1064 nm (Fig 3.3). The energy per pulse is 8.4 μJ with a repetition rate of 5-7 kHz with a laser divergence less than 0.3 mrad. The collected backscattered signal is collected with a telescope with 0.45 mrad of field of view. The signal is detected by an avalanche photodiode in photon counting mode. The complete overlap is reached about 1500 m above the instrument (Heese et al., 2010), but according to the overlap function provided by manufacturer, the overlap is 90 % complete between 555 and 885 m agl (Cazorla et al, 2017). These systems have high spatial and temporal resolutions (15 m and 15 s, respectively) with a maximum height recorded about 15360 m agl. Further details are listed in Table 3.2. Ceilometers operates using the lidar principle (Sec. 2.3.1), but with the advantage of unattended 24/7 operation. This system is operational since 2012 at the IISTA-CEAMA station.

Figure 3 3. *Ceilometer CHM15k Jenoptik operating at IISTA-CEAMA station in Granada (Spain).*

***Table 3.**2 Characteristics of the ceilometer Jenoptik CHM 15k operating at CEAMA-GFAT station.*

Jenoptik ceilometer CHM 15k

Measurement principle: optic (lidar)
Range of the measurements: from 15 to 15000 m
Spatial resolution: standard: 15 m**,** optional: 5 m
Measures: aerosols and clouds
Parameters that measure: top base of the clouds, amount of clouds and thickness, vertical visibility and atmospheric boundary layer
Laser source: Nd:YAG
Wavelength: 1064 nm

A co-located Doppler lidar system (HALO photonics Stream Line), from now DL, is also operating at the IISTA-CEAMA station since May 2016 (Fig. 3.4). This system provides range-resolved measurements of attenuated backscatter based on the frequency shift associated to the movement of the particles and clouds in the atmosphere by means of heterodyne optical detection principle (Pearson et al., 2008). As this movement is linked to wind, the 3-D wind vector can be determined through the Doppler effect. Radial velocity measurements are taken every 2 s, and conical scans are performed every 10 min with 75º elevation angle and at 12 equidistant azimuth angles. The eye-safe laser transmitter vertically pointing to zenith operates at 1.5 μm, with low pulse energy (∼100μJ) and high pulse repetition rate (∼15 kHz) on a monostatic coaxial set up (Table 3.3). See Päschke et al. (2015) for further information of the system configuration.

Figure 3.4. *Doppler lidar system (HALO photonics Stream Line) operating at Granada (Spain).*

Table 3.3 *Principal characteristics of the Doppler lidar DL (HALO photonics Stream Line)*

Lidar Doppler (HALO photonics Stream Line)
Measurement principle: Doppler effect and optic (lidar)-with scanning mode
Rate frequency: 50 MHz (optional: 30 MHz)
Nyquist velocity: 10 m/s
Spatial resolution (m): 36 (standard, used in this thesis), 30 (optional)
Integration time (s): 30
Measurements: wind velocity and backscattering
Pulse length (μs): 0.2
Laser source: Class IV
Wavelength (μm): 1500

3.1.2 Passive remote sensors at the IISTA-CEAMA station

A ground-based MWR (RPG-HATPRO G2, Radiometer physics GmbH) used in this thesis belongs to MWRnet (http://cetemps.aquila.infn.it/mwrnet/) (Rose et al., 2005 and Caumont et al., 2016) (Fig 3.5). This is a passive remote sensor, which measures the emission of thermal radiation from the atmosphere in the microwave region. The MWR has a radiometric resolution between 0.3 and 0.4 rms at 1.0-s integration time and a high temporal resolution for vertical profiles, retrieving roughly one profile each two minutes. The MWR has two bands with seven channels each one. The K-band (22.24, 23.04, 23.84, 25.44, 26.24, 27.84 and 31.4 GHz) provides information about water vapor in the atmosphere, allowing to retrieve integrated column products such as integrated water vapor (IWV) and liquid water path (LWP). The V-band (51.26, 52.28, 53.86, 54.94, 56.66, 57.3 and 58.0 GHz) contains information about temperature profiles (Löhnert and Mainer, 2012; Navas-Guzmán et al., 2016), associated to the thermal emission from molecular oxygen in the atmosphere. Water vapor observations are performed at zenith position, while temperature information can be retrieved assuming horizontal homogeneity and performing vertical scanning observations (Löhnert et al., 2009).

Vertical profiles of temperature and RH are composed by 39 height-bins, where 25 are below 2 km of altitude (roughly inside de atmospheric boundary layer) with a variable resolution from 10 to 200 m. The vertical resolution in the upper levels (mainly in the free troposphere, 2 to 10 km) varies from 200 m to 2000 m (the last 14 height-bins). An absolute calibration is recommended to be performed at least every 6 months, by using cold liquid-nitrogen and hot loads as reference (Turner et al. 2007; Maschwitz et al., 2013). The accuracy of the temperature profile reported by the manufacturer is lower than 0.75 K RMSE in the range 1.2-4.0 km and larger than 1.0 K RMSE from 4 to 10 km. However, there is no reported accuracy for RH profile, because RH profiles are retrieved from the combination of temperature and absolute humidity profiles. The absolute humidity profiles have an accuracy up to ± 0.02 g/m^3 RMS from 0 to 1 km, within the atmospheric boundary layer up to ± 0.03 g/m^3 RMS (i.e. 1-2 km), and up to ± 0.04 g/m^3 RMS above 2 km. MWRs commonly use temperature inversion methods based on neural networks or linear regressions, which requires an extense temperature database taken close to the instrument for training them (Cimini, et al., 2015). To this aim, thousands of RSs are typically required for this aim, becoming it their principal disadvantage. On the other hand, other inversion algorithms based on Optimal Estimation Method (Rodgers,

2000) have been used in the last years to overcome this issue (Bernet et al., 2017; Navas-Guzmán et al., 2014b, 2017). Here, the manufacturer has performed the training of the MWR inversion algorithm by using neural networks.

Figure 3.5. *Microwave Radiometer (RPG-HATPRO G2, Radiometer physics GmbH) operating at the IISTA-CEAMA station in Granada (Spain).*

As a part of the IISTA-CEAMA radiometric station, a Sun/sky photometer (Cimel Electronique, Fig 3.6) CE-318-4 is also operative and co-located to the MULHACEN and MWR. This instrument belongs to AERONET (Holben et al., 1998), which processes the spectral Sun and sky measurements of the photometer and provides in its website (https://aeronet.gsfc.nasa.gov) the optical and microphysical aerosol properties integrated in the atmospheric column. Aerosol optical depths (AOD_λ) at 340, 380, 440, 500, 675, 870 and 1020 nm are among the basic AERONET products. Additionally, the Sun-photometer has also a channel at 940 nm, which allows for retrieving the total column water vapor (or precipitable water) (Eck et al., 1999).

The uncertainty in retrieved at AOD_λ associated with primary calibration is around 0.010-0.021 (with higher uncertainties in the UV region). For the inversion products, the study presented in Dubovik et al. (2000) showed that uncertainty in the single scattering albedo is ± 0.03 ($AOD_{440\,nm} > 0.4$) for high aerosol loads and solar zenith angle $\theta > 50°$, instead of low aerosol load ($AOD_{440\,nm} > 0.2$) with larger uncertainties between 0.02 and 0.07. For the imaginary part of refractive index, the uncertainty is about 20-50%. More information can be found in Table 3.4.

Figure 3.6. *Sun/sky photometer (Cimel Electronique) CE-318-4 operating at the IISTA-CEAMA station in Granada (Spain).*

Table 3.4 *Characteristics of the Sun photometer (CIMEL CE 318-4)*

Sun Photometer CIMEL CE 318 -4

Sun photometer model	CE 318-4
Detector	Si Fotodiodes
Number of filters/wavelengths	8/1020-936-870-675-500-440--380-340 nm
FWHM	10-10-10-10-10-4-2 nm
Numbers of collimators	2
FOV/Aperture	1.2°
For a precise tracking **on the sun**	4-quadrant position detector. Accuracy of 0.05
Measurement types	Direct, almucantar and principal plane
Applications	Atmospheric aerosol and Water vapor
Motoring system	Motor step-by-step azimuthal and zenithal
Batteries	Internal battery in electronic box, external batery for both motor and solar panel.

3.1.3 Ancillary instrumentation at the IISTA-CEAMA station

Co-located RS are occasionally launched when Raman lidar measurements are taken. The RS data are obtained with a GRAW DFM-06/09 system (GRAW Radiosondes, Germany), which provides temperature (resolution 0.01°C, accuracy 0.2 °C), pressure (resolution 0.1

hPa, accuracy 0.5 hPa) and RH (resolution 1%, accuracy 2%) profiles with vertical resolution depending on the sonde ascension velocity, usually around 5 m/s (Fig 3.7). Data acquisition and processing are performed by the GRAWmet software and GS-E ground station from the same manufacturer. More details are given in table 3.5.

Figure 3.7. *Radiosonde GRAW DFM-06/09 system (GRAW Radiosondes, Germany), located at the IISTA-CEAMA station in Granada (Spain).*

Finally, in order to distinguish between clear/cloudy conditions, we have used a cloud cover database obtained from co-located sky cameras installed on the IISTA-CEAMA roof-top (Fig 3.8). Cloud cover information from January 2012 to January 2015 was retrieved from the All Sky Imager shown in Cazorla et al. (2008) and Román et al. (2012), while from February 2015 to December 2016 cloud cover was obtained from the SONA sky camera described in Cazorla et al. (2015) and Román et al. (2017b). A full description of both cameras and methods for each one can be found in Cazorla et al. (2008) and Román et al. (2017a).

Table 3.5 Main characteristics of the RS (DFM-09)

Radiosonda DFM-09
Weight (g): < 90
Size (mm): 94 x 94 x 60
Battery: Dry Lithium
Bandwidth: <20kHz
Frequency and deviation : 400 to 406 MHz ± 5 kHz
Modulation: FSK
Error correction: Code-spreading, interleaving
Temperature precision: < 0.2 °C
RH resolution: 1 %
RH precision: < 5 %
Pressure precision: < 1hPa

Figure 3.8. *SONA sky camera located at the roof top of the the IISTA-CEAMA station in Granada (Spain).*

3.2 SIATA station

SIATA (Sistema de Alerta temprana de Medellín y el Valle de Aburrá) is a big project of science and technology created in the metropolitan area of the Medellin city (Colombia). SIATA becomes a strategy to manage the risk and monitoring the environmental

conditions in order to make easier to take decisions by the governmental organisms. At present, SIATA has also become into huge network around the Aburra's Valley, practically spreading along the valley with a wide set of instrumentation (in situ and remote sensors) for monitoring the air quality and extreme meteorological events. More information about the network is given in the webpage *https://siata.gov.co/siata_nuevo/*. In this thesis, we only use the information of the remote sensors, namely a Vaisala CL51 ceilometer and MWR MP3000A, both located at the facility known as SIATA-tower.

The SIATA-tower station is located in the Center-West of Medellín, Antioquia, Colombia (6.25°N, 75.58°W, 1470 m asl). Medellín city is surrounded by mountains with altitudes over 2800 m asl (Fig. 3.9) and it is located in the center of the Aburrá valley. This valley is located in the tropical Andean region and it is quite narrow in the north part (about 20 km wide), but in the center it could reach about 60 or 70 km wide, with a reduction in the south region about 10 km. The irregular topography of this valley and its wind dynamics make that aerosol particles can stagnate for long periods over the city under specific atmospheric conditions without efficient natural mechanisms to remove them. Indeed, the atmospheric boundary layer height is directly affected, when the valley is covered mostly by clouds and large aerosol loads. Under some atmospheric scenarios the atmospheric boundary layer height grows no more than a hundred of meters, causing a direct impact over visibility and people's health (Nisperuza, et al., 2014; Herrera-Mejia, 2015). In addition, the increase of the population, industry and vehicular park along the last decades makes that aerosol particles emissions increase considerably affecting the air quality of the region, mostly between April to May and September to October where precipitations are quite often (Herrera-Mejia, 2015).

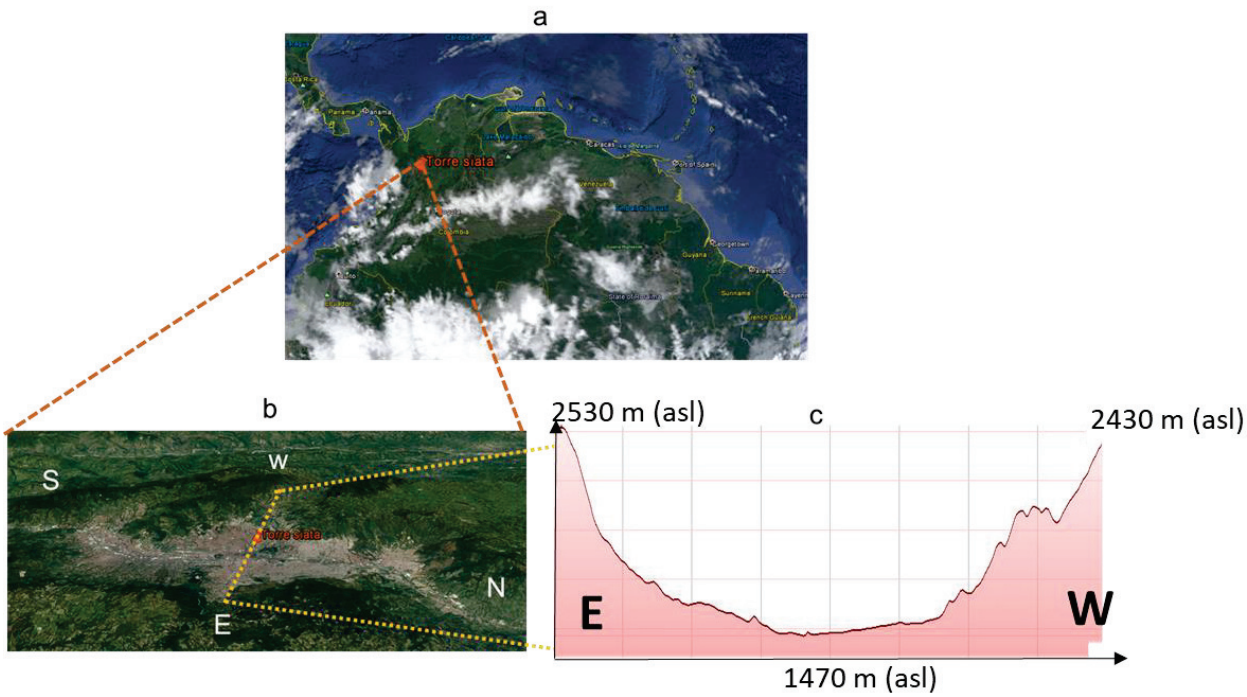

Figure 3.9. *Location of the SIATA-tower station at Medellín (Colombia).*

This region is highly influenced by a wide set of local aerosol particles (such as urban/industrial and mixed aerosol particless) and less by long range transported ones such as mineral dust and biomass burning particles (Alegría. 2015 and Bedoya-Velásquez et al., 2016), among others. The aerosol typing presented in Fig. 3.9 was performed using AERONET level 2.0 data for a total of 6 years of measurements with the Sun-photometer, located at Universidad Nacional de Colombia, sede Medellín, under the administration of the Lasers and Spectroscopy Group (abbreviation in Spanish GLEO).

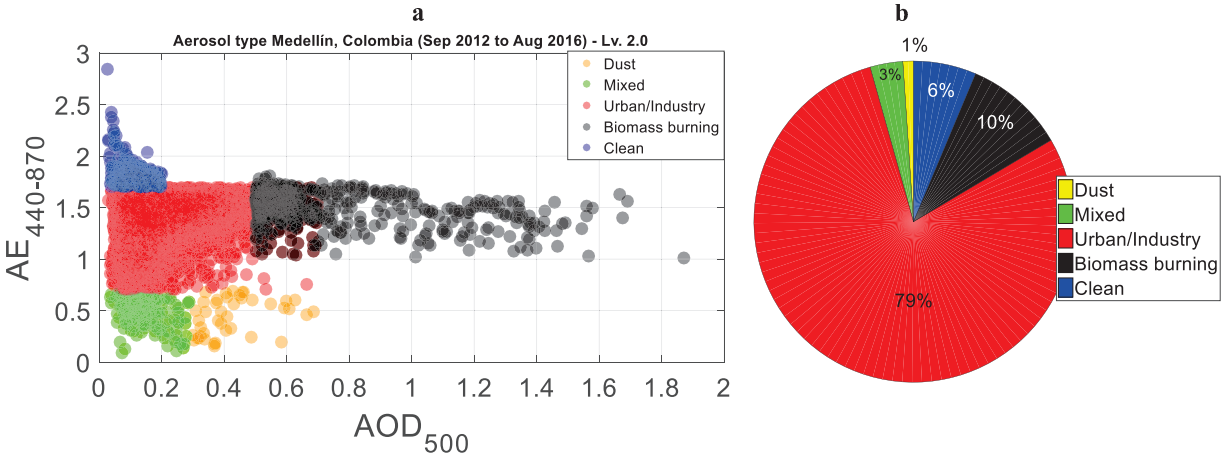

Figure 3.10. *Aerosol type characterization of Medellín.*

In the 6-year database a total of 4851 cases were evaluated between September 2012 to August 2016, with high missing data associated to the high clouds presence at Medellín city and some instrumental issues. This analysis shows that Medellín city is very influenced by urban/industrial (79 %) and biomass burning (10 %) particles, and with lower presence of clean (6 %), mixed (3%) and mineral dust particle (1 %) scenarios. The results obtained in Fig. 3.10 were obtained by using the criteria for aerosol sources classification developed by Giles et al. (2012) and Gharibzadeh et al. (2018), where AOD>0.25 and AE<0.7 refers to dust aerosols, AOD<0.3 and AE<0.7 classified as mixed aerosol, 0.01<AOD<0.7 and 0.7<AE<1.7 is associated to urban/mixed, AOD>0.5 and AE>1 linked to biomass burning and AOD <0.2 and AE>1.7 as clean aerosol.

3.2.1 Active remote sensors at the SIATA-tower

A Vaisala CL51 ceilometer (Fig. 3.11) is used in this thesis for the analysis in the Colombian territory. This instrument has the same physical and operational principle of lidar systems, allowing the possibility to retrieve the attenuated backscatter as its basic product. This system emits pulsed radiation towards the atmosphere generated by an InGaAS diode laser centered at 910 ± 10 nm at 25 °C. Its repetition rate is about 6.5 kHz, with averaged power close to 19.5 mW and a beam divergence up to ± 0.15 x ± 0.25 mrad (http://www.raimet.ru/imgs/db/catalog2_files/file_106.pdf). This system measures at

high temporal and spatial resolution (15 s and 10 m, respectively) with detection up to 4500 m , which is a lower height detection range than the one of the Jenoptik systems (up to 15000 m). One advantage of these systems is its full overlap height, which is reached up 50 m, and it can be reduced following the fabricant specifications and some data pre-processing to 10 or 20 m (Kotthaus et al., 2016). One of the main drawbacks of the Vaisala ceilometers is that the backscattered signal is affected by the water vapor absorption and, therefore, a correction must be performed by following the Wiegner et al. (2015) method. More information is detailed on Table 3.6.

Figure 3.11. *Vaisala CL 51 ceilometer located at the roof top of the SIATA-tower..*

Table 3.6 *Characteristics of the Vaisala CL51 ceilometer installed at the SIATA-tower station in Medellín (Colombia).*

Vaisala CL 51

Measurement range (m): 0 a 15000 m (here it is used until 4500 m)
Spatial resolution (m): 10 (standard)
Measurements: aerosols and clouds
Products: Three could layers simultaneously**,** vertical visibility and attenuated backscatter coefficient.

Laser source: InGaAs diode

Wavelength (nm): 910

3.2.2 Passive remote sensors at the SIATA-tower station

The MWR located at the SIATA-tower station is the MP-3000 A (*Radiometrics Corporation, 2012,* Fig. 3.12). The physical and operational principles are the same than RPG-HATPRO MWR presented in Sec. 3.1.2 with receptors in the 22-30 GHz y 51-59 GHz frequency bands. The first band is associated to humidity profiles and the second one to oxygen related to temperature profiles in the atmosphere. The temporal resolution is also about 2 min/profile and the vertical resolution is variable, reporting data each 50 m from surface until 500 m, then increasing to 100 m from 500 m to 2000 m and degraded to 250 m from 2000 m to 10000 m, which a total of 58 bins for each profile. The main products that MWR retrieve is atmospheric temperature, RH, water vapor density and liquid water profiles.

Figure 3.12. *Microwave radiometer MP-3000 A located at the SIATA-tower station in Medellín (Colombia).*

3.2.3 Ancillary instrumentation at the SIATA-tower station

RS lauches were performed during campaigns at SIATA-tower station. The co-located launches are performed from the ground level of the tower by using an IMET-1 RS system (Intermet Systems). The frequency of this RS is about 403 MHz with bandwidth of 6 kHz. The altitude that these systems reach is close to 30 km sampling at 1 Hz (see table 3.7). Temperature measurements have an accuracy of 0.2 °C with resolution <0.01°C in a range

from -95 to 50 °C, humidity is measure with accuracy up to 5 % with resolution < 0.1 % from 0 to 100 % and pressure is measured with 0.5 hPa of accuracy and it is <0.01 hPa of resolution from 2 to 1070 hPa.

Figure 3.13. *Radiosonde IMET-1used at the experimental SIATA station Medellín (Colombia).*

Table 3.7. *Characteristics of the iMET-1 RS used in the SIATA-tower station*

iMET-1 RS
Weight: <260 g
Nominal frequency: 403 MHz
Battery: Alkaline Dry Cell
Bandwidth: 6 kHz
Range:>250 km
Altitude: > 30 km
Sampling: 1 Hz
Temperature precision: < 0.2 °C
Humidity resolution: < 0.1 %
Humidity precision: < 5 %
Pressure precision: < 0.5 hPa

3.3 SIRTA observatory

SIRTA observatory (Site Instrumental de Recherche par Télédétection Atmosphérique, htttp//sirta.ipsl.fr) is located approximately 20 km Southwest of Paris city center, on the Saclay plateau (2.21ºE, 48.71º N, 160 m asl). This 'supersite' is surrounded by suburban facilities, forests, agricultural fields and roads connecting to Paris. It is part of the European Research Infrastructure for the observation of Aerosol, Clouds, and Trace gases (ACTRIS) and EARLINET (Pappalardo et al., 2014), including active and passive remote sensing instrumentation operative since 2002 (Haeffelin et al., 2005) and in-situ equipment operating continuously since 2011 (Petit et al., 2015). Atmospheric composition measurements performed at SIRTA are considered to be representative of background conditions for the Paris region. Regarding seasonal features, winter and early spring periods frequently experience pollution episodes, mainly related to wood-burning, mobile sources (road transportation), and agricultural emissions at a regional scale along with the transport of polluted air masses associated with high pressure mesoscale systems (Petit et al., 2014, 2015; Dupont et al., 2016). During summer and autumn, the region remains clean; nevertheless, with a maximum impact of road traffic emissions on air quality during the September-October period (Petit et al., 2015).

3.3.1 Meteorological sensors at the SIRTA station

The meteorological instruments used from this observatory are located on an instrumented-tower at 1, 2, 5, 10, 20, and 30 m agl, described in Haeffelin et al. (2016). Here, it are used meteorological measurements just at 30 m agl. Temperature and relative humidity were obtained from Young 41382 and 43408 sensors with a temporal resolution of 1 min. Both sensors have a temperature range from -50°C to 50 °C with ± 0.3 °C of precision, while the range for relative humidity ranges from 0 to 100 % with ± 0.2°C of precision. Wind velocity and direction were measured using a sonic anemometer (Metec sonic anemometers) operating at 10 Hz for raw data (1 min-averaged) with uncertainties of 0.1 m/s and ± 2°, for speed and direction, respectively.

3.3.2 In-situ aerosol instruments at the SIRTA station

Aerosol chemical composition of non-refractory submicron aerosols was obtained with an Aerosol Chemical Speciation Monitor (ACSM, Aerodyne Research Inc.). A detailed description of this instrument and its operation at SIRTA can be found in Ng et al. (2011) and Petit et al. (2015). The ACSM measures on-line submicron concentration of organic aerosol (OA), ammonium (NH_4^+), nitrate (NO_3^-) and sulfate (SO_4^{2-}) particles with a temporal resolution of 30 min. Black carbon (BC) mass concentration has been obtained from measurements of the absorption coefficient at 880 nm performed with a multi-wavelength Aethalometer (AE33 model, Magee Scientific) at 1-min resolution. The AE33 measurement principle is described in Drinovec et al. (2014). In this thesis, concentrations of BC and non-refractory chemical species are used as hourly data, and PM_1 mass concentration is estimated as the sum of these compounds. The in-situ monitoring station is located 5 km east of the instrumented tower (SIRTA zone 5).

3.3.3 Vaisala ceilometer at the SIRTA station

This system operates under the same lidar's principle, sending radiation towards the atmosphere at 905 ± 10 nm at 298 K, as stated by the laser manufacturer. It has a typical spectral width (full width at half maximum, FWHM) is 4 nm. The laser source is an InGaAS diode which measures at high temporal and spatial resolution (15 s and 10 m, respectively) with relative lower height detection range compared to CL51 up to 7500 m. Regarding to the huge advantage of this instruments respect to lidars, the full overlap can be minimize to 10 or 20 m (Kotthaus et al., 2016). As it was explained for CL51, due to their emission wavelength it is affected by water vapor absorption, and here it is corrected using the method proposed by Weigner et al. (2015). Table 3.8.summarizes the main characteristics.

Table 3.8. *Characteristics of the Vaisala CL31 ceilometer installed at the SIRTA observatory in Saclay Plateau (France).*

Vaisala CL 31

Measurement range (m): 0 a 7500 m
Spatial resolution (m): 5 or 10 (standard, used in this thesis)
Measurements: aerosols and clouds
Parameters that measure: Three could layers simultaneously, vertical visibility and attenuated backscatter coefficient
Laser source: InGaAs diode
Wavelength (nm): 910

3.4 References

Alegría Campo, D. L.: Propiedades microfísicas de los aerosoles troposféricos derivadas de medidas de fotómetro solar y Lidar en el Valle de Aburrá. Maestría thesis, Universidad Nacional de Colombia - Sede Medellín, 2015.

Alados-Arboledas, L., Müller, D., Guerrero-Rascado, J., Navas-Guzmán, F., Pérez-Ramírez, D., and Olmo, F.: Optical and microphysical properties of fresh biomass burning aerosol retrieved by Raman lidar, and star-and sun-photometry, Geophys. Res. Lett. 38, L01807, doi: 10.1029/2010GL045999, 2011.

Bedoya-Velásquez, A.E., Nisperuza, D.J., Alegría, D.L., Munera, M., Guerrero-Rascado, J.L., Zapata, C., Jiménez, J.F., Landulfo, E., and Bastidas, A.E.: Strong Saharan Dust Event Detected at Lalinet LOA-UNAL Station, over Medellín, Colombia by Active and Passive Remote Sensing. The European Physical Journal Conferences 119:08006, doi: 10.1051/epjconf/201611908006, 2016.

Bedoya-Velásquez, A. E., Navas-Guzmán, F., Granados-Muñoz, M. J., Titos, G., Román, R., Casquero-Vera, J. A., Ortiz-Amezcua, P., Benavent-Oltra, J. A., de Arruda Moreira, G., Montilla-Rosero, E., Hoyos, C. D., Artiñano, B., Coz, E., Olmo-Reyes, F. J., Alados-Arboledas, L., and Guerrero-Rascado, J. L.: Hygroscopic growth study in the framework

of EARLINET during the SLOPE I campaign: synergy of remote sensing and in situ instrumentation, Atmos. Chem. and Phys., 18, 7001-7017, https://doi.org/10.5194/acp-18-7001-2018, 2018.

Benavent-Oltra, J. A., Román, R., Granados-Muñoz, M. J., Pérez-Ramírez, D., Ortiz-Amezcua, P., Denjean, C., Lopatin, A., Lyamani, H., Torres, B., Guerrero-Rascado, J. L., Fuertes, D., Dubovik, O., Chaikovsky, A., Olmo, F. J., Mallet, M., and Alados-Arboledas, L.: Comparative assessment of GRASP algorithm for a dust event over Granada (Spain) during ChArMEx-ADRIMED 2013 campaign, Atmos. Meas. Tech., 10, 4439-4457, https://doi.org/10.5194/amt-10-4439-2017, 2017.

Bernet, L., F. Navas-Guzmán and N. Kampfer: The effect of cloud liquid water on tropospheric temperature retrievals from microwave measurements, Atmos. Meas. Tech., 10, 442-4437, https://doi.org/10.5194/amt-10-4421-2017, 2017.

Caumont, O., Cimini, D., Löhnert, U., Alados-Arboledas, L., Bleisch, R., Buffa, F., Ferrario, M.E., Haefele, A., Huet, T., Madonna, F., Pace, G. Assimilation of humidity and temperature observations retrieved from ground-based microwave radiometers into a convective-scale NWP model. Quarterly Journal of the Royal Meteorological Society, 142 (700), pp. 2692-2704, 2016.

Cazorla, A., Casquero-Vera, J. A., Román, R., Guerrero-Rascado, J. L., Toledano, C., Cachorro, V. E., Orza, J. A. G., Cancillo, M. L., Serrano, A., Titos, G., Pandolfi, M., Alastuey, A., Hanrieder, N., and Alados-Arboledas, L.: Near-real-time processing of a ceilometer network assisted with sun-photometer data: monitoring a dust outbreak over the Iberian Peninsula, Atmos. Chem. Phys., 17, 11861-11876, https://doi.org/10.5194/acp-17-11861-2017, 2017.

Cazorla, A., Husillos, C., Antón, M., Alados-Arboledas, L.: Multi-exposure adaptive threshold technique for cloud detection with sky imagers. Sol. Energy, 114, 268–277, 2015

Cazorla, A., Olmo, F.J., Alados-Arboledas, L.: Development of a sky imager for cloud cover assessment. Opt. Soc. Am. A., vol 25, No. 1, 2008.

Cimini, D., Nelson, M., Güldner, J., and Ware, R.: Forecast indices from a ground-based microwave radiometer for operational meteorology, Atmos. Meas. Tech., 8, 315-333, https://doi.org/10.5194/amt-8-315-2015, 2015.

Córdoba-Jabonero, C., Sorribas, M., Guerrero-Rascado, J.L., Adame, J.A., Hernández, Y., Lyamani, H., Cachorro, V., Gil, M., Alados-Arboledas, L., Cuevas, E., De La Morena, B.: Synergetic monitoring of Saharan dust plumes and potential impact on surface: A case study of dust transport from Canary Islands to Iberian Peninsula. Atmos. Chem. and Phys., 11, 7, 3067-3091, 2011.

Drinovec, L., Moˇcnik, G., Zotter, P., Prévôt, A. S. H., Ruckstuhl, C., Coz, E., Rupakheti, M., Sciare, J., Müller, T., Wiedensohler, A., and Hansen, A. D. A.: The "dual-spot" Aethalometer: an improved measurement of aerosol black carbon with real-time loading compensation, Atmos. Meas. Tech. 8, 1965-1979, https://doi.org/10.5194/amt-8-1965-2015, 2015.

Dupont, J.-C., Haeffelin, M., Badosa, J., Elias, T., Favez, O., Petit, J.-E., Meleux, F., Sciare, J., Crenn, V., and Bonne, J.-L.: Role of the boundary layer dynamics effects on an extreme air pollution event in Paris, Atmos. Environ., 141, 571-579, doi: 10.1016/j.atmosenv.2016.06.061, 2016

Dubovik, O., King, M.D.: A flexible inversion algorithm for retrieval of aerosol optical properties from sun and sky radiance measurements. J. Geophys. Res. Atmos. 105, 20673–20696, 2000.

Eck, T. F., B. N. Holben, J. S. Reid, O. Dubovik, A. Smirnov, N. T. O'Neill, I. Slutsker, and S. Kinne, Wavelength dependence of the optical depth of biomass burning, urban, and desert dust aerosols, Journal of Geophysical Research: Atmospheres (1984–2012), 104(D24), 31333-31349, 1999.

Fernald, F. G., Herman, B. M., Reagan, J. A.: Determination of aerosol height distribution by lidar, J. Appl. Meteorol. 11, 482-48, 1972.

Fernald, F. G.: Analysis of atmospheric lidar observations- Some comments, Appl. Optics, 23, 652–653, 1984.

Gharibzadeh, M., Alam, K., Abedini, Y., Bidokhti, A.A., Masoumi, A., Bibi, H.: Characterization of the aerosol optical properties using multiple clustering techniques over Zanjan, Iran, during 2010-2013. Appl. optics, 57 No 11/10, 2881-2889, 2018

Giles, D.M., Holben, B.N., Eck, T.F., Sinyuk, A., Smirnov, A., Slutsker, I., Dickenson, R.R., Thompson, A.M., and Schafer, J.S.: An analysis of AERONET aerosol absorption

properties and classification representative of aerosol source regions. J. Geophys. Res., 117, D17203, doi:10.1029/2012JD018127, 2012.

Guerrero-Rascado, J.L., Costa, M.J., Bortoli, D., Silva, D., Lyamani, H., and Alados-Arboledas, L.: Infrared lidar overlap function: An experimental determination. Opt. Express, 18, 20350-20359, 2010.

Guerrero-Rascado, J.L., Olmo, F.J., Avilés-Rodríguez, I., Navas-Guzmán, F., Pérez-Ramírez, D., Lyamani, H., Alados-Arboledas, L.: Extreme Saharan dust event over the southern Iberian peninsula in september 2007: Active and passive remote sensing from surface and satellite. Atmos. Chem. and Phys., 9, 21, 8453-8469, 2009.

Guerrero-Rascado, J.L., Ruiz, B., Alados-Arboledas, L.: Multi-spectral Lidar characterization of the vertical structure of Saharan dust aerosol over southern Spain. Atmos. Environ. Volume 42, Issue 11, 2668-268, 2008a.

Haeffelin, M., Barthès, L., Bock, O., Boitel, C., Bony, S., Bouniol, D., Chepfer, H., Chiriaco, M., Cuesta, J., Delanoë, J., Drobinski, P., Dufresne, J.-L., Flamant, C., Grall, M., Hodzic, A., Hourdin, F., Lapouge, F., Lemaître, Y., Mathieu, A., Morille, Y., Naud, C., Noël, V., O'Hirok, W., Pelon, J., Pietras, C., Protat, A., Romand, B., Scialom, G., and Vautard, R.: SIRTA, a ground-based atmospheric observatory for cloud and aerosol research, Ann. Geophys., 23, 253–275, doi:10.5194/angeo-23-253-2005, 2005.

Haeffelin, M., Laffineur, Q., Bravo-Aranda, J.-A., Drouin, M.-A., Casquero-Vera, J.-A., Dupont, J.-C., and De Backer, H.: Radiation fog formation alerts using attenuated backscatter power from automatic lidars and ceilometers, Atmos. Meas. Tech., 9, 5347-5365, https://doi.org/10.5194/amt-9-5347-2016, 2016.

Heese, B., Flentje, H., Althausen, D., Ansmann, A., and Frey, S.: Ceilometer lidar comparison: backscatter coefficient retrieval and signal-to-noise ratio determination, Atmos. Meas. Tech., 3, 1763–1770, https://doi.org/10.5194/amt-3-1763-2010, 2010

Herrera Mejía, L.: Caracterización de la capa límite atmosférica en el Valle de Aburrá a partir de la información de sensores remotos y radiosondeos. Maestría thesis, Universidad Nacional de Colombia - Sede Medellín, 2015.

Holben, B. N., Eck, T. F., Slutsker, I., Tanre, D., Buis, J. P., Setzer,A., Vermote, E., Reagan, J.A., Kaufman, Y. J., Nakajima,T., Lavenus, F., Jankowiak,, I., and Smirnov, A.:

AERONET –A Federated Instrument Network and Data Archive for Aerosol Characterization, Remote Sens. Environ., 66, 1–16, 1998.

Klett, J. D.: Lidar inversion with variable backscatter/extinction ratios, Appl. Optics, 24, 1638–1643, 1985.

Kotthaus, S., O'Connor, E., Münkel, C., Charlton-Perez, C., Haeffelin, M., Gabey, A. M., and Grimmond, C. S. B.: Recommendations for processing atmospheric attenuated backscatter profiles Atmos. Meas. Tech., 9, 5347–5365, 2016 from Vaisala CL31 ceilometers, Atmos. Meas. Tech., 9, 3769–3791, doi:10.5194/amt-9-3769-2016, 2016.

Löhnert, U. and Maier, O.: Operational profiling of temperature using ground-based microwave radiometry at Payerne: prospects and challenges, Atmos. Meas. Tech., 5, 1121–1134, doi: 10.5194/amt-5-1121-2012, 2012.

Löhnert, U., Turner, D. D., and Crewell, S.: Ground-Based Temperature and Humidity Profiling Using Spectral Infrared and Microwave Observations. Part I: Simulated Retrieval Performance in Clear-Sky Conditions, Journal of Applied Meteorology and Climatology, 48, 1017–1032, doi:10.1175/2008JAMC2060.1, 2009.

Lyamani, H., Olmo, F. J., Alcántara, A., and Alados-Arboledas, L.:Atmospheric aerosols during the 2003 heat wave in southeastern Spain I: Spectral optical depth, Atmos. Environ., 40, 6453–6464, 2006a.

Maschwitz, G., Löhnert, U., Crewell, S., Rose, T., and Turner, D. D.: Investigation of ground based microwave radiometer calibration techniques at 530 hPa, Atmos. Measur. Tech., 6, 2641–2658, doi: 10.5194/amt-6-2641-2013, 2013.

Navas-Guzman F., Tropospheric water vapour and relative humidity profiles from lidar and microwave radiometry. Atmos. Chem. and Phys., 7, 1201-1211, 2014.

Navas-Guzmán, F., Bravo-Aranda, J.A., Guerrero-Rascado, J.L, Granados-Muñoz, M.J, and Alados-Arboledas, L.: Statistical analysis of aerosol optical properties retrieved by Raman lidar over Southeastern Spain. Tellus B, 65, 21234, 2013.

Navas-Guzmán, F., Guerrero Rascado, J. L. and Alados Arboledas, L.: Retrieval of the lidar overlap function using Raman signals. Ópt. Pura y Apl. 44, 71–75, 2011.

Navas-Guzmán, F., N. Kämpfer, and A. Haefele: Validation of brightness and physical temperature from two scanning microwave radiometers in the 60 GHz O2 band using radiosonde measurements, Atmos. Meas. Tech., 9, 4587-4600, 2016.

Navas-Guzmán, F., N. Kämpfer, F. Schranz, W. Steinbrecht, and A. Haefele: Intercomparison of stratospheric temperature profiles from a ground-based microwave radiometer with other techniques, Atmos. Chem. and Phys., 17, 14085-14104, https://doi.org/10.5194/acp-17-14085-2017, 2017.

Ng, N. L., Herndon, S. C., Trimborn, A., Canagaratna, M. R., Croteau, P. L., Onasch, T. B., Sueper, D.,Worsnop, D. R., Zhang, Q., and Sun, Y. L.: An aerosol chemical speciation monitor (ACSM) for routine monitoring of the composition and mass concentrations of ambient aerosol, Aerosol Sci. Tech., 45, 780–794, 2011.

Nisperuza, D.J., Bedoya-Velásquez, A.E., Alegría, D.L., Múnera, M., Jiménez, J.F., Zapata, C.E., and Bastidas, A.: Lidar measurements and wavelength covariance transform method to estimate the atmospheric boundary layer heights in Medellín, Colombia. Opt. Pura Apl. 47 (2) 123-130, doi: http://dx.doi.org/10.7149/OPA.47.2.123, 2014.

Ortiz-Amezcua, P., Guerrero-Rascado, J. L., Granados-Muñoz, M. J., Bravo-Aranda, J.A., Alados-Arboledas, L.: Characterization of atmospheric aerosols for a long range transport of biomass burning particles from Canadian forest fires over the southern Iberian Peninsula in July 2031. Óptica Pura y Aplicada, 47-1, pp.43-49, 2014.

Ortiz-Amezcua, P., Guerrero-Rascado, J. L., Granados-Muñoz, M. J., Benavent-Oltra, J. A., Böckmann, C., Samaras, S., Stachlewska, I. S., Janicka, Ł., Baars, H., Bohlmann, S., and Alados-Arboledas, L.: Microphysical characterization of long-range transported biomass burning particles from North America at three EARLINET stations, Atmos. Chem. and Phys., 2017.

Pappalardo, G., Amodeo, A., Apituley, A., Comeron, A., Freudenthaler, V., Linné, H., Ansmann, A., Bösenberg, J., D'Amico, G., Mattis, I., Mona, L., Wandinger, U., Amiridis, V., Alados-Arboledas, L., Nicolae, D., and Wiegner, M.: EARLINET: towards an advanced sustainable European aerosol lidar network. Atmos. Meas. Tech., 7, 2389-2409, doi:10.5194/amt-7-2389-2014, 2014.

Päschke, E., Leinweber, R., Lehmann, V.: An assessment of the performance of a 1.5μm Doppler lidar for operational vertical wind profiling based on a 1-year trail. Atmos. Meas. Tech., 8, 2251-2266, 2015.

Pearson, G., Davies, F., Collier, C.: An ananlysis of the performance of the UFAM pulsed Doppler lidar for observing the boundary layer. Journal of atmospheric and oceanic technology, 26, 240-250, 2008.

Pereira, S., Preißler, J., Guerrero-Rascado, J.L., Silva, A.M., and Wagner, F.: Forest Fire Smoke Layers Observed in the Free Troposphere over Portugal with a Multi-wavelength Raman Lidar: Optical and Microphysical Properties. The Scientific World Journal, 2014 (11 pages), Article ID 421838, 2014.

Petit, J.-E., Favez, O., Sciare, J., Canonaco, F., Croteau, P., Mo P., MoP., Mo, P., MoWorsnop, D., and Leoz-Garziandia, E.: Submicron aerosol source apportionment of wintertime pollution in Paris, France by double positive matrix factorization (PMF2) using an aerosol chemical speciation monitor (ACSM) and a multi-wavelength Aethalometer, Atmos. Chem. and Phys., 14, 13773-13787, 10.5194/acp-14-13773-2014, 2014.

Petit, J.-E., Favez, O., Sciare, J., Crenn, V., Sarda-Estda-, R., Bonnaire, N., Mo, N., MoN.Dupont, J. C., Haeffelin, M., and Leoz-Garziandia, E.: Two years of near real-time chemical composition of submicron aerosols in the region of Paris using an Aerosol Chemical Speciation Monitor (ACSM) and a multi-wavelength Aethalometer, Atmos. Chem. and Phys., 15, 2985-3005, 10.5194/acp-15-2985-2015, 2015.

Preißler, J., Wagner, F., Guerrero-Rascado, J.L., and Silva, A.M.: Two years of free-tropospheric aerosol layers observed over Portugal by lidar. Journal of Geophysical Research Atmospheres, 118, 9, 3676-3686, 2013.

Preißler, J., Wagner, F., Pereira, S.N., and Guerrero-Rascado, J.L.: Multi-instrumental observation of an exceptionally strong Saharan dust outbreak over Portugal, JGR, 116, D24204, doi:10.1029/2011JD016527, 2011.

Rodgers, C.: Inverse Methods for Atmospheric Sounding: Theory and Practice, World Scientific Publishing Company, Incorporated, Singapore, 2000.

Román, R., Antón, M., Cazorla, A., Miguel, A. D., Olmo, F. J., Bilbao, J., Alados-Arboledas, L.: Calibration of an all-sky camera for obtaining sky radiance at three wavelengths, Atmos. Meas. Tech., 5, 2013–2024,doi:10.5194/amt-5-2013-2012, 2012.

Román, R., Cazorla, A., Toledano, C., Olmo, F.J., Cachorro, V.E., de Frutos, A., Alados-Arboledas, L.: Cloud cover detection combining high dynamic range sky images and ceilometer measurements. Atmos. Res., 196, 224-236, http://dx.doi.org/10.1016/j.atmosres.2017.06.006, 2017

Román, R., Torres, B., Fuertes, D., Cachorro, V.E., Dubovik, O., Toledano, C., Cazorla, A.,Barreto, A., Bosch, J.L., Lapyonok, T., González, R., Goloub, P., Perrone, M.P., Olmo, F.J., de Frutos, A., Alados-Arboledas, L.: Remote sensing of lunar aureole with a sky camera: Adding information in the nocturnal retrieval of aerosol properties with GRASP code. Remote Sensing of Environment, 196, 238-252, http://dx.doi.org/10.1016/j.rse.2017.05.013, 2017

Rose, T., S. Crewell, U. Löhnert, C. Simmer.: A network suitable microwave radiometer for operational monitoring of the cloudy atmosphere. Atmospheric Research, Vol.75, No.3, 183-200, 2005.

Sicard, M., Molero, F., Guerrero-Rascado, J.L., Pedrós, R., Expósito, F. J., Córdoba-Jabonero, C., Bolarín, J. M., Comerón, A., Rocadenbosh, F., Pujadas, M., Alados-Arboledas, L., Martínez-Lozano, J.A., Díaz, J.P., Gil, M., Requena, A., Navas-Guzman, F., Moreno, J.M.: Aerosol lidar intercomparison in the framework of SPALINET-The Spanish lidar network: Methodology and results, IEEE Transactions on Geoscience and Remote Sensing, 47(10), 25, 3547-3559, 2009.

Titos, G., del Águila A., Cazorla, A., Lyamani, H., Casquero-Vera, J.A., Colombi, C., Cuccia, E., Gianelle, V., Alastuey, A., Alasdos-Arboledas, L.: Spatial and temporal variability of carbonaceous aerosols: assessing the impact of biomass burning in the urban environment. Science of the Total Environmental, 578: 613-625, http://hdl.handle.net/10481/47096, 2017.

Titos, G., Foyo-Moreno, I., Lyamani, H., Querol, X., Alastuey, A., and Alados-Arboledas, L.: Optical properties and chemical composition of aerosol particles at an urban location: An estimation of the aerosol mass scattering and absorption efficiencies, J. Geophys.Res.-Atmos., 117, D04206, doi:10.1029/2011JD016671, 2012.

Titos, G., Jefferson, A., Sheridan, P. J., Andrews, E., Lyamani, H., Alados-Arboledas, L., and Ogren, J. A.: Aerosol light-scattering enhancement due to water uptake during the TCAP campaign, Atmos. Chem. and Phys., 14, 7031–7043, doi:10.5194/acp-14-7031-7043,2014.

Turner, D. D., Clough, S. A., Liljegren, J. C., Clothiaux, E. E., Cady-Pereira, K. E., and Gaustad, K. L.: Retrieving Liquid Water Path and Precipitable Water Vapor From the Atmospheric Radiation Measurement (ARM) Microwave Radiometers, IEEE Transactions on Geoscience and Remote Sensing, 45, 3680–3690, doi:10.1109/TGRS.2007.903703, 2007.

Valenzuela, A., Olmo, F.J., Lyamani, H., Granados-Muñoz, M.J., Antón, M., Guerrero-Rascado, J.L., Quirantes, A., Toledano, C., Perez-Ramírez, D., Alados-Arboledas, L.: Aerosol transport over the western mediterranean basin: Evidence of the contribution of fine particles to desert dust plumes over Alborán island. Journal of Geophysical Research, 119, 24, 14,028-14,044, 2014.

Wiegner, M. and Gasteiger, J.: Correction of water vapor absorption for aerosol remote sensing with ceilometers, Atmos. Meas. Tech., 8, 3971–3984, doi:10.5194/amt-8-3971-2015, 2015.

4. Methodology

This thesis is composed of four methodologies designed under two frames (temporal and vertical), in order to fulfill the objectives proposed. Before going into the methodology developed, the error characterization of the MWRs for temperature and RH profiles is needed. The main drawback with this instrument yields on its operational principle and the way that it retrieves vertical profiles. Thus, to deal with these issues it was performed a bias calculation between RS and MWR profiles together with an interannual seasonal study in both the IISTA-CEAMA and SIATA-tower stations (see section 4.1).

The first methodology refers to the vertical evolution hygroscopic growth studies carried out at the IISTA-CEAMA station between the synergy of RL and DL as active remote sensors, and MWR as a passive remote sensing instrument, plus ancillary information from RS (methodology V1, Fig. 4.1). Section 4.2.2 explains the methodology T1, for temporal the evolution of aerosol hygroscopic growth studies by using a co-located ceilometer operating close to the meteorological instrumented tower plus in situ instrumentation at the SIRTA observatory. This set up allows measuring the RH at 30 m agl together with β^{att} from ceilometer at the same high. Finally, in temporal evolution frame (methodology T2) and in vertical evolution frame (methodology V2) are evaluated. This study of the vertical and temporal evolution of aerosol hygroscopicity only involve ceilometers and MWRs in both stations, namely IISTA-CEAMA and SIATA-tower stations, presented in section 4.2.3 and 4.2.4.

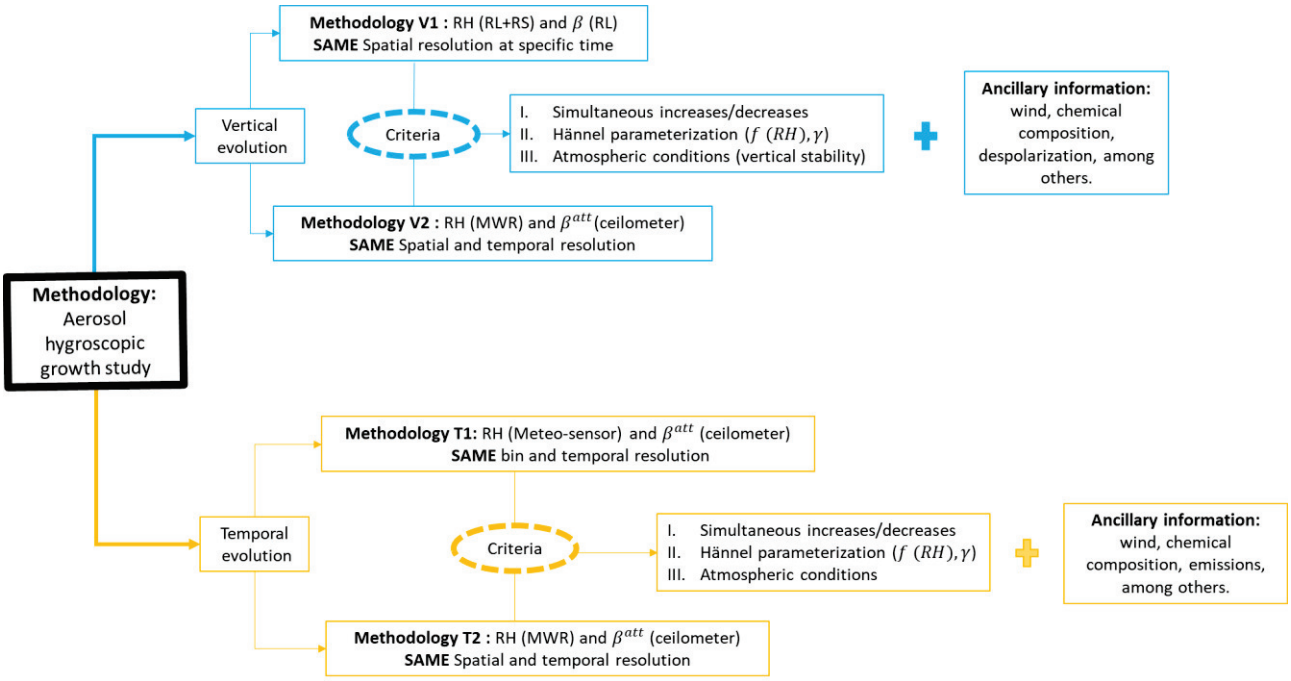

Figure 4 1. *Methodology for aerosol hygroscopic growth studies in two frames, vertical and temporal evolution.*

4.1 MWR uncertainties calculation for IISTA-CEAMA and SIATA-tower stations

In order to characterize the accuracy and precision of the physical temperature and RH profiles from the MWR retrieved at the IISTA-CEAMA station, a statistical analysis based on the comparison with RS has been done. During a 5-year period from 2012 to 2016, simultaneous measurements of RS and MWR were available, with a total of 55 RS launches of which 23 RS were launched under cloud-free conditions and the rest of them under all-weather conditions. Thus, the comparison was done by means of the $\overline{bias}$ (Eq. 4.1), which was interpreted as the accuracy of the MWR measurements:

$$\overline{bias}(z) = \frac{1}{j}[\sum_{i=1}^{j}(MWR_i(z) - RS_i(z))] \qquad (4.1)$$

Both $MWR_i$and $RS_i(z)$ refers to temperature and RH retrieved from MWR and RS respectively, and the standard deviation (SD) (Eq. 4.2), that provided information about the precision of the MWR:

$$SD_{bias}(z) = \sqrt{\frac{\sum_{i=1}^{j}(bias_i\,(z) - \overline{bias\,(z)})^2}{j-1}} \qquad (4.2)$$

where z is the altitude and j is the total data-samples. In order to perform the comparison between RS and MWR profiles, all RS measurements were degraded to the MWR spatial resolution, which has a lower vertical resolution, and the MWR profiles were 30 min-averaged after the RS launch time. In addition, we also analyzed the error in the IWV product of MWR at IISTA-CEAMA, considering RS as reference. The relative mean-bias error (MBE) calculation was performed as follows:

$$MBE = \frac{1}{j}\sum_{i=1}^{j}\frac{IWV_{MWR_i} - IWV_{RS_i}}{IWV_{RS_i}} \tag{4.3}$$

Each IWV_i value was obtained by integrating in the column for the corresponding time of the RS lauch. The criteria defined for classifying cloud-free conditions days was based on two flags. Firstly, we used the cloud cover from sky camera database assuming cloud cover ≤ 1.0 oktas as cloud-free conditions. Secondly, we defined a threshold by the observation of the LWP and by checking the cloud base height from MWR (product obtained directly from the instrument as ZENITH.CBH archive), finding a representative threshold of LWP for cloud-free days $\leq 40 g/m^2$. In addition, we used the MWR rain flag provided by the manufacturer to exclude rainy days from database.

The MWR performance for IWV was also characterized by means of the mean bias error and also calculating the correlation between the IWV from MWR and the integration of the water vapor mixing ratio (r (z)) derived by RS from 0 to 10 km (without degradation of spatial resolution of the RS). At IISTA-CEAMA station, this evaluation was also performed for cloud-free conditions and all-weather conditions classification. A sub-classification was performed only for cloud-free conditions between daytime and night-time, considering daytime the measurements obtained under sunlight presence and night-time measures under absence of sunlight, according to the seasons, resulting in 11 comparison cases during daytime and 12 comparison cases during night-time. All this results are showed in section 5.

The same analysis was performed at the SIATA-tower station for temperature and RH, using an intense RS campaign was carried out between January and February 2015, where 41 RS coincident to MWR were available. For this station, only all-weather conditions calculation were performed because of the high cloud presence over this region. The results of this instrumental characterization are showed in section 6.

4.2 General methodology for aerosol hygroscopic growth studies

The following sections describe in detailhow each type of the methodology, i.e. temporal evolution (methodology T1 and methodology T2), and vertical evolution (methodology V1 and methodology V2) are applied under specific atmospheric conditions and combined with different instruments to the aim of isolating aerosol hygroscopic growth cases.

Previous to the application of the different types of methodologies, several criteria have to be fulfilled (like simultaneous increases in β or β^{att} and RH, and also a good adjusts in the Hänel parameterization). This implies a previous data pre-processing and spatial and temporal resolution scaling, depending on the instruments involved. Despite this, while each methodology is explained, information like parameters for good Hänel adjusts, RH ranges, among the others, are detailed. The atmospheric conditions will be detailed on each methodology, mostly because studies have been performed by using different instrumentation and locations, which in fact could modify the atmospheric conditions or the mechanisms to measuring these conditions. Ancillary information is an important issue which will depend on the site and instrumentation availability, therefore it would be slightly different through the following sections.

4.2.1 Methodology V1: synergy among RL–DL-MWR as remote sensors, ancillary information from RS and high mountain in situ station at Granada

Methodology V1 is associated to the vertical evolution (see Fig. 4.1). To this aim, we use as optical property β_{par}, which is retrieved from lidar measurements. For the sake of simplicity from here to ahead the notation β is preferred instead. In addition, RH profiles are also needed1. In this section, the procedures to obtain RH by combining RL, RS and MWR are described (Sec. 4.2.1.1), and also the criteria that cases must fulfil to be labelled as aerosol hygroscopic growth cases (Sec. 4.2.1.2).

4.2.1.1 Retrieving RH-profiles by combination of RL and MWR

As it was mentioned in section 3.1.1, some RL systems can provide simultaneous aerosol and water vapor profiles with high vertical and temporal resolution. Therefore, on one hand, the water vapor mixing ratio r(z) can be obtained from the ratio of RL signals of water vapor (408 nm) and nitrogen (387 nm) multiplied by a calibration constant, C, that takes into account the fractional volume of nitrogen, the ratio between molecular masses, some range-independent constants and the Raman backscatter cross sections for nitrogen and water vapor molecules (e.g. Mattis et al., 2002; Guerrero-Rascado et al., 2008b; Navas-Guzmán et al. 2014). In this thesis, the calibration constant C has been calculated using the simultaneous and collocated radiosondes launched at the IISTA-CEAMA station. Thus, C is obtained as the average value of the ratio between the uncalibrated r(z) profile from RL and the r (z) profile from RS over a height-range that presents a high good signal-to-noise-ratio (Guerrero-Rascado et al., 2008b; Leblanc et al., 2012; Navas-Guzmán et al. 2014; Foth et al., 2015). C remains constant over periods when the lidar setup is not modified and the system presents good alignment and, thus, it allows retrieving r (z) profiles from the RL even when RS measurements are not available. If several RS launches are available during a certain period, C is obtained as the average between all calibrations performed over that particular period.

On the other hand, temperature profiles measured by the MWR are continuously (every 2 min) averaged over 30 min in order to match the temporal sampling of the averaged r (z) profiles, as proposed by Navas-Guzmán et al. (2014). 30-min averaged temperature and r (z) profiles are then used to retrieve the RH profiles required for aerosol hygroscopic growth studies. The following equation is used to calculate the RH profiles:

$$RH\ (z) = \frac{100P\ (z)\ r\ (z)}{e\ (z)\ [621{,}97 + r\ (z)]} \tag{4.4}$$

where r (z) is obtained from the calibrated water vapor channel, p (z) (hPa) is the ground-scaled pressure profile and e (z) is the water vapor pressure (hPa), calculated from the temperature profiles (List, 1951). Temperature profiles were scaled to lidar vertical resolution by linear interpolation.

4.2.1.2. Criteria for hygroscopic cases selection in the vertical evolution

Starting from the fact that criteria I and II are fulfilled for vertical evolution studies (methodology V1, Fig. 4.1), it is possible to evaluate a potential vertical hygroscopic growth cases. In this particular methodology, it is important to focus on the third criterion (atmospheric conditions), due to the lack of control over the environmental conditions. Thus, additional constraints need to be fulfilled. These constraints are used for guarantying those variations in the aerosol properties are due to water uptake and not to changes in the aerosol load or type. Therefore, the first constraint that needs to be satisfied is that the origin and pathways of the air masses arriving at different altitudes within the analyzed layer must be the same in order to avoid transport of different aerosol types from different source regions (e.g. Veselovskii et al., 2009; Granados-Muñoz et al., 2015). This evaluation is usually performed using some particle transport models, where the most common is the backward trajectories analysis using HYSPLIT model (Hybrid Single-Particle Lagrangian Integrated Trajectory) (Draxler and Rolph, 2003) with Global Data Assimilation System (GDAS) as meteorological input.

The second constraint is related to the atmospheric vertical-homogeneity. In order to evaluate the atmospheric vertical mixing and stability, virtual potential temperature $(\theta_v(z))$ and $r(z)$ profiles must be considered. The low vertical variability (vertical gradient) of those variables suggests atmospheric vertical homogeneity in the layer of study (Veselovskii et al., 2009; Fernández et al., 2015; Granados-Muñoz et al., 2015; Lv et al., 2017, Bedoya-Velásquez, et al., 2018). In addition, horizontal and vertical wind speeds and directions at different altitudes might be checked too, because low horizontal wind velocity measured at different altitudes is an indicator of no particle advection inside the layer analyzed, taking into account that wind direction must be constant during long time periods (longer than 3 hours). Currently, researches by DL and statistical methods are used to study the atmospheric turbulence through the different moments of the vertical wind speed distribution, where specifically the third moment (skewness) can be useful to evaluate the convection of air masses within the column studied (O'Connor et al., 2010; Moreira et al., 2018, 2019).

Finally, as ancillary information to reinforce the fact that an aerosol hygroscopic growth case has been isolated within the air column of evaluation, it is necessary to know about aerosol microphysical properties like effective radius, size distribution, and aerosol

concentration, and aerosol optical properties like AE, single scattering albedo (SSA), particle linear depolarization ratio ($PLDR$), among others. This ancillary information allows for characterizing size, type and sphericity of the aerosols within the air column evaluated. Thus, the decrease in AE and $PLDR$ within the layer evaluated points out the presence of larger and more spherical aerosol particles, reinforcing the fact that aerosol was water up taking like it was stabilised in previous studies like Granados-Muñoz et al. (2015); Fernández et al. (2015); Haarig et al. (2017).

4.2.2 Methodology T1: combination of co-located ceilometer and instrumented tower plus on-line in situ measurements at SIRTA observatory

The main challenge when dealing with uncontrolled atmospheric conditions is to be able to isolate the hygroscopic enhancement effect from other processes that are taken place simultaneously such as changes in air masses, emissions or advection of aerosol particles from local sources, among others. Therefore, here it was designed an easy-to-apply methodology T1 used for automatic co-located measurements of 24/7 instrumentation (ceilometer, meteorological station and in situ chemical composition analyzer) (Fig. 4.2), allowing for, on one hand, to identify cases that fulfil the criteria I and II in the temporal evolution frame (methodology T1, Fig. 4.1) and, on the other hand, to elucidate whether those increases/decreases are due to hygroscopic growth or not.

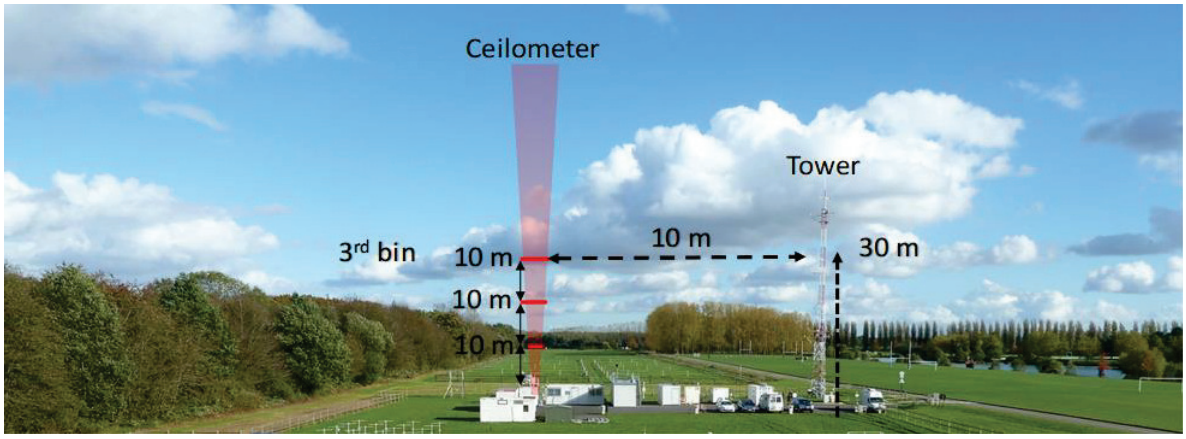

Figure 4.2. *Experimental setup (not in 1:1 scale) for studying hygroscopic growth by using the automatic instrumentation (ceilometer and hygrometer) at the SIRTA observatory.*

4.2.2.1. *Data pre-processing: Vaisala CL 31 water vapor correction*

Methodology V1 uses a Vaisala CL31 ceilometer and, therefore, a water vapor correction has to be performed in order to apply the criteria I and II. Thus, this correction was performed starting from (Eq. 2.1) for transmittance of the radiation in the atmosphere, isolating the term linked to water vapor as follows:

$$T_{wv}(z,t) \equiv exp\left(-\int_{z_1}^{z_2} \sigma_{a,wv}(\xi,t)d\xi\right) \tag{4.5}$$

where $\sigma_{a,wv}$ is the water vapor absorption coefficient in the atmosphere, and z_1 and z_2 define the air volume of interest. Taking into account the term of water-vapor-attenuated backscatter (Eq. 2.28), it is possible to focus the attention on water vapor effect. Therefore:

$$\beta_{wv}^{att}(z,t) \equiv \beta^{att}(z,t)T_{wv}^2(z,t) = \frac{P(z,t)z^2}{\mathrm{C}\,(\mathrm{t})O(z,t)} \tag{4.6}$$

From the enhancement factor (Eq. 2.24) defined as the ratio between two signals from the atmosphere, it is possible to determine the net effect of the water vapor:

$$f_{\beta_{wv}^{att}}(RH) \equiv \frac{\beta_{wv}^{att}(z_{ref},t)}{\beta_{wv}^{att}(z_{ref},t_d)} = \frac{\beta^{att}(z_{ref},t)T_{wv}^2(z_{ref},t)}{\beta^{att}(z_{ref},t_d)T_{wv}^2(z_{ref},t_d)} \tag{4.7}$$

Thus, combining Eq. (4.6) and (4.7):

$$f_{\beta_{wv}^{att}}(RH) = \frac{P(z_{ref},t){z_{ref}}^2/\mathrm{C}\,(t)O(z_{ref},t)}{P(z_{ref},t_d){z_{ref}}^2/\mathrm{C}\,(t_d)O(z_{ref},t_d)} \tag{4.8}$$

Assuming that the calibration factor and the overlap function are stable enough during the period considered, the attenuated-backscatter enhancement factor affected by water vapor absorptioncan be expressed as follows:

$$f_{\beta_{wv}^{att}}(RH) = \frac{P(z_{ref},t)}{P(z_{ref},t_d)} \tag{4.9}$$

and thus, it is possible to directly retrieve $f_{\beta_{wv}^{att}}(RH)$. Finally, it is just needed to estimate the transmittance ratio due the water vapor absorption in order to determine $f_{\beta^{att}}$ as:

$$f_{\beta^{att}}(RH) = f_{\beta_{wv}^{att}}(RH)\frac{T_{wv}^2(z_{ref},t_d)}{T_{wv}^2(z_{ref},t)} \tag{4.10}$$

The water vapor term can be re-written using Eq. (4.5):

$$\frac{T_{wv}^2(t_d)}{T_{wv}^2(t)} = exp\left(-\int_{z_1}^{z_2}\left(\sigma_{a,wv}(t_d) - \sigma_{a,wv}(t)\right)dz\right) \quad (4.11)$$

where the height-dependence has been omitted for the sake of clarity. Following Wiegner et al. (2015), the extinction coefficient due to water vapor absorption is given by:

$$\sigma_{a,wv}(t) = n_{wv}(t)\sigma_{wv} = 7.25 \cdot 10^{22}\, q(t) R_{wv}\sigma_{wv} \quad (4.12)$$

where σ_{wv} is the water vapor absorption cross section and $n_{wv}(t)$ is water vapor number of concentration, $R_{wv} = 0.462\, Jg^{-1}K^{-1}$ is the gas constant of water vapor and q is the absolute humidity. For this evaluation, we assume that $\sigma_{wv} = 2.4 \cdot 10^{-22} cm^2$ simulated at 908.957 nm (Wiegner et al., 2015, 2018). Then, replacing Eq. (4.12) in Eq. (4.11), we obtain:

$$\frac{T_{wv}^2(t_d)}{T_{wv}^2(t_w)} = \exp\left(-2\int_{z_1}^{z_2}\left(\sigma_{a,wv}(t_d) - \sigma_{a,wv}(t)\right)dz\right) = \exp\left(-2K_{wv}\int_{z_1}^{z_2}(q(t_d) - q(t))dz\right) \quad (4.13)$$

where K_{wv} gathers all the constants such as σ_{wv}, R_{wv} and Δz (30 m in our instrument setup). Assuming that the absolute humidity is constant in height within the first 30 meters, we can simply the Eq. (4.13) to the final correction equation:

$$\frac{T_{wv}^2(t_d)}{T_{wv}^2(t)} = \exp(-2K_{wv}\Delta q \Delta z) \quad (4.14)$$

where $\Delta q = q(t) - q\left(t_{ref}\right)$. An important fact showed on Eq. (4.14) is that water vapor correction is only affected by the relative difference of the absolute humidity in the explored time frame. The setup used here allows for obtaining the experimental value of $q(t)$ in order to perform the calculation proposed in Eq. (4.14).

Once the $f_{\beta^{att}}(RH)$ is obtained, it is necessary to deal with the fact that β^{att} is influenced by the transmittance of the atmospheric layer evaluated. In this regard, the link between β^{att} and β_{par} at 30 m (layer of the interest for this specific study at the SIRTA observatory) was evaluated in detail in Haeffelin et al. (2016) to guarantee the suitability of using the β^{att} for hygroscopicity studies. Indeed, Haeffelin et al. (2016) found differences between $f_{\beta^{att}}(RH)$ and the $f_{\beta_{par}}(RH)$ lower than 10% by assuming a lidar

ratio between 30 and 80 sr (at RH_{ref}) in the simulations and $f_{\alpha}(RH) > f_{\beta^{att}}(RH)$. Therefore, hereafter, we assume $f_{\beta^{att}}(RH) \cong f_{\beta_{par}}(RH)$.

4.2.2.2. *Criteria for temporal evolution analysis*

To this analysis, a sliding temporal window of 3 to 5 hour-length was used to minimize the influence of changing emission sources and air masses. For the $f_{\beta}(RH)$ calculations, only those cases that fulfill the following conditions were selected:

i. $R^2 > 0.80$, assuring high data-correlation following Hänel parameterization.
ii. $\Delta RH > 30\%$, in order to have enough RH-range to apply the Hänel parameterization, being ΔRH the difference between final and initial RH within the time window under evaluation. This parameter can also change depending on the region where studies are carrying out.
iii. $RH_{ref} < 60$ %, allow us to choose the driest β_{ref}^{att} without losing hygroscopic growth cases.
iv. The analysis is restricted to RH<99% to avoid air masses with RH=100% or supersaturated
v. Low variability (< 35%) in both wind speed, $W_s(t)$, and direction $W_d(t)$. This criterion aims to minimize the impact of air masses changes during the time-window under evaluation. Numerically, this variability was calculated by dividing the standard deviation by its mean value.

Ancillary information used for this analysis was the aerosol concentration, in order to discard that the increase/decrease observed in β^{att} is not related to an increase/decrease in the aerosol mass concentration, and it is due to only the increase/decrease in RH. In our case, it was used data from the ACSM (Aerosol Chemical Speciation Monitor) and Aethalometer (Sec. 3.3.2), to specifically look into the aerosol chemical components. In this step of the methodology, it was defined the ratio-index (RI) as the ratio between $f_{\beta^{att}}$ (RH) and f_{PM1}(RH) in order to evaluate if the increase in β^{att} is associated to an increase in the aerosol load. Therefore those potential hygroscopic enhancement cases that showed RI < 0.5 were rejected. More details can be found in Bedoya-Velásquez et al. (2019).

4.2.3 Methodology V2: Potential hygroscopic growth cases by combining Ceilometer and MWR: vertical evolution study at IISTA-CEAMA and SIATA-tower station.

The evaluation of the potential aerosol hygroscopic cases at IISTA-CEAMA was performed over 11 bins, from bin#14 (550 m) to bin#25 (2000 m), because of the ceilometer full overlap and the region with lower RH mean-bias (according to the bias evaluation shown in Sec. 4.1). Meanwhile, the evaluation performed in Medellín was over 15 bins, from bin#2 (50 m) to bin#16 (1000 m), for the same reasons exposed above. Additionally, at this point it must be known the trustworthy regions of the temperature and RH profiles of the MWR for defining the layers of evaluation, in order to minimize the systematic error in the upcoming $f_{\beta^{att}}$ (RH) calculations. Detailed information will be given in chapter 5.

The vertical evolution, methodology V2 (Fig. 4.1), is analyzed. The criteria I and II does not change at all, but the main difference yields in the data pre-processing, depending on the type of ceilometer and MWR used. As it was shown in Sec. 3, the ceilometer used in Granada is a Jenoptik CHM15k ceilometer, which has the full ovelap upper (about 550 m) than Vaisala CL51 (above 10 m) used in Medellín, with spatial resolution about 15 m and 10 m respectively, and temporal resolution about 15 s/profile. The RH profiles in Granada are retrieved from a HATPRO MWR with variable spatial resolution and 39 bins of height, while in Medellín they are retrieved from a MP-3000A, with variable spatial resolution and 58 bins of height, and temporal resolution about 2 min/profile for both.

Once different setups are taking into account, the criteria I and II presented on Fig. 4.1 can be applied, but firstly a sliding spatial window is defined according to the spatial resolution of the instruments. The spatial window must have a minimum range of evaluation equivalent to more than three bins (~150 m) (Fig. 4.3), because the necesity of assuring a minimum atmosphere volume to look for the phenomena. This must be defined by the end-user, associated to the knowledge of the atmospheric dynamics of the region. Once, spatial window is ran for the first 3 bins, one bin more is added to the analysis (4 bin), and then pass to the next one until a spatial scanning of the total bins is complete.

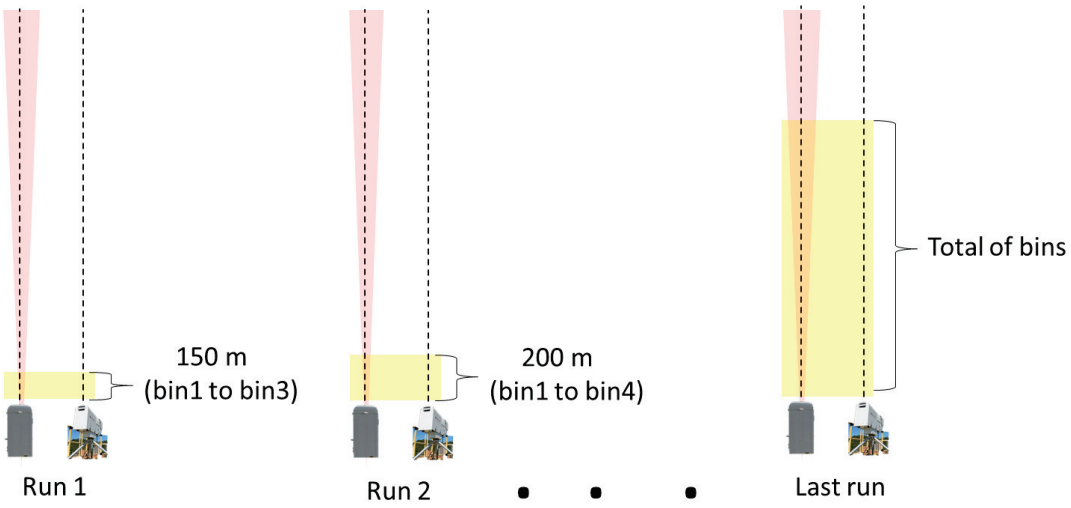

Figure 4.3. *Methodology for vertical hygroscopic growth evaluation by using ceilometer and MWR.*

For the same reasons exposed above, the Hänel adjust must fulfill that,

i. $R^2 > 0.90$
ii. $\Delta RH > 20\%$
iii. $RHref < 60\ \%$

As atmospheric conditions criterion, the 2-min temperature and RH profiles obtained from MWR and the mean pressure profile obtained from RS are used for retrieve profiles of θ_v (z) and r (z). The low variation of the vertical gradients of these profiles (θ_v (z)$\sim$0 and r (z)$\sim$0) assures a good mixing of the layers and no air masses advection within the volume evaluated. In addition, it is possible to use the IWV temporal series acquired at the IISTA-CEAMA station and vapor density profiles at the SIATA-tower station derived from MWRs, in order to assess the water vapor content in the air column of interest.

Ancillary information used for this analysis were aerosol optical/microphysical properties and wind, in order to discard that the increase/decrease observed in β^{att} is not related with a local aerosol emissions, and it is due to the increase/decrease in RH. In addition, wind information in the column is necessary to reinforce the fact of no changing or advection of the air masses in the volume evaluated. This data can be retrieve from DL, wind radar or co-located RS around the time of the measurement. Particularly, the

vertical wind profiles were taken at the IISTA-CEAMA station using DL (in operation since 2016), meanwhile surface measurements and RS launches were used at the SIATA-tower station (operating since 2015).

4.2.4 Methodology T2: Potential hygroscopic growth cases by combining Ceilometer and MWR: Temporal evolution study methodology for IISTA-CEAMA and SIATA stations

This part of the methodology follows the same data pre-processing explained in Sec. 4.2.3. However, due to this analysis is associated to temporal evolution, a sliding temporal window has to be defined. This temporal window was selected as it is shown on Fig. 4.4, assuring that aerosol changes are not affected by emissions or rapid changes in the air masses, choosing a 3 hour time window for both stations. Because the SIATA-tower station ceilometer has a very low overlap, it was decided to use the 600 m- integrated β^{att} (Iβ^{att}) after some tests and the first bin RH data to run criterion I (see Fig. 4.1), meanwhile for the IISTA-CEAMA station, it was used β^{att} and RH at each height level of evaluation. After that, the evaluation process begins running for the first bin, then pass to the next one, repeating this procedure until temporal scanning of the 11 bins is ended for the IISTA-CEAMA station, meanwhile at the SIATA-tower station only one run was needed.

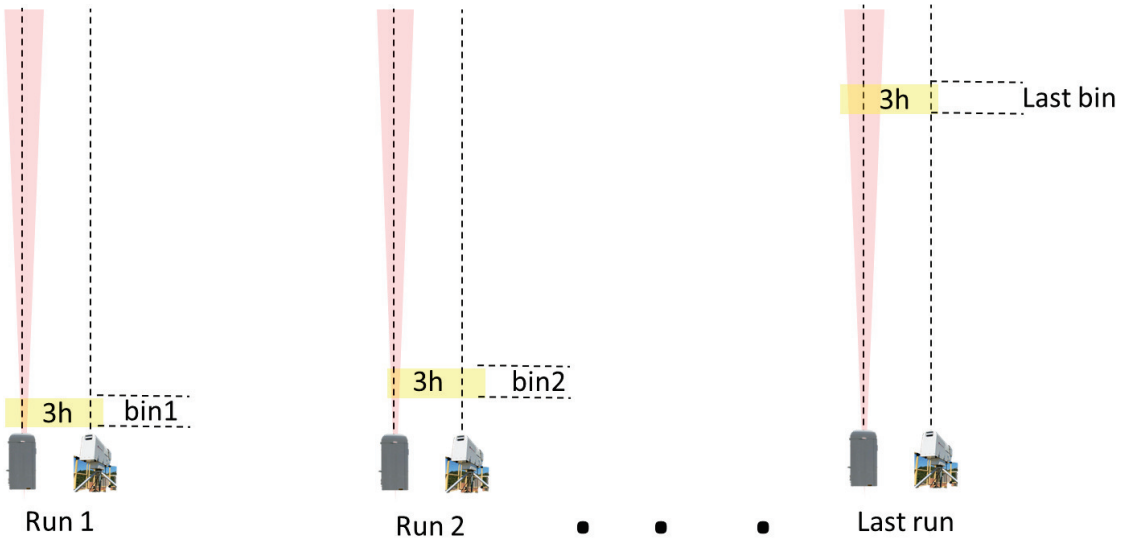

Figure 4.4. *Methodology for temporal hygroscopic growth evaluation by using ceilometer and MWR.*

For applying the Hänel adjust, only those cases that fulfill the following criteria were selected:

i. $R^2 > 0.90$
ii. $\Delta RH > 30$
iii. $RH_{ref} < 60\ \%$

The atmospheric conditions studied in order to assure the no-air masses advection and good mixing of the air volume studied are the no abruptly changes in $r\ (t)$ and $q(t)$, together with temperature and wind speed and direction, during the 3 hours window of evaluation.

As ancillary information was used the aerosol concentration and chemical composition, depending on the station capabilities. In this case, $PM_{2.5}$ analysis was performed in order to check that particle emission do not govern the β^{att} behaviour, mainly for bins close to the ground at the SIATA-tower station.

4.3 References

Bedoya-Velásquez, A. E., Navas-Guzmán, F., Moreira, G., Román, R., Cazorla, A., Ortiz-Amezcua, P., Benavent-Oltra, J.A., Alados-Arboledas, L., Olmo-Reyes, F.J., Foyo-Moreno, I., Montilla-Rosero, E., Hoyos, C.D., Guerrero-Rascado, J.L.: Seasonal analysis of the atmosphere during five years by using microwave radiometry over a mid-latitude site, Atmos. Res., Volume 218, 78-89, ISSN 0169-8095, https://doi.org/10.1016/j.atmosres.2018.11.014, 2018a.

Bedoya-Velásquez, A. E., Navas-Guzmán, F., Granados-Muñoz, M. J., Titos, G., Román, R., Casquero-Vera, J. A., Ortiz-Amezcua, P., Benavent-Oltra, J. A., de Arruda Moreira, G., Montilla-Rosero, E., Hoyos, C. D., Artiñano, B., Coz, E., Olmo-Reyes, F. J., Alados-Arboledas, L., and Guerrero-Rascado, J. L.: Hygroscopic growth study in the framework of EARLINET during the SLOPE I campaign: synergy of remote sensing and in situ instrumentation, Atmos. Chem. and Phys., 18, 7001-7017, https://doi.org/10.5194/acp-18-7001-2018, 2018b.

Bedoya-Velásquez, A.E., Titos, G., Bravo-Aranda, B.A., Haeffelin, M., Favez, O, Petit, J.E., Casquero-Vera, J.A, Olmo-Reyes, F.J., Montilla-Rosero, E., Hoyos, C.D., Alados-

Arboledas, L., and Guerrero- Rascado. J.L.: Long-term aerosol optical hygroscopicity study at the ACTRIS SIRTA observatory: synergy between ceilometer and in-situ measurements. Atmos. Chem. and Phys. Discussion, https://doi.org/10.5194/acp-2019-12, 2019.

Draxler, R. R. and Rolph, G. D.: HYSPLIT (HYbrid Single-Particle Lagrangian Integrated Trajectory) model access via NOAA ARL READY website (http://ready.arl.noaa.gov/HYSPLIT.php), NOAA Air Resources Laboratory, Silver Spring, 2003.

Dubovik, O., Lapyonok, T., Litvinov, P., Herman, M., Fuertes, D., Ducos, F., Torres, B., Derimian, Y., Huang, X., Lopatin, A., Chaikovsky, A., Aspetsberger, M., and Federspiel, C.: Grasp: a versatile algorithm for characterizing the atmosphere. SPIE Newsroom, 25, 2014.

Fernández, A. J, Apituley, A., Veselovskii, I.Suvorina, A., Henzing, J., Pujadas., M ad Artiñano., B.: Study of aerosol hygroscopic events over Cabauw experimental site for atmospheric research (CESAR) using the multi-wavelength Raman lidar Caeli, Atmos. Env., 120, 484-498, 2015.

Foth, A., Girolamo, P.Di., Pospichal, B.: Water vapor profiles from Raman lidar automatically calibrated by microwave radiometer data during HOPE, Atmos.Chem. Phys., 15, 7753-7763, 2015.

Granados-Muñoz M.J, Navas-Guzmán, F., Bravo-Aranda, J. A., Guerrero-Rascado, J. L., Lyamani, H., Valenzuela, A., Titos, G., Fernández-Gálvez, J., and Alados-Arboledas, L.: hygroscopic growth of atmospheric aerosol particles based on active remote sensing and radiosounding measurements: selected cases in southeastern Spain. Atmos. Meas. Tech., 8, 705–718, 2015.

Guerrero-Rascado, J.L., Ruiz, B., Chourdakis, G., Georgoussis, G., and Alados-Arboledas, L.: One year of water vapour Raman lidar measurements at the Andalusian Centre for Environmental Studies (CEAMA), Int. J. Remote Sens., 29, 5437–5453, 2008b.

Haarig, M., Ansmann, A., Gasteiger, J., Kandler, K., Althausen, D., Baars, H., Radenz, M., and Farrell, D. A.: Dry versus wet marine particle optical properties: RH dependence of depolarization ratio, backscatter, and extinction from multiwavelength lidar

measurements during SALTRACE, Atmos. Chem. and Phys., 17, 14199-14217, https://doi.org/10.5194/acp-17-14199-2017, 2017.

Leblanc, T., McDermid, I. S., and Walsh, T. D.: Ground-based water vapor raman lidar measurements up to the upper troposphere and lower stratosphere for long-term monitoring, Atmos. Meas. Tech., 5, 17–36, doi:10.5194/amt-5-17-2012, 2012.

List, R. J.: Smithsonian meteorological Tables, 6th rev. Edn., compiled by: Robert, J., List. Washington, D.C., Smithsonian Inst., 527 pp., 1951.

Lv M., Liu D., Li Z., Mao J., Sun Y., Wang Z., Wang Y. and Chenbo X.: hygroscopic growth of atmospheric aerosol particles based on lidar, radiosonde, and in situ measurements: case studies from the Xinzhou field campaign. Journal of Quantitative Spectroscopy & Radiative Transfer, 188 60-70, 2017.

Mattis, I., Ansmann, A., Althausen, D., Jaenisch, V., Wandinger, U., Müller, D., Arshinov, Y. F., Bobrovnikov, S. M., and Serikov, I. B.: Relative-humidity profiling in the troposphere with a Raman lidar, Appl. Optics, 41, 6451–6462, 2002.

Moreira, G. A., Guerrero-Rascado, J. L., Bravo-Aranda, J. A., Benavent-Oltra, J. A., Ortiz-Amezcua, P., Román, R., Bedoya-Velásquez, A. E., Bravo-Aranda, J. A., Olmo-Reyes, F.J., Landulfo, E., Alados-Arboledas, L.: Analysisg the turbulence in the Planetary Boundary Layer by the synergic use of remote sensing systems: Doppler wind lidar and aerosol elastic lidar, Atmos. Chem. and Phys. Discuss., https://doi.org/10.5194/acp-2018-276, 2018.

Navas-Guzmán, F., Fernández-Gálvez, J., Granados-Muñoz, M.J, Guerrero-Rascado, J.L., Bravo-Aranda, J.A., and Alados-Arboledas, L.: Tropospheric wáter vapour and relative humidiyty profiles from lidar and microwave radiometry. Atmos. Meas. Tech., 7, 1201-1211, 2014.

O'Connor, E. J., Illingworth, J., Brooks, I. M., Westbrook, C. D., Hogan, R. J., Davies, F., Brooks, B. J.: A method for estimating the turbulent kinetic energy dissipation rate from vertical pointing Doppler lidar, and independent evaluation from ballon-borne in situ measurements, Journal of Atmospheric and Oceanic Technology, 27, 1652-1664, 2010.

Román, R., Benavent-Oltra, J.A., Casquero-Vera, J.A., Lopatin, A., Cazorla, A., Lyamani, H., Denjean, C., Fuertes, D., Pérez-Ramírez, D., Torres, B., Toledano, C., Dubovik, O.,

Cachorro, V.E., de Frutos, A.M., Olmo, F.J., Alados-Arboledas, L.: Retrieval of aerosol profiles combining sunphotometer and ceilometer measurements in GRASP code. Atmos. Res. 204 (2018) 161–177, doi: https://doi.org/10.1016/j.atmosres.2018.01.021, 2018.

Veselovskii, I., Whiteman, D. N., Kolgotin, A., Andrews, E., and Korenskii, M.: Demonstration of aerosol property profiling by multi-wavelength lidar under varying relative humidity conditions, J. Atmos. Ocean. Tech., 26, 1543–1557, 2009.

Wiegner, M. and Gasteiger, J.: Correction of water vapor absorption for aerosol remote sensing with ceilometers, Atmos. Meas. Tech., 8, 3971–3984, doi:10.5194/amt-8-3971-2015, 2015.

Wiegner, M., Mattis, I., Pattantyús-Ábrahám, M., Bravo-Aranda, J. A., Poltera, Y., Haefele, A., Hervo, M., Görsdorf, U., Leinweber, R., Gasteiger, J., Haeffelin, M., Wagner, F., Cermak, J., Komínková, K., Brettle, M., Münkel, C., and Pönitz, K.: Aerosol backscatter profiles from ceilometers: validation of water vapor correction in the framework of CeiLinEx2015, Atmos. Meas. Tech. Discuss., https://doi.org/10.5194/amt-2018-307, in review, 2018.

5. MWR characterization at IISTA-CEAMA and SIATA-tower stations

This chapter is devoted to analyze the error characterization of the MWRs, and also the seasonal, interannual and diurnal cycle of atmospheric variables such as temperature, RH, among others at both stations, IISTA-CEAMA and SIATA-tower. Sec. 5.1 presents the results for the IISTA-CEAMA station, meanwhile Sec. 5.2 is associated to the SIATA-tower station.

5.1 Uncertainty and seasonal analysis over 5-year dataset at IISTA-CEAMA station

The results obtained to IISTA-CEAMA station are an adaptation of the published article with the following reference:

Bedoya-Velásquez, A. E., Navas-Guzmán, F., de Arruda Moreira, G., Román, R., Cazorla, A., Ortiz-Amezcua, P., Benavent-Oltra, J. A., Alados-Arboledas, L., Olmo-Reyes, F. J., Foyo-Moreno, I., Montilla-Rosero, E., Hoyos, C. D., and Guerrero-Rascado, J. L.: Seasonal analysis of the atmosphere during five years by using microwave radiometry over a mid-latitude site, *Atmospheric Research*, 218, 78-89, 2018.

This work focuses on the analysis of the seasonal cycle of temperature and relative humidity (RH) profiles and integrated water vapor (IWV) obtained from microwave radiometer (MWR) measurements over the mid-latitude city of Granada, southern Spain. For completeness the study, the maximum atmospheric boundary layer height ($ABLH^{max}$) is also included. To this end, we have firstly characterized the HATPRO-RPG MWR errors using 55 co-located radiosondes (RS) by means of the mean-bias ($\overline{bias}$) profile and the standard deviation (SD_{bias}) profile classified under all-weather conditions and cloud-free conditions.

This characterization pointed out that temperature from HATPRO-MWR presents a very low $\overline{bias}$ respects RS mostly below 2.0 km agl, ranging from positive to negative values under all-weather conditions (from 1.7 to -0.4 K with SD_{bias} up to 3.0 K). Under cloud-free conditions, the bias was very similar to that found under all-weather conditions (1.8 to -0.4 K) but with smaller SD_{bias} (up to 1.1 K). The same behavior is also seen in

this lower part (ground to 2.0 km agl) for RH. Under all-weather conditions, the mean RH bias ranged from 3.0 to -4.0 % with SD_{bias} between 10 to 16.3 % while under cloud-free conditions the bias ranged from 2.0 to -0.4 % with SD_{bias} from 0.5 to 13.3 %. Above 2.0 km agl, the SD_{bias} error increases considerably up to 4 km agl (up to -20 %), and then decreases slightly above 7.0 km agl (up to -5 %). In addition, IWV values from MWR were also compared with the values obtained from the integration of RS profiles, showing a better linear fit under cloud-free conditions (R^2= 0.96) than under all-weather conditions (R^2= 0.82). The mean bias under cloud-free conditions was -0.80 kg/m^2 while for all-weather conditions it was -1.25 kg/m^2. Thus, the SD_{bias} for all the statistics (temperature, RH and IWV) of the comparison between MWR and RS presented higher values for all-weather conditions than for cloud-free conditions ones. It points out that the presence of clouds is a key factor to take into account when MWR products are used.

The second part of this work is devoted to a seasonal variability analysis over five years, leading us to characterize thermodynamically the troposphere over our site. This city atmosphere presents a clear seasonal cycle where temperature, ABLH^{max} and IWV increase from winter to summer and decrease in autumn, meanwhile RH decreases along the warmer seasons. This city presents cold winters (mean daily maximum temperature: 10.6 ± 1.1 °C) and dry/hot summers (mean daily maximum temperature of 28.8 ± 0.9 °C and mean daily maximum of surface RH up to 55.0± 6.0 %) at surface (680 m asl). Moreover, considering temporal trends, our study pointed out that only temperature and RH showed a linear increase in winters with a mean-rate of (0.5 ± 0.1) °C/year and (3.4 ± 1.7) %/year, respectively, from ground to 2.0 km agl, meanwhile IWV presented a linear increase of 1.0 kg·m^{-2} /year in winters, 0.78 kg·m^{-2} /year in summers and a linear decrease in autumns of -0.75 kg·m^{-2} /year.

5.1.1 Characterization of MWR performances versus RS

Figure 5.1. presents the ($\overline{bias}$ and SD_{bias}) between MWR radiometer and RS for temperature and relative humidity under clear and all-weather conditions. These two statistic parameters are interpreted as the accuracy and the precision, respectively, of the MWR measurements. Figure 5.1.a shows high variability of the temperature $\overline{bias}$ for all-

weather conditions mostly in the first hundreds of meters, passing from positive to negative values.

The larger deviations observed close to ground have been observed in similar comparisons for previous studies and could be due to the larger uncertainties of the radiative transfer models for the most transparent MWR channels, which affect more the temperature retrievals in the lowest layers (Navas-Guzmán et al., 2016). In general, below 2.0 km agl, the variability shows low-temperature $\overline{bias}$ values from 1.7 to -0.4 K. The variability starts to increase from negative to positive within 2.0 to 4.0 km agl (up to 1.0 K). This $\overline{bias}$ increases up to 1.8 K above 4.0 km agl, indicating the losing of accuracy with altitude always with positive values. The SD_{bias} of the temperature deviation profiles in all-weather conditions shows values lower than 3.0 K below 2.0 km agl, increasing up to 3.2 K from 2.0 to 4.0 km agl, and keeping constant close to 3.0 K from 4 to 7 km agl. The cloud-free conditions analysis shows the same variability in the mean bias within the first hundreds of meters than the one observed for all-weather conditions, after this region the $\overline{bias}$ changed from positive to negative values, oscillating from 1.8 to -0.4 K (below 2.0 km agl). Then, between 2.0 to 4.0 km agl, the bias passes from negative to positive. Above 4.0 km agl some variability lower than 1.7 K, indicating the losses of the accuracy as altitude increases. The temperature SD_{bias} profile under cloud-free conditions presents values lower than 1.1 K from ground to 2.0 km agl, while they increase (up to 1.8 K) for higher altitudes. It is important to point out the lower SD_{bias} values observed under cloud-free conditions, indicating a higher precision of temperature MWR measurements under clear conditions than for all-weather conditions.In addition, the surface heating caused by solar radiation tends to increase the variability of the temperature profiles over the firsts kilometers of the troposphere (up to 3.0 km agl). Above this altitude the atmosphere becomes cooler and the SD_{bias} profiles becomes quite constants.

The same analysis was performed for RH under all-weather conditions (Fig 5.1.a) and cloud-free conditions (Fig 5.1.b). Under all-weather conditions, the RH $\overline{bias}$ profile shows relatively low deviations, passing from positive values (from surface to 1.6 km agl) to negative (from 1.6 until 2.0 km agl) (from 3 to-4.0 %). The RH $\overline{bias}$ becomes greater (up to -18.0 %) from 2 to 4 km agl; then above 4 km agl reach up -11.0%. The SD_{bias} ranges from 10 to 16.3 % from ground to 2 km agl, above this altitude it presents a variation from 15 to 21.0 % (from 2 to 4 km agl).Then, it decrease from 4 to 7 km agl

from 21 to 17 %. Cloud-free conditions $\overline{bias}$ profile has a similar behavior below 2 km agl (ranging from 2.0 to -4.0 %), then increasing up from -4.0 to -21.4 % until 4 km. Finally, a decrease is seen to -4.5% from 4 to 7 km agl. Regarding SD_{bias}-RH profile in cloud-free conditions, from ground to 2 km agl the discrepancy was ranging from 0.5 to 13.3 %, increasing from 2 to 3.0 km agl up to 19.3 %, then decreasing up to 15 % until 4.0 km agl. From 4.0 km agl to the top of the profile, decreasing until 9.3 %. This losing of precision, mostly between 2 to 4 km agl, might be associated to the method for retrieving the RH profiles. This type of profile loses accuracy above the ABL, mainly because at this altitudes the absolute humidity is typically quite low (due to the low temperatures) becoming very difficult a proper detection of this property by microwave radiometry and, therefore, the RH retrievals loose precision. The SD_{Bias}-RH profile of all-weather conditions presents higher variability respect to cloud-free conditions, showing a difference around 5 % over almost all the profile, which might be associated to the cloud presence.

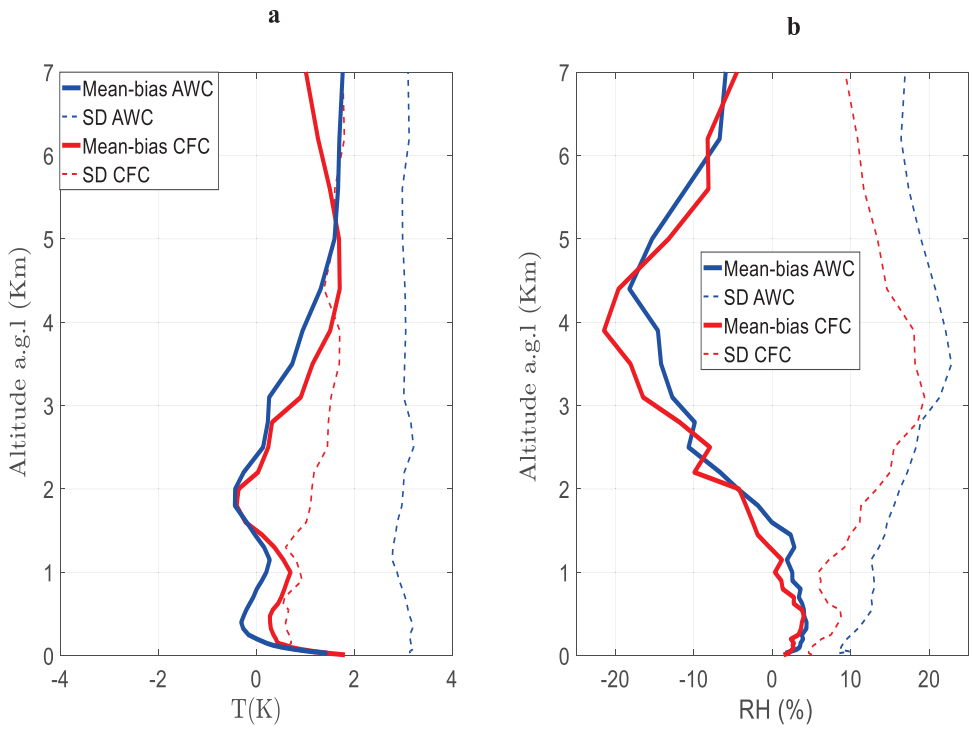

Figure 5.1. *Mean bias (solid line) and standard deviation (dashed line) on all-weather conditions (AWC, blue) and cloud-free conditions (CFC, red) for temperature (a) and RH (b) profiles between RS and MWR.*

Summarizing this inter-comparison, it is worth to point out that temperature profiles obtained from MWR makes an underestimation of those taken by RS just between 1.5 to 2.3 km agl, the profile below 1.5 and above 2.3 km agl presented an overestimation. The RH $\overline{bias}$ profile exhibits an overestimation below 1.5 km agl, but above this altitude, an underestimation of the RH profiles is seen from MWR respect to the obtained for RS.

In order to characterize the performance of MWR to retrieve IWV (IWV_{MWR}), an integration of the r (z) profile calculated from RS was performed to derive IWV_{RS}. Figure 5.2 shows the scatter plot between IWV_{MWR} and IWV_{RS}. The fit for cloud-free conditions shows a slope closer to one (0.85±0.03) and a better determination coefficient (R^2_{CFC} = 0.96) than all-weather conditions (slope = 0.68 ± 0.03, R^2_{AWC} = 0.82), which determines that cloud-free days fit better. This fact is associated to the vertical and horizontal homogeneity that atmosphere presents under cloud-free conditions, which is not seen for RS and MWR measurements under cloud presence, evidencing high data dispersion in all-weather conditions (moving away to the 1:1 line). The MBE is also calculated to reinforce the fact that all-weather conditions introduce large errors respect to cloud-free conditions measurements, showing a MBE to cloud-free conditions up to -0.80 kg/m^2, meanwhile for all-weather conditions the MBE is up to-1.25 kg/m^2. As seen in Fig 5.2, the cloud presence introduces high data-dispersion, weakening the correlation.

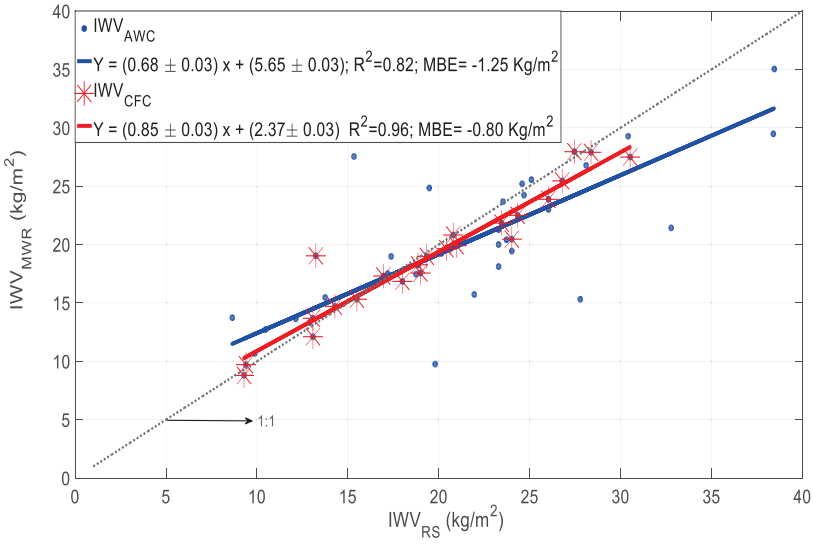

***Figure 5.2**. IWV from MWR versus RS for all-weather conditions (AWC, in blue) and cloud-free conditions (CFC, in red). The gray dashed-line refers to 1:1 line.*

The performance of the MWR has also been analyzed distinguishing between daytime and night-time measurements (Fig. 5.3), but only for cloud-free conditions since it is the scenario with better performance. The temperature $\overline{bias}$ is up to 2.0 K reached in the first hundreds of meters, which is the region with higher variability. Above that, a positive temperature $\overline{bias}$ is observed below 1.8 km agl, ranging from 0.7 to 1.0 K for daytime and from 0.5 to 0.6 K until 1.5 km agl for night-time, showing lower variability during night-time because of the sunlight absence. The $\overline{bias}$ becomes negative from 1.8 to 3.5 km agl (up to -0.5 K) for daytime and from 1.5 to 2.3 km agl (up to -0.5 K) to night-time. The $\overline{bias}$ becomes positive above 3.5 km agl reaching 1.7 K for daytime and 1.8 K above 2.3 km agl for night-time. The SD_{bias} analyzed under the same three ranges of altitude, presented lower values for daytime close to 0.6 K, 1.3 K and 1.7 K than night-time 1.0 K, 1.2 K and 2.0 K, in fact the night-time is relatively more variable under the first 2 km agl, maybe associated to the thermal inversions during the night.

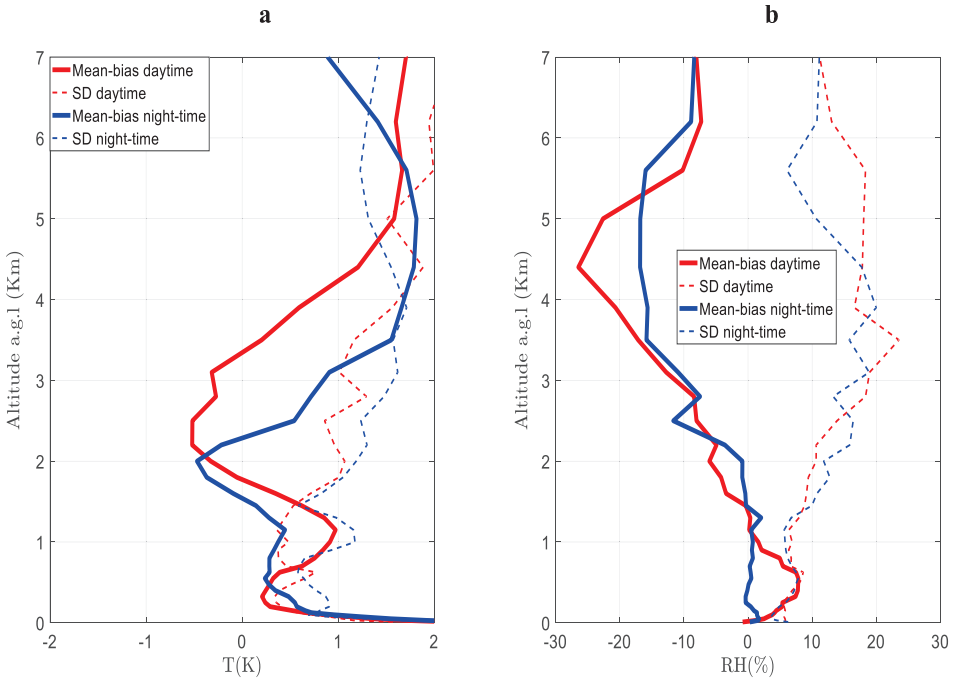

Figure 5.3. *Mean bias (solid line) and standard deviation (dashed line) on daytime (red) and night-time (blue) for T (a) and RH (b) profiles between MWR and RS, all for cloud-free conditions (CFC).*

The same behavior is also seen on RH $\overline{bias}$-profile where the daytime profile is more variable within the first 1.5 km agl (up to 8 %) than night-time one (up to 2 %), which is almost constant in the first 1.5 km. The variability at daytime is mostly associated to the Sun presence, because the temperature modifies the water vapor pressure. From this altitude until 4.5 km agl for daytime and 5.5 km agl at night-time, the RH $\overline{bias}$ becomes negative decreasing up to -26.5% and -16.8 %, respectively. From 4.5 to 7 km agl for daytime and night-time from 5.5 to 7 km agl, the RH mean-bias decreased to -8.1 % and -8.4 %, respectively. RH-SD_{bias} presented the following values according to the altitude ranges exposed above, for daytime from 6 to 8.8% (up to1.5 km agl), up to 23.5% (up to 4.5 km agl) and decreasing to 18.3 % (up to 7 km agl), while night-time variates from 5 to 10.0% (within 1.5 km agl), increasing to 20.0 % (up to 4.5 km agl) and it starts to descend up to 11.1% at 7.0 km agl. From this analysis, we can point out that the MWR present quite good performance for RH in the first two kilometers, with mean bias and SD_{bias} lower than 10%. Above 2 km (agl) these profiles should be used more carefully, taking into account that error might be as high as 20 %, affecting strongly the calculations performed.

5.1.2 Statistical analysis of Five-years of MWR measurements

To strengthen the statistical analysis, it was used an algorithm to calculate the ABLH, only by using MWR measurements which is described in detail in Moreira et al. (2018). In order to clarify the procedure at obtaining ABLH, it is important to know that this algorithm combines two methodologies: the parcel method (PM) and the temperature gradient method (TGM), which are based on the vertical temperature ($T(z)$) and potential temperature profiles ($\theta(z)$) obtained from MWR by using the definition proposed in Stull (2011).

Thus, the $\theta(z)$ was analyzed in order to classify the atmospheric conditions as stable or unstable. This analysis was performed by the comparison of the surface potential temperature ($\theta(z_0)$) with all points in the $\theta(z)$ profile below 5 km. The situation was classified as stable if all $\theta(z)$ data points had values larger than $\theta(z_0)$ and thus, TGM is applied. Otherwise, the condition was classified as unstable and, therefore, PM is used. The PM assumes the ABLH as the height z where the $\theta(z)$ is equal to surface potential

$\theta(z_0)$, because z is the altitude where an air parcel with ambient temperature (T) can rise adiabatically from the ground by convection (Holzworth, 1964). Such method is applicable only under unstable situations, i.e. inside a convective boundary layer.

The TGM (Stull, 1988) detects the ABLH in stable situations based on two definitions. Firstly, the surface-based temperature inversion, meaning that TGM detects the first height z where T decrease as a function of altitude. Secondly, the top of the stable boundary layer, meaning that TGM finds the first height where $^{d\theta}/_{dz} = 0$. The first step is to detect the altitude z where the surface-base temperature inversion is situated (from T profile). Then, from z is found the top of stable boundary layer in the $\theta(z)$. If surface-base temperature inversion or top of stable boundary layer is not found, the ABLH is classified as "not identified".

5.1.2.1 Diurnal cycle analysis

In order to investigate the diurnal cycle of the temperature and RH profiles in the troposphere, the hourly-mean cycle for temperature and RH profiles is analyzed for each season and every year from 2012 to 2016 (Fig. 5.4 and Fig. 5.5, respectively). To complete the study, $ABLH^{max}$ retrievals have been included. Figure 5.4 shows the hourly-mean behavior of the temperature profiles, where we can see that the maximum effect of the solar irradiation at surface level is close to 16 UTC and the minimum around 7 UTC, variating slightly depending on the season. In addition, due to the solar heating of the surface, the lowermost troposphere is heated with a variable vertical extension, reaching up to 6 km agl in summer, and up to 5 km agl in autumn, becoming lower in winter (up to 2 km agl) and spring (up to 4 km agl). This effect mainly drives the evolution of the mean-ABLH, which is a crucial parameter for studying aerosol dynamics and air masses transport (Moreira et al., 2018a,b).

The algorithm implemented for ABLH retrieval presented in Moreira et al. (2018a,b) and Bedoya-Velásquez et al. (2018b) allows us to retrieve the altitude where temperature profile evidences an abrupt change under stable or unstable atmospheric conditions. Thus, the mean-$ABLH^{max}$ presented on Fig. 5.4, increases gradually from winter (~ 2.1 km agl) to summer (~ 3.7 km agl), because of the increasing in solar incoming radiation that reaches the Earth´s surface. In autumn, the mean-$ABLH^{max}$ starts

to decrease (~ 2.2 km agl), in agreement with the ABL studies reported by Moreira et al. (2018b) over this area. $ABLH^{max}$ starts to increase lately in the morning in winter (~ 7 UTC), meanwhile summer exhibits faster increase up from 6 UTC, associated to the incoming solar insolation that begins earlier to warm up the surface.

Fig. 5.4 determines that the warmest year of this study was 2015, with mean values at 16 UTC up to 11.6 ± 4.0 °C, 19.0 ± 4.1 °C and 30.0 ± 1.8 °C at surface level in winter, spring and summer, respectively. Autumn was an exception, becoming autumn 2013 the warmest in the period 2012-1016, with mean-maximum temperature of 23.1 ± 5.7 °C. The coldest mean values at ground level by season were reached in winter 2012 (10.5 ± 3.5 °C), spring 2013 (15.6 ± 7.6 °C), summer 2013 (27.5 ± 2.1 °C) and autumn 2012 (19.2 ± 6.4 °C).

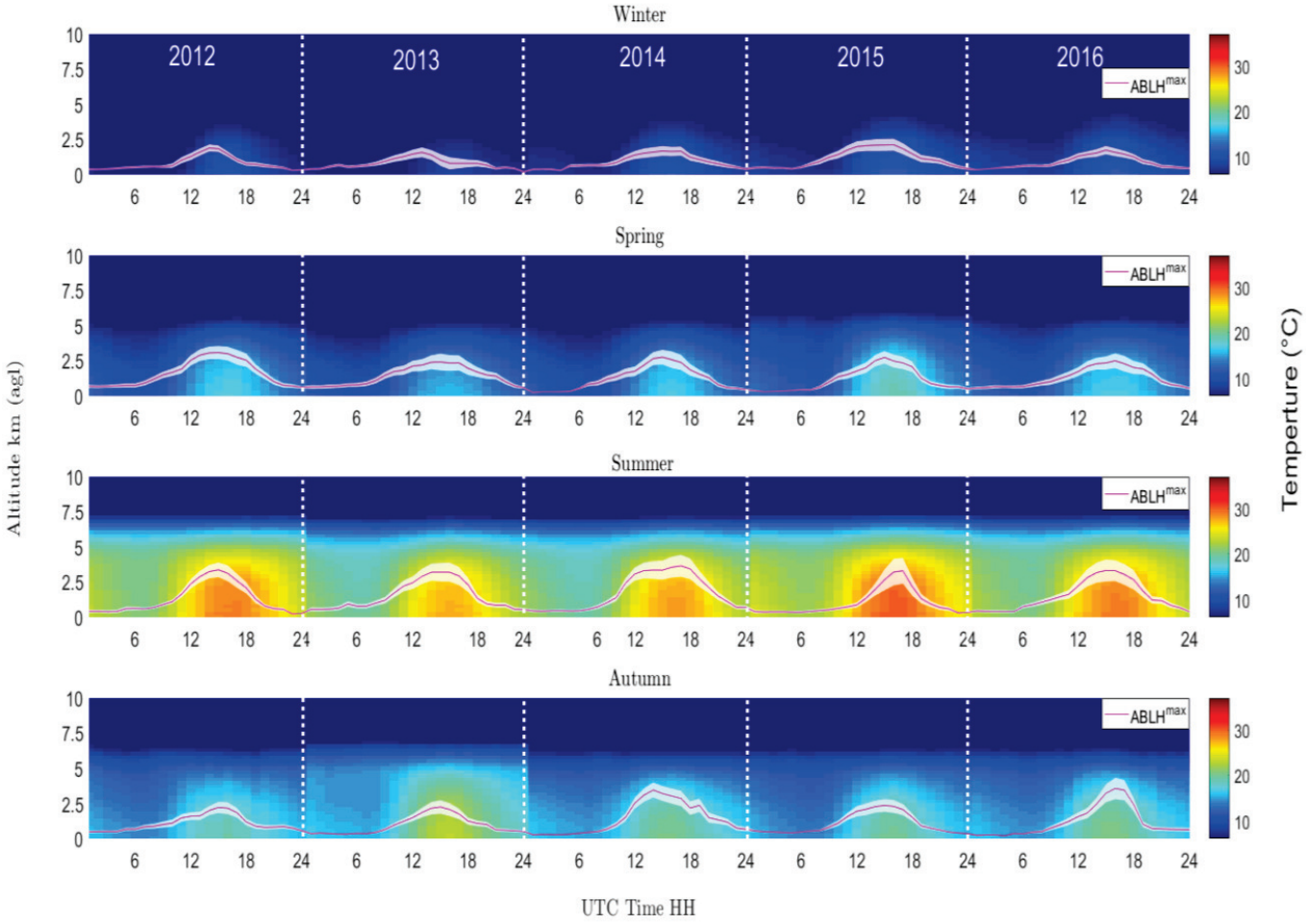

Figure 5.4. *Mean 24-h cycle for temperature profiles and ABLH by season and year. The magenta line refers to the mean* $ABLH^{max}$ *and the white contour is the SD.*

Fig. 5.5 presents the same analysis for RH, where the hourly-mean maximum values for the RH profile at surface level are observed close to 7 UTC. This is consistent with the lower temperature values, since the diurnal cycle between temperature and RH is opposite. The intervals with higher RH are in late night and mornings (from 2 to 10 UTC) and night (from 21 to 24 UTC), where solar heating is weaker or absent. In the mornings,

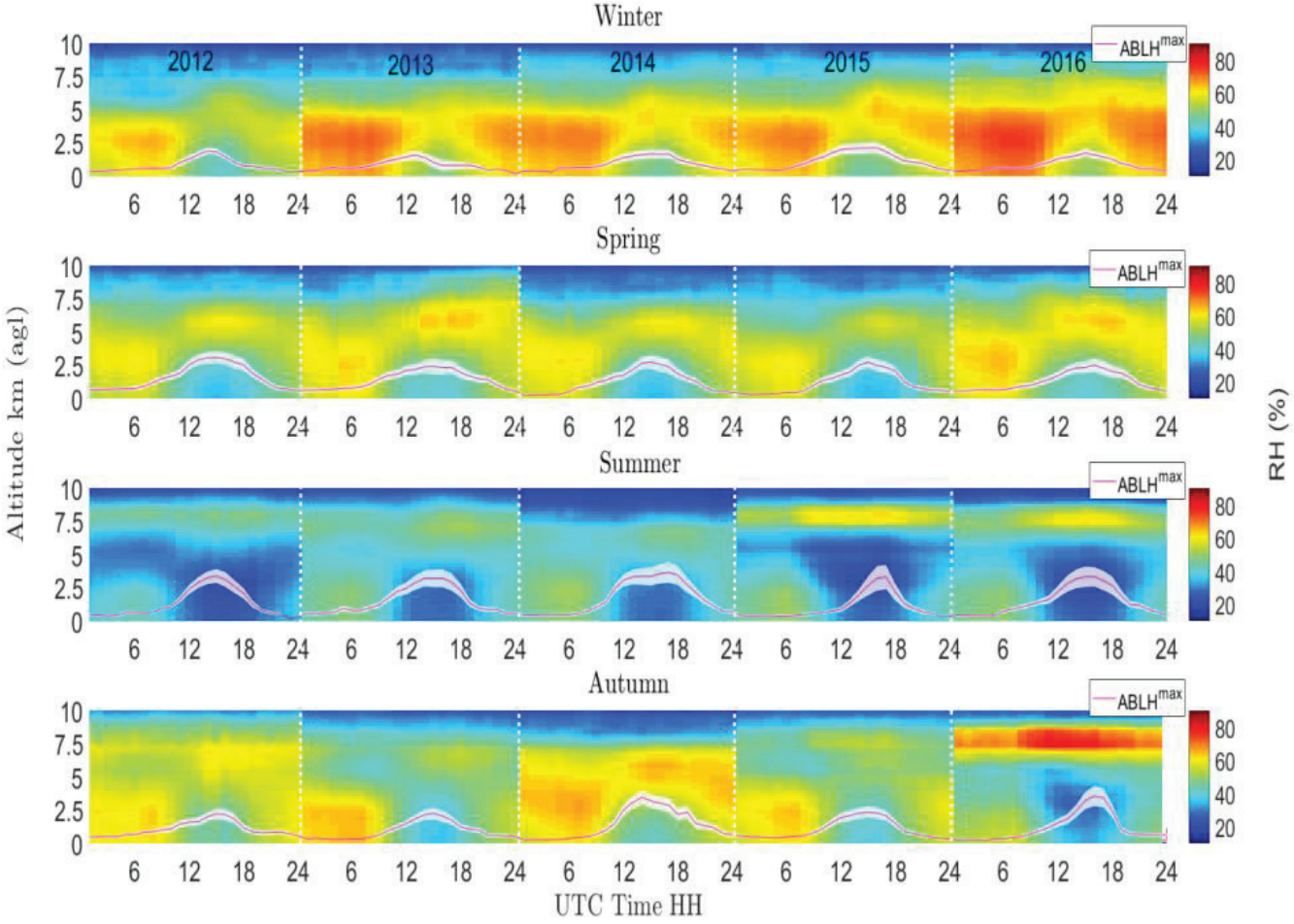

Figure 5.5. *Mean 24-h cycle for RH profiles and ABLH by season and year. The magenta line refers to the mean ABLH^{max} and the white contour is the SD.*

From Figs. 5.4 and 5.5, it is detected a clear seasonal cycle in temperature, RH and ABLH^{max}, governed by solar radiation. Granada is characterized by cold winters (mean hourly maximum temperature at surface of 10.6 ± 1.1 °C) and warmer summers (mean-hourly maximum of 28.8 ± 0.9 °C). In summer, RH at surface can be as low as 18.5 ± 1.9 % (mean-hourly minimum value) in the driest part of the day and in the

mornings where humidity is higher; it could reach a mean-hourly maximum of 55± 6 %, evidencing the dry conditions of this city.

5.1.2.2 Statistical analysis of temperature and RH in the vertical coordinate

In this section, a seasonal variability study of atmospheric variables like temperature and RH in altitude and IWV in column is presented. Figure 5.6 shows the temperature boxplots by year and season. In addition, we divided the profile by nine bins to cover the whole troposphere, allowing us to investigate effects inside the low troposphere, which is directly linked with ABL (typically from 0 to 3 km agl) and middle and high troposphere (from 3 km agl to 10 km agl). Accordingly, to the results obtained in Sec. 5.1.1., we are only interested on studying when temperature exhibits their maximum value along the day over all seasons (RH behaves oppositely); therefore, this statistical analysis will be performed at 16 UTC. Around this hour, the ABL is fully developed and the atmosphere is good mixed.

Temperature boxplots dataset shows that 25 % of the lowest and 25% of the highest temperatures are symmetrically distributed respect to the median value showing low data dispersion for most of height-ranges evaluated. In general, all seasons presented in 2013 smaller boxes than the other seasons, mostly between H1 to H4. Figure 5.6 presents that outliers are more frequent within H1 to H5, increasing in summer, associated to the increase of the variability caused by high temperatures within ABLH.

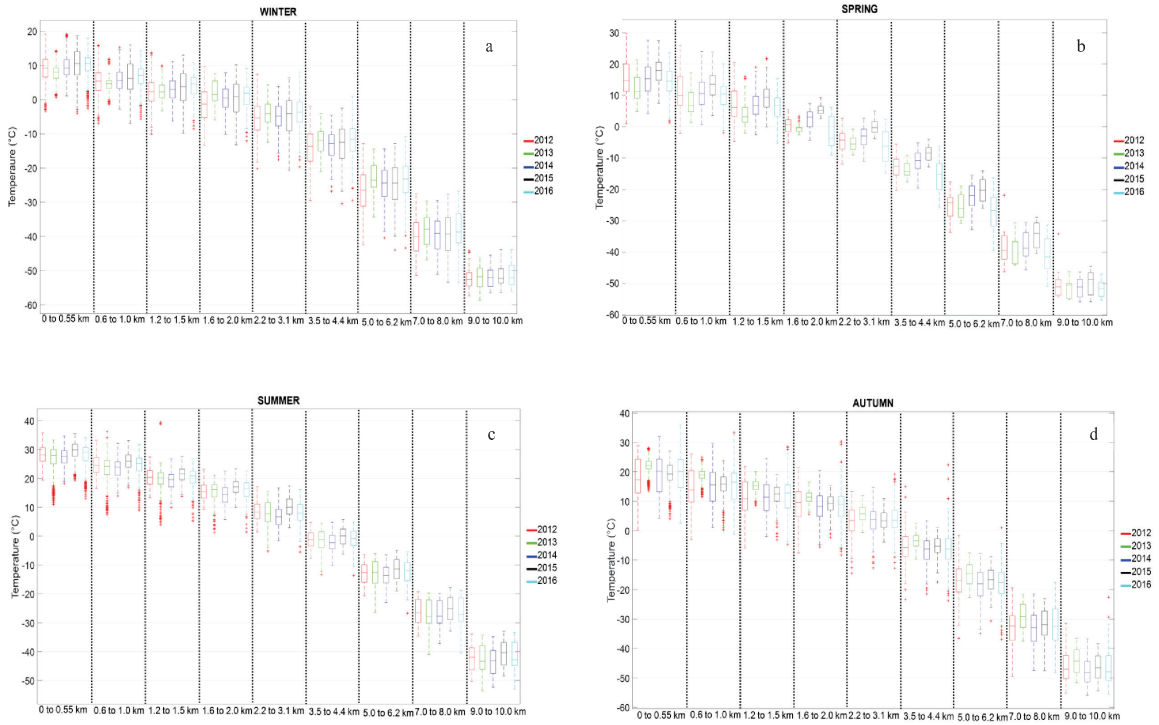

Figure 5.6. *Seasonal boxplots of temperature presented for nine atmospheric volumes covering the 39 bins of the MWR for the years 2012 (red), 2013 (green), 2014 (blue), 2015 (black) and 2016 (cyan). Winter (panel a), spring (panel b), summer (panel c), and autumn (panel d). In the boxes are represented the 25 and 75 percentile, the median, the maximum and minimum, and the outliers marked with asterisks.*

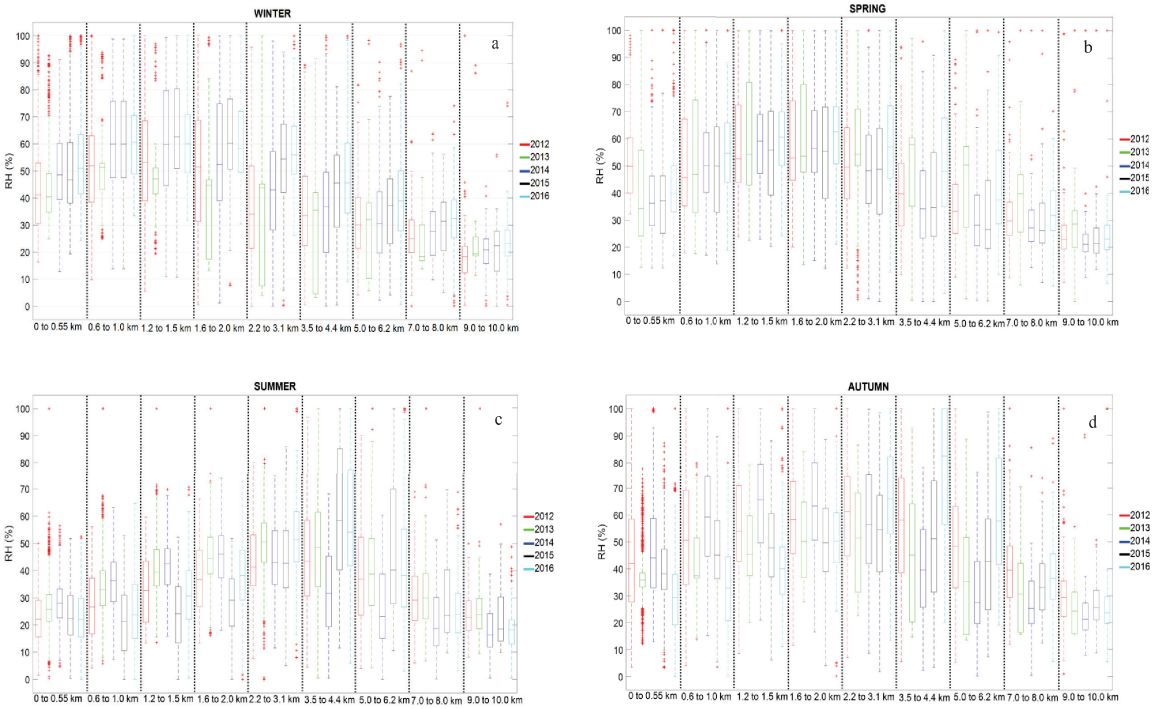

Figure 5.7. *Seasonal boxplots of RH presented for nine atmospheric volumes covering the 39 bins of the MWR for the years 2012 (red), 2013 (green), 2014 (blue), 2015 (black) and 2016 (cyan). Winter (panel a), spring (panel b) summer (panel c) and autumn (panel d). In the boxes are represented the 25 and 75 percentile, the median, the maximum and minimum, and the outliers marked with asterisks.*

RH boxes (Fig. 5.7) are quite larger than temperature pointing a higher data dispersion. In addition, RH shows much more outliers (both above and below the boxes), mainly associated to (i) the cloud presence and (ii) the decrease of the absolute humidity with altitude, making less accurate the radiometric measures. This fact makes that MWR retrievals present higher or lower values than real measurements above 2.0 km agl, producing more outliers. RH presents a trend to increase from H1 to H3 and decreasing from H4 to H9 for winter, spring and autumn. This trend is broke up in summer when this increase reaches higher altitudes (from H1 to H6), and decreases from H7 to H9.

In general, IWV data boxplots presented in Fig. 5.8 exhibit less data-dispersion. The distribution of the data shows high equilibrium below 25 % and above 75 %, meaning that values are relatively well distributed around the median with lower data outliers. This variable presents a seasonal trend to increase from winter to summer and decreasing in autumn, showing their high relation with temperature seasonal trend.

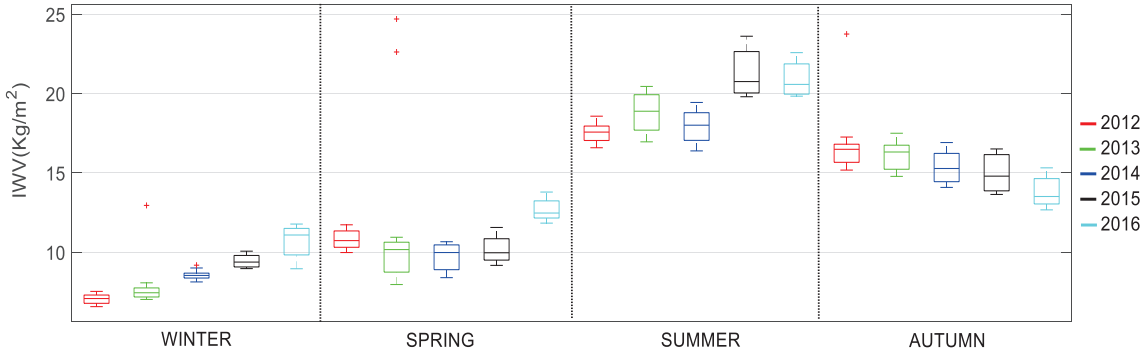

***Figure 5.8**. Seasonal boxplots of IWV the years 2012 (red), 2013 (green), 2014 (blue), 2015 (black) and 2016 (cyan). The line within the box refers to the median value, and the top and bottom of the box are the 75 and 25 quartiles, respectively. The outliers are marked with a red cross symbol.*

5.1.3 Inter-annual trend analysis by season

Table 5.1 reports for each season the inter-annual trend of temperature and RH computed by means of the calculation of the linear fits of the median values registered. Temperature only exhibits an inter-annual increase from H1 to H7 in winter season, from 0 to 1.0 km agl, increased between 0.4 and 0.6 °C/year, depending on the height range. Thus, winters

in Granada are becoming warmers along the years mostly within the first 2.0 km agl. With a weaker correlation (R^2 = 0.44), summers exhibit an increase of 0.4 ºC/year only close to surface (H1). The rest of the seasons do not present a clear inter-annual trend, with determination of R^2 coefficients below 0.50 for all height-ranges.

The results of the inter-annual increase of temperature are in agreement with climatological studies performed at Iberian Peninsula by Río et al. (2011) and Coll et al. (2017), reporting a surface temperature increasing trend in winter in the South and South-Eastern of the peninsula, where Granada station presented the drier conditions in the southern region of the peninsula. The results obtained here presents higher values for the inter-annual trend of temperature respect to those reported in literature, mainly because the instrumentation involved, the dataset size and the statistical techniques used in the datasets. Moreover, the inter-annual temperature increases in winter season reported in this study are also in agreement to the report of CALIMA (Caracterización de Aerosoles originados por Intrusiones de Masas de aire Africanas, *characterization of African air masses outbreaks,* http://www.calima.ws/episodiosocurridos.html), which is a program in charge to quantify the Saharan dust events over Iberian Peninsula. Its record indicates that from 2013 to 2015 the Saharan dust outbreaks have increased their number and become more intense in winter season, mostly within the second fortnight of February.

Table 5.1. *Inter-annual trends of temperature and RH by season and height-range, with W (winter), SP (spring), SU (summer) and A (autumn).*

		H1	**H2**	**H3**	**H4**	**H5**	**H6**	**H7**	**H8**	**H9**	
T (K)	slope (°C/year)	0.5 ± 0.6	0.5 ± 0.5	0.6 ± 0.3	0.6 ± 0.5	0.4 ± 0.8	0.4 ± 0.8	0.6 ± 0.5	0.1 ± 1.8	0.1 ± 3.1	W
	R^2	0.60	0.73	0.90	0.52	0.70	0.50	0.50	0.06	0.06	
	slope (°C/year)	0.7 ± 0.3	0.8 ± 0.3	0.8 ± 0.3	-0.3 ± 0.3	0.1 ± 0.4	0.1 ± 0.3	0.1 ± 0.3	-0.2 ± 0.3	0.1 ± 0.8	SP
	R^2	0.18	0.26	0.29	0.001	0.01	0.001	0.001	0.01	0.01	
	slope (°C/year)	0.4 ± 0.7	0.3 ± 0.9	0.3 ± 1.1	0.3 ± 0.8	0.2 ± 0.7	0.2 ± 1.0	0.3 ± 1.0	0.2 ± 0.8	0.1 ± 0.7	SU
	R^2	0.44	0.36	0.28	0.22	0.001	0.12	0.24	0.01	0.03	
	slope (°C/year)	0.3 ± 0.5	0.4 ± 0.4	0.1 ± 0.5	-0.3 ± 0.7	-0.2 ± 0.7	-0.3 ± 0.7	-0.3 ±0.6	-0.3 ± 0.6	-0.4 ± 0.5	A
	R^2	0.01	0.08	0.01	0.20	0.10	0.16	0.15	0.11	0.18	
RH (%)	slope (%/year)	2.6 ± 0.1	2.6 ± 0.1	2.9 ± 0.1	7.4 ± 0.1	5.42 ± 0.03	---	---	---	---	W
	R^2	0.79	0.77	0.54	0.56	0.91	---	---	---	---	
	slope (%/year)	-1.7 ± 0.1	2.1 ± 0.1	1.7 ± 0.2	2.1 ± 0.1	0.9 ± 0.2	---	---	---	---	SP
	R^2	0.19	0.91	0.68	0.76	0.15	---	---	---	---	
	slope (%/year)	-0.4 ± 0.3	-1.7 ± 0.1	-2.0 ± 0.1	-1.2 ± 0.1	1.3 ± 0.2	---	---	---	---	SU
	R^2	0.04	0.19	0.18	0.08	0.17	---	---	---	---	
	slope (%/year)	-2.3 ± 0.1	-2.8 ± 0.1	-2.6 ± 0.1	-1.7 ± 0.1	1.3 ± 0.2	---	---	---	---	A
	R^2	0.40	0.17	0.17	0.18	0.12					

Regarding RH, winter presents a clearly linear increase for all the altitudes analyzed (note that information at ranges H6-H9 are not included due to the loose of accuracy and precision of the RH retrievals). The highest rates of increasing are in the middle of the troposphere (between H4 and H5, 7.4 and 5.4 %/year, respectively). In spring, the RH increases linearly from H2 to H4. In summer and autumn, non-significant inter-annual trend were observed.

Table 5.2 presents the inter-annual trend of IWV and precipitable water (PW) by season. Our computations indicate that IWV is increasing over the years with high correlations in winter (1.0 ± 0.1 kg·m^{-2} /year, $R^2 = 0.95$) and summer (0.8 ± 0.1 kg·m^{-2} /year, $R^2 = 0.73$), while PW only experimented an increasing trend high correlated (0.07 ± 0.03 cm/year, $R^2 = 0.6$) in winter. This behavior in winter pointed out that every year during our study Granada is becoming more humid; furthermore, the likelihood of precipitations is higher in winter than in the rest of seasons. The IWV in spring presented no-correlation (up to 0.26) due to the higher median value found in 2016 (up to 12.5 kg·m^{-2}), this value tends to change the real tendency to decrease of this season (also seen in Fig. 5.8). If we perform the analysis hiding spring 2016 median data, IWV in spring presents a decreasing tendency with a slope up to -0.2 kg·m^{-2}/year and $R^2 = 0.80$. The fact of IWV in 2016 becomes higher is not clearly seen in this study, just we could associate to the statistical weight, because in March the percentage of missing data is up to 64.5 % (11 days measured), so the median value of the month could affect the seasonal median. IWV in autumn presented a strong correlation ($R^2 = 0.95$) with a linear decrease up to – 0.75 kg·m^{-2} /year which is not really linked with inter-annual temperature cycle. This analysis showed no-correlation of PW in spring, summer and autumn, however the seasonal trends for both IWV and PW are the same, increasing from winter to summer and decreasing in autumn. The higher values of IWV were reached in spring and summer, mostly associated to the vegetation presence and high temperatures, which increases the evapotranspiration process. Finally, it is important to taking into account the warm air mases that comes from Atlantic Ocean and Mediterranean Sea, with high temperatures, this fact increase the capacity of these air masses to harbor water vapor before saturation.

Table 5.2. *Inter-annual trend of IWV and IWV AERONET by season in the period 2012-2016.*

	slope (kg·m^{-2}/year)	R^2	Season
IWV_{MWR} (kgm^2)	1.0 ± 0.1	0.95	WINTER
	0.3 ± 0.7	0.26	SPRING
	0.8 ± 0.1	0.73	SUMMER
	-0.8 ± 0.2	0.95	AUTUMN
$IWV_{aeronet}$ (cm)	0.07 ± 0.03	0.60	WINTER
	0.01 ± 0.05	0.02	SPRING
	0.03 ± 0.03	0.30	SUMMER
	-0.03 ± 0.04	0.20	AUTUMN

5.2 Uncertainty and diurnal cycle over 4-year dataset at theSIATA-tower station

This chapter is devoted to the error analysis on temperature and RH by following the same procedure applied in Sec. 5.1. The error calculation is done by means of the bias between RS and MWR, where accuracy refers to $\overline{bias}$ and precision to SD_{bias}. The RS dataset it was taken from a 2-week intense campaign, launching a RS every 3 hours from 00:00 to 24:00 hours (8 RS per day). This information was analyzed along with co-located MWR measurements, finding coincidence in 41 RS for temperature, but only 13 RS for RH profiles due to some technical issues. Due to the location, with complex terrain and the wind role above the mountains, comparison between RS and MWR is meaningless above 3.0 km agl and, therefore, this study is focused on the first 3.0 km agl.

5.2.1. Characterization of MWR against RS

Figure 5.9 shows that in the first 3.0 km agl, the temperature $\overline{bias}$ was relatively high in the first 0.4 km agl (up to 2.2 °C), and the same behaviour had the SD_{bias}. Both parameters were always positives evidencing an overestimation of the MWR temperature profile over

RS. The main issue is at this height below 0.4 km agl, due to the effect of the surface forcing associated to the human activity and atmospheric dynamic at that scale. The rest of the temperature $\overline{bias}$ and SD_{bias} profile (above 0.4 km agl) behaves quite stable, reaching up 1°C and 0.9 °C, respectively, and the SD_{bias} is nearly constant from 0.4 to 3.0 km agl, assuring a good precision of the measurements.

RH $\overline{bias}$ and SD_{bias} profiles had the same behavior in the first 0.25 km agl, but $\overline{bias}$ were ranging from negative (-4 %) to positive (4 %) values, and SD_{bias} from 5 % to 8 %. Then, RH $\overline{bias}$ held positive (close to 2 %) from 0.25 km agl to 0.7 km agl, after that it became negative until 3.0 km agl (up to -5.7 %), showing a relative high variability. The RH SD_{bias} was relatively constant above 0.25 km agl reaching up 9.5 %, pointing out that the error is lower than 10 % for this variable.

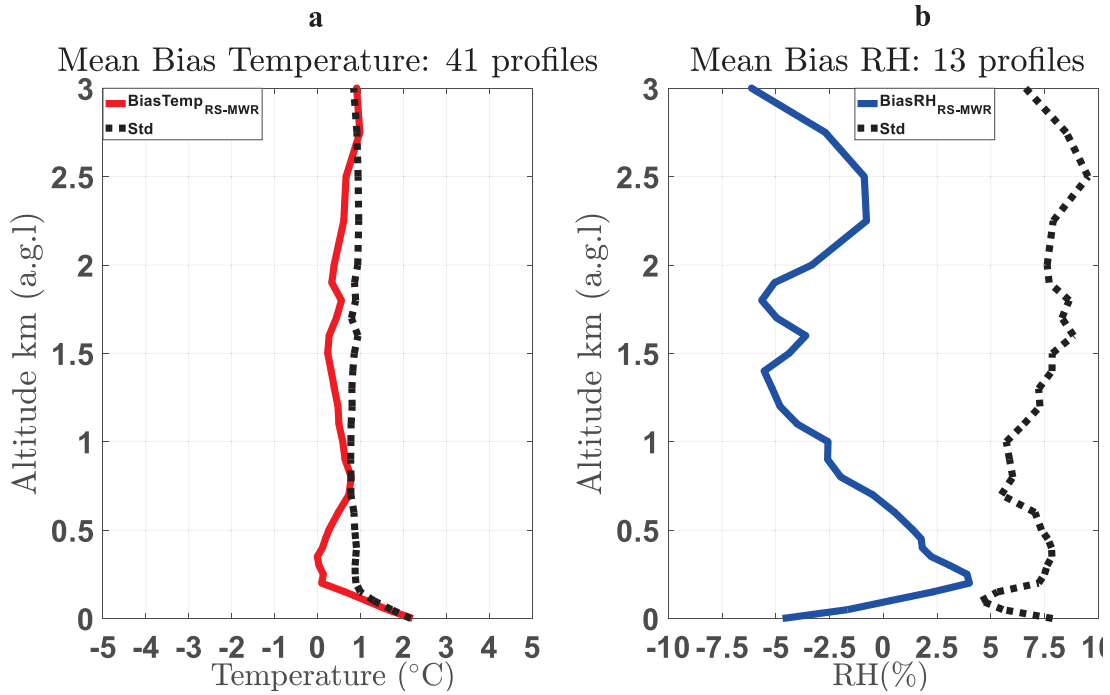

Figure 5.9. *Mean bias (solid red line) and standard deviation (dashed black line) on all-weather conditions (AWC, blue) between RS and MWR for (a) temperature and (b) RH profiles.*

As it was performed before, a subdivision of the error analysis between daytime and night-time have been done. Table 5.3 reports the results obtained for the first 3 km agl. 26 temperature profiles were coincident for daytime and 15 during night-time conditions, while 8 RH profiles were coincident for daytime and 5 during night-time. The most evident aspect in the temperature was the effect of the solar radiation within the first

200 m agl, showing high values in the SD_{bias} (~2.5 °C) at daytime, while night-time SD_{bias} was up to 1.7 °C. The $\overline{bias}$ profile was close for daytime and night-time (2.2 °C and 2.3 °C, respectively). A it is observed on Fig. 5.10.a, the shape of the profiles was very similar from 0.2 to 1.8 km agl, but night-time $\overline{bias}$ profile was ranging from negative to positive values (-0.28 ± 0.03 °C to 0.5 ± 0.9 °C), meanwhile daytime $\overline{bias}$ was always positive (up to 1.0 ± 1.0 °C). The last region evaluated (from 1.8 to 3.0 km agl), behaves quite similar for daytime and night-time up to 1.0 ± 1.0 °C, with a very constant SD_{bias} profile around 1ºC.

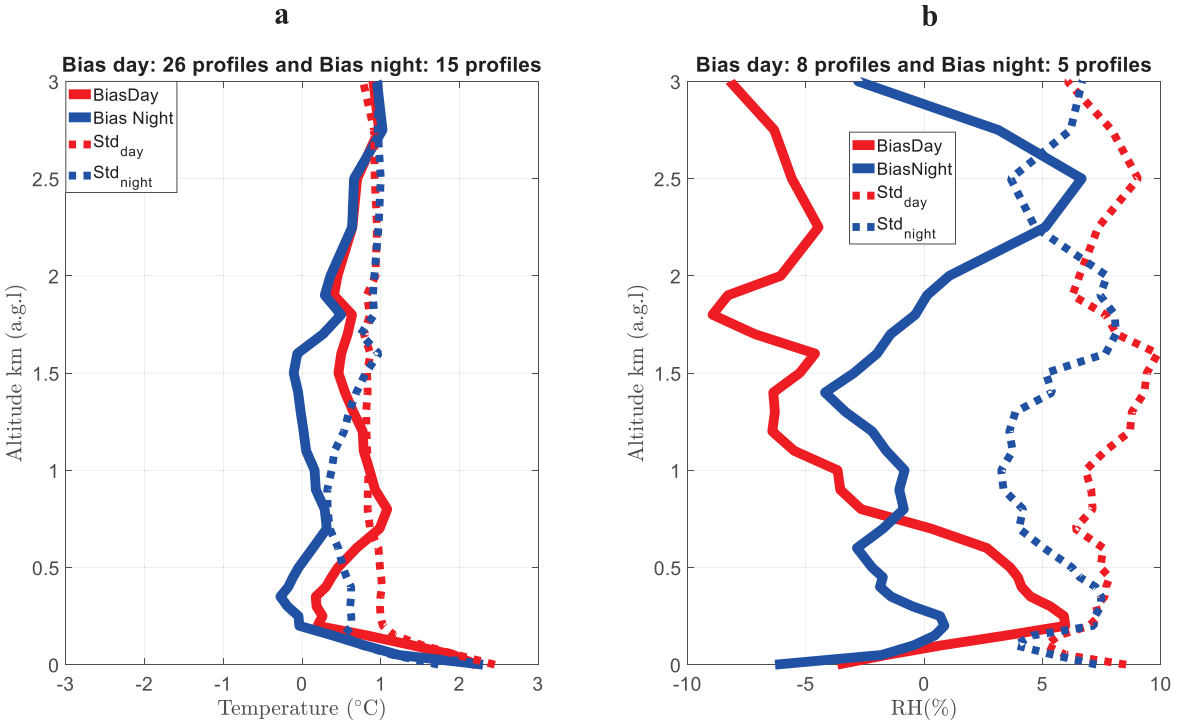

Figure 5.10. *Mean bias (solid lines) and standard deviation (dotted lines) at daytime (red) and night-time (blue) for (a) temperature and (b) RH profiles between RS and MWR.*

Regarding RH, a high variability of the $\overline{bias}$ is seen within the closest region to the surface (below 300 m agl), mainly for daytime (-4.0 ± 8.0 % to 6.0 ± 7.0 %) than night-time (-6.0 ± 7.0 % to 0.9 ± 7.0 %) conditions which is linked to the Sun effect over the measurements. From 0.3 to 1.4 km agl, night-time profile was always pointed out a subestimation of the measurements (-3.0 ± 3.0 %), while daytime was ranging from positive to negative (5.0 ± 7.0 % to -6.0 ± 9.0 %). As it was expected, daytime and night-time profiles increase their variation above 1.4 km agl as is well seen in Fig. 5.10.b.

Table 5.3. *Daytime and night-time error analysis for MWR at the SIATA-tower station.*

	$\overline{bias}$	SD_{bias}	altitude range [km] agl
Temperature daytime [°C]	[0.2, 2.2]	[1.0, 2.5]	0.0-0.2
	[0.2, 0.8]1	[0.8, 1.0]	0.2-1.8
	[0.2, 1.0]	[0.7, 0.8]	1.8-3.0
Temperature night-time [°C]	[2.3, -0.1]	[1.7, -0.1]	0.0-0.2
	[-0.2, 0.5]	[0.03, 0.9]	0.2-1.8
	[0.3, 1.0]	[0.8, 1.0]	1.8-3.0
RH daytime [%]	[-4.0, 6.0]	[8.0, 7.0]	0.0-0.3
	[5.0, -6.0]	[7.0, 9.0]	0.3 - 1.4
	[-5.0, -9.0]	[10.0, 6.0]	1.4 - 3.0
RH nighttime [%]	[-6.0, 0.9]	[7.0, 7.0]	0.0-0.3
	[-0.5, -3.0]	[7.0, 3.0]	0.3 - 1.4
	[-4.0, 6.6]	[8.0, 3.7]	1.4 - 3.0

5.2.2. Annual and diurnal analysis at the SIATA-tower station

As Medellín is located to equator, there is no seasonal variability (i.e. winter, spring, summer and autumn) in variables like temperature and RH, among others. However, there is a strong diurnal cycle, in which the Sun is practically in the zenith position around the 12 hour of local time (LT). Some studies performed by Nisperuza et al. (2014) and Herrera (2015) pointed out that ABL presents the higher activity between 9 to 13 h LT, where the solar radiation on the surface makes that convection increase, cleaning the atmosphere. Figure 5.11 allows the diurnal cycle evaluated from January 2015 to August 2018 for temperature, RH, liquid water and vapor density profiles.

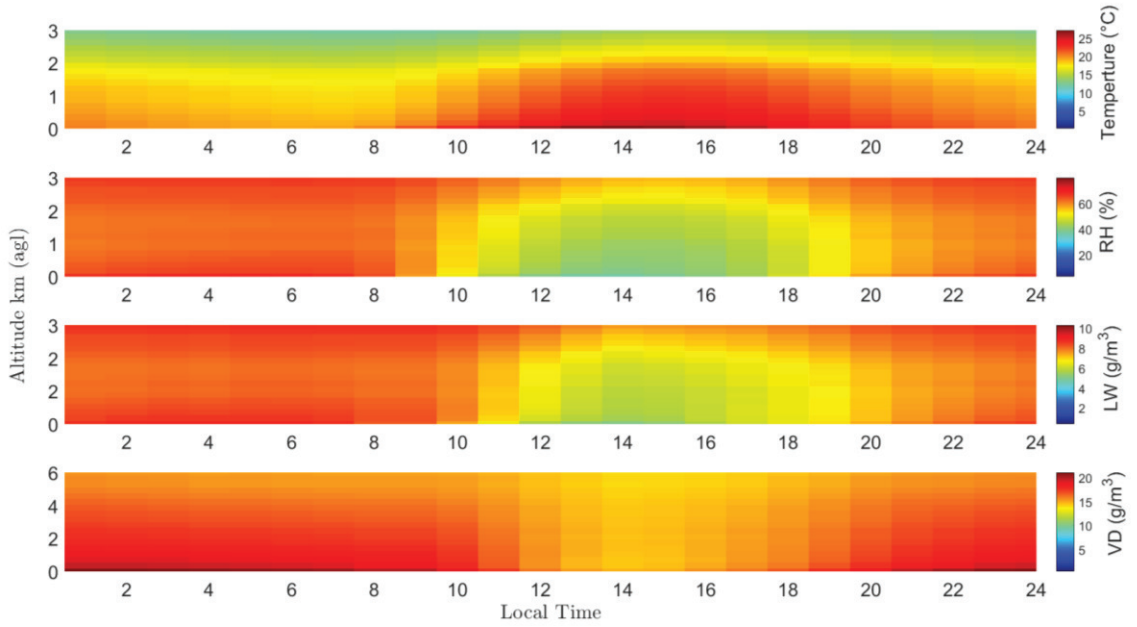

Figure 5.11. *Mean diurnal cycle of temperature (first panel), RH (second panel), liquid water (third panel) and vapor density (fourth panel). obtained from MWR. The results covers 4-year dataset from January 2015 to August 2018.*

From Fig. 5.11, it is possible to determine that the higher values of mean temperature are ranging roughly from 12 to 16 h LT, becoming this time-frame the driest along the day (i.e. low values of RH, liquid water and vapor density profiles). The mean values for the maximum of temperature at surface level in the warmest hours of the day, were around 27.1 ± 2.2°C, while RH were up to 36.5 ± 8.0 %, liquid water were up to 5.1 $g \cdot m^{-3}$ and vapor density values were 14.8 $g \cdot m^{-3}$. On the contrary, the values obtained for the coldest hours (from 5 to 6 LT) pointed out that temperature was about 19.2 ± 2.2°C and RH, liquid water and vapor density were higher, up to 68.8 ± 8.0 %, 8.9 $g \cdot m^{-3}$ and 20.8 $g \cdot m^{-3}$, respectively.

This evaluation allows for defining potential hours of the day where could be studied for example ABL, turbulence and aerosol hygroscopicity, among others. Thus, focusing in the goal of this thesis and according to the bases established in previous sections, it is possible to define periods in which potential aerosol hygroscopic cases may be found, considering the criteria ofRH changing monotonically (decreasing or increasing) simultaneously to changesaerosol properties.

5.3 Summary of chapter 5

Regarding the analysis over a 5-year dataset of the RPG-HATPRO MWR leads to quantify its accuracy and precision by means of the mean-bias and standard deviation for temperature and RH vertical profiles under cloud-free conditions and all-weather condition, and IWV column product. In addition, an analysis of the MWR performances during night- and day-time was carried out under cloud-free conditions. It was found that the temperature $\overline{bias}$ profile under all-weather conditions exhibited high confidence, mostly below 2 km agl with values ranging from 1.7 to -0.4K. The SD_{bias} under all-weather conditions was quite constant in altitude, with values around 3 K in the whole troposphere. Under cloud-free conditions, the mean bias showed quite similar values than under all-weather conditions, although some differences were found in the lowest layer (below 1.5 km) and between 3 and 5 km (agl), where the mean bias was slightly higher under cloud-free conditions reaching up 1.8 K. An important point to be remarked is the lower SD_{bias} that was observed under cloud-free conditions. The SD_{bias} profile presented values ranging between 1.1 and 1.8 K in the whole troposphere, indicating a higher precision of the MWR under these conditions.

The performance for RH under all-weather conditions showed from surface to 2 km agl that $\overline{bias}$ was ranging from 3.0 to -4.0 % with SD_{bias} between 10 to 16.3 %, and from 2 to 4 km the $\overline{bias}$ was up to -18 % with SD_{bias} ranging between 15 to 21 %. Above 4 km the $\overline{bias}$ reached up to -11.0 with SD_{Bias} ranging from 12 to 17 %. The same altitudes ranges were evaluated under cloud-free conditions showing high confidence within the first 2 km, ranging from 2.0 to -0.4 with SD_{bias} from 0.5 to 13.3 %, then from 2 to 3 km agl were up to -4.0 to -21.4 with SD_{bias} 19.3 %, and decreasing up to -4.5 % with SD_{bias} 9.3 %. The temperature and RH SD_{bias} showed a positive offset close to 2.5 K and 5 %, respectively, between all-weather conditions and cloud-free conditions, associated with cloud presence. Finally, a performance of the IWV product allows seeing the effect of the cloud presence over this product. Thus, the determination coefficient was up to 0.82 for all-weather conditions, meanwhile it increases up to 0.96 under cloud-free conditions The MBE was lower for all-weather conditions (-0.80 kg/m^2) than cloud-free conditions (-1.25 kg/m^2).

The cloud-free conditions database (temperature and RH) was investigated under daytime and night-time scenarios. This classification exhibited a time-dependency

associated to the solar heating on the surface, becoming more variable during daytime respect to night-time. The temperature $\overline{bias}$ profile was ranging from 0.7 ±1.0 K and 1.0 ±1.0 K with at daytime below 1.8 km agl and from 0.5 ± 0.6 K to 0.6 ± 0.6 K at night-time below 1.5 km. This error increase with altitude. The RH also presented low errors below 1.5 km agl up to 8 % at daytime with SD_{bias} ranging from 6 to 8.8 % and up to 2 % with SD_{bias} ranging from 5 to 10 % at night-time. After this altitude, the accuracy and precision increase rapidly with height.

The second part of this analysis was focused on a statistical study over a 5-year dataset. Firstly, it was observed that temperature, IWV and $ABLH^{max}$ daily-seasonal cycle presents an increasing trend from winter to summer, decreasing in autumn, meanwhile, RH daily-seasonal cycle is opposite, maximum in winter decreasing until summer and then increasing again in autumn; all of them governed by the solar radiation. The maximum temperature values were around 16 UTC coinciding with the minimums RH values, instead, RH maximums are located from 2 to 10 UTC and from 21 to 24 UTC. The hourly- mean cycle leading us to conclude that 2015 was the warmest year for all seasons, except in autumn 2013 that showed up an abrup increase of temperature respect to other years. The coldest seasons do not follow a yearly pattern, becoming the coldest winter 2012, spring 2014, summer 2014 and autumn 2015. The highest RH values were found in winter 2016, spring 2016, summer 2015 and autumn 2016; and the lowest RH values in winter 2012, spring 2014, summer 2014 and autumn 2014. Finally, the inter-annual study is linked with seasonal, pointing out that temperature and RH showed up an inter-annual linear increase in winter with a mean-trend up to (0.5 ± 0.1) °C/year and (3.4 ± 1.7) %/year, respectively, from the ground to 6 km agl. IWV presented an inter-annual linear increase up to 1 kgm^{-2} /year in winter and 0.78 kgm^{-2} /year in summer. The autumn presents a linear decrease trend up to -0.75 kgm^{-2} /year.

The results obtained here allows assessing the reliability range of the HATPRO MWR G2 system, in order to use products like temperature, RH and IWV in further applications like foresting models, ABL studies, and aerosol hygroscopic growth, among others at this mid-latitude region.

The performance of the MWR MP3000 A showed good results under the first 3.0 km agl, being measurements less accurate and precise close to the surface (temperature: 2.2 ±2.2 °C, and RH: from -4±5 % to 4±8 %). An improving on $\overline{bias}$ and SD_{bias}.was

seen from 0.4 to 3.0 km agl (temperature 1 ± 0.9 °C and RH: -5.7 ± 9.5 %) From this study, it is possible to conclude that MWR measures will provide solid ancillary information for ongoing investigations on topics such as aerosol hygroscopic growth, forecast models, aerosol transport and ABLH calculations over this region by using MWR products in Medellín city, mostly under the first 3.0 km agl.

The same analysis was done by dividing the dataset in daytime and night-time lead it to see the same effect of solar radiation over $\overline{bias}$ and SD_{bias} profiles, mostly close to the surface. The high values of SD_{bias} (~2.5 °C) were found at daytime, while night-time up to 1.7 °C for temperature, and $\overline{bias}$was relative the same for both conditions (up to 2.3 °C). RH profiles presented high variability close to surface too, at daytime (-4.0 $\pm$ 8.0 % to 6.0 $\pm$ 7.0 %) and night-time (-6.0 $\pm$ 7.0 % to 0.9 $\pm$ 7.0 %). From 0.3 to 1.4 km agl, night-time profile was always pointed out a sub estimation of the measurements, but relatively constant (-3.0 $\pm$ 3.0 %), meanwhile daytime was ranging from positive to negative (5.0 $\pm$ 7.0 % to -6.0 $\pm$ 9.0 %).

The relatively well behavior of temperature and RH profiles, together with diurnal evaluation, allowed to define the hours of the day where potential aerosol hygroscopic cases may be found. On this way, evening and early morning could be the best moments along the day where this phenomenon may occur, perhaps it may be considered the atmospheric stability criteria for isolating correctly the best time frames where aerosols can uptake water.

5.4. References

Bedoya-Velásquez, A. E., Navas-Guzmán, F., Moreira, G., Román, R., Cazorla, A., Ortiz-Amezcua, P., Benavent-Oltra, J.A., Alados-Arboledas, L., Olmo-Reyes, F.J., Foyo-Moreno, I., Montilla-Rosero, E., Hoyos, C.D., Guerrero-Rascado, J.L.: Seasonal analysis of the atmosphere during five years by using microwave radiometry over a mid-latitude site, Atmos. Res., Volume 218, 78-89, ISSN 0169-8095, https://doi.org/10.1016/j.atmosres.2018.11.014, 2018b.

Coll, J., Aguilar, E. and Ashcroft, L.: Drought variability and change across the Iberian Peninsula. TheorApplClimatol 130: 901. https://doi.org/10.1007/s00704-016-1926-3, 2017.

Herrera, L.: Caracterización de la capa límite atmosférica en el Valle de Aburrá a partir de la información de sensores remotos y radiosondeos. Maestría thesis, Universidad Nacional de Colombia - Sede Medellín, 2015.

Moreira, G. A., Guerrero-Rascado, J. L., Bravo-Aranda, J. A., Benavent-Oltra, J. A., Ortiz-Amezcua, P., Román, R., Bedoya-Velásquez, A. E., Bravo-Aranda, J. A., Olmo-Reyes, F.J., Landulfo, E., Alados-Arboledas, L.: Analysisg the turbulence in the Planetary Boundary Layer by the synergic use of remote sensing systems: Doppler wind lidar and aerosol elastic lidar, Atmos. Chem. Phys. Discuss., https://doi.org/10.5194/acp-2018-276, 2018b.

Moreira, G. de A., Guerrero-Rascado, J. L., Bravo-Aranda, J. A., Benavent-Oltra, J. A., Ortiz-Amezcua, P., Román, R., Bedoya-Velásquez, A. E., Landulfo, E., and Alados-Arboledas, L. Study of the planetary boundary layer by microwave radiometer, elastic lidar and Doppler lidar estimations in Southern Iberian Peninsula, Atmos. Res., https://doi.org/10.1016/j.atmosres.2018.06.007, 213, 185-195, 2018a

Navas-Guzmán, F., N. Kämpfer, and A. Haefele: Validation of brightness and physical temperature from two scanning microwave radiometers in the 60 GHz O2 band using radiosonde measurements, Atmos. Meas. Tech., 9, 4587-4600, 2016.

Nisperuza, D.J., Bedoya-Velásquez, A.E., Alegría, D.L., Múnera, M., Jiménez, J.F., Zapata, C.E., and Bastidas, A.: Lidar measurements and wavelength covariance transform method to estimate the atmospheric boundary layer heights in Medellín, Colombia. Opt. Pura Apl. 47 (2) 123-130, doi: http://dx.doi.org/10.7149/OPA.47.2.123, 2014.

Río, S., Herrero, L., Pinto-Gomes, C., Penas, A.: Spatial analysis of mean temperature trends in Spain over the period 1961–2006,Global and Planetary Change, Volume 78, Issues 1–2, Pages 65-75, ISSN 0921-8181,https://doi.org/10.1016/j.gloplacha.2011.05.012, 2011.

6. Aerosol hygroscopic growth by using RL + DL + MWR and in situ at the IISTA-CEAMA station

This chapter is an adaptation of the published article with the following reference:

Bedoya-Velásquez, A. E., Navas-Guzmán, F., Granados-Muñoz, M. J., Titos, G., Román, R., Casquero-Vera, J. A., Ortiz-Amezcua, P., Benavent-Oltra, J. A., de Arruda Moreira, G., Montilla-Rosero, E., Hoyos, C. D., Artiñano, B., Coz, E., Olmo-Reyes, F. J., Alados-Arboledas, L., and Guerrero-Rascado, J. L.: Hygroscopic growth study in the framework of EARLINET during the SLOPE I campaign: synergy of remote sensing and in-situ instrumentation, *Atmospheric Chemistry and Physics*, 18, 1-17, 2018.

This study focuses on the analysis of aerosol hygroscopic growth during Sierra Nevada Lidar AerOsol Profiling Experiment (SLOPE I) campaign by using the synergy of active and passive remote sensors at ACTRIS Granada station and in-situ instrumentation at a mountain station (Sierra Nevada, SNS). To this end, a methodology based on simultaneous measurements of aerosol profiles from an EARLINET multi-wavelength Raman lidar (RL) and relative humidity (RH) profiles obtained from a multi-instrumental approach is used. This approach is based on the combination of calibrated water vapor mixing ratio (r) profiles from RL and continuous temperature profiles from a microwave radiometer (MWR) for obtaining RH profiles with a reasonable vertical and temporal resolution. This methodology is validated against the traditional one that uses RH from co-located radiosounding (RS) measurements, obtaining differences in hygroscopic growth parameter (γ) lower than 5% between the methodology based on RS and the one presented here. Additionally, during SLOPE I campaign the remote sensing methodology used for aerosol hygroscopic growth studies has been checked against Mie calculations of aerosol hygroscopic growth using in-situ measurements of particle number size distribution and submicron chemical composition measured at SNS. The hygroscopic case observed during SLOPE I showed an increase in particle backscatter coefficient at 355 and 532 nm with relative humidity (RH ranged between 78 to 98%), but also a decrease in backscatter-related Ångström exponent (AE) and particle linear depolarization ratio (PLDR) indicating that the particles became larger and more spherical due to hygroscopic processes.Vertical and horizontal wind analysis is performed

by means of a co-located Doppler lidar system, in order to evaluate the horizontal and vertical dynamics of the air masses. Finally, the Hänel parameterization is applied to experimental data for both stations and we found good agreement on γ measured with remote sensing ($\gamma^{532} = 0.48 \pm 0.01$ and $\gamma^{355} = 0.40 \pm 0.01$) respect to the values calculated using Mie theory ($\gamma^{532} = 0.53 \pm 0.02$ and $\gamma^{355} = 0.45 \pm 0.02$), with relative differences between measurements and simulations lower than 9 % at 532 nm and 11 % at 355 nm.

6.1. Combination of RL and MWR method for retrieving RH profiles

The synergetic method proposed by Navas-Guzmán et al. (2014) for retrieving RH profiles is used here for the first time to study aerosol hygroscopic growth. In this section, two particular cases (case I on 22nd July 2011 at 20:00-20:30 UTC and case II on 22nd July 2013 at 20:30-21:00 UTC) are analysed with this new methodology. These two cases were already presented in Granados-Muñoz et al. (2015) using the classical approach that combines RH profiles obtained from RS and the lidar aerosol properties. Results obtained here are compared with those in Granados-Muñoz et al. (2015) in order to evaluate the synergetic method proposed here.

In this work, we have also checked the RH calculation for the case of 22nd June 2013 by using temperature profiles from MWR and GDAS modelled data, which were compared to RS RH profiles (Fig. 6.1). This comparison allows us to investigate the feasibility of the use of GDAS temperature information to compute the RH profiles in combination with RL profiles, in order to increase the database for hygroscopicity studies. However, the results present larger bias when they are compared with the RS RH profiles, up to 20 % for $RH_{LIDAR+GDAS}$ in almost the whole profile instead of the10% for the $RH_{LIDAR+MWR}$ (Fig. 6.1). Thus, the use of GDAS data seems not to be appropriate in this study, mainly because of two reasons: (i) the complex terrain where the measurement station is located, surrounded by mountains of high elevation (up to more than 3000 m asl. in a very short horizontal distance of few tenths of kilometres) that makes more difficult for models to provide accurate thermodynamics profiles for this location; (ii) GDAS profiles have a lower temporal resolution (3 h) than the MWR, which gives temperature profiles each 2 min.

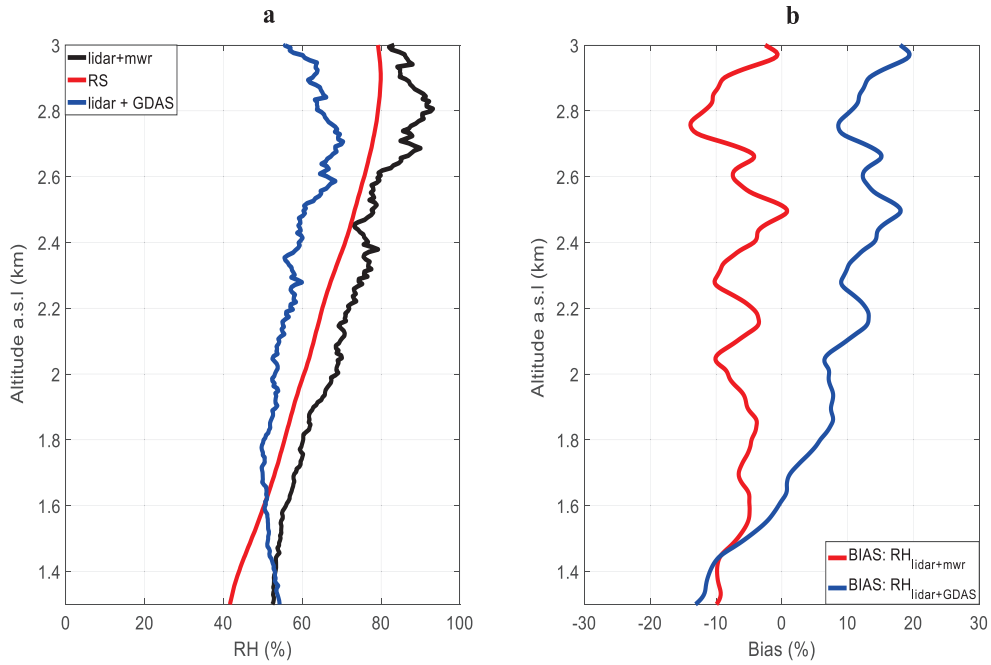

Figure 6.1. *RH comparison for 22nd Jul 2013 around 20:00-21:00 UTC. (a) RH profiles retrieved from combination of lidar+MWR (black line), lidar+GDAS (blue line) and RS (red line) and (b) Bias calculation between lidar+MWR (redline) and lidar+GDAS (blue line).*

Figure 6.2 shows, from left to right, the RH profiles obtained from both the RS (black line) and the synergy RL+MWR (red line), the bias between both profiles ($RH_{RS} - RH_{RL+MWR}$), β_{532nm} profiles retrieved from the lidar system and f_β (RH). The upper panels correspond to case I on 22nd July 2011 and the bottom panels to case II on 22nd July 2013. Horizontal dashed lines mark the region of interest analysed for each case, ranging from 1.3 to 2.3 km asl for case I and 1.3 to 2.7 km asl for case II.

RH profiles (Fig. 6.2 a and e, red line) calculated by the combination between RL calibrated r (z) profile and MWR temperature profiles were obtained following the methodology presented in section 4.2.1.1 by using Eq. 4.4. Good agreement is observed, with biases (Fig. 6.2 b and f) lower than 10% within the analysed region. The differences obtained in the RH profiles might be associated to the discrepancies between the temperature profiles from MWR and RS, due to the lower vertical resolution of the MWR. Additionally, discrepancies are also expected because of the radiosonde drift and the different temporal sampling (the lidar data correspond to a 30-min average, whereas the

RS provides instantaneous values that build the profile in the region of interest in less than 5 minutes).

The discrepancies between the two RH profiles are especially relevant in the lower part of the analyzed data since differences of RH in this region lead to variations in RH_{ref}. For case I, $RH_{ref} = 60\%$ for RS and $RH_{ref} = 68\%$ for the RL+MWR combination, whereas for case II, $RH_{ref} = 40\%$ for RS and $RH_{ref} = 50\%$ for RL+MWR methodology. Additionally, the RH discrepancies in the upper region of the profiles (from 2.1 to 2.3 km asl for case I and from 2.6 to 2.7 km asl for case II), which can reach up to 5%, are also relevant since they are associated to the maximum values of RH and may modify the data tendency on Hänel's parameterization, leading to variations in $\gamma\ (\lambda)$ depending on the methodology used for the retrieval of RH. Despite these discrepancies, the differences between $\gamma\ (\lambda)$ parameters obtained from both methodologies are low (Table 6.1). On case I, $\gamma\ (\lambda) = 0.59 \pm 0.05$ obtained from RL+MWR is larger than that obtained from RS ($\gamma = 0.56 \pm 0.01$). While on case II the γ obtained with RH from RS ($\gamma = 0.99 \pm 0.01$) is larger than the one from RL+MWR ($\gamma = 0.95 \pm 0.02$). We have to keep in mind that uncertainties reported on γ are obtained by the polynomial fitting and they do not include the propagation error result. The relative differences on both cases are below 5%, which is relatively good compared to the expected uncertainties reported in Titos et al. (2016) and considering the differences between the two methodologies.

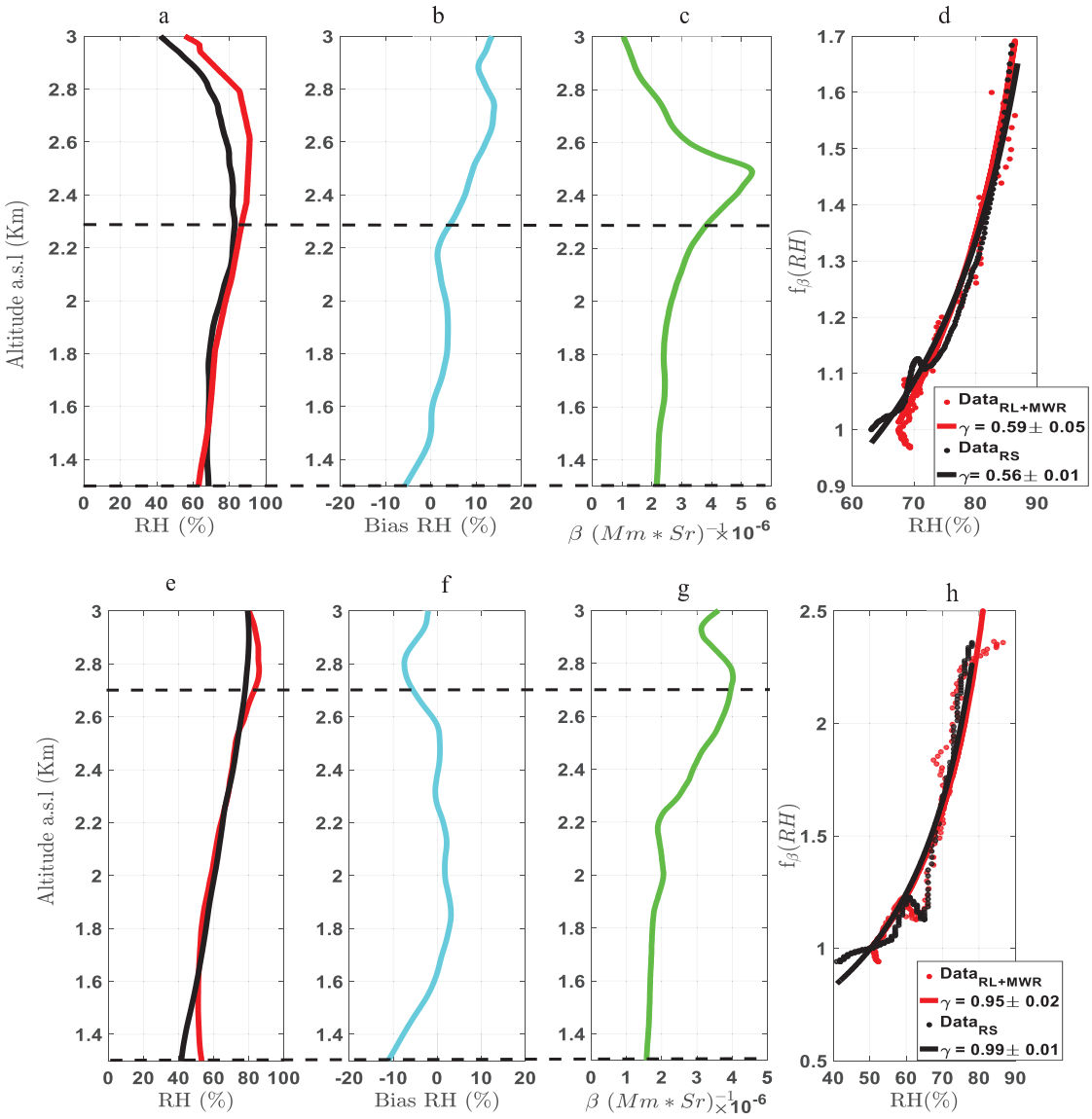

Figure 6.2. *(a, e) Profiles of RH retrieved from RS (black line) and by the synergy RL+MWR (red line), (b, f), RH bias profiles (cyan line), (c, g) β_{par} retrieved by using Klett-Fernald algorithm and lidar ratio of 65 Sr (green line), (d, f) f_β (RH) calculated for RS (black dots) and by the synergy RL+MWR (red dots) and the corresponding Hänel parameterizations (solid lines), where red line refers to RL+MWR method (case I: γ=0.59±0.05, case II: γ = 0.95 ±_0.02) and black line refers to RS method (case I: γ = 0.56 ±_0.01, case II: γ = 0.99 ±_0.01) .The top row corresponds to case I (22nd July 2011, 20:30-21:00 UTC) and the bottom row to case II (22nd July 2013, 20:00-20:30 UTC). Horizontal dashed lines indicate the altitude range analysed for each case (1.3 to 2.3 km for case I and 1.3 to 2.7 km for case II). All these profiles were measured at the EARLINET IISTA-CEAMA station.*

Table 6.1. *Results obtained for each case analysed by means of new methodology combining RL+MWR and the classical approach using RS data.*

	Case I	**Case II**
RS: RH_{ref} [%]	60	40
RL+MWR: RH_{ref} [%]	68	50
RS: f_β(85%)	1.50	2.60
RL+MWR: f_β(85%)	1.46	2.30
γ_{RS}	0.56 ± 0.01	0.99 ± 0.01
γ_{RL+MWR}	0.59 ± 0.05	0.95 ± 0.02

The obtained values of f_β (85%) using both methodologies are presented in Table 6.1. For case I, f_β (85%) = 1.50 for RS and f_β (85%) = 1.46 for RL+MWR, with a relative difference below 3%. For case II, f_β (85%) = 2.6 for RS and f_β (85%) = 2.3 for RL+MWR showing a relative difference of 11%. Even though the relative difference is larger for case II, for both cases the discrepancies lie within the uncertainty associated to the calculation of f_β (85%) which is around 20% according to Titos et al. (2016). Thus, the RL+MWR methodology presented by Navas-Guzmán et al. (2014) to obtain RH profiles in a continuous time base is a promising technique for hygroscopic growth studies. This methodology will allow for expanding the RH profile database and it opens new opportunities for the detection of hygroscopic cases during night-time periods.

6.2 Hygroscopic study during SLOPE I

6.2.1 Conditions for hygroscopic growth

Aerosol hygroscopic growth was observed during SLOPE I campaign in 2016 combining the remote sensing instruments and the RS. Figure 6.3 shows the time series of range corrected signal (RCS) at 532 nm derived by the EARLINET lidar system at the IISTA-CEAMA station on 16th June 2016. The presence of clouds is observed in the late afternoon (~3.0 km asl.) before 19:00 UTC, with clouds vanishing after that during the

remaining measurement period. The red lines in Fig. 6.3 mark the 30 min set of profiles (from 20:30 to 21:00 UTC) where an intensification of the RCS is observed at 2.5 km asl, which could be an indication of potential aerosol hygroscopic growth.

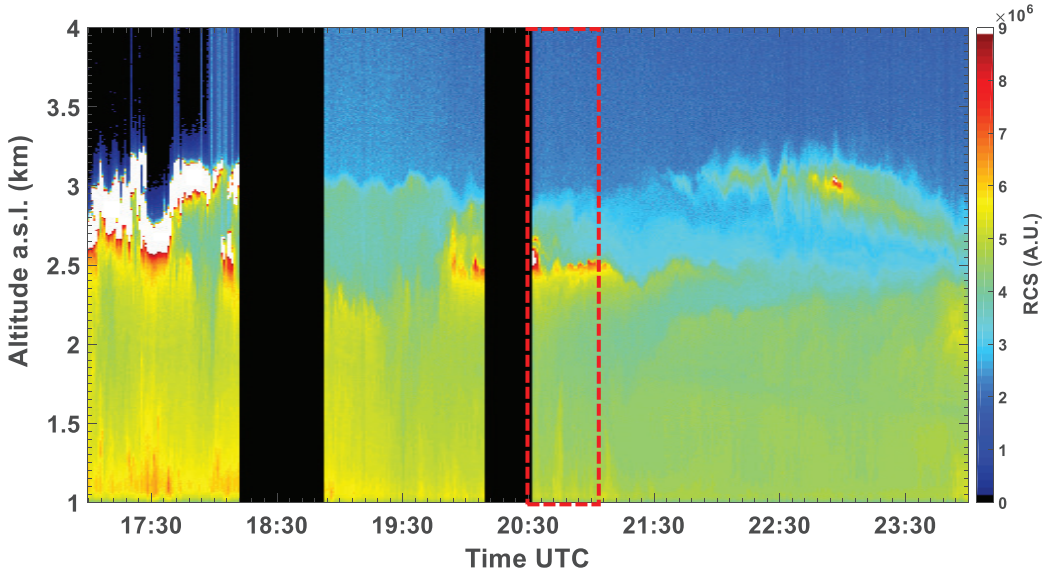

Figure 6.3. *EARLINET IISTA-CEAMA lidar RCS time series at 532 nm, 16th June 2016 (17:00 to 00:00 UTC). The sunset estimated for this day was at 21:30 UTC local time.*

Figure 6.4 shows profiles of r (z), θ_v, RH, β_{par} at 355 and 532 nm, backscatter-related *AE* between 355 and 532 nm ($AE_{355-532}$) and $PLDR_{532}$ (particle linear depolarization ratio at 532 nm) obtained on 16th June 2016 between 20:30 and 21:00 UTC. For aerosol hygroscopicity analysis it must be ensured that ranges where RH increases correspond to an increase in β_{par}, which is well seen along the layer between 1.5 and 2.4 km asl (Fig. 6.4). The RH profile was calculated by using the method combining RL+MWR. In this case, the calibration constant for the RL r (z) profile was calculated using the six RSs launched at night-time during this campaign. A calibration constant of 110 ± 2 g/kg was obtained as the mean value of the different calibrations.

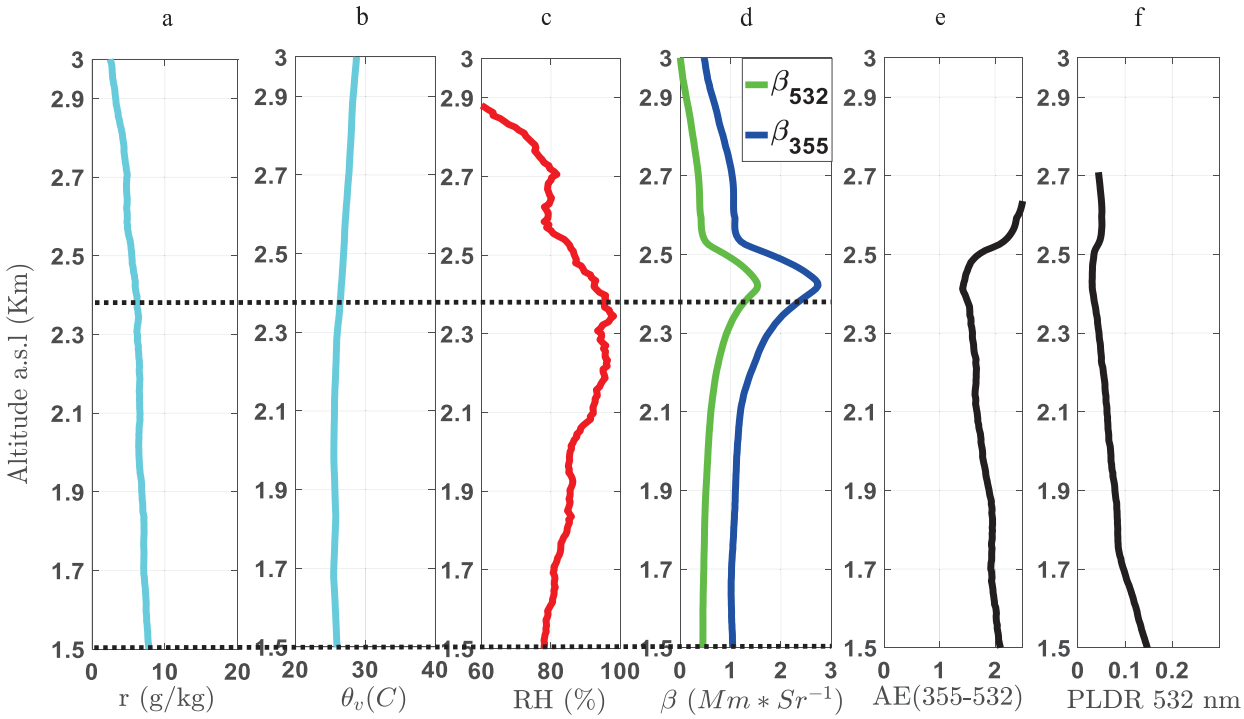

Figure 6.4. *(a) Water vapor mixing ratio, (b) virtual potential temperature, (c) relative humidity obtained from synergy RL+MWR, (d) particle backscatter coefficient at 355 and 532 nm, (e) backscatter-related Ångström exponent (355-532 nm) and (f) particle linear depolarization ratio. All profiles correspond to a 30 min-average from 20:30 to 21:00 UTC on 16th June 2016 at the EARLINET IISTA-CEAMA station.*

In order to fulfil all the requirements discussed in previous sections for hygroscopic growth studies, together with the RH and β_{par} increase within the layer, atmospheric stability must be ensured through the evaluation of thermodynamic variables such as θ_v and r (z). Here, r (z) shows relatively low vertical variation within the region of interest (1.5 to 2.4 km asl), decreasing monotonically with altitude at a rate of $-1.9\ \frac{g}{kg \cdot km}$ (Fig. 6.4a) and θ_v shows a monotonic increase at a rate $\frac{\partial \theta_v}{\partial z} = 0.03\ \frac{°C}{km}$ within the same region.

$AE_{355-532}$ and $PLDR_{532}$ were also retrieved in order to describe the mean size and shape of the aerosol particles. For this case, we observe a decrease in both parameters in the region of interest. A decrease in $AE_{355-532\ nm}$ ($\sim$0.4 km^{-1}) means an increase in the predominance of larger particles and a decrease of the $PLDR_{532\ nm}$ ($\sim$0.13 km^{-1}) is related to particles becoming more spherical. This correlation between $AE_{355-532}$ and PLDR has been observed in previous studies associated to hygroscopic growth (Granados-Muñoz et al., 2015; Haarig et al., 2017).

In order to determine the origin of the aerosol particles over the analysed layer, we present a horizontal wind speed and direction and vertical wind analysis from DL data. The 10 min resolved horizontal wind direction time series (Fig. 6.5.b) indicate that from 18:00 to 21:00 UTC the wind over IISTA-CEAMA station mainly came from the North-West, within the region of interest (1.5 to 2.4 km asl) with relative low horizontal wind velocity (up to 6 m/s) (Fig. 6.5.a), which means that aerosol particles were being transported from the same direction, likely coming from the same source, at relative low horizontal velocity.

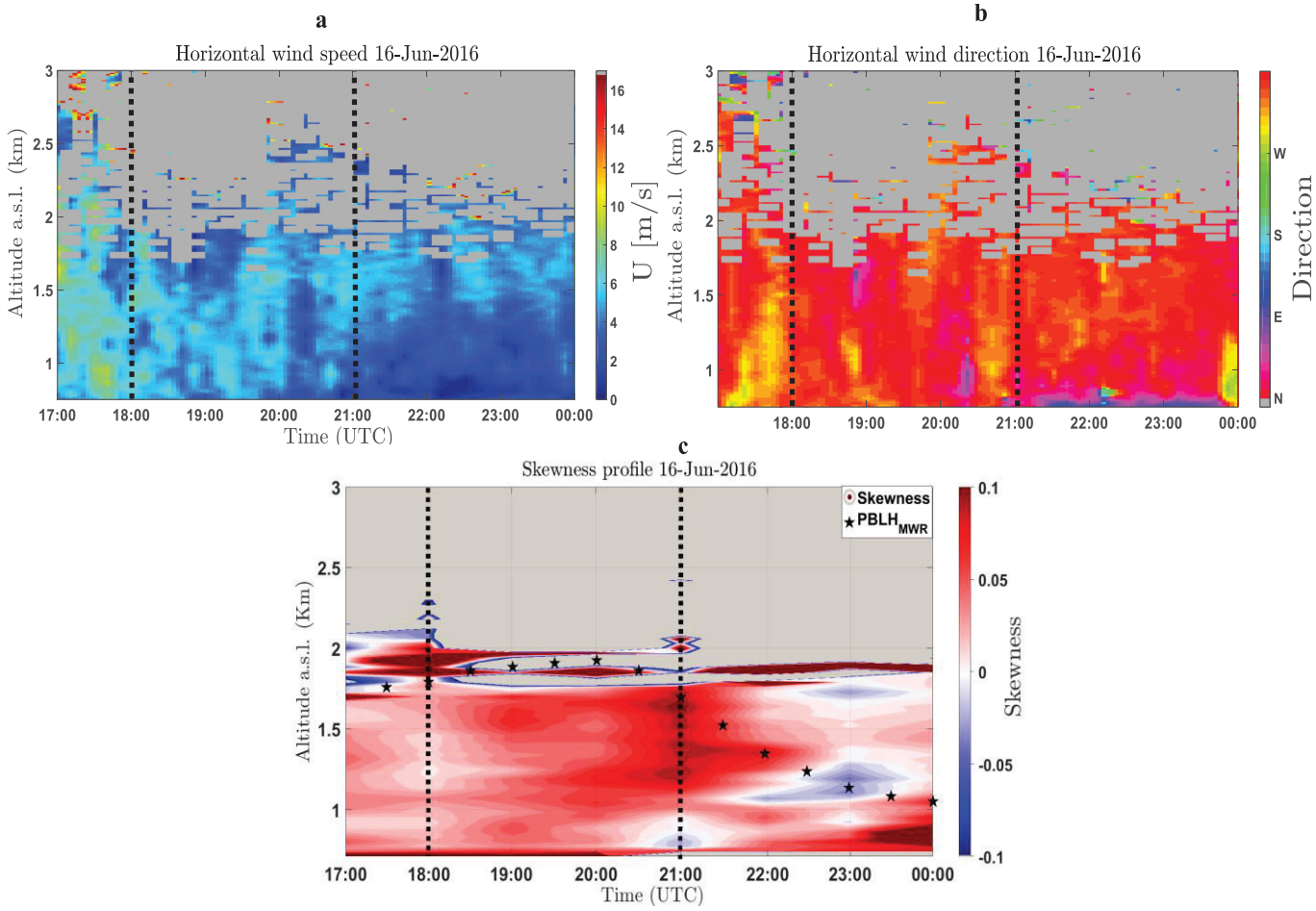

Figure 6.5. *Time series of (a) horizontal wind velocity, (b) horizontal wind direction, and (c) skewness retrieved from Doppler turbulence calculations for 16th June 2016 at 20:30 to 21:00 UTC. The ABLH retrieved from MWR is presented in black stars.*

A turbulence analysis was also performed to reinforce the fact that vertical fluxes within the aerosol column are associated to increases of RCS observed in Fig. 6.3. The aerosol RCS increases in a region where RH increases as we see in Fig. 6.4, thus we associate this increases in RCS with water uptake by aerosols inside this atmospheric column. The vertical wind velocity can be statistically studied to obtain the higher

moments of the velocity distribution (O'Connor et al., 2010; Moreira et al., 2018a). This statistical analysis is deeply developed for turbulence studies. Here the third moment of the frequency distribution (skewness) (Fig. 6.5c) represents the direction of the convection (positive skewness is associated to predominance of upward wind velocity whereas negative skewness means predominance of downward wind) in the region of interest. Supporting this analysis, the black stars represent the calculation of the atmospheric boundary layer height (ABLH, Fig. 6.5c) obtained from the MWR data by using the combination of parcel and gradient methods in convective and stable atmospheric conditions (Holzworth, 1964; Moreira et al., 2018b).

In this case, close to 21:00 UTC (Fig. 6.5.c), the particles tend to ascend into the column, as indicated by positive values reached in the skewness linked with highly convective movement. The PBLH reach its maximum at 15:00 UTC (2.5 km asl) but after 16:00 UTC the weakening of convection tends to decrease the ABLH, keeping the ABLH around 2 km asl until 21:00 UTC. All this wind information might be interpreted as transported particles coming from the same direction at relative low horizontal velocities, suggesting that aerosol source is not changing and new aerosol particles are not being advected into the studied layer. The turbulence analysis allows us to support that vertical wind movement within the layer of interest drives to well mixing processes during the analysed time interval.

The 6-day backward trajectories were calculated at three different heights (0.9, 1.5 and 1.9 km agl), which were selected within the region of interest in order to guarantee the height-independency of the air masses pathway. The three air masses came from North America, crossing the Atlantic Ocean, reaching the continental platform through Portugal and then advected to Granada reaching the station at 21:00 UTC (not shown here). This information supports the horizontal wind analysis performed before.

6.2.2 $f_{\beta}^{\lambda}(RH)$ measured and retrieved by combining in-situ data and Mie theory

The humidogram presented in Fig. 6.6 shows the measured $f_{\beta}^{\lambda}(RH)$ at 355 and 532 nm as a function of RH between 1.5 and 2.4 km asl retrieved by using the lidar data. The calculated $f_{\beta}^{\lambda}(RH)$ was obtained by using the measured chemical composition and size distribution at SNS station (2.5 km asl) as inputs to the Mie model (Fig. 6.6). The humidogram exhibits a monotonic positive increase at both wavelengths, for RH between

78 and 98%. The RH $_{ref}$ = 78 % was selected as the lowest RH value into the evaluated column, and this same RH was used as reference for the Mie calculation in order to make both calculations comparable.

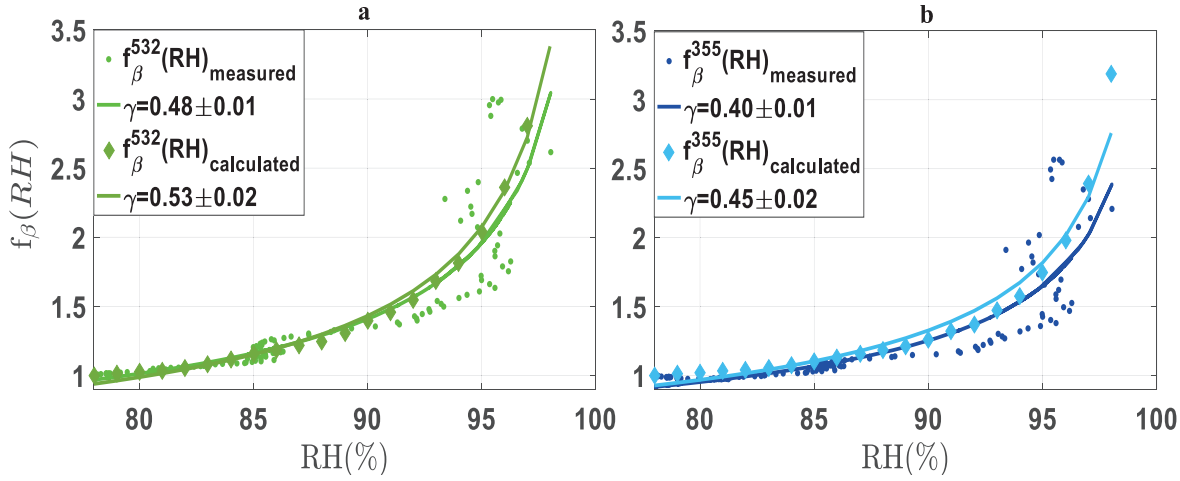

Figure 6.6. *Humidograms calculated (a) at 532 nm and (b) at 355 nm, within 1.5 to 2.4 km asl aerosol layer from the RL+MWR measurements and calculated using Mie theory and measured chemical composition and size distribution at 2.5 km asl. At RH_{ref} = 78 % was used for both methods.*

During the hygroscopic growth event at SNS station, the mean aerosol particle number size distribution shows two main peaks at around 35 and 115 nm, with most of the aerosol in the fine mode (< 1 μm). The sub-micron mass concentration measured with ACSM indicates high concentration of organic particles during daytime (from 12:00 to 17:00 UTC), with values around 7 μg/m^3 at 15:00 UTC. OA concentrations decreased slowly to values around 3.0 μg/m^3 at 00:00 UTC. In particular, during the hygroscopic growth case under study (from 20:00 to 21:00 UTC) the aerosol composition was mainly made up of organic particles (62%) followed by sulphate (24%), nitrate (10%), ammonia (2%) and black carbon (2%). Thus, the predominant aerosol studied during the event is a combination of smoke and urban polluted aerosol.

The assumption about the aerosol type is supported by the relatively high sulphate concentration observed at SNS and the results already discussed above (lidar properties and backward trajectories analyses). This chemical composition with high predominance of organic particles is consistent with the γ values obtained with the RL+MWR method. Fernández et al. (2015) reported a similar γ^{532} value of 0.59 in Cabauw (Netherlands) associated with high concentration of organic particles while they observed a significantly

larger γ^{532} of 0.88 associated with marine particles. Lower values are reported by Lv et al. (2017) in one of their case studies ($\gamma^{532} = 0.24$ and $\gamma^{355} = 0.12$) in Xinzhou (China) associated with the presence of dust particles. Although the behaviour of the backscatter coefficient at enhanced RH is expected to differ from the scattering coefficient, a qualitative comparison can be performed due to the scarcity of backscatter-related γ values in the literature. For example, using in-situ techniques, Zieger et al. (2015) reported a low scattering enhancement of boreal aerosol in Hyytiälä (Finland) ($\gamma^{525} = 0.25$) related to the high contribution of organic aerosols at this site that contribute to decrease the hygroscopic enhancement. At Cape Cod (USA), Titos et al. (2014) reported significantly lower γ values for polluted aerosols ($\gamma^{550} = 0.4 \pm 0.1$) compared with marine aerosols ($\gamma^{550} = 0.7 \pm 0.1$).

Calculated and measured values of f_β^λ (RH) are compared in Table 6.2 and Figure 6.6. In general, there is a good agreement between measured and calculated hygroscopicity parameters. For both wavelengths, slightly higher values are predicted by the model compared with the measurements, especially at RH > 90% where the differences are higher than at RH < 90%. The values retrieved from the RL measurements are $f_\beta^{355}(85\%) = 1.07 \pm 0.03$ and $f_\beta^{532}(85\%) = 1.20 \pm 0.03$ and with Mie theory are $f_\beta^{355}(85\%) = 1.10 \pm 0.01$ and $f_\beta^{532}(85\%) = 1.15 \pm 0.01$. The good agreement found in this analysis is confirmed by the low relative differences observed (lower than 4 %). The hygroscopic growth parameter (γ) shows also good agreement between the measured ($\gamma^{532} = 0.48 \pm 0.01$ and $\gamma^{355} = 0.40 \pm 0.01$) and the calculated ones using Mie theory ($\gamma^{532} = 0.53 \pm 0.02$ and $\gamma^{355} = 0.45 \pm 0.02$), with relative differences of 9 % at 532 nm and 11 % at 355 nm. The good agreement between the measured and theoretical backscatter enhancement factor evidences the robustness of the proposed method for hygroscopic studies in a systematic manner.

Table 6.2. *Results obtained for hygroscopic case on 16th June 2016, evaluated with RL (IISTA-CEAMA station) and in-situ (SNS) stations.*

	Measured	**Calculated**
RH_{ref} [%]	78	78
$f_{\beta}^{532}(85\%)$	1.20	1.15
$f_{\beta}^{355}(85\%)$	1.07	1.10
γ^{532}	0.48 ±_0.01 (R^2=0.84)	0.53 ±_0.02 (R^2 = 0.94)
γ^{355}	0.40 ±_0.01(R^2=0.65)	0.45 ±_0.02 (R^2 = 0.93)

The principal sources of error in the comparison between calculated and measured data are associated with the method for the retrieval of RH profiles, as well as the errors associated with theoretical Mie calculation mainly by the assumption of g (RH) based on the chemical composition. Finally, the horizontal distance between stations could also lead to differences in the comparison. The uncertainties affecting our study are the result of the contributions of the particle backscatter uncertainties and experimental uncertainties associated to determination of the backscatter enhancement factor, thus further studies should center their efforts on this research field to constraint the range of uncertainty.

In addition, the multi-wavelength results lead us to see a clear spectral dependence on γ (λ). The efficiency due to changes in f_{β}^{λ} (RH) associated to β is stronger at 532 nm than at 355 nm, finding that $f_{\beta}^{532}(85\%) = 1.20 > f_{\beta}^{355}(85\%) = 1.07$. This is also seen on the gamma parameter ($\gamma^{532} = 0.48 \pm 0.01 > \gamma^{355} = 0.40 \pm 0.01$, with correlations of 0.84 and 0.65, respectively). This spectral dependency has also been reported in Kotchenruther et al. (1999) for in-situ measurements at 450, 550 and 700 nm, obtaining increasing enhancement factors with wavelength, and in Zieger et al. (2013), where the same behaviour is observed for marine aerosols. As it is reported in Haarig et al. (2017) the enhancement factor dependency with wavelength suggests that larger wavelengths have an enhancement factor larger than short ones which in fact was also evidenced on this work.

6.3 Summary for chapter 6

Results obtained in the vertical evaluation of aerosol hygroscopic growth cases by combining RL, RS and MWR. The methodology proposed for calculating RH profiles by combining calibrated r (z) from RL and temperature profiles from MWR has been used in this work to study aerosol vertical hygroscopicity. With this method, a way to retrieve RH profiles without the necessity of co-located RS is presented at IISTA-CEAMA station. In order to validate this methodology, hygroscopic growth cases which use RS data were selected. The relative differences on the f_β^λ (RH) obtained using the RH profiles from the RS and from the combination of RL and MWR measurements were calculated, finding relative differences below 11 % on f_β (85%). The relative differences on γ were below 5 %, supporting the fact that this methodology is valid for aerosol hygroscopicity studies.

Aerosol hygroscopic growth observed during SLOPE I field campaign (16th June 2016, 20:30 to 21:00 UTC) was studied by means of particle backscatter coefficient retrieved from the EARLINET multi-wavelength RL, backscatter-related-Ångström exponent ($AE_{355-532}$) and particle linear depolarization ratio ($PLDR_{532}$) as optical properties and the combined RL+MWR RH profiles. Stability analysis confirmed good mixing conditions in the atmospheric layer studied. In addition, DL data analysis allowed us to evaluate the vertical profiles of horizontal wind velocity and direction. Thus, it was concluded that particles came mainly from the North-West region of Granada at low velocities. Furthermore, the skewness analysis let infer that particles presented an upward movement during the 30 min evaluated period within the column of interest. These results were confirmed by ABLH calculations from MWR data. From the experimental data from RL, values of $f_\beta^{355}(85\%) = 1.07 \pm 0.03$ and $f_\beta^{532}(85\%) = 1.20 \pm 0.03$ at $RH_{ref} = 78\,\%$ were obtained within the evaluated column and also $\gamma^{532} = 0.47 \pm 0.01$ (R^2=0.84) and $\gamma^{355} = 0.40 \pm 0.01$ (R^2 = 0.65), which were in agreement with the literature.

For the study case during SLOPE I the results was validated against Mie simulations with experimental data from SNS data obtaining a good agreement between the values retrieved with RL ($f_\beta^{355}(85\%) = 1.07$ and $f_\beta^{532}(85\%) = 1.20$) and Mie theory ($f_\beta^{355}(85\%) = 1.10$ and $f_\beta^{532}(85\%) = 1.15$) reaching relative differences lower than 4% when taking the calculated data as a reference. It was also found good agreement

between the measured hygroscopic growth parameter (γ) ($\gamma^{532} = 0.48 \pm 0.01$ and $\gamma^{355} = 0.40 \pm 0.01$) and the calculated one ($\gamma^{532} = 0.53 \pm 0.02$ and $\gamma^{355} = 0.45 \pm 0.02$), with relative differences up to 9 % at 532 nm and 11 % at 355 nm, taking the calculated data as reference.

These results show that under favorable atmospheric conditions (vertical homogeneity, consistent aerosol sources and low horizontal velocity within the analyzed layer) and in the absence of advected air masses into the evaluated column, the hygroscopic behavior of the particles evaluated by remote sensing at IISTA-CEAMA station is in accordance with that evaluated for those particles transported to SNS. It is evidenced the potentiality of combining $r(z)$ from RL and temperature from MWR to retrieve RH profiles with high temporal/spatial resolution to analyze aerosol hygroscopic growth. Results obtained here will expand the database of hygroscopic growth cases studied with remote sensing techniques, showing the high advantage to have aerosol properties and RH within the same atmospheric column.

6.4 References

Fernández, A. J, Apituley, A., Veselovskii, I.Suvorina, A., Henzing, J., Pujadas., M ad Artiñano., B.: Study of aerosol hygroscopic events over Cabauw experimental site for atmospheric research (CESAR) using the multi-wavelength Raman lidar Caeli, Atmos. Env., 120, 484-498, 2015.

Granados-Muñoz M.J, Navas-Guzmán, F., Bravo-Aranda, J. A., Guerrero-Rascado, J. L., Lyamani, H., Valenzuela, A., Titos, G., Fernández-Gálvez, J., and Alados-Arboledas, L.: hygroscopic growth of atmospheric aerosol particles based on active remote sensing and radiosounding measurements: selected cases in southeastern Spain. Atmos. Meas. Tech., 8, 705–718, 2015.

Haaring, M., Ansmann, A., Gasteiger, J., Kandler, K., Althausen, D., Baars, H., Farrell, A.: Dry versus wet marine particle optical properties: RH dependence of depolarization ratio, backscatter and extinction from multi-wavelength lidar measurements during SALTRACE. Atmos. Chem. Phys., doi.org/10.5194/acp-17-14199-2017, 2017.

Holzworth, G. C.: Estimates of mean maximum mixing depths in the contiguous United States, Mon. Weather Rev., 92, 235–242, 1964.

Kotchenruther, R. A., Hobbs, P. V., and Hegg, D. A.: Humidification factors for atmospheric aerosols off the mid-Atlantic coast of the United States, Journal of Geophysical Research: Atmospheres, 104, 2239–2251, doi:10.1029/98JD01751, http://dx.doi.org/10.1029/98JD01751, 1999.

Lv M., Liu D., Li Z., Mao J., Sun Y., Wang Z., Wang Y. and Chenbo X.: hygroscopic growth of atmospheric aerosol particles based on lidar, radiosonde, and in situ measurements: case studies from the Xinzhou field campaign. Journal of quantitative spectroscopy & Raditive Transfer ,188 60-70, 2017.

Moreira, G. A., Guerrero-Rascado, J. L., Bravo-Aranda, J. A., Benavent-Oltra, J. A., Ortiz-Amezcua, P., Román, R., Bedoya-Velásquez, A. E., Bravo-Aranda, J. A., Olmo-Reyes, F.J., Landulfo, E., Alados-Arboledas, L.: Analysisg the turbulence in the Planetary Boundary Layer by the synergic use of remote sensing systems: Doppler wind lidar and aerosol elastic lidar, Atmos. Chem. Phys. Discuss., https://doi.org/10.5194/acp-2018-276, 2018b.

Moreira, G. de A., Guerrero-Rascado, J. L., Bravo-Aranda, J. A., Benavent-Oltra, J. A., Ortiz-Amezcua, P., Román, R., Bedoya-Velásquez, A. E., Landulfo, E., and Alados-Arboledas, L. Study of the planetary boundary layer by microwave radiometer, elastic lidar and Doppler lidar estimations in Southern Iberian Peninsula, Atmospheric research, https://doi.org/10.1016/j.atmosres.2018.06.007, 213, 185-195, 2018a

Navas-Guzmán, F., Fernández-Gálvez, J., Granados-Muñoz, M.J, Guerrero-Rascado, J.L., Bravo-Aranda, J.A., and Alados-Arboledas, L.: Tropospheric wáter vapour and relative humidiyty profiles from lidar and microwave radiometry. Atmos. Meas. Tech., 7, 1201-1211, 2014.

O'Connor, E. J., Illingworth, J., Brooks, I. M., Westbrook, C. D., Hogan, R. J., Davies, F., Brooks, B. J.: A method for estimating the turbulent kinetic energy dissipation rate from vertical pointing Doppler lidar, and independent evaluation from ballon-borne in situ measurements, Journal of Atmospheric and Oceanic Technology, 27, 1652-1664, 2010.

Titos, G., Cazorla, A., Zieger, P., Andrews, E., Lyamani, H., Granados- Muñoz, M.J., Olmo, F.j and Alados-Arboledas, L.: Effect of hygroscopic growth on the aerosol light-scattering

coefficient: A review of measurements, techniques and error sources. Atmos. Env., 141, 494-507, 2016.

Titos, G., Jefferson, A., Sheridan, P. J., Andrews, E., Lyamani, H., Alados-Arboledas, L., and Ogren, J. A.: Aerosol light-scattering enhancement due to water uptake during the TCAP campaign, Atmos. Chem. Phys., 14, 7031–7043, doi:10.5194/acp-14-7031-7043,2014.

Zieger, P., Aalto, P.P., Aaltonen, V., Äijälä, M., Backman, J., Hong, J., Komppula, M., Krejci, R., Laborde, M., Lampilahti, J., de Leeuw, G., Pfüller, A., Rosati, B., Tesche, M., Tunved, P., Väänänen, R., Petäjä, T.: Low hygroscopic scattering enhancement of boreal aerosol and the implications for a columnar optical closure study. Atmos. Chem. Phys., 15, 7247-7267, 2015.

Zieger, P., Fierz-Schmidhauser, R., Weingartner, E., and Baltensperger, U.: Effects of relative humidity on aerosol light scattering: results from different European sites, Atmos. Chem. Phys., 13, 10 609–10 631, doi:10.5194/acp-13-10609-2013, http://www.atmos-chem-phys.net/13/10609/2013/, 2013.

7. Aerosol hygroscopic growth by combining co-located instrumented tower and ceilometer with on-line in situ

The results that will be showed were adapted from the following paper which is in discussion phase in Atmospheric Chemistry and Physics,

Bedoya-Velásquez, A.E., Titos, G., Bravo-Aranda, B.A., Haeffelin, M., Favez, O, Petit, J.E., Casquero-Vera, J.A, Olmo-Reyes, F.J., Montilla-Rosero, E., Hoyos, C.D., Alados-Arboledas, L., and Guerrero- Rascado. J.L.: Long-term aerosol optical hygroscopicity study at the ACTRIS SIRTA observatory: synergy between ceilometer and in-situ measurements. Atmospheric Chemistry and Physics Discussions, https://doi.org/10.5194/acp-2019-12, 2019.

An experimental setup to study aerosol hygroscopicity is proposed based on the temporal evolution of attenuated backscatter coefficients from a ceilometer co-located to an instrumented-tower equipped with meteorological sensors at different heights. This setup is used to analyse a 4.5-year database at the ACTRIS SIRTA observatory in Palaiseau (Paris, France, 48.713 º N, 2.208 ºE, 160 m asl). A strict criterion-based procedure has been established to identify hygroscopic growth cases using ancillary information such as on-line chemical composition, resulting in eight hygroscopic growth cases from a total of 107 potential cases. For these eight cases, the hygroscopic growth-related properties such as the attenuated backscatter enhancement factor $f_\beta\ (RH)$ and the hygroscopic growth parameter γ are evaluated. This study evidences that the hygroscopicity parameter γ is anti-correlated with the aerosol organic mass fraction while it shows a positive correlation with the aerosol inorganic mass fraction. Among inorganic species, nitrate exhibited the highest correlation.

This is the first time that hygroscopic enhancement factors are directly retrieved under ambient aerosols using remote-sensing techniques combined with on-line chemical

composition in situ measurements, in order to evaluate the role of the different aerosol species on aerosol hygroscopicity.

7.1 Two case studies of the methodology implementation

As an example of the methodology implementation, this section shows two of the final eight hygroscopic growth cases found in this study (Fig.7.1 and Fig.7.2). These examples correspond to 25 June 2013 from 07:17 to 10:17 UTC (case 3) and 17 May 2016 from 07:40 to 10:40 UTC (case 8), respectively. Figure 7.1a and Fig. 7.2a present the time-evolution of β, T, RH, q, W_s, W_d, dew point temperature T_d, and 1h-averaged aerosol chemical composition (BC, OA, NH_4^+, $NO_3^-$and SO_4^{2-}). Figure 7.1b and Fig. 7.2b show $f_\beta(RH)$ and $f_{PM1}(RH)$, and Fig. 7.1c and Fig. 7.2c contain a pie chart with the mean contribution of each chemical compound during the hygroscopic event.

These cases were selected in order to show two different situations found in this study (the other six cases are shown in appendix 1, Fig. A1.5-A1.10). Case 3 presents high contribution of OA (58 %) and SO_4^{2-}(15 %) with lower $\gamma = 0.5 \pm 0.4$, meanwhile case 8 shows a higher $\gamma = 0.9 \pm 0.6$ associated with higher contribution of SO_4^{2-} (19 %) and NH_4^+ (12 %) and lower OA contribution (46 %). Moreover, case 3 presented higher concentration of BC (17 %), than case 8 (8%), which in indeed is related with their lower γ.The shadowed region in Fig.7.1a and Fig.7.2a highlights the selected time-window in which β and RH simultaneously increases/decreases.

Once simultaneous monotonic decrease was seen for β and RH on case 3 and case 8, we apply the Hänel parameterization, obtaining the corresponding γ. During case 3 the predominant wind direction was NW with relatively low wind speed ($W_s = 2.5$ m/s), with some variability up to ΔW_s =24.5 % and $\Delta W_d = 33.9$ % and the chemical composition was relatively constant in most compounds over the time-window studied. The average chemical composition (Fig. 7.1c) pointed out to a high contribution of OA (58%) and BC (17%) particles and the total aerosol mass (PM_1) was almost constant during the hygroscopic case (from 7:15 to 10:15 UTC), showing no correlation with RH. The relative high presence of BC and OA (less hygroscopic compounds) may reduce the hygroscopicity properties obtaining a $f_\beta\ (RH = 85\ \%) = 1.7 \pm 0.2$ ($\gamma = 0.5 \pm 0.2$). These values are in agreement with rural and sub-urban values presented by Chen et al.

(2014) in Wuqing (China), Zieger et al. (2014) in Melpitz (Germany) and Titos et al. (2014a) in Granada (Spain) by using σ_{sp} (scattering coefficient) from in situ instrumentation. A detailed discussion of the origin of the air masses will be given in Sec. 7.2.

Case 8 presented predominant westerly wind with a relatively high mean wind speed (5 m/s) and low variability in both wind speed and wind direction (ΔW_s =20.7% and $\Delta W_d = 6.4\,\%$), with a slight increase in PM_1 with RH was observed (Fig. 7.2b). However, the enhancement of β is significantly higher with respect to the variation in PM_1. In fact, the RI remains within the selected range (RI= 0.60), denoting that most of the increase in attenuated backscatter coefficient can be attributed mostly to hygroscopic growth. The chemical composition during case 8 shows a predominance of OA (46 %) but also with important contribution of secondary inorganic compounds SO_4^{2-}(19 %) and NH_4^+(12 %), which are highly hygroscopic, and low contribution of BC (8%). This case exhibited higher aerosol hygroscopic properties than case 3 with $\gamma = 0.9 \pm 0.6$ and $f_\beta\ (RH = 85\,\%) = 2.5\ \pm 0.3$, this behaviour could be linked with the lower contribution of OA and BC, and higher contribution of inorganic aerosols (IA). Studies performed close to SIRTA site by Randriamiarisoa et al. (2006) at Saclay (France) reports a high $\gamma = 1.04$ and $f_\sigma\ (RH = 80\,\%) \sim 2.0$, linked to low contribution of OA and high IA contribution associated to anthropogenic and marine aerosols. In the following sections a wider description will be given of this case.

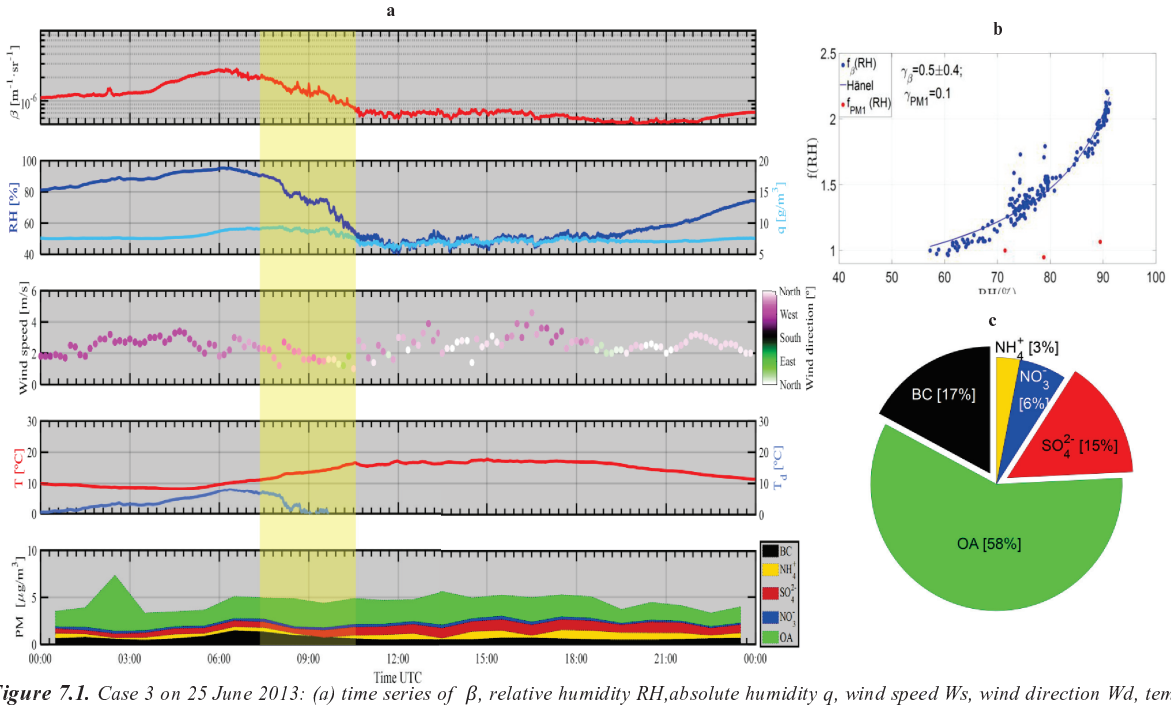

Figure 7.1. *Case 3 on 25 June 2013: (a) time series of β, relative humidity RH,absolute humidity q, wind speed Ws, wind direction Wd, temperature T, dew point temperature Td, and the PM_1 chemical species concentration according to the legend; (b) PM1-related $f_{PM1}(RH)$ and β-related $f_\beta(RH)$; and (c) pie chart of the chemical composition. (b) and (c) are measured for the hygroscopic event time-window. The highlighted region in yellow (from 07:17 to 10:17 UTC) represents the time-window where the aerosol hygroscopic growth is evaluated.*

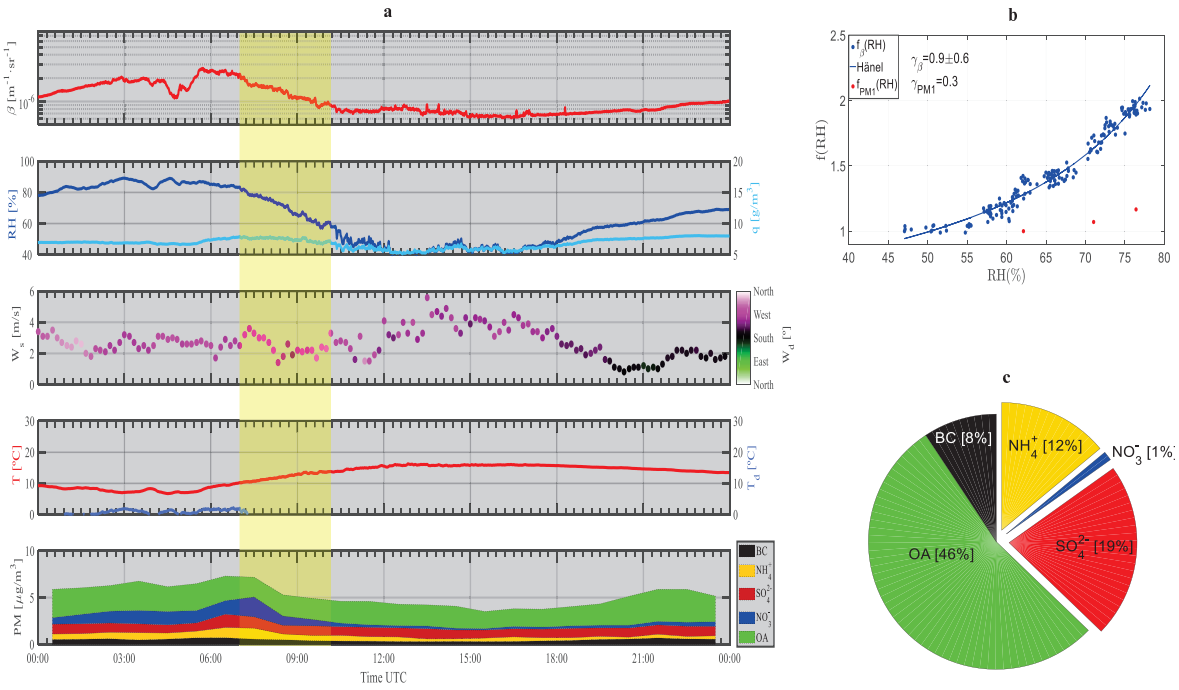

Figure 7.2. *As in Figure 7.1 but in case 8 on 17 May 2016 with the highlighted region from 07:40 to 10:40 UTC.*

7.2 Relationship between aerosol hygroscopicity properties and chemical composition

Table 7.1 reports the eight aerosol hygroscopic growth cases found with the described methodology applied to the 4.5-year database. Three cases were observed in spring (case 6, case 7 and case 8), presenting relatively high concentrations of SO_4^{2-} and NO_3^-, except for case 8 in which NH_4^+ was higher than NO_3^- (case 6 with 11 % and 21 %, respectively, case 7 with 36 % and 10 %, respectively, and case 8 with 19 % and 1 %, respectively, with high concentration of NH_4^+ (12%)). The high sulphate concentration in this season could be mainly related to the advection of air masses containing petrochemical and shipping emissions over this area and the typical increases of the nitrate and ammonia in spring that might be linked to the formation of particulate ammonium nitrate from road transport and agricultural gaseous emission under favorable meteorological conditions (Petit et al., 2015). Four cases were found in summer (case 1, case 3, case 4, and case 5), a period of the year commonly characterized by low wind speed at the ACTRIS SIRTA observatory (Petit et al., 2015), which reduces long-range transport of aerosol particles. Finally, a case was observed in September (case 2), showing the highest concentrations of PM_1 up to 10 μg/m^3 with major presence of OA (56 %), SO_4^{2-} (18 %) and NH_4^+ (15 %).

All these cases were found to occur between 6:00 and 14:00 UTC, when temperature monotonically increased with almost constant absolute humidity and, thus, RH decreased. In this area, OA is considered as a regional background component that dominates the PM_1 chemical composition, independent on the wind direction (Petit et al., 2015). According to previous studies, the higher concentrations of OA seen in this region might be associated to local influence, mainly in winter and autumn because of the wood-burning and road traffic pollution increase (e.g. Zhang et al., 2007; Putaud et al., 2010; Petit et al., 2014; Petit et al., 2015).

Table 7.1. *Enhancement factor (f_β (RH=85 %)) at RH_{ref} of the case and also extrapolated at RH_{ref}=40 %, γ, wind speed, variability of wind speed and wind direction and the index of variability between Δf_{PM1} and $\Delta f_\beta(RH)$. These variables are used for performing the analysis of the aerosol hygroscopic cases.*

	RH_{ref} [%]	β_{ref} $[m^{-1} \cdot sr^{-1}]$	f_β(RH=85)	f_β(RH=85/40)	γ	W_s [m/s]	ΔW_s [%]	ΔW_d [%]	RI
case 1: 29/072012	52.9	$6.2 \cdot 10^{-7}$	1.8±0.2	2.3 ±0.2	0.6±0.6	1	14.2	3.6 (W)	0.7
case 2: 02/09/2012	49.6	$6.6 \cdot 10^{-7}$	2.1±0.2	2.6±0.2	0.7±0.4	2.5	20.7	23.0 (NW)	0.7
case 3: 25/06/2013	57.3	$9.1 \cdot 10^{-7}$	1.7±0.2	2.0±0.2	0.5±0.4	2.5	24.5	33.9 (NW)	0.6
case 4: 28/07/2014	53.7	$5.1 \cdot 10^{-7}$	2.2±0.2	2.6±0.2	0.7±0.7	5	15.4	2.7 (W)	0.7
case 5: 17/08/2014	56.7	$4.1 \cdot 10^{-7}$	1.6±0.1	2.0±0.1	0.5±0.2	5.5	20.4	2.4 (SW)	0.8
case 6: 21/05/2015	55.1	$6.7 \cdot 10^{-7}$	2.4±0.2	3.0±0.2	0.7±0.4	2.5	18.5	4.4 (W)	0.5
case 7: 15/04/2016	51.6	$8.6 \cdot 10^{-7}$	2.3±0.3	3.0±0.3	0.8±0.3	6	10.9	1.7 (SW)	0.6
case 8: 17/05/2016	47.1	$7.2 \cdot 10^{-7}$	2.5±0.3	3.3±0.3	0.9±0.6	3	20.7	6.4 (W)	0.6

Cases 2, 4 and 6 present values similar to the ones reported by Fernández et al. (2015) of $f_\beta\ (RH = 85\ \%)$ = 2.04 with $\gamma = 0.589 \pm 0.007$ at Cabauw station (Netherlands) using lidar measurements, with presence of marine salt particles, ammonium nitrate and organic matter. The composition of these particles were linked to anthropogenic activities, oceanic air masses and agriculture over this region. In addition, Fernández et al. (2018) found values of $f_{\beta^{par}}\ (RH = 85\ \%)$ = 2.05 ($\gamma = 0.92 \pm 0.02$) for marine particles, based on measurements from the Madrid-CIEMAT station (Spain), that are close to the values of case 7 and case 8 of our study. These results from literature are consistent with the predominant chemical composition found in our study. Case 5 exhibited relatively high concentrations of SO_4^{2-} (20 %) and OA (58 %), leading to $f_\beta\ (RH = 85\ \%)$= 1.6 ± 0.1 ($\gamma = 0.5 \pm 0.2$). These values are comparable with those reported by Bedoya-Velásquez et al. (2018) for a mixture of anthropogenic and smoke particles at the IISTA-CEAMA station (Granada, Spain). Nevertheless, the values presented in this work are not fully comparable with previous remote sensing literature since the $f_\beta\ (RH)$ is derived at 910 nm whereas most enhancement factor values in the literature are reported at 532 nm. This fact would slightly change the efficiency of the backscatter cross sections of the aerosol particles analysed and, consequently, $f\ (RH = 85\ \%)$ may also change. Another difference with most of the remote sensing studies is that we have studied the temporal-change of the aerosol hygroscopicity (RH and β), while most studies investigate the change in the vertical coordinate.

Results obtained in this study can also be compared with previous studies based on in situ data, taking into account that the remote sensing and in situ techniques have different working principles and the intrinsic difference of the optical property investigated (attenuated backscatter coefficient and integrated scattering coefficient). Remote sensing operates under unmodified ambient conditions and the optical property evaluated is β, while hygroscopic growth in situ measurements are performed by controlling RH (starting mostly from RH_{ref} = 40%) and it uses σ_{sp} (scattering coefficient) as the optical property. Therefore, results between techniques are not directly comparable, thus to make the studies more comparable, we performed an extrapolation of $f_\beta\ (RH = 85)$ to 40 % like most of the in situ studies. The cases with lower hygroscopic properties in our study are case 1, case 3 and case 5, presenting $f_\beta\ (RH = 85/40\ \%) \sim 2.3 \pm 0.2, 2.0 \pm 0.2, 2.0 \pm 0.1$ with $\gamma = 0.6 \pm 0.6$, $\gamma = 0.5 \pm 0.4$ and $\gamma = 0.5 \pm 0.2$, respectively.

Similar values are reported for $f_\sigma\ (RH = 80/40\ \%)$ and $f_\sigma\ (RH = 85/40\ \%)$ at RH_{ref} = 40% by Sheridan et al. (2002) in the Indian Ocean, Titos et al. (2014b) in Cape Cod (US) and Chen et al. (2014) in Wuqing (China) for polluted, marine and mixed aerosols (urban and sub-urban), using in situ techniques. In this study, these three cases have low concentration of NO_3^- and relative higher concentrations of OA and BC, which pointed out an aerosol mixture with predominance of less hygroscopic particles than the other five cases. The cases 2, 4, 6, 7 and 8 presented similar values of $f_\beta\ (RH = 85/40\ \%)$ ranging from 2.6 to 3.3, while γ laid between $0.7 < \gamma < 0.9$, showing higher NO_3^- concentration, except for case 8 that exhibited higher concentration of SO_4^{2-} and NH_4^+. The $f_\beta\ (RH = 80\ \%)$ and γ values can be well compared to reported ones in in situ studies performed by Kotchenruther et al. (1999) (East Coast, US) and Randriamiarisoa et al. (2006) (Saclay, France), when they probed air masses influenced by anthropogenic and marine (clean and polluted) aerosols.

Table 7.2 presents the relationship between chemical composition and aerosol hygroscopicity. To this end, we have calculated the organic mass fraction (OMF) defined as OA mass concentration divided by the total mass concentration (PM_1) and inorganic mass fraction (IMF), calculated as the IA divided by the total mass concentration. Figure 7.3a shows an anti-correlation between OMF and γ (y= (-1.5 ± 0.1) x + (1.5 ± 0.1), R^2= 0.67), and Fig. 7.3b shows that IMF exhibits a positive correlation with γ (y= (1.2 ± 0.1) x + (0.2 ± 0.1), R^2= 0.42). In order to compare both hygroscopic properties ($f\ (RH = 85)$ and γ) with in situ literature, we also performed an extrapolation of the $f\ (RH = 85)$ to 40 %, like most of the in situ studies report, evidencing the same tendency for OMF (y= (-4.81 ± 0.04) x + (5.3 ± 0.1), R^2= 0.60) and IMF (y= (3.8 ± 0.1) x + (1.1 ± 0.1), R^2= 0.40), but with higher slopes. These results are in agreement with in situ studies that correlate the chemical composition with $f_\sigma\ (RH = 85/40)$ and γ, showing that aerosol hygroscopicity decreases as the relative contribution of OA in the total aerosol load increases (e.g. Kamilli et al., 2014; Zieger et al., 2014; Titos et al., 2014a; Zhang et al., 2015; Jefferson et al., 2017 and Chen et al., 2018).

The extrapolated slopes presented in Table 7.2 for $f_\beta\ (RH = 85/40\ \%)$ versus OMF and IMF are in good agreement with the results expected according to literature, showing a negative correlation of $f_\beta\ (RH = 85/40\ \%)$ with OMF and positive correlation with IMF. However, the slopes are substantially higher, than those reported

by Zieger et al. (2014) at Melpitz (Germany), slope of OMF with γ = -3.1 ± 0.1 and R^2= 0.57, and slope of IMF with γ = 2.2 ± 0.1 and R^2=0.57.

The same tendencies were also reported by Zhang et al. (2015) at Lin'an, China for OMF (slope of -1.20 and R^2 = 0.88) and for IMF (slope of 0.93 and R^2 = 0.57). Similarly, Titos et al. (2014a) reported a slope of -1.9 (R^2 = 0.74) at an urban site in Southern Spain. The in situ slope values are significantly lower compared with our results extrapolated to RH_{ref} = 40%. These differences are likely due to the different measurement techniques. Since this is the first remote sensing based hygroscopicity study including chemical composition, the comparison is not straightforward, although a clear tendency exists.

Table 7.2. *Linear fits of the extrapolated f_β (85/40) and γ versus the OMF and IMF for the eight cases and between OA, γ, and, the amount of IA (Fo). Fo is defined by (a) $Fo = OA/(OA + SO_4^{2-})$, (b) $Fo=OA/(OA + NO_3^-)$ and (c) $Fo=OA/(OA + SO_4^{2-} + NO_3^-)$.*

	SLOPE	INTERCEPT	R^2
f_β $(RH = 85/40)$ vs OMF	-4.81 ± 0.04	5.3± 0.1	0.60
f_β $(RH = 85/40)$ vs IMF	3.8 ± 0.1	1.1 ± 0.1	0.40
γ vs OMF	-1.5 ± 0.1	1.5 ± 0.1	0.67
γ vs IMF	1.2 ± 0.1	0.2 ± 0.1	0.42
γ vs Fo =$(OM/(OM + SO_4^{2-}))$	-0.7 ± 0.2	1.2 ± 0.2	0.18
γ vs Fo =$(OM/(OM + NO_3^-))$	-1.3 ± 0.1	1.8 ± 0.1	0.32
γ vs Fo = $(OM/(OM + SO_4^{2-} + NO_3^-))$	-1.2 ± 0.2	1.4 ± 0.1	0.40

To identify the inorganic compound that plays a stronger role in the aerosol hygroscopicity, we performed the calculation of the relative amount of OA ($F_o = C_{OA}/(C_{OA} + C_{IA})$) against γ, where C_{OA} and C_{IA} are the mass concentration of organic and inorganic aerosols, respectively. This calculation showed two different trends when NO_3^- and NH_4^+were added, reinforcing the negative correlation. The relative amount calculation of $F_o = OA/(OA + SO_4^{2-} + NO_3^-)$ with fitting line y= (-1.2± 0.2) Fo + (1.4± 0.1,) R^2=0.40 and $F_o = OA/(OA + SO_4^{2-} + NO_3^- + NH_4^+)$ y= (-1.3± 0.2) Fo + (1.4± 0.1,) R^2=0.51. After that, we performed an individual calculation each inorganic compound,

obtaining that $F_o = OA/(OA + SO_4^{2-})$ showed the lowest correlation coefficient ($y = (-0.7 \pm 0.2)\, Fo + (1.2 \pm 0.2)$, R^2=0.18), following by $F_o = OA/(OA + NH_4^+)$ with slightly high correlation (y=(- 1.1± 0.1) Fo + (1.6± 0.1,) R^2=0.26), and then the correlation increase for $F_o = OA/(OA + NO_3^-)$ (y=(- 1.3± 0.1) Fo + (1.8± 0.1), R^2=0.32), suggesting that NO_3^- is more determinant than other inorganic compounds at the ACTRIS SIRTA station as aerosol hygroscopic compound. The tendencies found can be compared with obtained in Zhang et al. (2015) at Lin'an, China, where it was found also that NO_3^- played a stronger role than SO_4^{2-}, pointed out that increases in NO_3^- would be associated to the decreases in $SO_4^{2-}$by the Shangai megacity influence. Despite this study presented lower correlations coefficients than Zhang's, data behaviour could suggest an influence from the Paris over Saclay region. This approach pointed out that larger data analysis should be performed studying the role of these compounds on aerosol hygroscopicity, in order contribute to future warnings about the control of the emissions of some organic compounds.

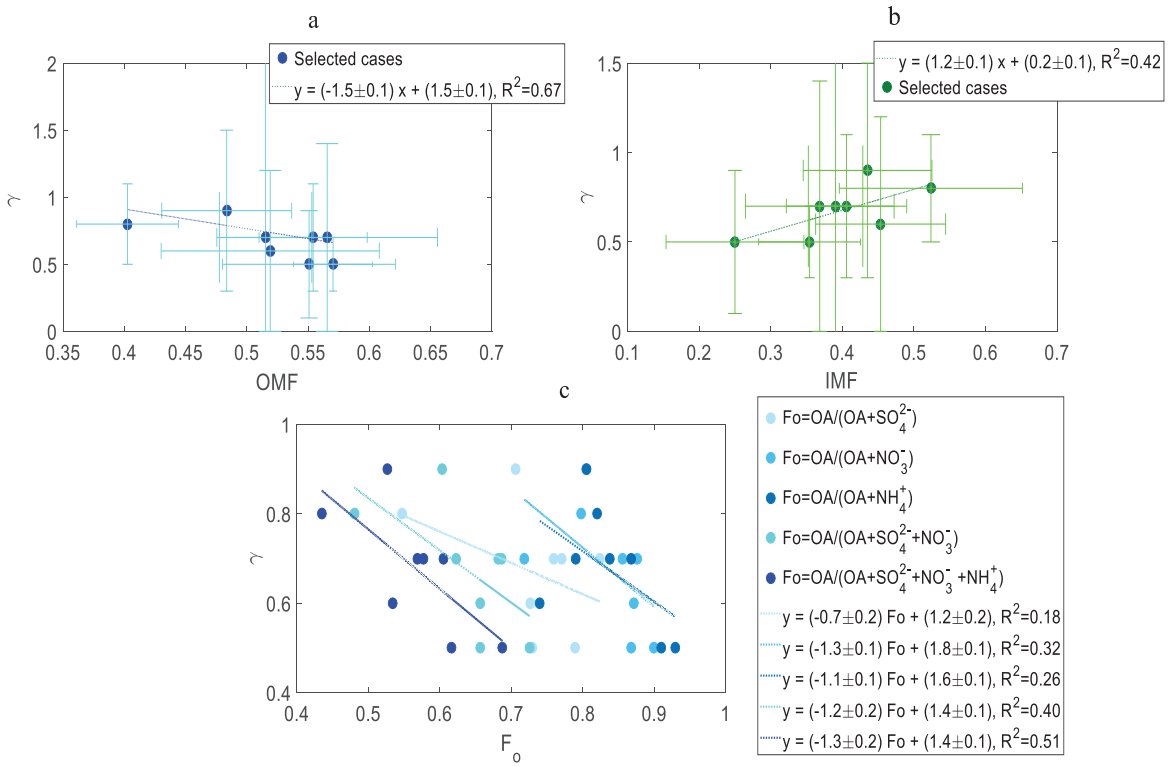

Figure 7.3. *Mass fraction and γ parameter correlation for the eight hygroscopic growth cases. (a) The OMF against γ, in blue dots with error bars and the dashed line is the linear fit, (b) the IMF and γ correlation in green dots with the respective error bars of the gamma and the OMF/IMF uncertainties, and the dashed line represents the linear fit, and (c) the correlations of the relative amount of OA and IA (Fo) versus γ. Fo is defined according to the legend.*

7.3 Summary of chapter 7

It was applied successfully the new methodology to investigate temporal aerosol hygroscopic growth based on a 4.5 dataset at the SIRTA observatory. To our knowledge, this is the first time that such a study is conducted under unmodified atmospheric conditions using long-term in situ and ceilometer instrumentation. 120 potential cases of hygroscopic growth were obtained with the methodology proposed here. From this cases database it was possible to clearly identify 8 cases fulfilling the strictly criteria defined to isolate events where the hygroscopic enhancement effect dominated over all other possible atmospheric processes.

The hygroscopic parameters were compared to on-line chemical composition retrievals. All cases presented a high concentration of OA, which is considered as a background component over the study region. Hygroscopic growth properties were compared with previous remote sensing and in situ studies, obtaining similar values for anthropogenic, polluted marine and mixed aerosols particles (urban and suburban areas).

The relationship between chemical composition and γ parameter was evaluated, obtaining that hygroscopicity backscattering enhancements linearly decrease as the contribution of organic aerosols increases. In this sense, the organic mass fraction (OMF) is anticorrelated with γ and f_β $(RH = 85/40)$, while IMF shows a positive correlation with γ and with f_β $(RH = 85/40)$. This relationship of OMF and IMF is in agreement with the literature although the magnitude of the trend varies among studies. These tendencies pointed out that the role of IA is determinant in the aerosol hygroscopic growth behavior. To determine the inorganic compound role, it was calculated the contribution of $SO_4^{2-}NO_3^-$, and NH_4^+ to the IA concentrations, obtaining that NO_3^- plays a more important role than other inorganic compounds in this hygroscopic growth studies at this region.

As we evaluate here the role of IA in aerosol hygroscopicity, it is important to conduct detailed studies on the role of OA as these components can be soluble. Thus, further research on this topic may focus on the role of the different OA fractions like hydrocarbon-like organic, peat and non-peat biomass burning and oxygenated organic aerosols in the aerosol hygroscopic properties. A relevant aspect is associated to the aerosol acidification that should be evaluated for determining the aged or fresh aerosols

role in the hygroscopic properties, and its impacts on OA. Finally, further investigation extending the study period is important in order to obtain statistically robust results over this region by using automatic remote sensors.

7.4 References

Bedoya-Velásquez, A. E., Navas-Guzmán, F., Granados-Muñoz, M. J., Titos, G., Román, R., Casquero-Vera, J. A., Ortiz-Amezcua, P., Benavent-Oltra, J. A., de Arruda Moreira, G., Montilla-Rosero, E., Hoyos, C. D., Artiñano, B., Coz, E., Olmo-Reyes, F. J., Alados-Arboledas, L., and Guerrero-Rascado, J. L.: Hygroscopic growth study in the framework of EARLINET during the SLOPE I campaign: synergy of remote sensing and in situ instrumentation, Atmos. Chem. Phys., 18, 7001-7017, https://doi.org/10.5194/acp-18-7001-2018, 2018.

Chen, J., Budisulistiorini, S. H., Miyakawa, T., Komazaki, Y., and Kuwata, M.: Secondary aerosol formation promotes water uptake by organic-rich wildfire haze particles in equatorial Asia, Atmos. Chem. Phys., 18, 7781-7798, https://doi.org/10.5194/acp-18-7781-2018, 2018.

Chen, J., Zhao, C.S., Ma, N., Yan, P.: Aerosol hygroscopicity parameter derived from the light scattering enhancement factor measurements in the North China Plain. Atmos. Chem. Phys. 14, 8105e8118, 2014.

Fernández, A. J, Apituley, A., Veselovskii, I.Suvorina, A., Henzing, J., Pujadas., M ad Artiñano., B.: Study of aerosol hygroscopic events over Cabauw experimental site for atmospheric research (CESAR) using the multi-wavelength Raman lidar Caeli, Atmos. Env., 120, 484-498, 2015.

Fernández, J., Molero, F., Becerril-Valle, M., Coz, E., Salvador, P., Artíñano, B., Pujadas, M.: Application of remote sensing techniques to study aerosol water vapour uptake in a real atmosphere, Atmos. Res., Volume 202, Pages 112-127, ISSN 0169-8095, https://doi.org/10.1016/j.atmosres.2017.11.020, 2018.

Jefferson, A., Hageman, D., Morrow, H., Mei, F., and Watson, T.: Seven years of aerosol scattering hygroscopic growth measurements from SGP: Factors influencing water uptake, J. Geophys. Res. Atmos., 122, doi:10.1002/2017JD026804, 2017.

Kamilli, K. A., Poulain, L., Held, A., Nowak, A., Birmili, W., and Wiedensohler, A.: Hygroscopic properties of the Paris urban aerosol in relation to its chemical composition, Atmos. Chem. Phys., 14, 737-749, https://doi.org/10.5194/acp-14-737-2014, 2014.

Kotchenruther, R. A., Hobbs, P. V., and Hegg, D. A.: Humidification factors for atmospheric aerosols off the mid-Atlantic coast of the United States, Journal of Geophysical Research: Atmospheres, 104, 2239–2251, doi:10.1029/98JD01751, http://dx.doi.org/10.1029/98JD01751, 1999.

Petit, J.-E., Favez, O., Sciare, J., Canonaco, F., Croteau, P., Mo P., MoP., Mo, P., MoWorsnop, D., and Leoz-Garziandia, E.: Submicron aerosol source apportionment of wintertime pollution in Paris, France by double positive matrix factorization (PMF2) using an aerosol chemical speciation monitor (ACSM) and a multi-wavelength Aethalometer, Atmos. Chem. Phys., 14, 13773-13787, 10.5194/acp-14-13773-2014, 2014.

Petit, J.-E., Favez, O., Sciare, J., Crenn, V., Sarda-Estda-, R., Bonnaire, N., Mo, N., MoN.Dupont, J. C., Haeffelin, M., and Leoz-Garziandia, E.: Two years of near real-time chemical composition of submicron aerosols in the region of Paris using an Aerosol Chemical Speciation Monitor (ACSM) and a multi-wavelength Aethalometer, Atmos. Chem. Phys., 15, 2985-3005, 10.5194/acp-15-2985-2015, 2015.

Putaud, J.-P., Van Dingenen, R., Alastuey, A., Bauer, H., Birmili, W., Cyrys, J., Flentje, H., Fuzzi, S., Gehrig, R., Hansson, H. C., Harrison, R. M., Herrmann, H., Hitzenberger, R. , Huglin, C., ¨ Jones, A. M., Kasper-Giebl, A., Kiss, G., Kousa, A., Kuhlbusch, T. A. J., Loschau, G., Maenhaut, W., Molnar, A., Moreno, T., ¨ Pekkanen, J., Perrino, C., Pitz, M., Puxbaum, H., Querol, X., Rodriguez, S., Salma, I., Schwarz, J., Smolik, J., Schneider, J., Spindler, G., ten Brink, H., Tursic, J., Viana, M., Wiedensohler, A., and Raes, F.: A European aerosol phenomenology – 3: Physical and chemical characteristics of particulate matter from 60 rural, urban, and kerbside sites across Europe, Atmos. Env., 44, 1308–1320, 2010.

Randriamiarisoa, H., Chazette, P., Couvert, P., Sanak, J., and Mégie, G.: Relative humidity impact on aerosol parameters in a Paris suburban area, Atmos. Chem. Phys., 6, 1389-1407, https://doi.org/10.5194/acp-6-1389-2006, 2006.

Sheridan, P.J., Jefferson, A., Ogren, J.A.: Spatial variability of submicrometer aerosol radiative properties over the Indian Ocean during INDOEX. J. Geophys. Res. 107 (D19), 8011, 2002.

Titos, G., Jefferson, A., Sheridan, P. J., Andrews, E., Lyamani, H., Alados-Arboledas, L., and Ogren, J. A.: Aerosol light-scattering enhancement due to water uptake during the TCAP campaign, Atmos. Chem. Phys., 14, 7031–7043, doi:10.5194/acp-14-7031-7043,2014b.

Titos, G., Lyamani, H., Cazorla, A., Sorribas, M., Foyo-Moreno, I., Wiedensohler, A., Alados-Arboledas, L.: Study of the relative humidity dependence of aerosol light-scattering in southern Spain. Tellus B 66, 24536. http://dx.doi.org/10.3402/tellusb.v66.24536, 2014a.

Zhang, L., Sun, J.Y., Shen, X.J., Zhang, Y.M., Che, H.C., Ma, Q.L., Zhang, Y.W., Zhang, X.Y., Ogren, J.A.: Observations of relative humidity effects on aerosol light scattering in the Yangtze River Delta of China. Atmos. Chem. Phys.15, 8439e8454. http://dx.doi.org/10.5194/acpd-15-2853-2015, 2015.

Zhang, Q., Jimenez, J. L., Canagaratna, M. R., Allan, J. D., Coe, H., Ulbrich, I., Alfarra, M. R., Takami, A., Middlebrook, A. M., Sun, Y. L., Dzepina, K., Dunlea, E., Docherty, K., DeCarlo, P. F., Salcedo, D., Onasch, T., Jayne, J. T., Miyoshi, T., Shimono, A., Hatakeyama, S., Takegawa, N., Kondo, Y., Schneider, J., Drewnick, F., Borrmann, S., Weimer, S., Demerjian, K., Williams, P., Bower, K., Bahreini, R., Cottrell, L., Griffin, R. J., Rautiainen, J., Sun, J. Y., Zhang, Y. M., and Worsnop, D. R.: Ubiquity and dominance of oxygenated species in organic aerosols in anthropogenically-influenced Northern Hemisphere midlatitudes, Geophys. Res. Lett., 34, L13801, doi:10.1029/2007GL029979, 2007.

Zieger, P., Fierz-Schmidhauser, R., Poulain, L., Müller, T., Birmili, W., Spindler, G., Wiedensohler, A., Baltensperger, U., Weingartner, E.: Influence of water uptake on the aerosol particle light scattering coefficients of the Central European aerosol. Tellus B 66, 22716. http://dx.doi.org/10.3402/tellusb.v66.22716, 2014

8. Hygroscopic growth studies by using automatic remote sensors (ceilometer and MWR): temporal and vertical evaluation at the SIATA-tower and the IISTA-CEAMA stations

This chapter is devoted to the study of potential aerosol hygroscopic growth cases by using automatic instrumentation (ceilometer and MWR), applying for the methodologies V2 and T2 (Fig. 4.1) for vertical and temporal evolution. Thus, the analysis here will involve a Vaisala ceilometer CL51 and a MP 3000 MWR at the SIATA-tower station, and a Jenoptik CHM-15k and a HATPRO MWR at the IISTA-CEAMA station. To this aim, the data pre-processing considering the different temporal and vertical resolutions must be taken into account (Sec. 4.2.3).

8.1 Hygroscopic growth analysis by remote sensors at the SIATA-tower station

The SIATA-tower station is located close to the center of the Aburra's Valley at Medellín. The topography of the region helps that aerosol particle can be suspended for long time periods under certain atmospheric conditions, mainly at altitude levels close to the ground (Fig. 8.1.). This fact favours the interactions between aerosol particles and water vapor in the valley. According to the results shown in sec. 5.2.1, this region presents a strong diurnal cycle in RH driven by temperature, where RH is really high in the early mornings and nights (up to 75 %), enhancing the possibility to water uptake by aerosol particles and, therefore, increasing the possibility hygroscopic growth to take place.

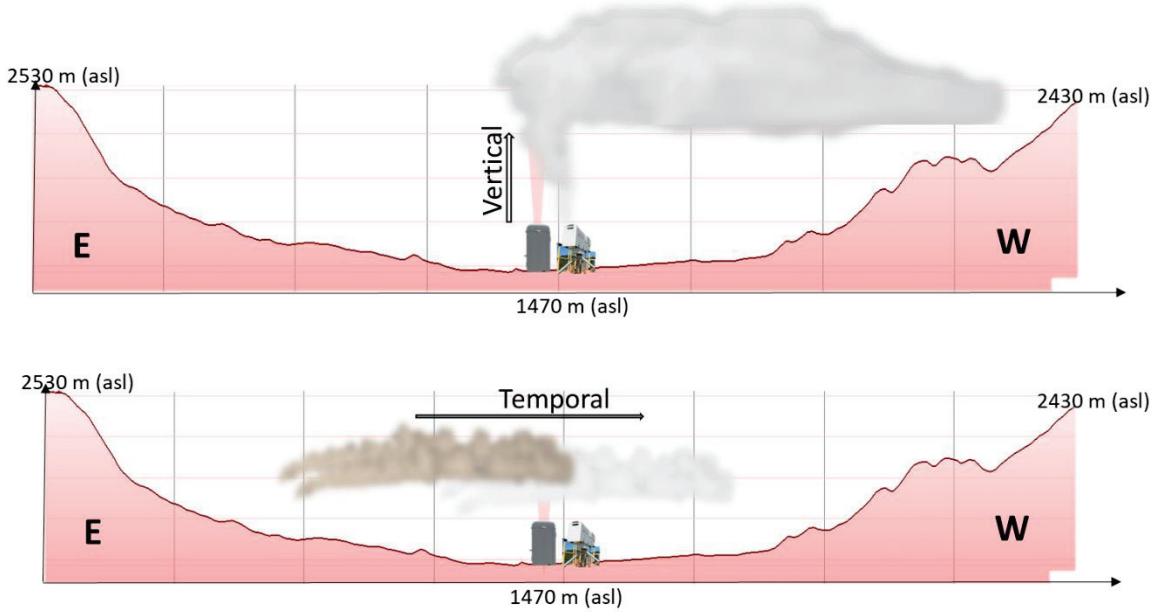

Figure 8.1. *Picture of the Aburra's Valley topography and the relative location of the SIATA-tower station. The vertical evolution (upper panel) and temporal evolution (bottom panel) setups for analysis are also included.*

Due to the amotpheric dynamicis of the valley and the error characterization of the MWR, we focus our attention in a region between surface and 1 km agl, where aerosol-water vapor interactions are expected to be predominant. The instrumentation setup involves a co-located Vaisala CL51 ceilometer and a MP 3000 MWR to perform an automatic process to identify aerosol hygroscopic growth phenomena (criteria I of the methodologies T2 and V2). The equipment is located on the roof-top of the SIATA-tower station (~ 60 m agl) together with a meteorological station and also is considered an in situ station measuring particulate matter concentrations ($PM_{2.5}$) away to the tower (up to 2 km in straight line) at estación sede Agronomía (25).

According to the results obtained in Sec. 5.9, the study on the MWR performance pointed out that, for the first kilometer, the accuracy and precision on temperature and RH were quite stables and showed low values (1.0 ± 0.4 °C and 2.0 ± 9.5 %), assuring the reduction of the error propagation.

8.1.1 Aerosol hygroscopicity temporal evolution at the SIATA-tower station

As it was established in sec.4.2.4, the temporal analysis for this station was performed by calculating the $I\beta^{att}$ from surface up to 600 m agl. This procedure is feasible because β^{att} is an intensive optical property and, therefore, the integral value is a measurement of the aerosol load in the air column evaluated. The criteria I and II of the methodology T2 were applied for a 3.5-year database (from January 2015 to August 2018), obtaining a total of 17 cases with simultaneous decreases of the $I\beta^{att}$ and RH (from now defined as DOWN cases) and 12 cases for simultaneous increases of theses variables (from now defined as UP cases).

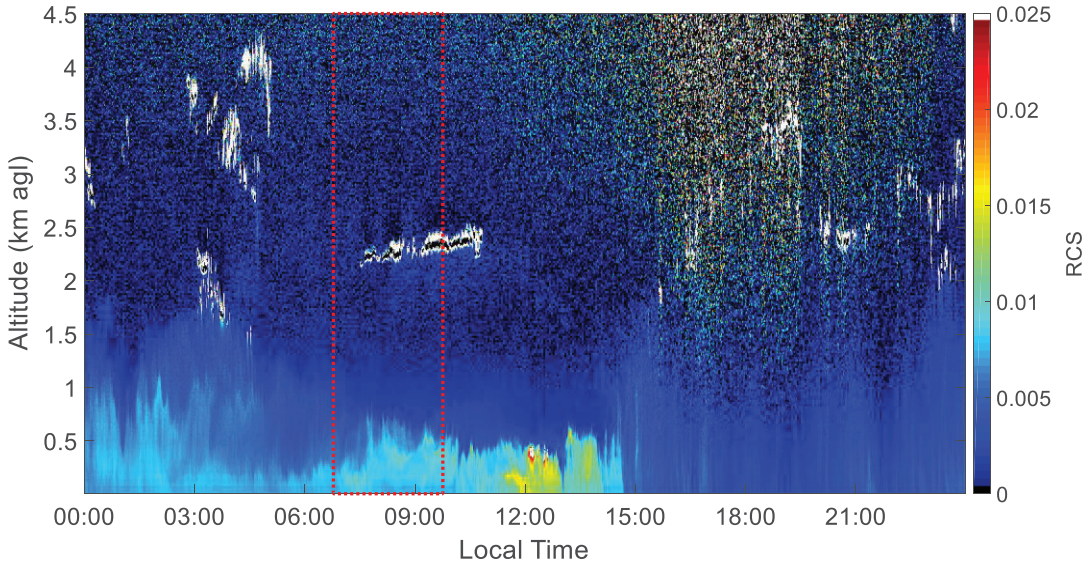

Figure 8.2. *Temporal evolution of range corrected signal at 915 nm obtained from the CL51 Vaisala ceilometer from 06:55 to 09:55LT on 28/07/2015 s. Black line highlights the time frame evaluated.*

Figure 8.2 shows the temporal evolution of RCS from the CL51 Vaisala ceilometer. This is used as ancillary information to identify the region where β^{att} is increasing or decreasing. In addition, $PM_{2.5}$ concentration is evaluated for this day (Fig. 8.3), in order to reinforce the fact that particle emission peaks observed are no influencing directly the behavior of the $I\beta^{att}$. Figure 8.3 shows two peaks related mostly to the vehicular emission, one in the morning (from 07:00 to 09:00 LT) and the other in the late afternoon (from 18:00 to 20:00 LT). The highlighted region refers to the temporal window where the hygroscopic event is evaluated, evidencing an increase in $PM_{2.5}$ concentration.

The important fact that Fig. 8.4 shows is that $I\beta^{att}$ and RH are decreasing in this region, which pointed out that $PM_{2.5}$ is independent of the $I\beta^{att}$.

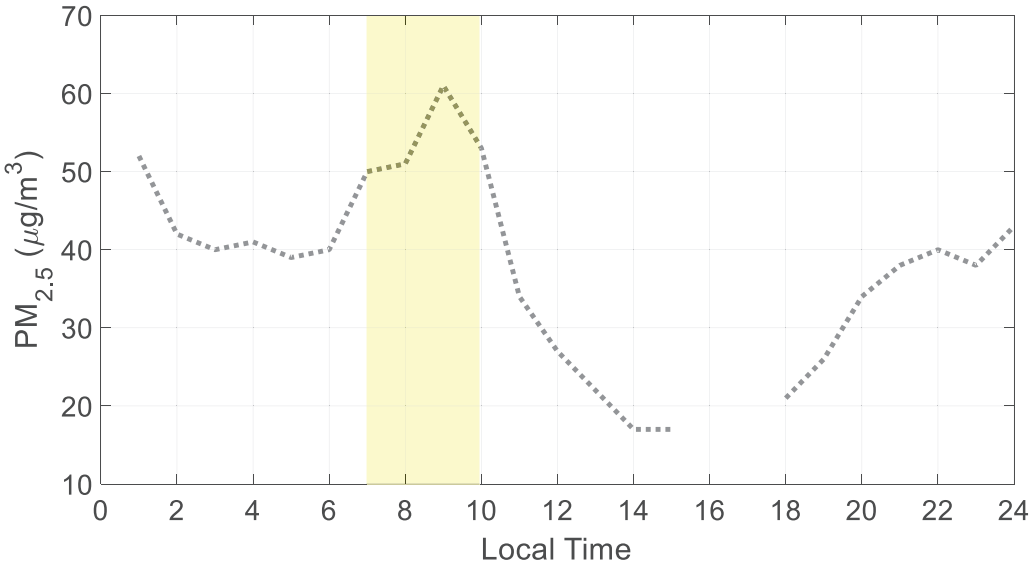

Figure 8.3 *$PM_{2.5}$ concentration on 28/07/2015. The highlighted region refers to the time window of the aerosol hygroscopic growth. The measurements are hourly-resolved.*

The atmospheric conditions were evlauted as it is shown in the example case on Fig. 8.4, the panel contains all variables studied to assure no advection of new air masses within the air volume studied. In this study, surface wind evaluation (Fig.9.4, the bottom plot of the panel) was performed in order to determine the variability of the W_d and W_s within the time window evaluated, because $I\beta^{att}$ can be driven by surface emissions, both vehicular and industrial ones. After this calculation, we established a limit for wind direction variability (ΔW_d < 40%). This condition, that helps to better isolate the hygroscopic growth cases, implied a reduction in the number of hygroscopic growth cases identified, leaving three UP cases and four DOWN cases, as it is reported in Table 8.1.

Figure 8.4 shows that $I\beta^{att}$ and RH are decreasing simultaneously in the time frame from 06:55 to 09:55 LT. Other important aspect is that $q(t)$ is stable during the evaluations, which is a good indicator of the negligible impact of the water absorption on the beta_att signal. The changes in $q(t)$ are lower than 0.02 kg/m^3 and, as it was demonstrated in Bedoya-Velásquez et al. (2019), the water absorption effect on β^{att}signal can be neglected (see appendix 1). $r\,(z)$ was relatively stable during the 3 hours evaluated, which pointed out no abrupt air masses changes at the ground level and

at 0.6 km. The no advection of different air masses is also supported by the fact of winds are always coming from NE at ~ 7 m/s.

The humidogram associated to the analyzed DOWN case I is presented on Fig. 9.5. The RH range is relatively high (up to 33.4%), which ensures enough range to study the aerosol hygroscopic growth, resulting in a Hänel parameterization given by $\gamma = 0.3 \pm 0.9$.

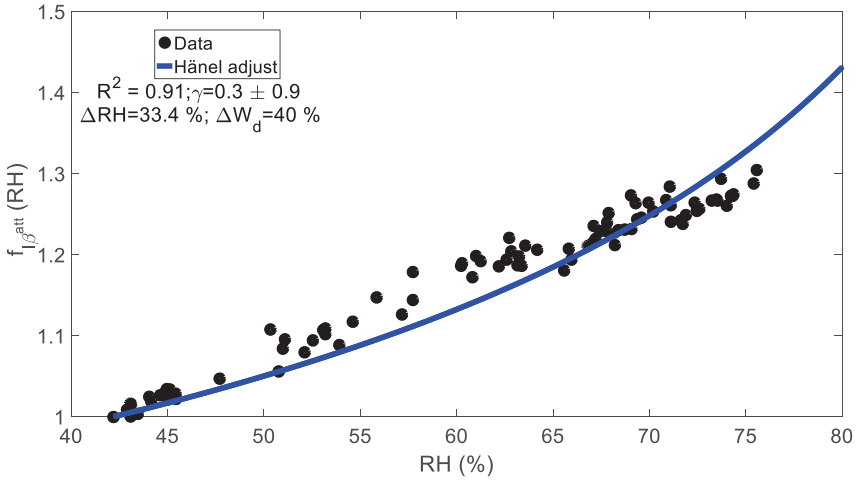

Figure 8.4 *Humidogram for DOWN case I obtained on 28/07/2015 from 06:55 to 09:55 LT.*

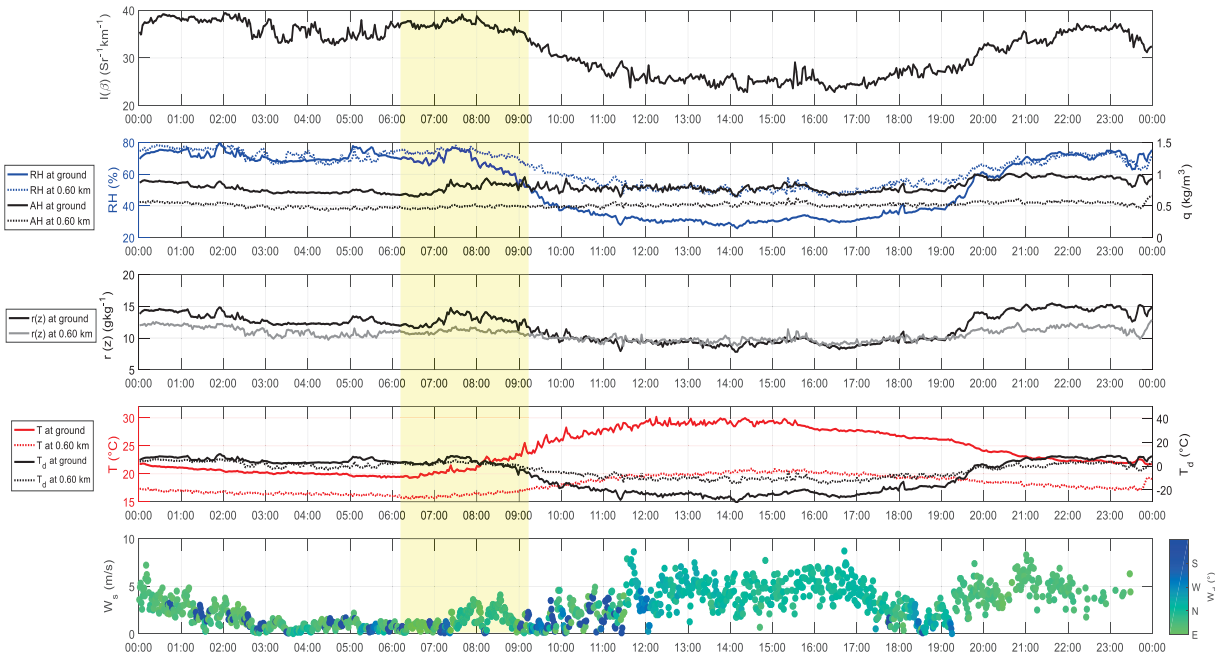

Figure 8.5. *Analysis of the aerosol hygroscopic case on 28/07/2015 from 06:55 to 09:55 LT. From up to down: the first panel is the $I\beta^{att}$; the second panel contains RH at ground level (blue solid line) and RH at 0.6 km agl (cyan solid line), and q at ground level (blue dotted line) and q at 0.6 km agl (cyan dotted line); the third panel refers to $r(z)$ at ground level (black line) and at 0.6 km agl (grey line); the fourth panel shows the surface wind speed and direction.*

The same procedure has been applied for the rest of the cases (temporal: UP and DOWN) presented in Table 8.1. UP cases were found in the late afternoon, between 17:00 to 20:00 h LT, and the DOWN cases in the morning from 06:00 to 12:00 h LT. The MWR diurnal analysis done in Sec. 5.2.1 evidenced that RH tends to increase in the mornigs when solar radiation is becoming strong and the contrary effect was seen in the aternoons. As it is shown in Fig. 8.10, the $PM_{2.5}$ diurnal cycle for the 3.5-year study evidences intense emission peaks in the intervals from 07:00 to 09:00 and slightly lower from 17:00 to 20:00 h LT, mainly associated to vehicular and industrial emissions. This fact could affect the hygroscopicity analysis by playing a crucial role on β^{att} time evolution signal, being stronger for the lowermost atmospheric region.

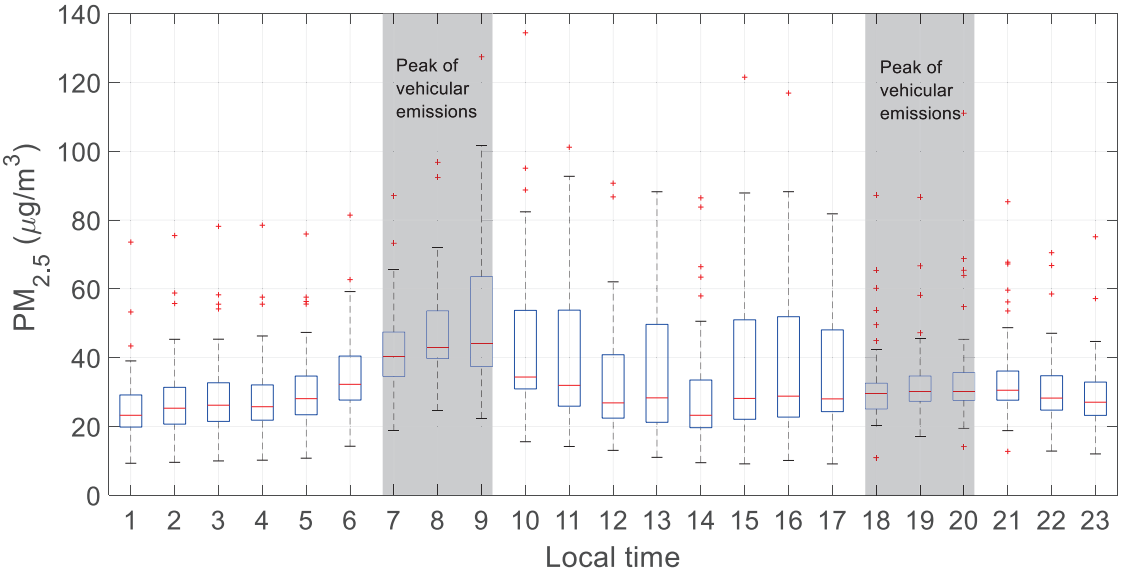

Figure 8.6. *$PM_{2.5}$ concentration diurnal cycle at Universidad Nacional de Colombia, Sede Medellín, Estación sede Agronomía (25) obtained from January 2015 to August 2018.*

Figure 8.6 presents the box plot for 3.5-years $PM_{2.5}$ measurements. The median is relatively well distributed around the 25 and 75 pecentiles from 00:00 to 07:00 LT and from 18:00 to 24:00 LT when solar radiation presence is weaker or null. The contrary behaviour is seen for boxes from 08:00 to 17:00, in which the median is close to 25 percentile of the dataset and boxes are larger, pointing out high data dispersion. It is also evidenced that in central hours of the day, median decreases because the atmosphere

presents high convection and a natural atmospheric cleaning effect is seen (median up to 21 μg/m^3).

Table 8.1*. Characterization of the different cases found from temporal evaluation criteria.*

Date	R^2	γ	$f\,(RH = 80\%)$	RH_{ref} [%]	ΔRH [%]	ΔW_d [%]	ΔW_s [%]
UP cases							
Case I: 16/07/2015 17:31	0.94	0.5 ± 0.2	1.7 ± 0.1	42.8	31.1	40 NE	27
Case II: 07/10/2015 17:00	0.98	0.5 ± 0.5	1.6 ± 0.3	41.4	30.4	30 NE	27
Case III: 23/06/2016 17:21	0.93	0.6 ± 0.4	1.0 ± 0.2	35.0	37.4	33 NE	32
DOWN cases							
Case I: 28/07/2015 06:55	0.91	0.3 ± 0.9	1.4 ± 0.8	42.2	33.4	40 NW	66
Case II: 09/05/2016 09:07	0.94	0.3 ± 0.9	1.2 ± 0.7	54.6	33.6	29 W	56
Case III: 27/10/2017 07:24	0.96	0.4 ± 0.3	1.4 ± 0.1	46.3	32.6	30 NW	57
Case IV: 13/04/2018 07:28	0.91	0.4 ± 0.3	1.5 ± 0.1	47.8	34.3	36 NW	60

Overall, all the potential hygroscopic growth cases for temporal evolution identified as UP cases presented a γ parameter between 0.50 to 0.60, which suggests a very similar aerosol composition advected mainly from the NE region. Regarding to DOWN cases γ was slightly lower then UP cases, ranging from 0.3 to 0.4 with NW wind directions prevailing.

8.1.2 Aerosol hygroscopicity vertical evolution

Following the same structure of the last section, the vertical evolution study of potential aerosol hygroscopic growth cases is performed, but taking into account the scheme shown in Fig. 8.1, the methodology V2 and the conditions proposed on section 4.2.3.

In order to apply the criteria I and II proposed on methodology, the temporal and vertical resolution of the ceilometer, i.e. 15 s and 10 m, respectively, were degraded to the MWR ones, i.e. 2 min and variable spatial resolution, respectively, by applying a ceilometer profile average around the MWR time/height. According to the relative high

humid conditions in Medellín, a relative extense database of potential cases was found (Fig. 8.7). Analysing the 3.5-year database, a total of 250 cases were found, corresponding to 90 cases (36%) at daytime and 160 cases (64%) at night-time. Also, May and August the favourable months to find potential cases, representing 16.8 % and 17.6 % of the total number of cases, respectively.

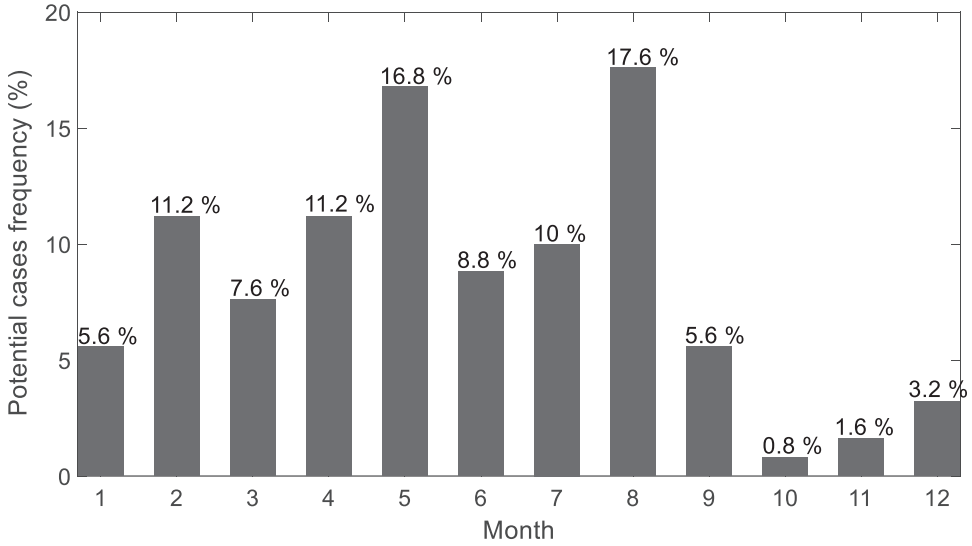

Figure 8.7. *Hourly distribution of potential hygroscopic growth cases in vertical evaluation, from a total of 250 potential cases found in the 3.5-year database.*

Figure 9.8 presents the atmospheric conditions evaluation for all the potential cases found in order to identify which of them fulfill the atmospheric criterion related to the low variability in vertical gradients of $\theta_v(z)$ and r(z). Fig. 9.8.a presents the scatter plot between vertical gradients of both variables, with medium correlation (R^2=0.55). The required atmospheric conditions of nearly constant $\theta_v(z)$ and r(z) happens mainly between 11:00 to 15:00 h LT (Fig. 9.8). The main drawback is that at this time window the atmospheric convection is too high.

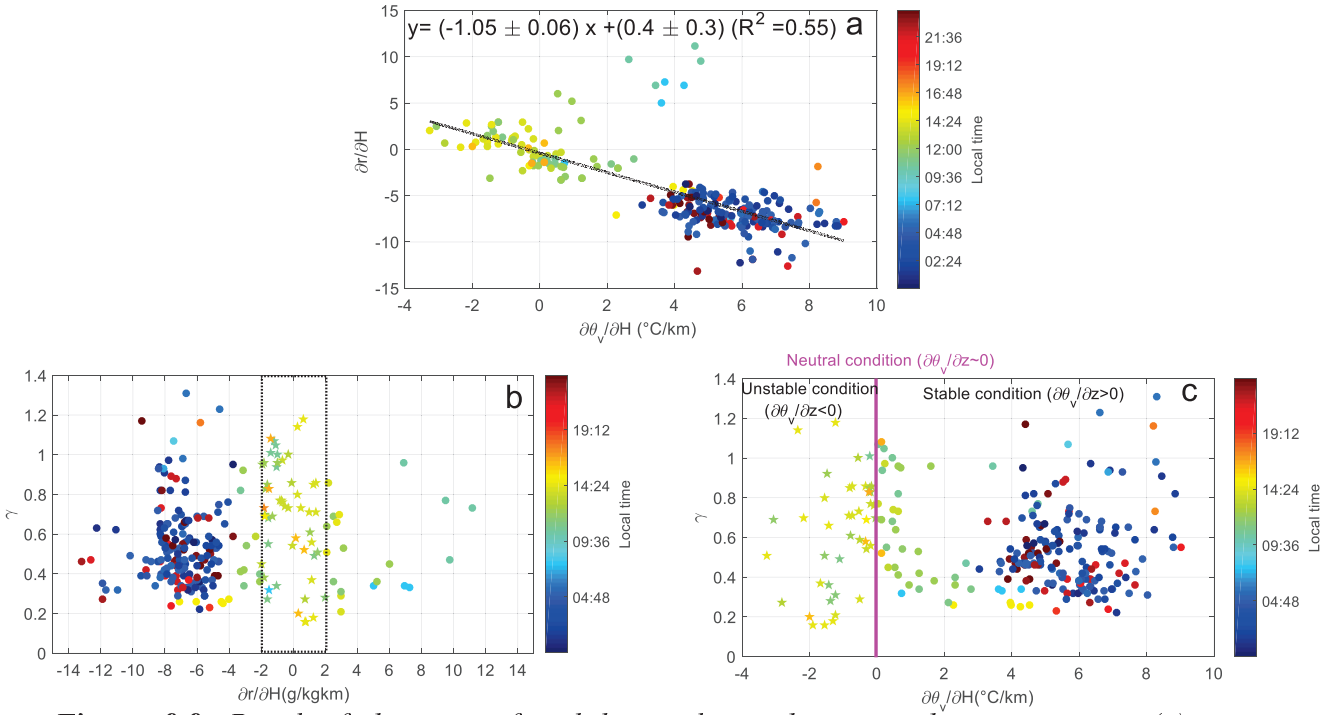

Figure 8.8. *Panel of the cases found by applying the atmospheric criterion. (a) correlation between gradient of r (z) and $\theta(z)$, (b) the γ versus $r(z)$ gradient and (c) refers to γ versus $\theta(z)$ gradient. Color bar refers to local time.*

The $\theta_v(z)$ and r(z) gradients calculation reinforced the last statement because cases close to neutral condition ($\theta_v(z)$ ~±1 °C/km) occur around midday (Fig. 8.8.b and 8.8.c). Thresholds for r (z) and $\theta_v(z)$ were defined according to literature (i.e. Veselovskii, et al., 2009; Granados-Muñoz, et al., 2015; Bedoya-Velásquez, et al., 2018a). The suggested procedure discarded cases when the atmosphere was unstable and stable, leaving only 11 cases. It is important to remark that, albeit under neutral conditions atmosphere remains homogeneous (i.e well mixed), the fact that almost all neutral cases are close 12:00 local time surely assures high convection, therefore aerosol may be being driven upwards within the air column enhancing the probability of new particles are injected, changing rapidly the hygroscopic scenario, leading it to the possible fake isolation of the phenomena. One possibility to fully demonstrate that under this strict criteria the aerosol particle size is increasing exclusively by up taking water is obtaining information about its vertical concentration, which for this study was not possible because of the absence of sun-photometric data.

Table 8.2. *Final database of aerosol hygroscopic potential cases in vertical evaluation*

γ	R^2	ΔRH [%]	z_i [km]	z_f [km]	$\partial\theta_v/\partial z$ [°C/km]	$\partial r/\partial z$ [°C g/kg·km]	Date
0.3±0.2	0.95	26.1	0.05	0.45	0.7	-1.5	02/01/2015 07:49
0.6±0.2	0.9	20.8	0.20	1.00	0.3	-1.6	13/01/2015 10:55
0.9±0.1	0.93	21.3	0.45	1.00	-0.3	2.1	19/01/2015 14:02
0.86±0.05	0.94	22.9	0.40	1.00	-0.7	1.4	19/01/2015 14:02
0.85±0.06	0.96	23.8	0.35	1.00	-0.8	1.2	19/01/2015 14:02
0.7±0.6	0.94	26.3	0.30	1.00	-0.8	0.9	19/01/2015 14:02
0.7±0.7	0.95	27.6	0.25	1.00	-0.7	1.4	19/01/2015 14:02
0.77±0.08	0.97	23.3	0.15	1.00	-0.2	-0.8	05/02/2015 13:46
0.7±0.1	0.96	20.6	0.30	1.00	0.6	-0.3	05/02/2015 13:46
0.7±0.1	0.96	21.3	0.25	1.00	0.5	-0.5	05/02/2015 13:46
0.77±0.08	0.97	22.3	0.20	1.00	0.03	-0.8	05/02/2015 13:46
1.0±0.7	0.98	21.9	0.15	1.00	-0.2	-1.4	27/02/2015 10:41
1.1±0.5	0.99	20.0	0.25	1.00	0.2	-1.1	27/02/2015 10:41
1.1±0.5	0.99	20.9	0.20	1.00	0.03	-1.2	27/02/2015 10:41
0.9±0.5	0.97	23	0.10	1.00	0.2	-1.1	27/02/2015 10:41
1.0±0.3	0.98	24.3	0.05	1.00	0.4	-1.0	27/02/2015 10:41
0.7±0.3	0.97	24.6	0.35	0.80	-0.6	0.5	27/02/2017 13:54
0.9±0.1	0.95	20.8	0.25	1.00	-0.2	-0.09	03/03/2017 12:57
1.0±0.1	0.99	26.6	0.10	0.40	0.6	-1.8	10/04/2017 12:02
1.0±0.3	0.99	30.9	0.05	0.45	0.7	-1.9	10/04/2017 12:02
0.6±0.2	0.97	21.2	0.60	1.00	-0.5	-2.3	24/02/2018 13:17
0.5±0.3	0.9	26.0	0.45	1.00	0.3	-2.0	24/02/2018 13:17
0.8±0.1	0.97	20.5	0.60	1.00	0.6	-3.3	25/02/2018 10:43
0.4±0.2	1	33.1	0.15	0.35	0.6	-3.3	05/04/2018 12:09
1.1±0.2	0.92	21.1	0.15	0.80	0.1	-1.4	29/06/2018 16:38

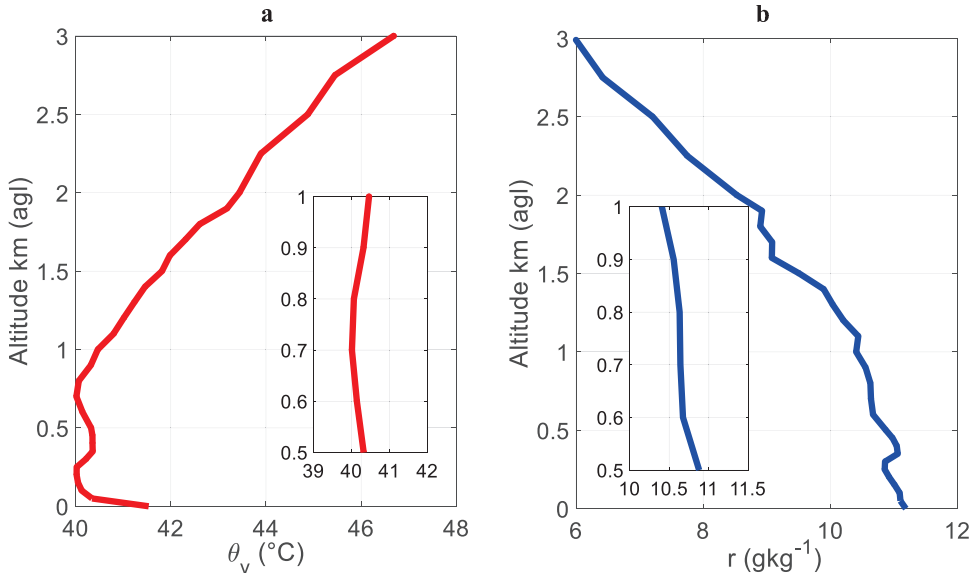

Figure 8.9. *Evaluation for case 05/02/2015 at 13:46 h LT: (a) virtual potential temperature, (b) water vapor mixing ratio.*

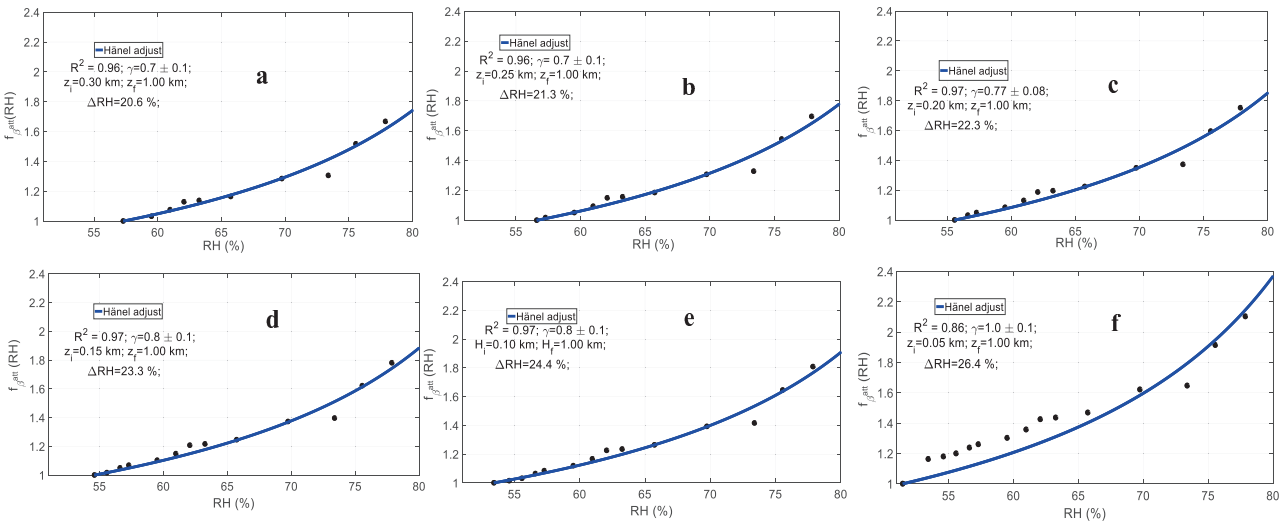

Figure 8.10. *Evaluation for case 05/02/2015 at 13:47 LT. In panel is presented the sequence of the enhancement factor: (a) from 0.30 km to 1 km, (b) from 0.25 km to 1 km, (c) from 0.20 km to 1 km, (d) from 0.15 km to 1 km, (e) from 0.10 km to 1 km and (f) from 0.05 km to 1 km.*

This vertical evolution methodology allows to elucidate not only hygroscopic properties of the aerosol particles within the air colum estudied, but it also helps to determine how is the local atmospheric dynamics involved. As an example Figure 8.9 shows the case on 05/02/2015 at 13:47 LT, presenting on Fig. 8.9 the condition of atmospheric homogenity for this day and it also showed how the vertical window operates on Fig. 8.10. Figure 8..9 is possible to see the low vertical variability of the $\theta_v(z)$ and

r(z), which becomes lower for $\theta_v(z)$ as the slidding vertical window increase the air volume evaluated. This result can be checked on table 8.2, where $\partial\theta_v/\partial z$=0.03 °C/km for 800 m air column evaluated (from 0.2 to 1.0 km agl), meanwhile, for 700 m it was $\partial\theta_v/\partial z$=0.64 °C/km from 0.3 to 1.0 km agl. This trend goes on from 700 to 900 m agl (from Fig. 8.10a to 8.10e). In Fig. 8.10f, the correlation becomes lower (R^2=0.86), the data at 50 m breaks the humidogram trend. Therefore, this last evaluation was skipt from the final results (it do not fulful condition i, Sec. 4.2.3).

Despite the statistics reported on Fig. 8.7, where the most probable months for potential hygroscopic growth are May and August, the final cases scrutinized on Table 8.2 occurred more in January and February. A possible explanation could be that frequently Medellín presents episodes of high contamination linked to the heavy rain period in May. This fact makes that β^{att}increases considerably and, as this city presents high RH levels along the year, the first two criteria of the methodology V2 could be easily satisfied. However, after atmospheric criterion (criterion III, methodology V2) is applied and ancillary information was used, most of the cases could be discarded.

Table 8.3. *Literature review of γ values obtained in this study, either for remote sensing and in situ at SIATA-tower station.*

Temporal evolution	Vertical evolution	γ obtained	Aerosol type	Remote sensing	In situ
UP case III	01/03/2015 10:55 24/02/2018 13:17	0.6	Nitrates, salt and Organic matter	Fernández et al., 2015. Cabaw station (Netherlands)	Sheridam et al., 2002. (Indian Ocean), Titos et al., 2014. (Cape Cod)
UP cases I and II	24/02/2018 13:17	0.5	Mixed anthropogenic and sulphate aerosols	Bedoya-Velásquez et al., 2018. IISTA-CEAMA (Spain)	Sheridam et al., 2002. Indian Ocean, Titos et al., 2014. Cape Cod and Chen et al., 2014. Wuqing (China)
DOWN cases III and IV	05/04/2018 12:09	0.4	Mixed urban	Bedoya-Velásquez et al., 2019. SIRTA observatory (Saclay, France)	Sheridam et al., 2002. Indian Ocean, Titos et al., 2014. Cape Cod and Chen et al., 2014. Wuqing (China)
DOWN cases I,II	02/01/2015 07:49	0.3	Coarse aerosol (i.e. Saharan dust, biomass burning)	Lv et al., 2017. Xinzhou (China)	Gassó et al., 2000. Eastern North Atlanctic Ocean, Pan et al., 2009. Xin'an (China), Titos et al., 2014a. Granada (Spain), Zhang et al., 2015. Lin'an (China) and Grass et al., 1999. Indonesia.
No cases found	19/01/2015 14:02 27/02/2015 10:41 03/03/2017 12:57 10/04/2017 12:02	> 0.9	Sulphates (fine mode) and marine (coarse mode)	Granados-Muñoz et al., 2015. Granada (Spain) and Veselovskii et al., 2009. Washington D.C.	Rault and Chazette, 2007. Paris, Gassó et al., 2000. Eastern North Atlantic Ocean. Randriamiarisoa et al., 2006. Saclay (Paris) and Titos et al., 2014b. Cape Cod
	19/01/2015 14:02 05/02/2015 13:46 27/02/2017 13:54	0.7 <γ <0.9	Anthropogenic and Salt particles	Fernández et al., 2018. CIEMAT station (Spain)	Kotchenruther et al., 1999. (East Coast, US) and Randriamiarisoa et al., 2006. Saclay (Paris)

This is the first time hygroscopic growth study carried out over this region. Therefore, no local references were available. However, it is possible to compare with other values reported in the literature according to aerosol type (Table 8.3). Studies using remote sensors (i.e. lidar/ceilometer) such as Fernández et al. (2015) at the Cabauw station (Netherlands) reported $\gamma = 0.589 \pm 0.007$ for salt particles, nitrate and organic matter similar to the UP case III from the temporal evaluation and it is also comparable with values found in vertical evaluation on 13/01/2015 at 10:55 and 24/02/2018 at 13:47 of this study (Table 8.2). Similar values are reported for in situ measurements in Sheridam et al. (2002) at the Indian Ocean and Titos et al. (2014) at Cape Cod.

UP cases I ($\gamma = 0.5 \pm 0.2$) and II ($\gamma = 0.5 \pm 0.5$) from the temporal analysis and on 24/02/2018 at 13:47 (Table 9.2) from the vertical study can be compared with Bedoya-Velásquez et al. (2018a) and Bedoya-Velásquez et al. (2019) remote sensing studies for mixed anthropogenic and sulphate aerosol particles at the IISTA-CEAMA station and polluted and mixed urban aerosol particles at the SIRTA observatory (Saclay, France). For the same ranges of γ, it is possible to compare with in-situ literature such as Sheridam et al. (2002) at the Indian Ocean, Titos et al. (2014a) at Cape Cod and Chen et al. (2014) at Wuqing (China).

DOWN cases I and II can be compared to remote sensing study at Xinzhou (China) by Lv et al. (2017), where $\gamma = 0.24$ at 532 nm pointed out the presence of coarse and relative hydrophobic particles like mineral dust. Making the same comparative, plenty of in situ studies can confirm these values obtained (e.g. Gassó et al., 2000; Pan et al., 2009; Titos et al., 2014b; Zhang et al., 2015; Grass et al., 1999). In this particular case, γ values are associated to organic material or particle emissions by vehicles/industries, particles that inhibit aerosol water uptake.

DOWN cases III and IV of temporal analysis and 05/04/2018 at 12:09 from the vertical evaluation presented values closer than reported by Bedoya-Velásquez et al. (2019) at the SIRTA observatory (Saclay, France). Finally, for $\gamma > 0.9$ obtained in the vertical evaluation (19/01/2015 14:02, 27/02/2015 10:41,03/03/2017 12:57 and 10/04/2017 12:02), it is possible to compare with remote sensing studies by Granados-Muñoz et al. (2015) at Granada (Spain) and Veselovskii et al. (2009) at Washington D.C, and in-situ investigations done by Rault and Chazette (2007) at Paris, Gassó et al. (2000) at Eastern North Atlantic Ocean, Randriamiarisoa et al. (2006) at Saclay (Paris) and Titos

et al. (2014a) at Cape Cod pointed, which pointed out that these values are related to the presence of sulphate and marine aerosols.

In addition, similar values for $0.7 < \gamma < 0.9$ on 19/01/2015 14:02, 05/02/2015 13:46 and 27/02/2017 13:54 were found for anthropogenic and salt particles in Fernández et al. (2018) at the CIEMAT station (Spain) by remote sensing, and in situ studies such as Kotchenruther et al. (1999) at (East Coast, US) and Randriamiarisoa et al. (2006) at Saclay (Paris) also reports close values for these γ values.

8.2 Hygroscopic growth analysis by remote sensors at the IISTA-CEAMA station

Figure 8.11 presents a scheme of the experiment developed in at the IISTA-CEAMA station, located at 680 m asl. Addittional details of the experimental site are given in Sec. 3.1, but here we focus on its topography that is also as complex as in Medellín, because of the role that Sierra Nevada mountain chain play. The presence of this high mountain chain modifies the wind dynamics of the region and it also influences other atmospheric variables such as temperature and RH and, it can act as a natural barrier to avoide that aerosol particles goes out of the city freely, deriving in some episodes of pollution. In addition, Saharan air masses are frequently advected over this city, causing a mixing with local emissions, increasing the levels of high aerosol load, too. RH is quite low over this area, which introduces some difficulties to chase aerosol hygroscopic growth cases (Bedoya-Velásquez et al., 2018b).

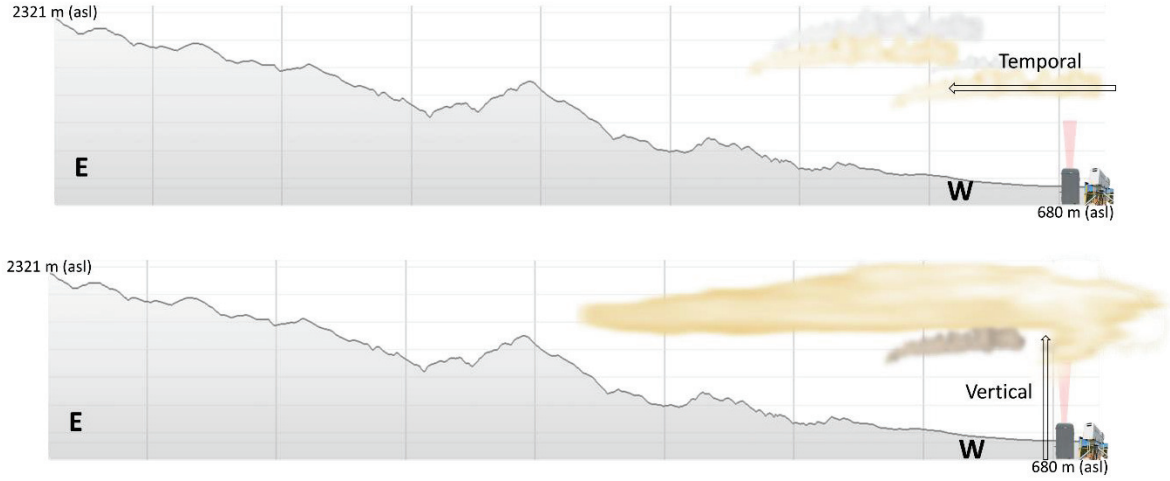

***Figure 8.101**. Picture of the Experimental setup for aerosol hygroscopic studies in the IISTA-CEAMA station in the context of Granadas's region topography: (a) temporal evolution and (b) vertical evolution.*

The instrumentation used involved a ceilometer Jenoptik CHM 15K and a RPG-HATPRO MWR, which are described in The main aspect to take into account is the relative high overlap of this ceilometer (above 550 m), which implies tointroduce some differences in the methodology of searching for aerosol hygroscopicity. Here, it is used each bin above 550 m up to 2000 m agl to study the phenomena in both, the vertical and temporal configurations. Co-located to these instruments are installed a DL, RL, SP and particle matter sizer (PM_{10}), which provide ancillary information. According to the error analysis of the MWR (Sec. 5.1.1), within the first 2 km agl the error in RH is lower than 10 % and, thus, the analysis will be performed up to this altitude.

After lots of analyses, which included to explore several temporal windows (i.e. 1, 3, 4 and 5 hours), to us different aerosol optical quantities (i.e. β^{att} and β_{par}) and to make flexible the criteria I and II of the methodology T2, our analyses based on temporal evolution do not return any satisfactory result. The main reasons are:

i. The Hänel fits were really poor ($R^2 < 0.75$), pointed out a mismatching on simultaneously increases/decreases in the optical property analyzed and RH.
ii. Many cases analyzed showed RH_{ref} below 30 % and the RH increase reached values up to 60%. This prevents to perform aerosol hygrscopic growth studies by the methodology

T2, due to both the dry conditions of the atmosphere in the lowermost atmospheric layers in Granada, but also for the error of the MWR RH retrievals.

iii. The high overlap of the ceilometer limits to explore the potential hygroscopic cases at altitudes above550 m, where the atmosphere becomes drier with altitude and, therefore, this fact reduces the possibilities to isolate aerosol hygroscopic cases.

8.2.1. Aerosol hygroscopicity vertical evolution

Vertical evolution analysis at IISTA-CEAMA station was also a hard task, mainly because the low RH and the constant presence of Saharan dust layers, causing aerosol multilayer events (inhomogeneous atmosphere). The evaluation of criterion I of the methodology V2 lead 16 potential cases ready to probe criterion II. In this first stage of the evaluation, all cases found were under UP conditions. Any DOWN case fulfilled the criterion I.

After applying criterion II, only six cases were defined as potential ones, two cases in March, two cases in May, one case in April and one case in November, meaning that spring was the most probable season to study aerosol hygroscopic growth. One factor associated to the high probability for finding potential cases on spring is the higher presence of vegetation, which increases the water vapor in the atmosphere by the evapotranspiration. As mentioned in Sec. 5.1.2.2, the increase of the IWV in Granada is observed in spring (Bedoya-Velásquez et al., 2018b). The finally selected six cases clearly revealed that that the more appropriateatmospheric conditions to study the phenomenon were during the interval from 12:00 to 16:00 UTC, because the atmosphere presented lower vertical gradients of $\theta_v(z)$ and r(z) (Table 8.4). In order to keep the number of potential cases, the criterion for r(z) was made more flexible than in the previous studies, accepting variability up to ± 3.5 g/kg·km, but only because the $\theta_v(z)$ criterion pointed out that atmosphere was well mixed.

Table 8.4 *Database of aerosol hygroscopic potential cases in vertical evaluation*

	γ	R^2	ΔRH [%]	z_i [km]	z_f [km]	$\partial\theta/\partial z$ [°C/km]	$\partial r/\partial z$ [° g/kgkm]	Date
Case I	0.44 ± 0.05	0.96	32.5	0.55	1.3	0.6	-3.5	17/03/2013 11:53
	0.44 ± 0.06	0.96	32.5	0.63	09	0.6	-3.4	17/03/2013 11:53
	0.39 ± 0.08	0.98	22.9	0.70	1.15	0.9	-2.7	17/03/2013 11:53
	0.53 ± 0.08	0.94	21.1	0.80	1	0.9	-2.3	17/03/2013 11:53
Case II	0.4± 0.1	0.96	20.1	0.70	1.15	0.8	-1.5	22/04/2013 13:32
Case III	0.2 ± 0.2	0.97	31.2	0.55	1.3	0.3	-1.1	03/05/2013 15:38
	0.2 ± 0.2	0.97	31.2	0.63	1.3	0.1	-0.9	03/05/2013 15:38
	0.2 ± 0.1	0.96	26.3	0.70	1.3	0.02	0.6	03/05/2013 15:38
	0.2 ± 0.1	0.96	21.4	0.55	1.3	-0.1	-0.3	03/05/2013 15:38
	0.2 ± 0.1	0.96	20.7	0.63	1.3	-0.2	0.1	03/05/2013 15:38
Case IV	0.6 ± 0.2	0.99	30.6	0.55	1.3	0.9	-2.7	04/05/2013 13:38
	0.6±0.1	0.99	25.5	0.63	1.3	0.7	-2.3	04/05/2013 13:38
	0.7±0.1	0.99	20.4	0.70	1.3	0.3	-2.2	04/05/2013 13:38
Case V	0.4±0.6	0.9	35.5	0.55	1.3	0.4	-2.1	22/11/2014 22:25
	0.5±0.7	0.95	26.4	0.63	1.3	0.3	-1.8	22/11/2014 22:25
	0.5±0.7	0.93	22.3	0.70	1.3	0.3	-1.5	22/11/2014 22:25
	0.5±0.8	0.91	21.1	0.80	1.3	0.3	-0.9	22/11/2014 22:25
	0.6±0.8	0.96	20	0.90	1.3	0.3	-0.4	22/11/2014 22:25
Case VI	1.2±0.3	0.96	20.6	0.55	1.3	0.5	-0.6	10/03/2016 13:45

To illustrate the analysis under this configuracion, Fig. 8.12 represents one selected case of the final six obtained. The sequence shows the effect of the vertical window selection over the aerosol hygroscopic properties. In Fig. 8.12a are evaluated seven bins (from 0.55 to 1.3 km) with RH_{ref} = 64.2 % with a relatively good range of RH (ΔRH=30.6 %), but from one bin to next, atmospheric properties may change rapidly. Particularly in this case, the gradient of $\theta_v(z)$ tends rapidly to zero (i.e. neutral stability condition), while the vertical window is shorter. The issue is that from one vertical window to another, the RH_{ref} changes, therefore modifying properties like γ.

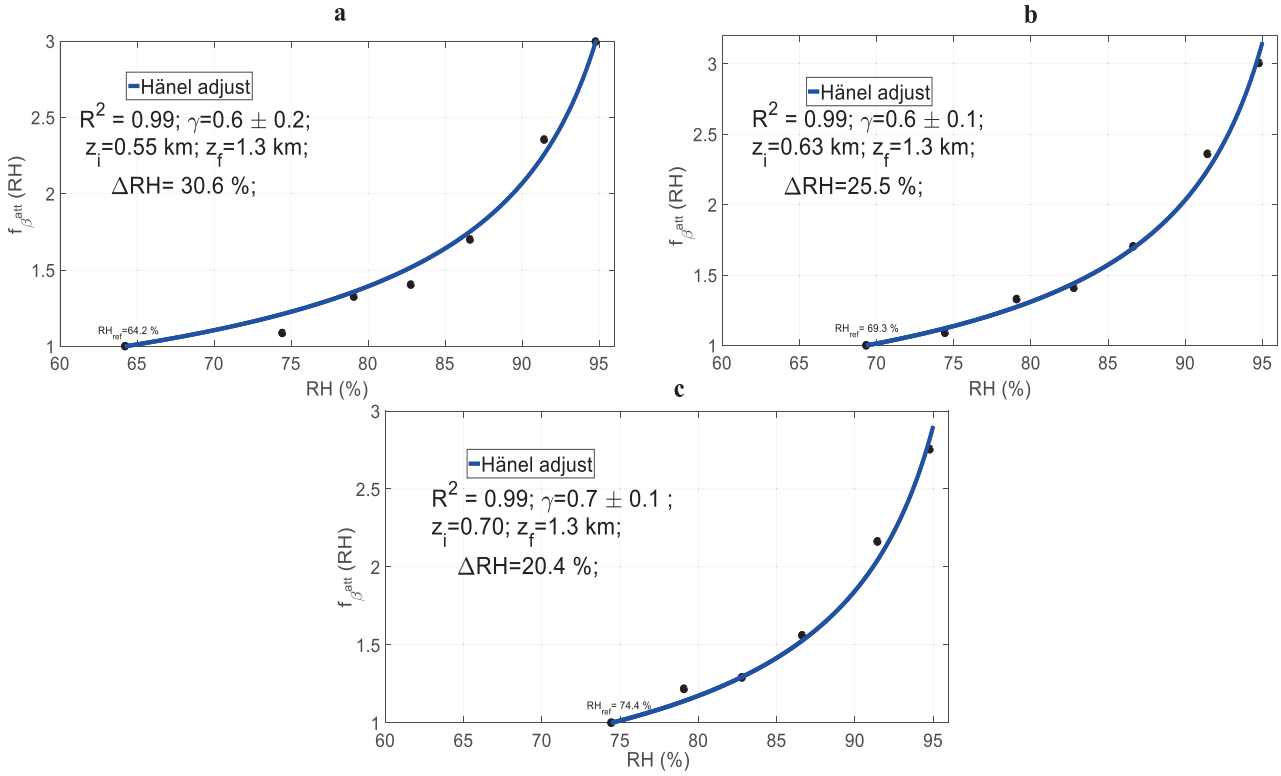

***Figure 8.11**. Humidograms on 04/05/2013 at 13:38 UTC for different vertical windows:(a) from 0.55 km to 1.3 km, (b) from 0.63 km to 1.3 km, and (c) from 0.70 km to 1.3 km.*

Figure 8.13 presents the RCS signal for each day labelled as potential case, where all panels show the same β^{att}increase in the region of interest, reinforcing the potentiality of these cases to be evaluated. This ancillary information also gives a clue of the increase and decreases of the β^{att}along the day. Additionally, 180-h back trajectories arriving to Granada at 680, 1500 and 3000 m agl have been retrieved by using Hysplit model, for completing the context of each case (Fig. 8.14). Figure. 8.14a indicates that cases I and VI contain aerosol long-range transported. For the case I air masses comes from Iceland

crossing the Atlantic Ocean and interacting with local aerosol, for this day SP data were no available, meanwhile for case VI, it was possible to see that air masses came from Canada crossing the Atlantic Ocean, then arriving directly to the Iberian Peninsula. In this day AOD_{500} was relatively low (~0.06), increased along the morning. $AE_{440\text{-}870}$ was close to 0.9 in the morning (at 07:00 UTC), but it decreased with time, reaching 0.7 at 11:00 UTC. This fact is a sign that aerosol particles were increasing their sizes. According to Duvovik et al. (2002) this might be strongly associated to biomass burning aerosol (single scattering albedo decreasing during the morning). For size distribution, the fine mode was predominant (< 0.1 μm) and the radius increased from 07:53 to 10:26 UTC, showing that particle concentration was always around 1 μm in accumulation mode.

Cases II, IV and V were related to local mixed aerosols with marine influence. For case II, the air masses came from Atlantic Ocean, crossing the South-East part of France and Mediterranean Sea before arriving to Granada. Case IV shows local aerosol mixed with marine, the air masses trajectories came from the Mediterranean Sea. Case V showed high influence from North African territory. The Case III is related with local aerosol particles mixed with marine air masses coming from the Mediterranean Sea.

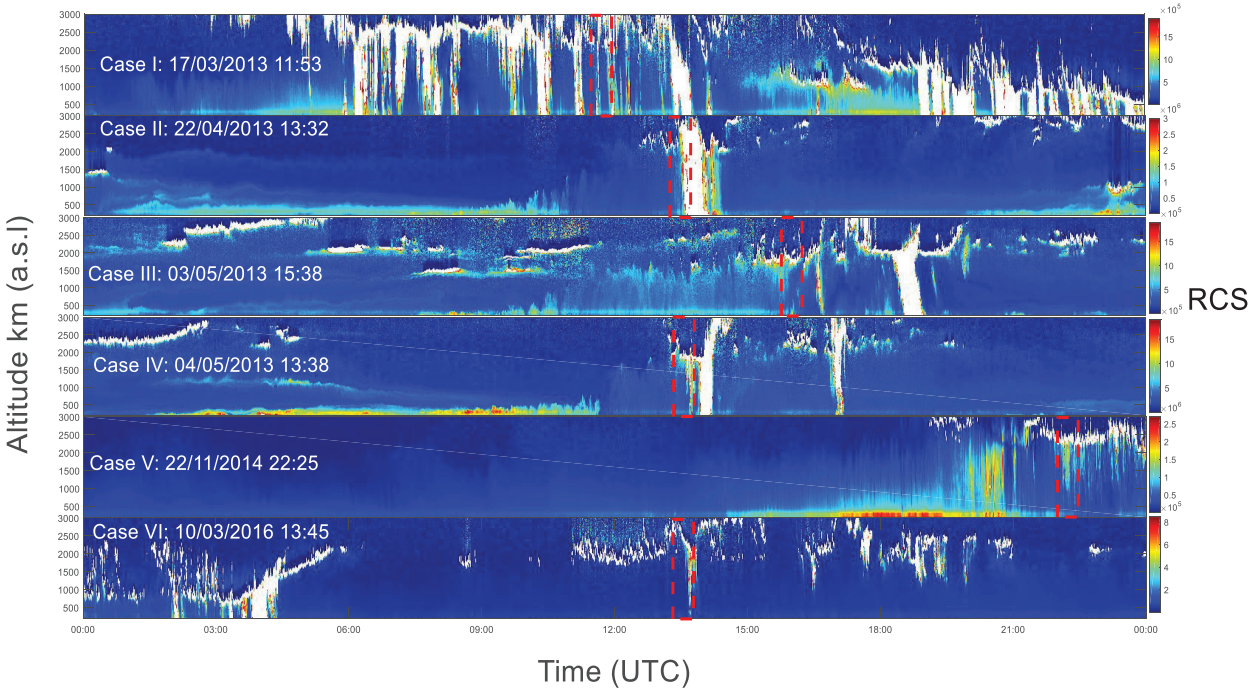

Figure 8.123. *Temporal serie of RCS at 1064 nm from the Jenoptik CHM 15K ceilometer for the six cases evaluated. The red dotted rectangle highlights the region studied.*

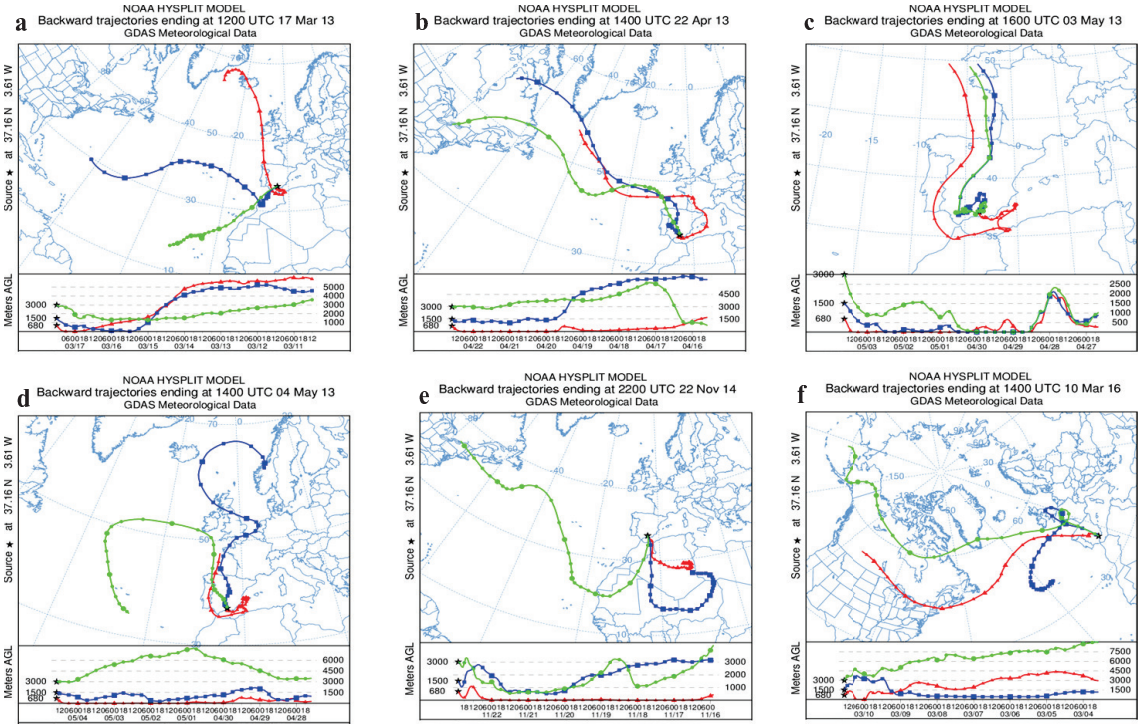

Figure 8.13. *180-h back trajectories for the six hygroscopic potential cases, calculated at 680, 1500 and 3000 m agl.*

Once the possible origin of aerosol was analyzed, the comparison with literature was performed. Case I, II and V reported the same range of γ, ranging from 0.4 to 0.5, which are in agreement with Bedoya-Velásquez et al. (2018a) and Bedoya-Velásquez et al. (2019) for mixed anthropogenic (polluted urban) and sulphate aerosol. Case IV can be compared to Fernández et al. (2015) for marine aerosol particles (salt crystals), nitrates and OA, reporting values of γ between 0.55 and 0.65. Case III ($\gamma < 0.24$) can be compared to Lv et al. (2017) study, the predominant aerosol analyzed is dust, which is very probable that some local aerosol can be mixed with Saharan dust in Granada along these days. Case VI presented relative high $\gamma = 1.19$, which can be compared with Granados-Muñoz et al. (2015) and Veselovskii et al. (2009) for sulphates mixed with marine aerosols.

8.3. Summary of chapter 8

The last results of this thesis are associated to vertical and temporal evolution studies at both SIATA-tower and IISTA-CEAMA stations by combinig automatic remote sensors, ceolometers and MWRs. The good conditions of high RH at SIATA-tower station allowed to get more that 250 posible cases to investigate in the vertical frame, but after rigorous criterias were applied, only 11 cases could be studied deeply. In the

temporal frame only seven cases fulfilled the criteria with temporal windows about 3 h. This results are the first of this kind over the area, thus its set a precedent, fousing about which kind of particles could be involved in this phenomena of interaction between aerosol and water vapor. The hygroscopic properties for verical analysis were ranging between $0.3 < \gamma < 1.0$, indicating that the presence of aerosols like anthropogenic, sulphate, nitrate, and biomass burning can drive the hygroscopic growth process in the atmosphere of Medellín. In the case of temporal evaluation γ held about 0.3 to 0.4, which suggests the presence of the nitrates mixed with salt and urban particles mostly according to literature.

At IISTA-CEAMA station there were only six potential cases associated to vertical evolution, while for temporal study there was not found potential case. The main drawback of that is due to the dry conditions of the atmosphere in Granada, leading to some difficulties at fulfilling the minimum conditions to evaluate hygroscopic growth cases. In the vertical frame γ parameter was oscillating from 0.2 to 1.2, pointing out the presence of dust, marine, sulphate and biomass burnig aerosols, which were checked with previous studies of the literature. .

8.4 References

Bedoya-Velásquez, A. E., Navas-Guzmán, F., Granados-Muñoz, M. J., Titos, G., Román, R., Casquero-Vera, J. A., Ortiz-Amezcua, P., Benavent-Oltra, J. A., de Arruda Moreira, G., Montilla-Rosero, E., Hoyos, C. D., Artiñano, B., Coz, E., Olmo-Reyes, F. J., Alados-Arboledas, L., and Guerrero-Rascado, J. L.: Hygroscopic growth study in the framework of EARLINET during the SLOPE I campaign: synergy of remote sensing and in situ instrumentation, Atmos. Chem. Phys., 18, 7001-7017, https://doi.org/10.5194/acp-18-7001-2018, 2018a.

Bedoya-Velásquez, A. E., Navas-Guzmán, F., Moreira, G., Román, R., Cazorla, A., Ortiz-Amezcua, P., Benavent-Oltra, J.A., Alados-Arboledas, L., Olmo-Reyes, F.J., Foyo-Moreno, I., Montilla-Rosero, E., Hoyos, C.D., Guerrero-Rascado, J.L.: Seasonal analysis of the atmosphere during five years by using microwave radiometry over a mid-latitude site, Atmospheric Research, Volume 218, 78-89, ISSN 0169-8095, https://doi.org/10.1016/j.atmosres.2018.11.014, 2018b.

Bedoya-Velásquez, A. E., Titos, G., Bravo-Aranda, J. A., Haeffelin, M., Favez, O., Petit, J.-E., Casquero-Vera, J. A., Olmo-Reyes, F. J., Montilla-Rosero, E., Hoyos, C. D., Alados-Arboledas, L., and Guerrero-Rascado, J. L.: Long-term aerosol optical hygroscopicity study at the ACTRIS SIRTA observatory: synergy between ceilometer and in-situ measurements, Atmos. Chem. Phys. Discuss., https://doi.org/10.5194/acp-2019-12, in review, 2019.

Chen, J., Zhao, C.S., Ma, N., Yan, P.: Aerosol hygroscopicity parameter derived from the light scattering enhancement factor measurements in the North China Plain. Atmos. Chem. Phys. 14, 8105e8118, 2014.

Dubovik, O., Holben, B., Eck, T. F., Smirnov, A., Kaufman, Y. J., King, M. D., Tanré, D., and Slutsker, I.: Variability of absorption and optical properties of key aerosol types observed in worldwide locations, J. Atmos. Sci., 59, 590–608, 2002.

Fernández, A. J, Apituley, A., Veselovskii, I.Suvorina, A., Henzing, J., Pujadas., M ad Artiñano., B.: Study of aerosol hygroscopic events over Cabauw experimental site for atmospheric research (CESAR) using the multi-wavelength Raman lidar Caeli, Atmospheric Environment, 120, 484-498, 2015.

Fernández, J., Molero, F., Becerril-Valle, M., Coz, E., Salvador, P., Artíñano, B., Pujadas, M.: Application of remote sensing techniques to study aerosol water vapour uptake in a real atmosphere, Atmospheric Research, Volume 202, Pages 112-127, ISSN 0169-8095, https://doi.org/10.1016/j.atmosres.2017.11.020, 2018.

Gassó, S., Hegg, D.A., Covert, D.S., Collins, D., Noone, K.J., Öström, E., Schmid, B., et al.: Influence of humidity on the aerosol scattering coefficient and its effect on the upwelling radiance during ACE-2. Tellus B 546e567, 2000.

Granados-Muñoz M.J, Navas-Guzmán, F., Bravo-Aranda, J. A., Guerrero-Rascado, J. L., Lyamani, H., Valenzuela, A., Titos, G., Fernández-Gálvez, J., and Alados-Arboledas, L.: hygroscopic growth of atmospheric aerosol particles based on active remote sensing and radiosounding measurements: selected cases in southeastern Spain. Atmos. Meas. Tech., 8, 705–718, 2015.

Gras, J.L., Jensen, J.B., Okada, K., Ikegami, M., Zaizen, Y., Makino, Y.: Some optical properties of smoke aerosol in Indonesia and Tropical Australia. Geophys. Res. Lett. 26 (10), 1393e1396, 1999.

Kotchenruther, R. A., Hobbs, P. V., and Hegg, D. A.: Humidification factors for atmospheric aerosols off the mid-Atlantic coast of the United States, Journal of Geophysical Research: Atmospheres, 104, 2239–2251, doi:10.1029/98JD01751, 1999.

Lv M., Liu D., Li Z., Mao J., Sun Y., Wang Z., Wang Y. and Chenbo X.: hygroscopic growth of atmospheric aerosol particles based on lidar, radiosonde, and in situ measurements: case studies from the Xinzhou field campaign. Journal of quantitative spectroscopy & Raditive Transfer,188 60-70, 2017.

Pan, X.L., Yan, P., Tang, J., Ma, J.Z., Wang, Z.F., Gbaguidi, A., Sun, Y.L.: Observational study of influence of aerosol hygroscopic growth on scattering coefficient over rural area near Beijing mega-city. Atmos. Chem. Phys. 9, 7519e7530, 2009.

Randriamiarisoa, H., Chazette, P., Couvert, P., Sanak, J., and Mégie, G.: Relative humidity impact on aerosol parameters in a Paris suburban area, Atmos. Chem. Phys., 6, 1389-1407, https://doi.org/10.5194/acp-6-1389-2006, 2006.

Raut, J.-C. and Chazette, P.: Retrieval of aerosol complex refractive index from a synergy between lidar, sunphotometer and in situ measurements during LISAIR experiment, Atmos. Chem. Phys., 7, 2797–2815, doi:10.5194/acp-7-2797-2007, 2007.

Sherman, J.P., Sheridan, P.J., Ogren, J.A., Andrews, E., Hageman, D., Schmeisser, L., Jefferson, A., Sharma, S.: A multi-year study of lower tropospheric aerosol variability and systematic relationships from four North American regions. Atmos. Chem. Phys. 15, 12487e12517. http://dx.doi.org/10.5194/acp-15-12487-2015, 2015.

Titos, G., Jefferson, A., Sheridan, P. J., Andrews, E., Lyamani, H., Alados-Arboledas, L., and Ogren, J. A.: Aerosol light-scattering enhancement due to water uptake during the TCAP campaign, Atmos. Chem. Phys., 14, 7031–7043, doi:10.5194/acp-14-7031-7043,2014.

Titos, G., Lyamani, H., Cazorla, A., Sorribas, M., Foyo-Moreno, I., Wiedensohler, A., Alados-Arboledas, L.: Study of the relative humidity dependence of aerosol light-scattering in southern Spain. Tellus B 66, 24536. http://dx.doi.org/10.3402/tellusb.v66.24536, 2014b.

Veselovskii, I., Whiteman, D. N., Kolgotin, A., Andrews, E., and Korenskii, M.: Demonstration of aerosol property profiling by multi-wavelength lidar under varying relative humidity conditions, J. Atmos. Ocean. Tech., 26, 1543–1557, 2009.

Zhang, L., Sun, J.Y., Shen, X.J., Zhang, Y.M., Che, H.C., Ma, Q.L., Zhang, Y.W., Zhang, X.Y., Ogren, J.A.: Observations of relative humidity effects on aerosol light scattering in the Yangtze River Delta of China. Atmos. Chem. Phys.15, 8439e8454. http://dx.doi.org/10.5194/acpd-15-2853-2015, 2015.

9. Conclusions

9.1 General conclusions

This section is devoted to present the main conclusions of each result obtained in the study of aerosol hygroscopic growth under unmodified atmospheric conditions. Due to this thesis involved different locations, practically each one required to apply specific steps of the methodologies proposed. The conclusions of this thesis are the following:

First of all, it was performed a rigorous characterization of the errors of both MWRs at the ISTA-CEAMA and SIATA-tower stations, finding the trustworthy regions to use temperature and RH profiles. Under the first 3.0 km agl both systems presented good behavior in terms of accuracy and precision. Also, it was defined an experimental approach to retrieve RH profiles by the calibration of the lidar water vapor Raman channel, enhancing the probability to have RH profiles with lidar vertical resolution.

Secondly, studies related to the seasonal, interannual and diurnal cycle of temperature, RH and also integrated products such as IWV and liquid water were performed, in order to define the best periods of the year (hourly) in which the probability to find aerosol hygroscopic growth cases is high. This evaluation was done for both stations, IISTA-CEAMA and SIATA-tower, finding very satisfactory results. At the IISTA-CEAMA, station spring and summer were the most probable seasons where hygroscopic growth cases can be found, probably because of the IWV increases due to the increase of the evapotraspiration process. At the SIATA-tower station, potential cases of aerosol hygroscopic growth were found mostly in the first four months of the year, but as Medellín experiences RH values really higher than Granada, there is a possibility to find cases in any period of the year, depending more if it is a dry or wet year according to climatology and the local aerosol dynamics.

The hardest task was the correct design of a methodology to study hygroscopicity by combining remote sensors, paying special attention to the evaluation with automatic ones. To this aim, it was designed four methodologies, two for temporal evolution and other two for vertical evolution of hygroscopicity events. One important aspect is that results of this thesis not only were evaluated by combining many instruments (Raman lidar, ceilometer, MWR, in situ, RS and meteorological sensors), but also probed on

different locations like IISTA-CEAMA (methodology V1), SIRTA observatory (methodology T1), and SIATA-tower and IISTA-CEAMA stations with methodology V2 and T2. Those last ones only involved automatic remote sensors, i.e. ceilometers and MWRs.

Finally, different kinds of algorithms were designed for each methodology proposed. In those routines it was possible to evaluate the optical property β together with RH, and also the calculations involved atmospheric conditions and other optical properties like AE, PLDR. Methodology V1 applied at the IISTA-CEAMA station allowed to characterize a case during the SLOPE I field campaign, where a valley (IISTA-CEAMA) and a high mountain (SNS) stations were compared in terms of the hygroscopic properties, obtaining good agreement between γ^{532}(lower than 9 %) and γ^{355} (lower than 11 %) between Mie simulations by using in situ data in the SNS as inputs and experimental data from remote sensing. The aerosol studied in this case was a mixture of smoke and urban polluted aerosol.

In addition, it was possible to perform in one location (SIRTA observatory) the calculation together with on-line in situ measurements of aerosol concentration (Methodology T1). Here, the organic and inorganic aerosol contributiona were evaluated, concluding the important role that nitrate plays in the hygroscopic growth process. In this study eight aerosol hygroscopic growth cases were evaluated.

The evaluation of the methodology V2 and T2 at SIATA-tower station left seven potential cases in the temporal frame and 11 in the vertical. The results were compared with literature and the presence of anthropogenic, mixed urban and organic matter was predominant over the region. At IISTA-CEAMA methodology V2 was evaluated, leaving six potential hygroscopic growth cases pointing out the main presence of marine, sulphate, dust and biomass burning aerosols as it was checked with the literature.

The main result obtained in this thesis was to get a new database of aerosol hygroscopic growth properties retrieved under real atmospheric conditions at different sites, showing the potentiality of using a combination of remote sensors to study complex atmospheric processes.

9.2 Recommendations and future work

To improve the hygroscopic growth studies at the SIATA-tower station, to have ancillary information available for the vertical evaluation such as turbulences would be necessary. This studies may be performed by using the methodology proposed by Moreira et al. (2018) using high temporal resolved lidar measurements. For Medellín, the calculation was performed but, unfortunately, the turbulent eddies cannot be correctly detected and erroneous results can be generated, because of the low time-scale of the ceilometer. On this way, it is strongly recommended to use high temporally-resolved lidar measurements (e.g. 1 s), in order to go deeper on this analysis. Option might be to use the wind radar located approximately at 3.2 km in a straight line to the tower station to investigate the dynamics of the air masses and vertical wind speed and direction. Unfortunately, these data were no available for this investigation yet.

As it was evaluated in this thesis, the role of IA is important in aerosol hygroscopicity studies, but it is also relevant to conduct detailed studies on the role of different fractions of the OA as these components can be soluble. In addition, a relevant aspect to be evaluated is associated with the aerosol acidification that should be evaluated for determining the role of aged or fresh aerosols in the hygroscopic properties, and their impacts on OA. Finally, further investigations should evaluate larger periods as studied here, in order to get statistically robust results over the different regions.

For the IISTA-CEAMA and SIATA-tower stations is highly recommended to acquire permanent in situ instrumentation like ACMS and Scanning Mobility Particle Sizer (SMPS), in order to continuous monitor concentration of different chemical compounds and size aerosol distribution.

The work coming in the near future is related to: (i) retrieve vertically-resolved aerosol microphysical properties, in order to study the impact of the water uptake on size/concentration of the aerosols (i.e. using the Generalized Retrieval of Aerosol and Surface Properties algorithm, GRASP), (ii) extend the database in order to make the results statistically robust, and (iii) analyze the temporal evolution cases together with other variables such as ABLH, optical parameters from Sun photometer (i.e. AOD, SSA, AE, size distribution), and gas emissions, in order to enrich the study.

9. Conclusiones

9.1 Conclusiones generales

Esta sección está dedicada a presentar las principales conclusiones de cada resultado obtenido en el estudio del crecimiento higroscópico de aerosoles en condiciones atmosféricas sin modificadas. Debido a que esta tesis involucró diferentes lugares, prácticamente cada uno de ellos requirió aplicar pasos específicos de las metodologías propuestas. Las conclusiones de esta tesis son las siguientes:

En primer lugar, se realizó una caracterización rigurosa de los errores de ambos MWR en las estaciones de ISTA-CEAMA y torre SIATA, encontrando regiones confiables para usar perfiles de temperatura y HR. En los primeros 3.0 km, ambos sistemas presentaron un comportamiento muy bueno en términos de la exactitud y precisión. Además, se definió un método experimental para obtener perfiles de HR mediante la calibración del canal Raman de vapor de agua del lidar, incrementando la probabilidad de tener perfiles HR con la resolución vertical del lidar.

En segundo lugar, se realizaron estudios relacionados con el ciclo estacional, interanual y diurno de la temperatura, HR y también productos como IWV y agua líquida, para definir los mejores períodos del año (por hora) en los que la probabilidad de encontrar casos de crecimiento higroscópico del aerosol era alto. Esta evaluación se realizó para ambas estaciones IISTA-CEAMA y torre SIATA, encontrando resultados muy satisfactorios. En IISTA-CEAMA, la primavera y el verano fueron las estaciones más probables donde se pueden encontrar casos de crecimiento higroscópico, probablemente debido a los aumentos de IWV debidos al aumento del proceso de evapotranspiración. En la estación torre SIATA, los casos potenciales de crecimiento higroscópico del aerosol se encontraron principalmente en los primeros cuatro meses del año, pero como Medellín tiene valores de HR realmente superiores a Granada, existe la posibilidad de encontrar casos en cualquier período del año, dependiendo de si es un año seco o húmedo según la climatología y la dinámica de aerosol local.

La tarea más difícil fue el diseño correcto de una metodología para estudiar higroscopicidad mediante la combinación de sensores remotos, centrándonos en la evaluación a través de sensores automáticos. Para ello, se diseñaron cuatro metodologías,

dos para la evolución temporal y otras dos para la evolución vertical de los eventos de higroscopicidad. Un aspecto importante es que los resultados de esta tesis no solo se evaluaron mediante la combinación de varios instrumentos (Raman lidar, ceilómetro, MWR, in situ, RS y sensores meteorológicos), sino que también se analizaron en diferentes lugares como IISTA-CEAMA (metodología V1), observatorio SIRTA (metodología T1), y estaciones torre SIATA e IISTA-CEAMA con metodología V2 y T2. Esos últimos solo involucraron sensores remotos automáticos.

Finalmente, fueron diseñados diferentes tipos de algoritmos que cumplieron con cada una de las metodologías propuestas. En esas rutinas fue posible evaluar la propiedad óptica β junto con RH y también los cálculos incluyeron condiciones atmosféricas y otras propiedades ópticas como AE, PLDR. La metodología V1 aplicada en la estación IISTA-CEAMA permitió caracterizar un caso durante la campaña SLOPE I, donde se compararon las estaciones del valle (IISTA-CEAMA) y de alta montaña (SNS) en términos de las propiedades higroscópicas, obteniendo un buen acuerdo entre γ^{532} (menor que 9 %) and γ^{355}(menor que 11 %)entre simulaciones de Mie, usando los datos in situ como datos de entrada en la SNS y datos experimentales de detección remota. Así, el aerosol estudiado durante el evento fue una mezcla de humo y aerosol urbano contaminado.

Además, fue posible realizar en un solo lugar (observatorio SIRTA), el cálculo junto con mediciones in situ de concentración de aerosoles (Metodología T1). Se evaluó la contribución de aerosoles orgánicos e inorgánicos, concluyéndose el importante papel que el nitrato juega en el proceso de crecimiento higroscópico. En este estudio se evaluaron ocho casos de crecimiento higroscópico de aerosoles.

El principal resultado de esta tesis fue construir una nueva base de datos de propiedades de crecimiento higroscópico de aerosoles obtenida en condiciones atmosféricas reales para diferentes sitios, mostrando la potencialidad de usar una combinación de sensores remotos para estudiar procesos atmosféricos complejos.

9.2 Recomendaciones y trabajos futuros

Para mejorar los estudios de crecimiento higroscópico en la estación de torre SIATA, sería necesario proporcionar información complementaria a la evaluación vertical tales como estudios de turbulencia. Estos estudios pueden realizarse utilizando la

metodología propuesta por Moreira et al. (2018), mediante el uso de mediciones lidar de alta resolución temporal. El cálculo se realizó en la ciudad de Medellín pero, desafortunadamente, los remolinos turbulentos no se pueden detectar correctamente y se pueden generar resultados erróneos, debido a la escala baja escala temporal del ceilómetro. De esta manera, se recomienda utilizar mediciones lidar de alta resolución (por ejemplo 1 s) para profundizar en este análisis. La otra opción podría ser usar el radar de viento ubicado aproximadamente a 3.2 km en línea recta a la estación de la torre para investigar la dinámica de las masas de aire y la dirección y velocidad vertical del viento. Desafortunadamente, estos datos aún no están disponibles para esta investigación.

Como se evaluó en esta tesis, el papel del aerosol inorgánico en la higroscopicidad de los aerosoles es importante, pero también es relevante llevar a cabo estudios detallados sobre el papel de las diferentes fracciones de aerosoles orgánicos, ya que estos componentes pueden ser solubles. Adicionalmente, un aspecto relevante para estudiar está asociado con la acidificación del aerosol el cual debe evaluarse para determinar el papel de los aerosoles envejecidos o frescos en las propiedades higroscópicas, y su impacto en los aerosoles orgánicos. Finalmente, futuras investigaciones deberían evaluar períodos más extensos que los estudiados aquí para obtener resultados estadísticamente más robustos en las diferentes regiones.

Como recomendaciones generales para la estación IISTA-CEAMA y torre SIATA, se debería considerar la adquisición de instrumentación permanente in situ como ACMS y Scanning Mobility Particle Sizer (SMPS), con el fin de monitorear continuamente la concentración de compuestos químicos y el tamaño de la distribución de aerosoles.

El trabajo que viene en camino está relacionado con: (i) mejorar los cálculos para obtener propiedades microfísicas resueltas verticalmente, para estudiar el impacto de la captación de agua en el tamaño/concentración de los aerosoles (usando por ejemplo The Generalized Retrieval of Aerosol and Surface Properties, GRASP), (ii) ampliar la base de datos para obtener resultados estadísticamente robustos, y (iii) analizar los casos de evolución temporal junto con otras variables como ABLH, parámetros ópticos de SP (e.g. AOD, SSA, AE, distribución de tamaño) y emisiones de gases, para enriquecer el estudio.

Appendix 1

A1.1 Effect of beta-attenuated water vapor correction on calculated $f_\beta(RH)$ and γ parameter

The β^{att} signal presents a dependency on water vapor absorption as shown in Sec. 4.2.2.1 (Eq. 4.6), associated with the wavelength emission. This dependency may cause direct effects over calculations retrieved by using β^{att}. Here, it is presented the correction applied to β^{att} and the effects on $f_\beta(RH)$ and γ calculations. Figure A1.1 (left-panels) represents the temporal-evolution of β^{att}, beta attenuated water vapor corrected (β_{wv}^{att}) signals over 3 h time-window, together with the temporal-evolution of q. Figure A1.1 (right-panels) shows the biases for beta ($bias_\beta$) and Δ_q obtained.

Case 1: 19/03/2014

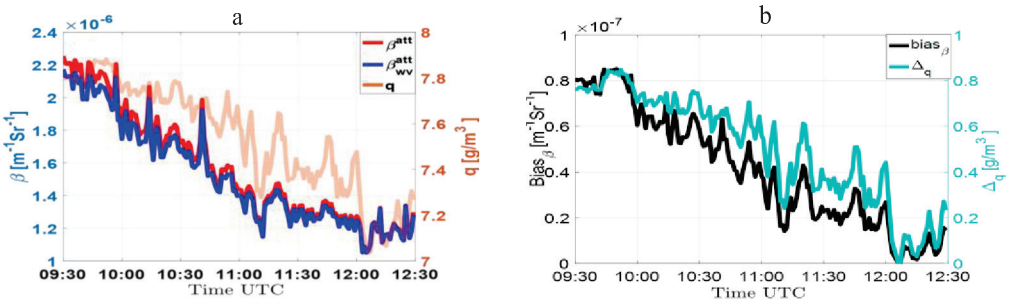

Case 2: 01/05/2016

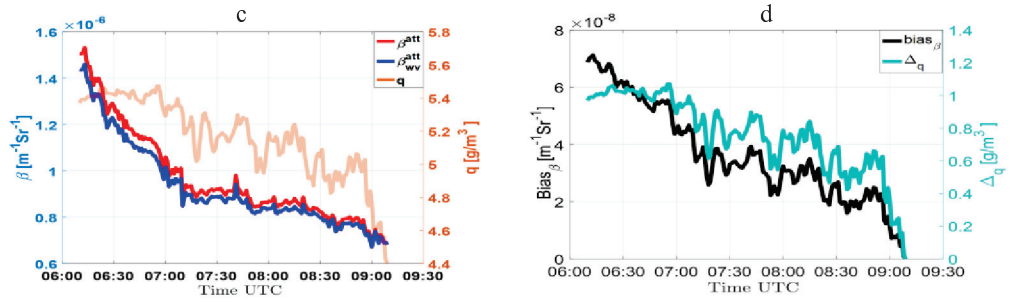

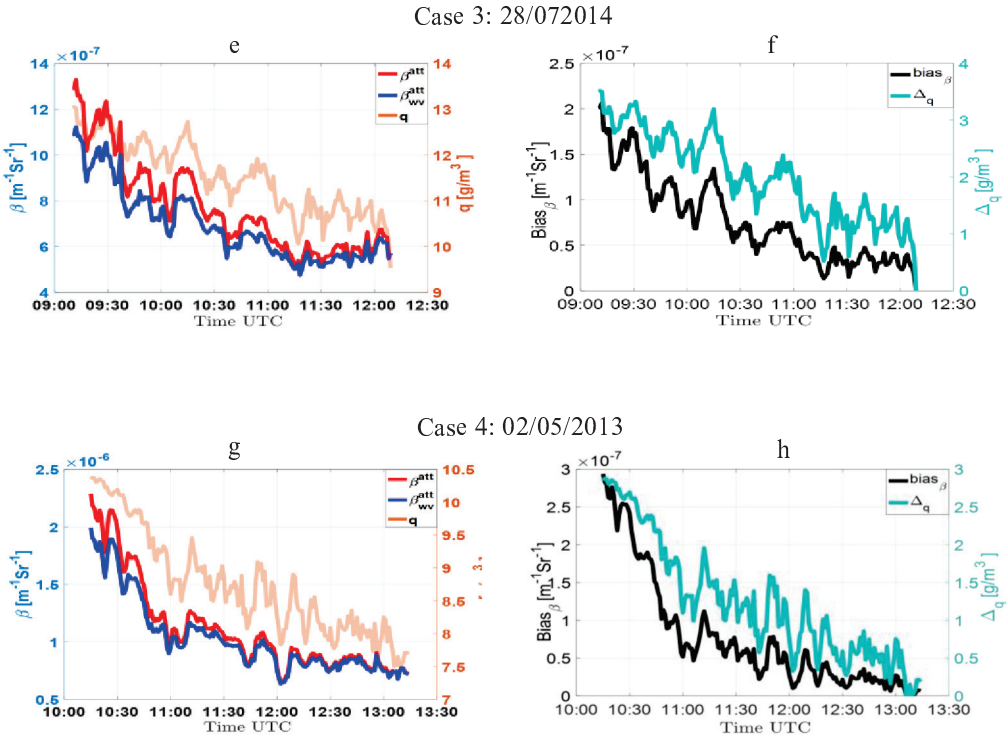

Figure A1.1 *Time evolution of β^{att} (blue line), β_c^{att} (red line) and q (orange line)[left panels (a,c,e,g $bias_\beta$ (black line) and Δ_q (green line) [right panel (b,d,f,h)].*

The quantifications are performed by means of the bias_β ($\beta^{att} - \beta_{wv}^{att}$) and Δ_q $\left(q(t) - q\,(t_d)\right)$ calculations. Figure A1.1ac presents two cases (case 1 and case 2) with low absolute-differences in q, which produces slight changes in β_{wv}^{att} signal respect to β^{att}. On the other hand, Fig. A1.1eg (case 3 and case 4) show that high absolute-differences in q are linked to high changes on β_{wv}^{att}. The right side of the panel (Fig. A1.1bd, case 1 and case 2), presents the bias quantification, showing that low bias_β are associated with low Δ_q and, on the contrary, Fig. A1.1fh (case 3 and case 4), show that increases in Δ_q makes that bias_β becomes higher. This analysis leads us to conclude that no-water vapor correction will produce an overestimation of the total β signal, being $\Delta_q$the parameter that rules the β correction. From now, we will use β instead of β^{att} for simplicity.

To see the effect of β_{wv}^{att} on $f_\beta(RH)$, we applied the Hänel parameterization to the same 4 cases studied above. Figure A1.2 presents the $f_\beta(RH)$ and the enhancement

factor water vapor corrected, $f_{\beta_{wv}^{att}}(RH)$. The results reinforce those obtained above (Fig A1.1), where low/high changes in Δ_q are linked with low/high bias_β and, on this way, this would affect $f_\beta(RH)$ calculation. Additionally, the water vapor correction tends to decrease γ (β_{wv}^{att} is lower than β). Therefore, cases with lower bias_β and Δ_q (case 1 and case 2), exhibits lower $bias_\gamma$ (0.02 and 0.05, respectively), meanwhile on case 3 and case 4 instead bias_β increase, the $bias_\gamma$ becomes higher (0.11 and 0.09, respectively).

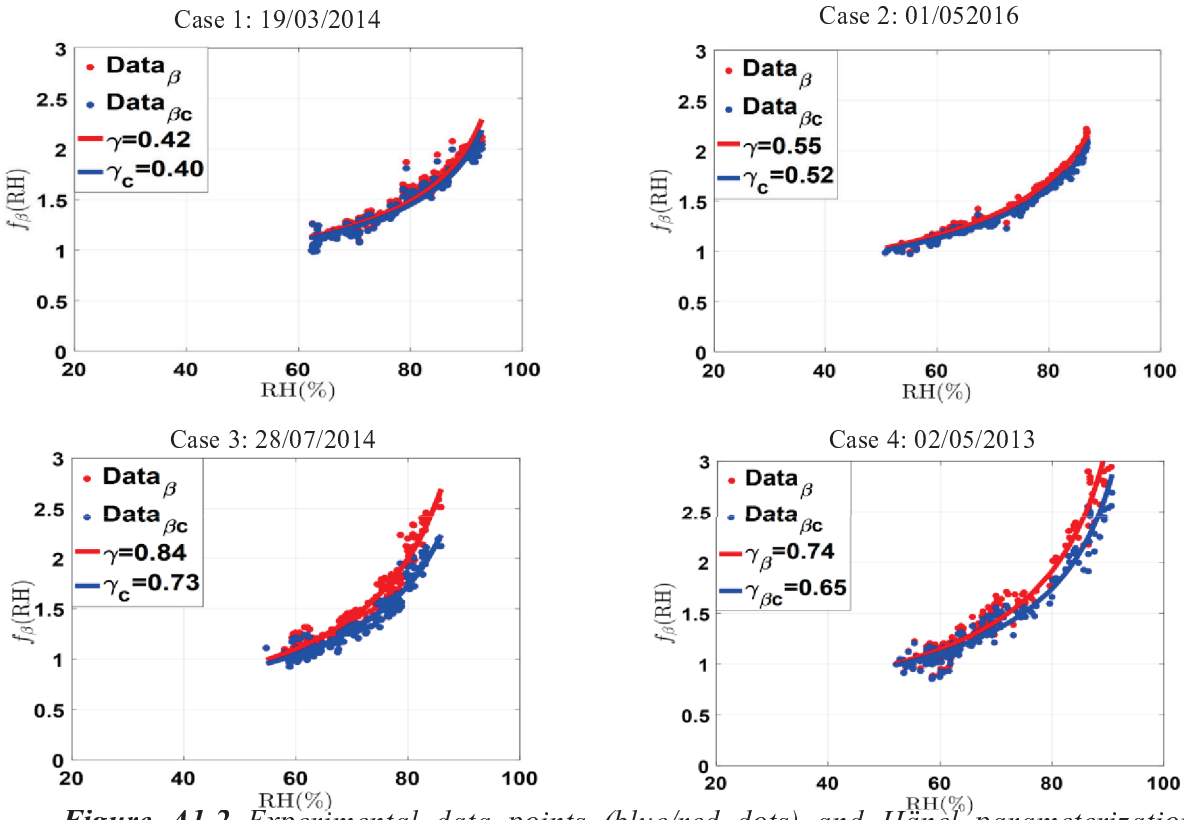

Figure A1.2 *Experimental data points (blue/red dots) and Hänel parameterization (blue/red lines). Case 1 and Case 2 show the effect of the lower* bias_β *and* Δ_q *differences over* $f_{\beta_{wv}^{att}}(RH)$ *and* $f_\beta(RH)$*. Case 3 and Case 4 present the effect of the higher* bias_β *and* Δ_q *differences over* $f_{\beta_{wv}^{att}}(RH)$ *and* $f_\beta(RH)$*.*

Once it is applied the criteria II of the methodology (Fig. 4.1), obtaining 94 hygroscopic potential cases for 3h time-window (Fig. A1.3a), 9 cases for 4h time-window (Fig. A1.3a) and 4 cases for 5h time-window (Fig. A1.3a), resulting in a total of 107 cases. To establish a bias error for this hygroscopic study, it was calculated the median of the bias_β and Δ_q, highlighting two main aspects: (i) The median bias_β follows the median Δ_q variability, remarking their dependency. This fact is well seen from the scatter plot (Fig. A1.3b), where these variables show a positive correlation, however the correlation

coefficient is not too high (R^2= 0.61), mainly because the data dispersion increases for $bias_\beta$ > 1.5 10^{-7} $m^{-1}\cdot sr^{-1}$ and Δ_q > 3.0 g/m^3; (ii) The mean bias error calculated for β_{wv}^{att} over the 107 potential cases evaluated is lower than $2.5\cdot10^{-7}$ $m^{-1}\cdot sr^{-1}$ and the mean Δ_q is lower than 5.5 g/m^3.

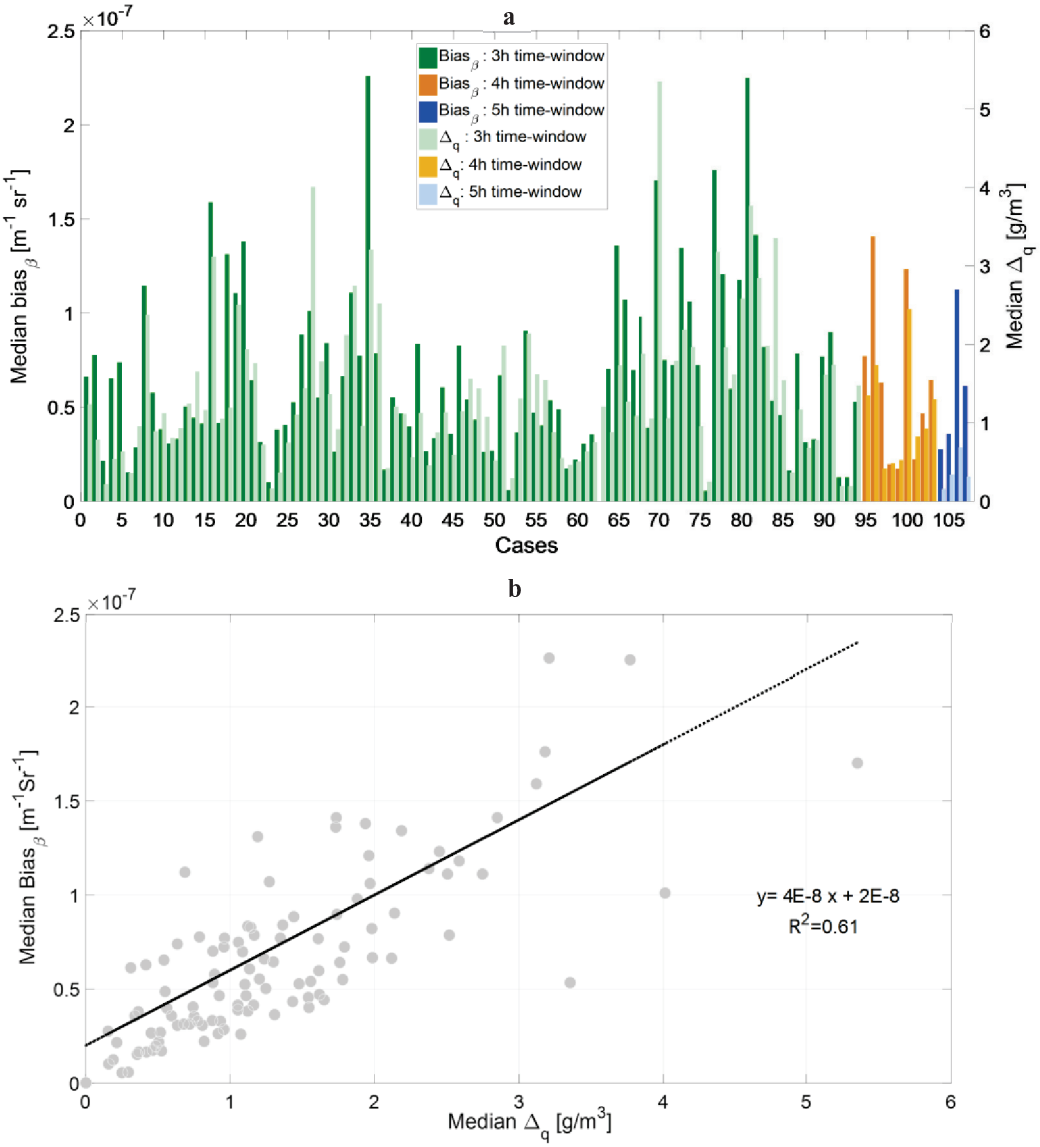

Figure A1.3 *Median of $bias_\beta$ and Δ_q for all potential cases found: (a) median of $bias_\beta$ and Δ_q to 3h time-window analysis (green bars), 4h time-window analysis (orange bars) and 5h time-window analysis (blue bars); (b) scatter plot correlating median of $bias_\beta$ and Δ_q for whole time-windows.*

Fig. A1.4 quantifies the effect of the β_{wv}^{att} over $f_\beta(RH)$ and γ hygroscopic properties, by means of the median $bias_{f_{\beta(RH)}}$ ($f_\beta(RH)$ - $f_{\beta_{wv}^{att}}(RH)$) and the $bias_\gamma$ ($\gamma_{\beta^{att}} - \gamma_{\beta_{wv}^{att}}$). Figure S4 reveals the no-correlation between $bias_\beta$ and $bias_{f_{\beta(RH)}}$. However, combining the results from Fig. A1.3 and Fig. A1.4, it is possible to establish

that $\text{bias}_{\beta} > 1\ \text{m}^{-1}\cdot\text{sr}^{-1}$ would cause an increment of $\text{bias}_{f_{\beta}(RH)}$ above 0.2, increasing the error on $f_{\beta}(RH)$. Finally, it was obtained that $\text{bias}_{f_{\beta}(RH)}$ and bias_{γ} for the whole study were lower than 0.3.

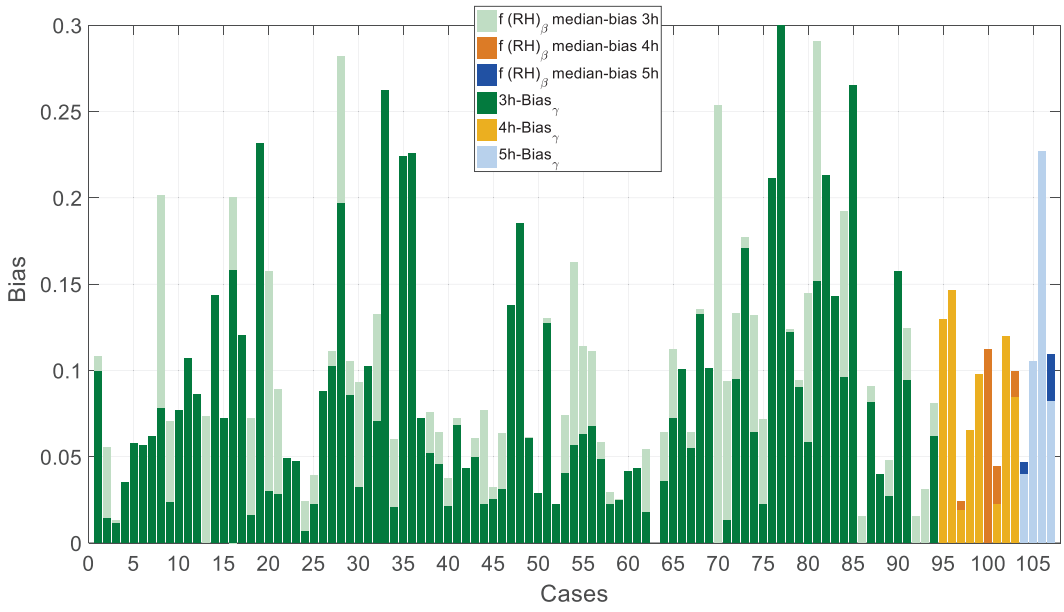

Figure A1.4 *$\text{bias}_{f_{\beta}(RH)}$ and bias_{γ} for all potential cases of hygroscopic growth found from 2012 to 2016 at the ACTRIS SIRTA observatory. $\text{bias}_{f_{\beta}(RH)}$ and bias_{γ} for 3h time-window analysis (green bars), 4h time-window analysis (orange bars) and 5h time-window analysis (blue bars).*

A1.2 Results

A1.2.1 Methodology applied to eight aerosol hygroscopic growth cases

The 8 hygroscopic growth cases reported in this study (Table 7.1, Sec. 7.2) were found at daytime in the early morning, with RH_{ref} around 50 % and the maximum RH reached was up to 90% over 3h time-window. For cases 1, 2, 4, 5, 6 and 7 the perceptual composition was dominated by OA with values up to 50 %, except on case 7 where OA decreased up to 38%. The BC concentration was relatively low almost for all cases found (close to 6 %). The concentration of inorganic compounds were dominated by SO_4^{2-} (lower than 21 %) and NH_4^+(lower than 19 %), however NO_3^- reached values of 21% on case 6. The air masses that come mainly from W-NW direction are related to case 1 (Δu=3.6 m/s W), case 2 (Δu=23.0 m/s NW) and case 6 (Δu=4.4 m/s W), with speed

variability up to 14.2 %, 20.7 % and 18.5 %, respectively; and the air masses that coming from W-SW direction at low wind direction variability are associated with case 4 (Δu=2.7 m/s W), case 5 (Δu=2.4 m/s SW), and case 7 (Δu=1.7 m/s SW), and wind speed variability about 15.4 m/s, 20.4 m/s and 10.9 m/s, respectively. All these cases fulfilled the threshold established for $\frac{\Delta f_{PM1}(RH)}{\Delta f_{\beta}(RH)} < 0.5$ indicating that increases/decreases in $f_{\beta}(RH)$ are not related with advected aerosol into the atmospheric volume studied. The Hänel parameterization is calculated for both $f_{\beta}(RH)$ and $f_{PM1}(RH)$ (see panel Fig. A1.5b to A1.10b.). The hygroscopicity properties of the 6 cases presented here were evaluated and compared against literature in the Sec. 7.2 of the article.

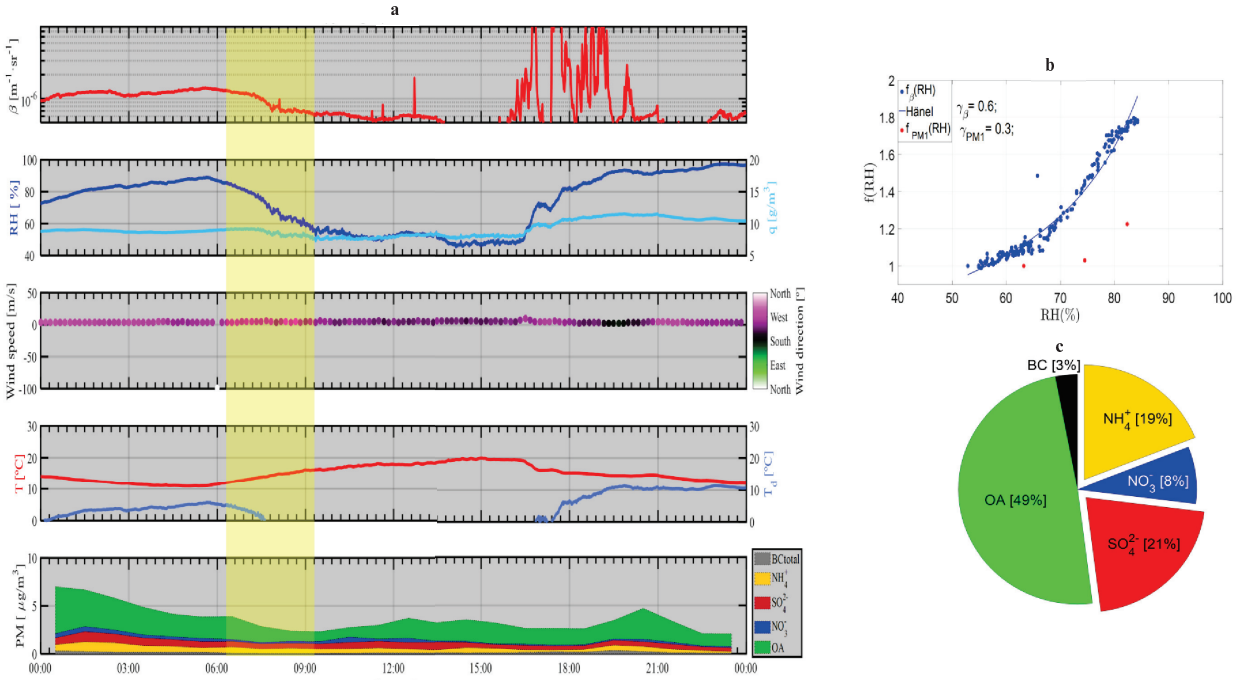

Figure A1.5 *Criterion for data selection: case 1 on 29/07/ 2012 from 06:30 to 09:30 UTC.*

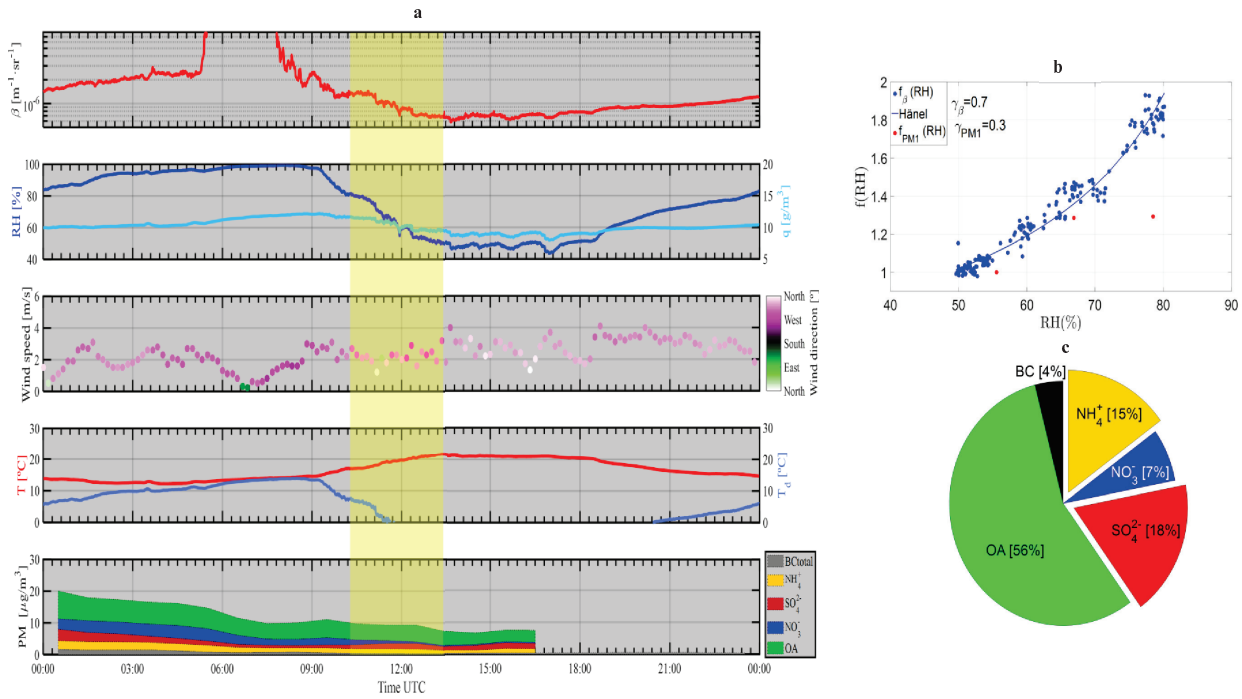

Figure A1.6 *Criterion for data selection: case 2 on 02/09/ 2012 from 10:30 to 13:30 UTC.*

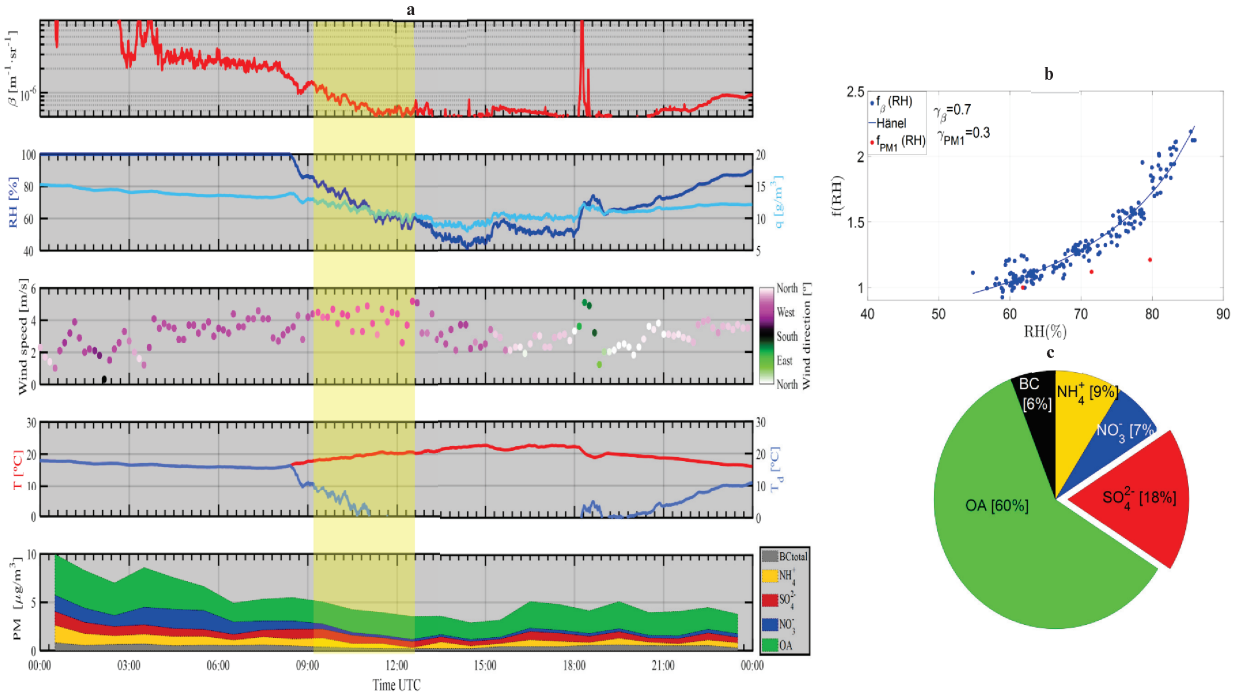

Figure A1.7 *Criterion for data selection: case 4 on 28/07/2014 from 09:10 to 12:10 UTC.*

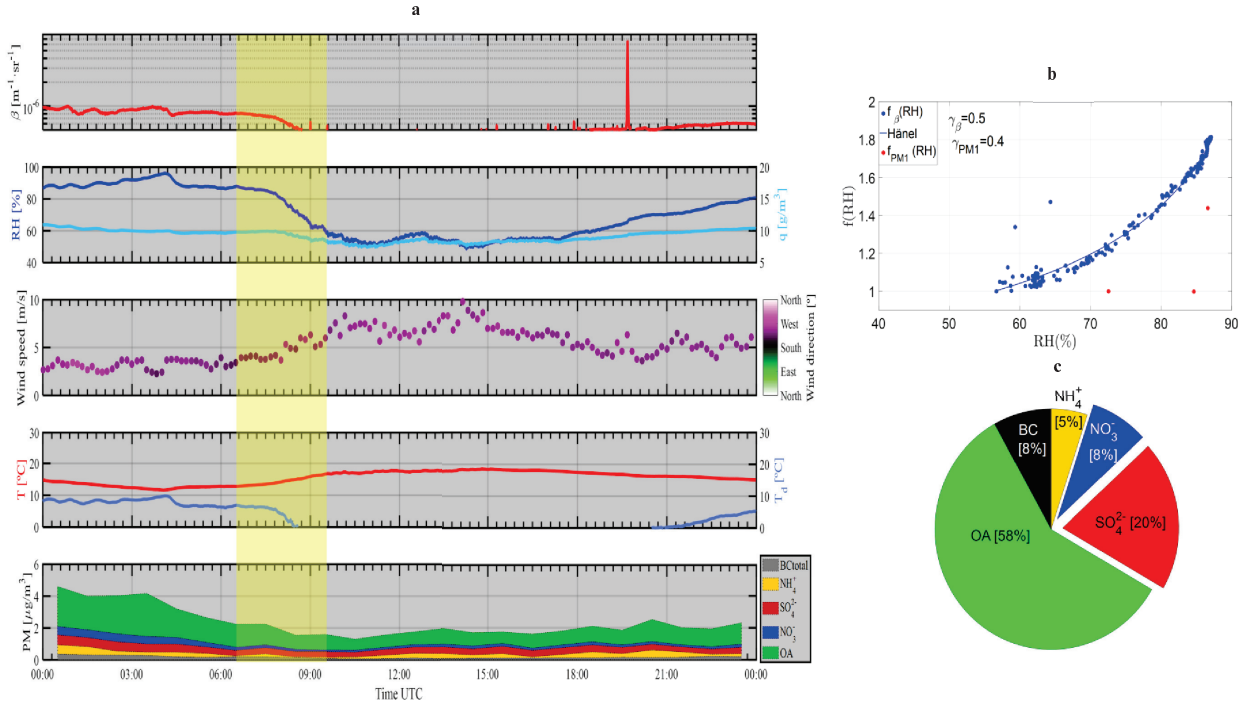

Figure A1.8 *Criterion for data selection: case 5 on 17/08/ 2014 from 06:40 to 09:40 UTC.*

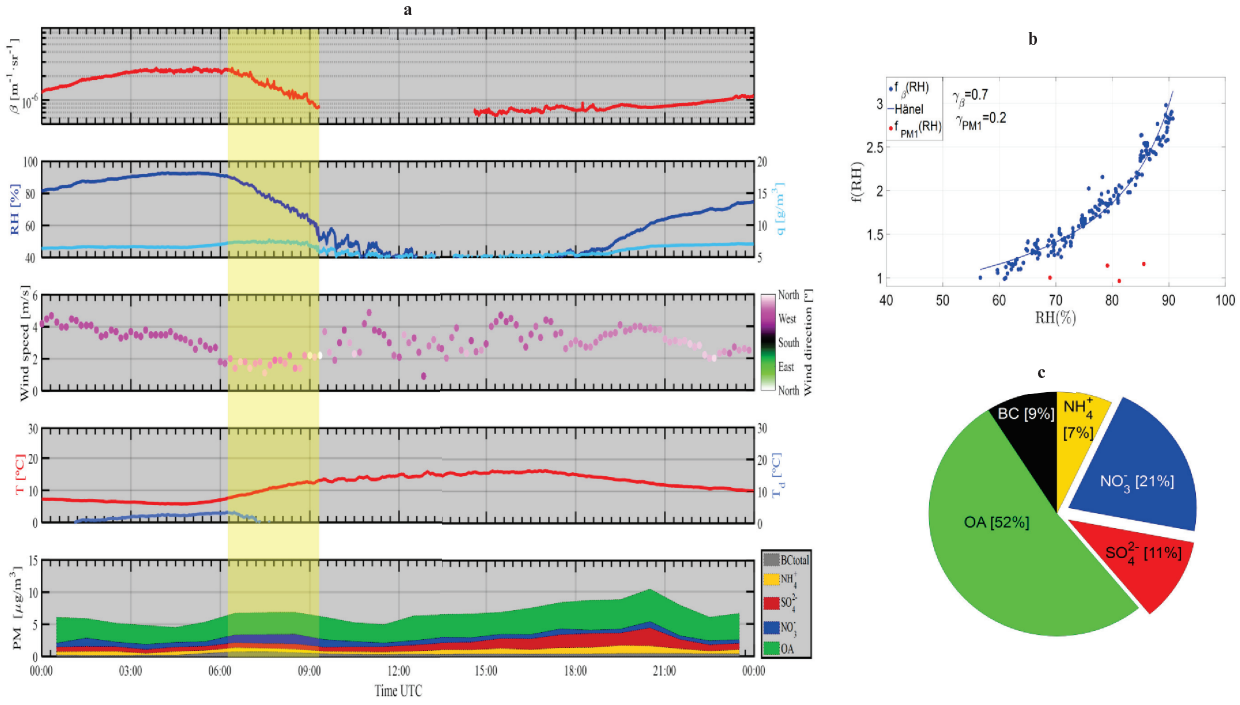

Figure A1.9 *Criterion for data selection: case 6 on 21/05/ 2015 from 06:15 to 09:15 UTC.*

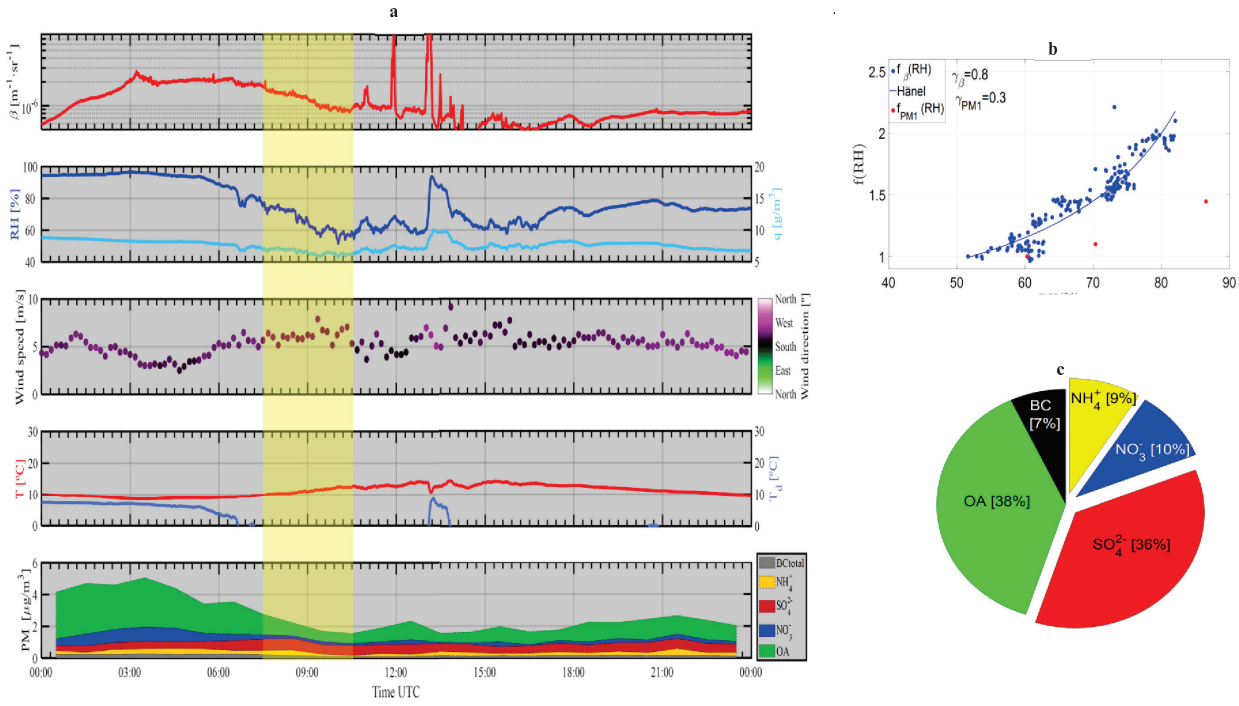

Figure A1.10 *Criterion for data selection: case 7 on 15/ 2016 from 07:05 to 10:05 UTC.*

Appendix 2: symbols and abbreviations

Symbol -Abbreviations	Description
ARI	Aerosol-radiation interaction
ACI	Aerosol-cloud interaction
CCN	Cloud condensation nuclei
IC	Ice nuclei
RH	Relative humidity
$f_{\xi}^{\lambda}(RH)$	Enhancement factor
g (RH)	Aerosol hygroscopic growth factor
HTDMA	Humidified Tandem Differential Mobility Analyzer
DASH-SP	Differential Aerosol Sizing and Hygroscopicity Spectrometer Probe
WHOPS	White-light humidified optical particle spectrometer
RS	Radiosoundes
RL	Raman lidar
$r(z)$	Water vapor mixing ratio profiles
DL	Doppler lidar
MWR	Microwave radiometer
$T(R,\lambda)$	Transmittance
$\alpha(R,\lambda)$	Total extinction coefficient
AOD	Aerosol optical depth
TOA	Top of the atmosphere
a	Radius of the particles
λ	Wavelength of the radiation
σ_R	Rayleigh scattering cross section
$\beta_{\pi}^{R}(\lambda)$	Backscattering coefficient
X	Size paramete
$Q_S(X,n)$	Mie efficiency terms
k	Wavelength number
σ_S^M	Mie scattering cross section

i_1	Mie intensity function
AE	Angström Exponent
$n(r)$	Number of particles
r	Particle radius
N	Total number of particles
$m(r)$	Mass size distribution
D_{dry}	Equilibrium particle diameter at dry conditions
OA	Organic aerosols
IA	Inorganic aerosols
e	Saturation water vapor pressure
a_w	Water activity
e_o	Saturation water vapor pressure of dry equilibrium
μ	Chemical potential
G	Gibbs free energy
S	Saturation ratio
σ	Surface tension
β_{par}	Particle backscatter coefficient
$f_\sigma(\lambda, RH)$	Scattering enhancement factor
$f_\beta(\lambda, RH)$	Backscattering enhancement factor
$O(z)$	Overlap factor
FOV	Field of view
β^{att}	Attenueated backscater
β_{wv}^{att}	Water vapor component of the attenueated backscater coefficient
RTE	Radiative transfer equation
α_{Th}^{a}	Absorption thermanl extinction coefficient
α_{Th}^{s}	Scattering thermanl extinction coefficient
I_ω	Intensity
I_ω^a	Absoption intensity
I_ω^{emi}	Emissivity intensity
$B(T)$	Plank function

$\boldsymbol{h}$	Planck constant
$\boldsymbol{k_b}$	Boltzmann constant
$\boldsymbol{T_B}$	Brightness temperature
$\boldsymbol{T_B^{cos}}$	Cosmic background
SIATA	Sistema de alerta temprana de Medellín y el Valle de Aburrá
IISTA-CEAMA	Instituto interuniversitario de investigación del sistema tierra en Andalucia
IWV	Integrated water vapor
LWP	Liquid water path
ABL	Atmospheric boundary layer
ABLH	Atmospheric boundary layer height
MBE	Mean-bias error
PLDR	Particle linear depolarization ratio
$\boldsymbol{\theta_v}$	Potential temperature
$\boldsymbol{W_S}$	Wind speed
$\boldsymbol{W_d}$	Wind direction
$\boldsymbol{f_{PM1}(RH)}$	PM1 enhancement factor
$\boldsymbol{q(t)}$	Absolute humidity
PW	Precipitable water
SNS	Sierra Nevada Station
$\boldsymbol{\gamma}$	Parameter related to the aerosol hygroscopicity
RCS	Range corrected signal
OMF	Organic mass fraction
IMF	Inorganic mass fraction
DRH	Deliquescence relative humidity
ERH	Efflorescence relative humidity

Published articles

1	2019	**Long-term aerosol optical hygroscopicity study at the ACTRIS SIRTA observatory: synergy between ceilometer and in-situ measurements** *Atmos. Chem. Phys. Discuss., https://doi.org/10.5194/acp-2019-12, in review, 2019.* **Bedoya-Velásquez, A.E**., Titos, G., Bravo-Aranda, B.A., Haeffelin, M., Favez, O, Petit, J.E., Casquero-Vera, J.A, Olmo-Reyes, F.J., Montilla-Rosero, E., Hoyos, C.D., Alados-Arboledas, L., and Guerrero- Rascado. J.L.
2	2018	**Hygroscopic growth study in the framework of EARLINET during the SLOPE I campaign: synergy of remote sensing and in-situ instrumentation** *Atmos. Chem. Phys, 18, 1-17* **Bedoya-Velásquez, A. E.,** Navas-Guzmán, F., Granados-Muñoz, M. J., Titos, G., Román, R., Casquero-Vera, J. A., Ortiz-Amezcua, P., Benavent-Oltra, J. A., de Arruda Moreira, G., Montilla-Rosero, E., Hoyos, C. D., Artiñano, B., Coz, E., Olmo-Reyes, F. J., Alados-Arboledas, L., and Guerrero-Rascado, J. L.
3	2018	**Seasonal analysis of the atmosphere during five years by using microwaveradiometry over a mid-latitude site** *Atmospheric Research,218, 78-89* **Bedoya-Velásquez, A. E.,** Navas-Guzmán, F., de Arruda Moreira, G., Román, R., Cazorla, A., Ortiz-Amezcua, P., Benavent-Oltra, J. A., Alados-Arboledas, L., Olmo-Reyes, F. J., Foyo-Moreno, I., Montilla-Rosero, E., Hoyos, C. D., and Guerrero-Rascado, J. L.
4	2018	**Study of the planetary boundary layer by microwave radiometer, elasticlidar and Doppler lidar estimations in Southern Iberian Peninsula** *Atmos. Res., 213, 185-195* de Arruda Moreira, G., Guerrero-Rascado, J. L., Bravo-Aranda, B.A., Benavent-Oltra, J. A., Ortiz-Amezcua, P., Román, R., **Bedoya-Velásquez, A. E.,** Ladulfo, E., and Alados-Arboledas, L.
5	2019	**Analyzing the turbulent Planetary Boundary Layer behavior by the synergic use of remote sensing systems: Doppler wind lidar, aerosol elastic lidar and microwave radiometer** *Atmos. Chem. Phys., 19, 1263-1280, https://doi.org/10.5194/acp-19-1263-2019, 2019* Gregori de Arruda Moreira, Juan Luís Guerrero-Rascado, Jose Antonio Benavent-Oltra, Pablo Ortiz-Amezcua, Roberto Román, **Andrés Esteban Bedoya-Velásquez,** Juan Antonio Bravo-Aranda, Francisco Jose Olmo-Reyes, Eduardo Landulfo, and Lucas Alados-Arboledas
6	2019	**February 2017 extreme Saharan dust outbreak in the Iberian Peninsula: from lidar-derived optical properties to evaluation of forecast models** *Under review. ATMOSRES_2019_249*

		Alfonso J. Fernández, Michaël Sicard, Maria J. Costa, Juan L. Guerrero-Rascado, José L. Gómez-Amo, Francisco Molero, Rubén Barragán, Sara Basart, Daniele Bortoli, **Andrés E. Bedoya-Velásquez**, María P. Utrillas, Pedro Salvador, María J. Granados-Muñoz, Miguel Potes, Pablo Ortiz-Amezcua, José A. Martínez-Lozano, Begoña Artíñano, Constantino Muñoz-Porcar, Rui Salgado, Roberto Román, Francesc Rocadenbosch, Vanda Salgueiro, José A. Benavent-Oltra, Alejandro Rodríguez-Gómez, Lucas Alados-Arboledas, Adolfo Comerón, and Manuel Pujadas
		Retrieval of optical and microphysical properties of transported Saharan dust over Athens and Granada based on multi-wavelength Raman Lidar measurements: study of the mixing processes
7	**2019**	*Under review. Atmos. Env., ATMENV-D-18-02053.*
		O. Soupiona, S. Samaras , P. Ortiz-Amezcua, C. Böckmann , A. Papayannis , G.A. Moreira , J.A. Benavent-Oltra, J.L. Guerrero-Rascado, **A.E. Bedoya-Velásquez** , R. Román, F.J. Olmo, M. Mylonaki , P. Kokkalis, L. Alados-Arboledas, C.A., Papanikolaou, R. Foskinis
		Extinction-related Angtröm exponent characterization of submicrometric volume fraction in atmospheric aerosol particles
8	**2019**	*Under review. Atmos. Env., ATMOSRES_2019_63.*
		Quirantes, A., Titos, G., Benavent-Oltra, J.A., Foyo-Moreno, I., **Bedoya-Velásquez, A.E**., Valenzuela Gutierrez, A., Cazorla, A., Olmo-Reyes, F.J., Lyamani, H., Ortiz-Amezcua, P.,-Ramírez D., Guerrero-Rascado, J.L., Bravo-Aranda, J.A., Alados-Arboledas, L.,Casquero-Vera, J.A.

Conferences

		Hygroscopic growth study during the SLOPE I campaign: synergy of remote sensing and in-situ instrumentation
1	**2017**	*Poster. ACTRIS-2, meeting*
		Bedoya-Velásquez A.E., Navas-Guzmán F., Granados-Muñoz M.J., Titos G., Román R., Casquero-Vera J.A., Ortiz-Amezcua P., Benavent-Oltra J.A., Moreira G.A., Montilla-Rosero E.8, Hoyos Ortiz C.D., Artiñano B., Coz E., Alados-Arboledas L. and Guerrero- Rascado J.L.
		Main features of an outstanding desert dust transport over Iberia
		Poster. Proceeding book of RICTA 2017
2	**2017**	Costa, M. J.; Guerrero-Rascado, J. L.; Sicard, M.; Gómez-Amo, J. L.; Ortiz-Amezcua, P.; Bortoli, D., Comerón, A.; Marcos, C.; **Bedoya-Velásquez, A. E**.; Muñoz-Porcar, C.; Benavent-Oltra, J. A.; Rodríguez-Gómez, A.; Román, R.; Pereira, S.; Cazorla, A.; Potes, M.; Valenzuela, A.; Alados-Arboledas, L.; Silva, A.M.
3	**2017**	**Instrumentation inter-comparison and atmospheric boundary layer height retrievals during SLOPE II campaign at Granada (Spain)**

		EMS Annual Meeting Abstracts, Vol. 14, EMS2017-686
		Juan Luis Guerrero-Rascado, Maria Joao Costa, Alberto Cazorla, Miguel Potes, **Andrés Esteban Bedoya-Velásquez**, Daniele Bortoli, Pablo Ortiz-Amezcua, Juan Antonio Benavent-Oltra, Roberto Román, Lucas Alados-Arboledas
4	**2017**	**Investigating aerosol hygroscopic enhancement factors by combination of automatic remote sensing instrumentation and chemical characterization**
		Oral. Delf. 3rd ACTRIS-2 WP2 Workshop
		Andrés Bedoya-Velásquez, Gloria Titos, Juan A. Bravo-Aranda, Martial Haeffelin, Olivier Favez, Valérie Gros, Juan Luis Guerrero-Rascado, and Lucas Alados-Arboledas
5	**2018**	**Studying the Turbulence During a Saharan Dust Outbreak in SLOPE-I Campaign**
		Poster. European Lidar Conference 2018 (ELC2018). Proceeding book of ELC2018, 72
		G. A. Moreira, J. L. Guerrero Rascado, P. Ortiz-Amezcua, J. A. Benavent-Oltra, R. Róman, **A. E. Bedoya-Velásquez**, F. J. Olmo-Reyes, E. Landulfo and L. Alados-Arboledas
6	**2018**	**Statisticalanalysisof aerosol propertiesretrieved by GRASP overSão Paulo (Brazil)**
		Poster. European Lidar Conference 2018 (ELC2018). Proceeding book of ELC2018, 72
		Benavent-Oltra, J. A.; Román, R.; Pérez-Ramírez, D.; Lopes, F. J. S.; Moreira, G. A.; **Bedoya-Velásquez A.E**.; Ortiz-Amezcua, P.; Casquero-Vera, J. A.; Lyamani, H.; da Silva, J. J.; Lopatin, A.; Guerrero-Rascado, J.L.; Artaxo, P.; Landulfo, E.; Olmo , F. J.; Alados-Arboledas, L.
7	**2019**	**Seasonal analysis of temperature and relative humidity profiles and integrated water vapor from microwave measurements over Granada (Spain)**
		Oral. X workshop on Lidar Measurements in LatinAmerica (WLMLA)
		Bedoya-Velásquez, A. E., Navas-Guzmán, F., de Arruda Moreira, G., Román, R., Cazorla, A., Ortiz-Amezcua, P., Benavent-Oltra, J. A., Alados-Arboledas, L., Olmo-Reyes, F. J., Foyo-Moreno, I., Montilla-Rosero, E., Hoyos, C. D., and Guerrero-Rascado, J. L.
8	**2019**	**Investigating aerosol hygroscopic enhancement factors by combination of automatic remote sensing and chemical analysis**
		Oral. X workshop on Lidar Measurements in LatinAmerica (WLMLA)
		Bedoya-Velásquez, A.E., Titos, G., Bravo-Aranda, B.A., Haeffelin, M., Favez, O, Petit, J.E., Casquero-Vera, J.A, Olmo-Reyes, F.J., Montilla-Rosero, E., Hoyos, C.D., Alados-Arboledas, L., and Guerrero- Rascado. J.L.
9	**2019**	**Remote sensing and in-situ instrumentation synergy for studying aerosol hygroscopic growth: case from SLOPE I campaign**
		Poster. X workshop on Lidar Measurements in LatinAmerica (WLMLA)
		Bedoya-Velásquez, A. E., Navas-Guzmán, F., Granados-Muñoz, M. J., Titos, G., Román, R., Casquero-Vera, J. A., Ortiz-Amezcua, P., Benavent-Oltra, J. A., de Arruda Moreira, G., Montilla-Rosero, E., Hoyos, C. D., Artiñano, B., Coz, E., Olmo-Reyes, F. J., Alados-Arboledas, L., and Guerrero-Rascado, J. L.

		Preliminary studies of aerosol hygroscopic growth using automatic remote sensing instrumentation at SIATA stations in Medellín (Colombia)
10	**2019**	*Poster. X workshop on Lidar Measurements in LatinAmerica (WLMLA)*
		Bedoya-Velásquez A.E., Montilla-Rosero E., Herrera Mejía L., Alados-Arboledas L., Guerrero-Rascado J.L., and Hoyos C.D.
		Retrieval of aerosol optical properties using vaisala CL51 ceilometer corrected data
11	**2019**	*Poster. X workshop on Lidar Measurements in LatinAmerica (WLMLA)*
		Juan Diego Areiza, **Andrés Esteban Bedoya-Velásquez**, Carlos Hoyos, Laura Herrera, and Elena Montilla -Rosero
		Retrieving Cloud Properties from Solar Background Signal by Ground-Based Lidar Measurements over the Southeastern Spain
12	**2019**	*Poster. X workshop on Lidar Measurements in LatinAmerica (WLMLA)*
		M. García-Reyes, J. A. Bravo-Aranda, P. Ortiz-Amezcua, J. A. Benavent-Oltra, **A. E. Bedoya-Velásquez**, L. Alados-Arboledas, J. L. Guerrero-Rascado
		Validation and statistical analysis of temperature, humidity profiles and Integrated Water Vapor (IWV) from microwave measurements over Granada (Spain)
13	**2017**	*Poster. Geophysical Research Abstracts, vol. 19, EGU 2017 – 10312*
		Bedoya-Velásquez, A. E., Navas-Guzman, F., Guerrero-Rascado, J.L., Alados-Arboledas, L
		Aerosol vertical properties retrieved by GRASP code during SLOPE I and II campaigns
14	**2018**	*Poster.The 9th International Workshop on Sand / Dust storm and Associated Dustfall - DUSTworkshop9. Proceeding book of DUST workshop 9, 193-194.*
		Benavent-Oltra, J. A.; Román, R.; Casquero-Vera, J. A.; Pérez-Ramírez, D.; Lyamani, H.; Ortiz-Amezcua, P.; **Bedoya-Velásquez, A. E**.; Guerrero-Rascado, J. L.; Dubovik, O.; Olmo, F. J.; Alados-Arboledas, L
		February 2017 extreme Saharan dust storm in the Iberian Peninsula
15	**2018**	*Poster.The 9th International Workshop on Sand / Dust storm and Associated Dustfall - DUST workshop 9. Proceeding book of DUST workshop 9, 113-114*
		Fernández, A. J.; Sicard, M.; Costa, M. J.; Guerrero-Rascado, J. L.; Basart, S.; Gómez-Amo, J. L.; Molero, F.; Barragán, R.; Bortoli, D.; **Bedoya-Velásquez, A. E**.; Utrillas, M. P.; Salvador, P.; Granados-Muñoz, M.J.; Potes, M.; Ortiz-Amezcua, P.; Martínez-Lozano, J. A.; Artíñano, B.; Muñoz-Porcar, C.; Salgado, R.; Román, R.; Rocadenbosch, F.; Salgueiro, V.; Benavent-Oltra, J. A.; Jorba, O.; Rodríguez-Gómez, A.; Alados-Arboledas, L.; Comerón, A.; Pujadas, M.
	2018	**Tropospheric and stratospheric impact of Canadian smoke plumes over the Iberian**

	Peninsula in August-September 2017
	Poster. European Lidar Conference 2018. Proceeding book of ELC2018, 22
16	Sicard, M.; Granados-Muñoz, M. J.; Papagiannopoulos, N.; Alados-Arboledas, L.; Barragán, R.;**Bedoya-Velásquez, A. E**.; Benavent-Oltra, J. A.; Bortoli, D.; Comerón, A.; Córdoba-Jabonero, C.; Costa, M.J.; del Águila, A.; Fernández, A. J.; Gómez-Amo, J. L.; Guerrero-Rascado, J. L.; Jorba, O.; Martínez-Lozano, J. A.; Molero, F.; Muñoz-Porcar, C.; Ortiz-Amezcua, P.; Potes, M.; Pujadas, M.; Rocadenbosch, F.; Rodríguez-Gómez, A.; Román, R.; Salgado, R.; Salgueiro, V.; Utrillas, M. P.; Yela, M.